Designing Stimuli-Responsive Porous Silica Materials using Solid Lipid Nanoparticles (SLN) and Magneto-responsive Surfactants for Delivery of Curcumin

Sanghoon Kim

Collégium SCIENCES & TECHNOLOGIES
Pôle scientifique Chimie Physique Moléculaires
Ecole Doctorale SESAMES ED 412

Thèse

Présentée pour l'obtention du titre de

Docteur de l'Université de Lorraine

en Chimie

par

Sanghoon KIM

Designing Stimuli-Responsive Porous Silica Materials using Solid Lipid Nanoparticles (SLN) and Magneto-responsive Surfactants for Delivery of Curcumin

Soutenance le 28 octobre 2015

Membres du jury :

Rapporteurs :	M. Jordi Esquena Moret	Directeur de Recherche Institut de Chimie Avancée de Catalogne, Espagne
	M. Werner Kunz	Professeur Université de Regensburg, Allemagne
Directrices de thèse :	Mme Andreea Pasc	Maitre de conférences (HDR) Université de Lorraine, Nancy
	Mme Marie-José Stébé	Directrice de Recherche Emérite CNRS Université de Lorraine, Nancy
Invité :	M. Alain Durand	Professeur Ecole Nationale Supérieure des Industries Chimiques (ENSIC), Université de Lorraine, Nancy

Table of contents

Acknowledgements

I would like to express my gratitude to the countless people who have helped and supported me during the course of my PhD work. This dissertation would not have been possible without you.

First and foremost, I would like to thank my advisors, Dr. Marie-José Stébé, Directrice de Recherche CNRS and Dr. Andreea Pasc, Maître de Conférences (HDR) at l'Université de Lorraine, for letting me be a part of their research group. Their encouragement to think independently, motivation and guidance during my PhD thesis made this research project successful.

I would also like to thank Dr. Jordi Esquena Moret, Research Director at the Institute of Advanced Chemistry of Cataluña in Spain and Prof. Dr. Werner Kunz at Universität Regensburg in Germany for agreeing to judge this work as rapporteurs.

Next, I would like to thank my dear colleagues, with whom I shared 3 years of happy memories. First my thanks go to Dr. Christine Bellouard, Dr. Nadia Canilho, Dr. Emmanuel Lamouroux, Dr. Roudayna Diab and Mélanie Emo with whom I worked closely on a number of research projects. I was lucky to be able to learn from these hardworking people. Their dedication has great impact on me during my PhD thesis, and raises the level of my research projects. These projects would never have come to fruition without you. I would also like to thank all members of Microbiology Laboratory, Prof. Raphaël E Duval, Dr. Stéphane Fontanay, Dr. Stéphanie Philippot and Dr. Mihayl Varbanov for their helpful advise and comments on our collaborative projects.

I would also like to thank all the students I have had the opportunity to work with: Jonathan, Carine, Philippe, Fernanda, Sijin, Ilieana, Issam, Marie, Lionel and Dominique for sharing your space and treating me as one of your own. It would have been a lonely few years without you.

Finally, I want to thank my family, my friends for their support during these three years. In closing, I will wish to dedicate this manuscript to my wife, Eun Jeong.

General Introduction

Since the first discovery of mesoporous silica materials in 1992, a lot of efforts have been addressed by scientists for applications of these materials in various fields. Due to their large surface area, pore size as well as well ordered pore network, mesoporous silica materials have shown their potential in applications, including catalysts, drug delivery system, chemical sensors, and so on. Moreover, since the surface functionalization, the control of pore size and the morphology modification could be easily achieved compared to other materials such as zeolite, the synthesis and the tailoring of these materials have been largely investigated within the past decades.

In biomedicine domain, mesoporous silica materials have gained much recent attention, due to their unique properties such as uniform pore network, but especially due to significant biocompatibility. Moreover, because of the ease of their functionalization, mesoporous silica materials have been considered as well-suited theranostic platform for drug delivery system. The bioavailability of hydrophobic drug molecules that exhibit an extremely low solubility and tend to be aggregated in physiological condition could be enhanced in mesopores. This results in reducing the size and the crystallinity of drug that would help the solubility.

It is also possible to design mesoporous silica materials with the stimuli-responsiveness for smart drug delivery system. The goal of designing stimuli-responsive drug delivery system is to control the release rate of drug, especially to prevent the burst release of drug before reaching the target and to control the release rate of drug. Among various methods, pore gate sealing, covalent or ionic bond between drug and functionalized mesopore surface have been mainly applied depending on different stimulus such as pH, redox, temperature or magnetic filed. Moreover, it should be noted that stimuli-responsive system with “zero-release’ before targeting is especially important for cancer treatment, in which the drug might induce serious side effects to normal tissue.

However, despite of some exciting results for well-designed smart drug delivery system with controlled drug release upon different stimulus and enhanced bioavailability, one needs to optimize the synthesis of drug delivery system based on mesoporous silica materials that should also meet the criteria (*i.e.* biocompatibility) in order to better target the specific needs like cancer treatment.

To achieve this aim, in this thesis, we focus on designing mesoporous silica materials that respond to two stimuli systems, pH and magnetic fields. A model hydrophobic anticancer drug molecule, curcumin is used to validate newly designed mesoporous silica materials. To

do so, first, a novel strategy that consists in using solid lipid nanoparticles (SLN) as template for meso-macroporous silica has been applied in various domains, but here, the development of stimuli responsive drug delivery system is mainly concerned. In addition, the post-synthesis modification method like pore sealing is employed to achieve multi-stimuli responsive drug nanovectors. Second, magnetic surfactants open a new route for the design of molecularly organized systems such as magnetic vesicles that provide insight look of self-assembly mechanism, when combined with magnetic properties measurement. Qfterward These types of self-assembled magnetic surfactants are used as template of magnetic porous silica materials either with or without metallic nanoparticles inside pore system.

Chapter 1 deals with the basic introduction of mesoporous silica materials as a promising candidate for stimuli-responsive drug delivery system. The main advantages of mesoporous silica materials over conventional drug delivery system are pointed out with their unique properties such as facile synthesis, modification and biocompatibility. The concept of stimuli-responsive (*i.e.* pH, temperature) mesoporous silica, and some examples of these materials are presented.

Chapter 2 contains three projects (Part 2.1 to 2.3) for development of drug delivery systems based on porous silica. First, the encapsulation and the release of a hydrophobic natural polyphenolic drug, curcumin, from a novel nanovector consisting of solid lipid nanoparciles (SLN) and mesoporous silica matrix are investigated in Part 2.1. The main idea is to mineralize curcumin loaded SLN dispersion using silica precursor, resulting in hierarchically ordered hybrid organic-inorganic porous silica. Here, SLN acts as reservoir of curcumin, while mesopores act as pathways to control drug release. This study also revealed a good biocompatibility of these hybrid silica materials due to high content of lipid.

The concept of combining solid lipid nanoparticles with porous silica is extended to obtain hybrid core-shell silica microcapsules as presented in Part 2.2. The studies of *in vitro* release, cytotoxicity and cellular uptake into Caco-2 cells that are the unique in vitro cell model approved by the FDA for *in vivo* bioavailability, demonstrated the potential application of novel hybrid silica capsule for oral administration.

Part 2.3 deals with the development of multi stimuli-responsive drug nanocarriers based on the post-synthesis modification method of mesoporous silica nanoparticles. One-step coating method using coordination complex of natural polyphenols, tannic acid and Fe (III) ions on the surface of silica was applied, resulting in pH- and glutathione-responsive release of

curcumin. The toxicity of these newly designed drug delivery systems was also investigated to validate this concept.

Chapter 3 (Part 3.1 to 3.3) describes the formation of molecularly organized systems solely from magneto-responsive surfactants and their applications in various fields such as catalysis. First, Part 3.1 focuses on the synthesis and self-assembly properties of magneto-responsive surfactants. The structure of vesicles that is self-assembled system of these magneto-responsive surfactants was investigated. Taking advantage of paramagnetic signal of the surfactants, the mechanism of vesicles formation is highlighted.

Part 3.2 describes a potential application of magneto-responsive surfactants for the synthesis of magnetic mesoporous silica. Soft colloidal templates, micelles, formed by magneto-responsive surfactants could imprint both mesoporosity and iron in hard silica materials. The magnetic properties for the resulting silica material are also investigated.

Magneto-responsive surfactants were then used for designing hierarchical meso-macroporous silica supported catalysts, as described Part 3.3. Solid lipid nanoparticles (SLN) stabilized by these surfactants was mineralised using silica precursor, resulting in metallic nanoparticles embedded meso-macroporous silica in one-pot process. Dark Fenton-like reaction towards methylene blue degradation was investigated to evaluate the performance of the newly designed catalyst.

Finally, the conclusions and the major contributions of this work are highlighted and the perspectives for future works are presented.

Introduction Générale

Depuis la découverte de matériaux silicatés mésoporeux en 1992, beaucoup d'efforts ont été déployés par les scientifiques pour des applications dans différents domaines. En raison de leur grande surface, leur taille de pores modulable ainsi que leur étonnante organisation des canaux poreux, les matériaux silicatés mésoporeux ont des potentielles applications, notamment comme catalyseurs, systèmes de vectorisation de médicament, capteurs chimiques, etc. En outre, puisque la fonctionnalisation de surface, le contrôle de la taille des pores et la modification de la morphologie peuvent être facilement obtenus comparés à d'autres matériaux tels que les zéolites, ces matériaux ont été beaucoup étudiées afin d'être adaptés à ces applications.

Dans le domaine de la biomédecine, les matériaux silicatés mésoporeux ont fait récemment l'objet de beaucoup d'attention, en raison de leurs propriétés spécifiques tel que le réseau de pores homogènes, mais surtout en raison de la biocompatibilité de la silice. En plus, en raison de la facilité de leur fonctionnalisation, les matériaux silicatés mésoporeux ont été considérés comme plate-forme théranostique bien adapté pour le système de liberation de médicament. La biodisponibilité de molécules hydrophobes qui présentent une très faible solubilité en milieu aqueux et qui ont tendance à être agrégés dans les conditions physiologiques pourrait être améliorée en utilisant ces matériaux silicatés mésoporeux. Ainsi, une réduction de la taille et de la cristallinité du médicament pourrait contribuer à une meilleure solubilité.

Il est également possible de concevoir des matériaux silicatés mésoporeux ayant des stimuli-responsivités pour la conception de systèmes intelligents de libération de médicaments. Le but de concevoir des systèmes stimuli-sensibles de délivrance de médicaments est de contrôler la vitesse de libération du médicament, afin de prévenir en particulier la libération rapide avant d'atteindre la cible ainsi que de maîtrier le taux de libération du médicament. Parmi les diverses méthodes, '*pores sealing'* et l'autre méthode associant une liaison ionique ou covalente entre le médicament et les matériaux mésoporeux ont été principalement employés avec des stimuli tels que le pH, le redox, la température ou le champ magnétique. En outre, il convient de noter que les systèmes '*zero-release*' avant la cible sont particulièrement important pour le traitement du cancer, puisque le médicament induit bien souvent des effets secondaires qui ravagerait pour les tissus sains.

Cependant, en dépit de certains résultats prometteurs, il faut optimiser la conception des systèmes de délivrance de médicaments à base de matériaux silicatés mésoporeux, qui doivent répondre également à plusieurs critères (*i.e.* biocompatibilité) afin de mieux cibler les besoins spécifiques.

Pour atteindre cet objectif, dans cette thèse, nous nous concentrons sur la conception de matériaux silcatés mésoporeux qui répondent à deux systèmes de stimuli, le pH et les champs magnétiques. Une molécule hydrophobe anticancéreuse, la curcumine est utilisée pour tester les matériaux silcatés mésoporeux mis au point dans ce travail. Tout d'abord, une nouvelle stratégie qui consiste à utiliser des nanoparticules lipidiques solides (SLN) en tant que '*template'* pour la synthèse des silices méso-macroporeuses a été mise en œuvre pour la libération de médicament. En outre, la modification post-synthèse par la méthode '*pore sealing*' a été utilisée pour développer des nano-vecteurs multi stimuli-sensibles. Deuxièmement, les tensioactifs magnétiques ouvrent une nouvelle voie pour la conception de systèmes moléculaires organisés tels que les vésicules magnétiques. Ces types de tensioactifs magnétiques sont ensuite utilisés comme '*template'* pour préparer des matériaux magnétiques silicatés poreux en présence ou non de nanoparticules métalliques à l'intérieur des canaux poreux.

Le chapitre 1 est une introduction pour présenter les matériaux silicatés mésoporeux comme candidat prometteur pour des systèmes stimuli-sensibles de délivrance de médicaments. Les principaux avantages des matériaux silicatés en comparaison avec les médicaments conventionnels sont décrits en détail. Le concept de matériaux silicatés mésoporeux répondant à des stimuli (pH, température) est expliqué à l'aide de nombreux exemples.

Le chapitre 2 contient est consacré au développement de systèmes d'administration de médicaments à base de silice poreuse. Tout d'abord, l'encapsulation et la libération d'un médicament polyphénolique naturel hydrophobe, la curcumine, à partir du *nanovecteur* constitué de nanoparticules solides lipidiques (SLN) et de la matrice de silice sont étudiées dans la partie 2.1. L'idée principale a été d'encapsuler la curcumine dans la dispersion SLN et de la protéger par minéralisation, en utilisant un précurseur de silice, pour former un système hybride organique-inorganique hiérarchisée. Les SLN peuvent être considérés ici comme réservoir de la curcumine, tandis que la présence des mésopores contrôle la libération du médicament.

L’association des nanoparticules lipidiques solides avec la silice poreuse est ensuite mise à profit pour obtenir des microcapsules hybrides de type core-couronne (*core-shell*) et les résultats sont présentés dans la partie 2.2. Les études de libération *in vitro*, la cytotoxicité et l'absorption cellulaire dans les cellules Caco-2 ont permis d’évaluer les microcapsule hybride à base de silice en voie d’une administration orale.

Partie 2.3 traite du développement des matériaux silicaté mésoporeux multi stimuli-sensibles par modification post-synthèse. Un procédé de revêtement en une seule étape, en utilisant des complexe de coordination de polyphénols naturels, l'acide tannique et Fe (III) a été mis en œuvre en rendant les systèmes sensibles à pH et au glutathion pour la libération de la curcumine. La toxicité de ces systèmes de délivrance de médicaments a également été étudiée.

Le chapitre 3 concerne la formation de systèmes moléculaires organisés à partir de tensioactifs magnéto-sensibles et leurs applications dans divers domaines comme catalyse. Tout d'abord, la partie 3.1 décrit sur la synthèse et les propriétés d'auto-assemblage de tensioactifs magnéto-sensibles ainsi que la structure des vésicules à base de ces composés. Profitant des réponses paramagnétiques des tensioactifs magnétiques, le mécanisme de formation de vésicules a été appréhendé.

Ensuite, les tensioactifs magnétiques sont utilisés pour la synthèse de silice mésoporeuse magnétique. Les micelles, formées par les tensioactifs magnétiques ont servi pour produire la mésoporosité et l’addition de fer dans les matériaux offre des possibilités d’applications.

Enfin, le développement de catalyseurs supportés sur la silice méso-macroporeuse hiérarchique est décrit à la fin de ce chapitre (partie 3.3). Les nanoparticules lipidiques solides (SLN) stabilisées par les tensioactifs magnetiques sont minéralisées en utilisant un précurseur de silice, en conduisant à cette formation de nanoparticules métalliques incorporés dans la silice méso-macroporeuse. La réaction de *Dark-Fenton* pour la dégradation de bleu de méthylène à été étudiée afin d’évaluer la performance du nouveau catalyseur.

Chapter 1

Literature Review

1.1 Silica responding to challenges in drug delivery

The ongoing development in drug delivery technologies tends to take into account primary factors such as the nature of therapeutics being delivered, the mode of administration beneficial to the patient, and cost.

1.1.1 Porous Materials

In addition, currently challenges consist of considering therapeutic and physiological criteria for the development of drug delivery devices that

- Improve drug efficiency

- Reduce drug side effects

- Control sustained drug release

- Increase drug bioavailability

- Facilitate drug administration and use compliance

Implants and cancer treatments have opened the way to new materials and biocompatible therapeutic systems.[1] Indeed, in this field, the nature of the vector is a strategic choice from the medical point of view. For a long-time, biocompatible polymers either pH or thermally sensitive, have been used as drug delivery systems (DDS). But polymeric carriers have a limited efficacy in terms of drug loading, especially due to their low porosity and, therefore, the researches oriented to porous materials, with high pore volume and specific surface. One example is carbon nanotubes (i.e. single walled and multi walled). These nanomaterials have shown interesting results as drug carriers, however their use is rather limited due to their lack of biodegradability and toxicity resulting from their accumulation in the body tissues. Therefore, inorganic biomaterials seem to be the most advantageous, due to their porosity, which stands loading capacity, thermal and chemical stability under physiological conditions. They are also appreciated for their good biocompatibility but present a lower degradable rate except for silica-based biomaterials. In addition, physical and chemical properties are easily tuneable in regards to the medical application. Hence, porous silica materials are the current subject of high interests through their biocompatibility and the high loading drug capacity. Moreover, therapeutics drug nanoparticles carriers are mainly designed to overcome some drug constraints such as poor solubility, limited stability, rapid metabolization, excretion of the drug, undesired side effects, and lack of selectivity toward specific cells types.

However, in order to design a specific drug release system (DDS), some criteria must be integrated to the porous silica support through several functionalization ways that are constantly under study and that contribute to control the molecular drug release with a proper rate.[2] Those criteria are also valid for oral drug release delivery of pharmaceutical molecules, protein and nucleotide-based drugs.

Among silica vectors, mesoporous silica nanoparticles (MSNs) are being extensively studied to design multifunctional cargo in order to achieve drug release under different stimuli-responsive trigger systems (Figure 1.1).[3]

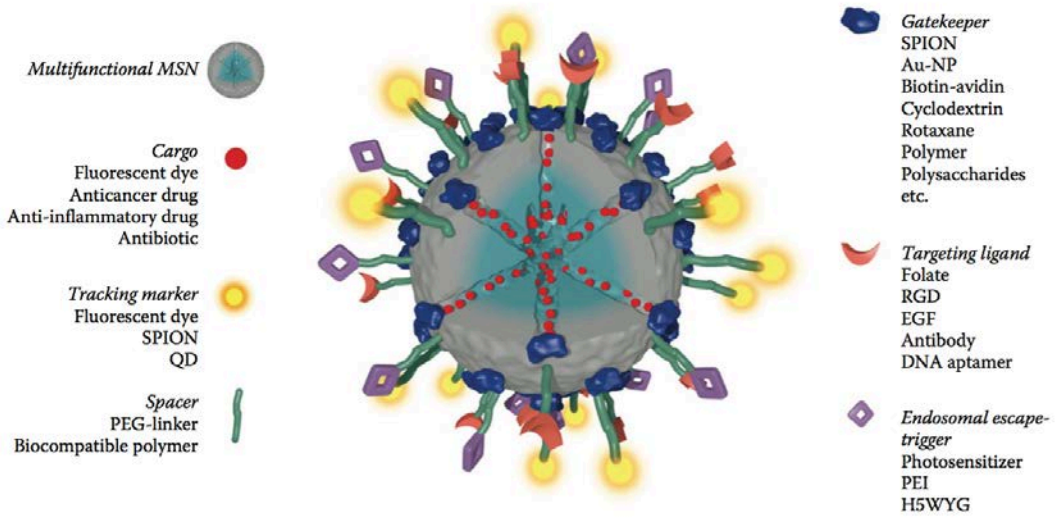

Figure 1.1. Schematic illustration of a multifunctional MSN containing the necessary features for a stimuli-responsive controlled release of the loaded cargo into the cytosol of a targeted cell. SPION, superparamagnetic iron oxide nanoparticle; QD, quantum dot; PEG, poly(ethylene glycol); Au-NP, gold nanoparticle; RGD, Arg-Gly-Asp amino acid sequence; EGF, epidermal growth factor; PEI, poly(ethylene imine); H5WYG, endosomolytic peptide.[3]

The tuning of MSNs must also improve biocompatibility and prevent endosomal escape. Thus, the nanoparticles can be hybrid organic-inorganic core-shell with targeting ligands for specific cellular recognition or markers for the particle tracking in the cells.

Another challenge for MSNs cargos is the particle sizing. In fact, it is now well known that some synthesis parameters such as concentrations, pH, chemical nature of the surfactants, temperature and reaction time allow controlling the morphology, the structure and the pore size of the mesoporous silica material.[4-9] Nevertheless, for drug delivery into cells, particle size must be less than 120 nm to facilitate endocytic uptake.[9]

1.1.2 Administration routes

Although the methods of treatment are relatively specific to each disease, in the case of cancer, multiple administration routes are explored:

- Intravenous injection

- Pulmonary inhalation

- Dermal application

- Oral uptake

- Local drug delivery.

There are specific constraints linked to the administration route. In the case of **local drug delivery systems** (LDDS), ordered nanoporous alumina and nanotubular titania are the most advanced and smart drug-releasing implants.[10] They are biocompatible materials, able to load important amounts of drug into the nanostructured matrix and release chemicals, with zero-order kinetics, under various release triggers (magnetic field, ultrasonication, radiofrequency). Despite the continuously extending range of applications, including bone therapies, cardiovascular stents, post-surgical healing, treatment of localized infection, inflammation or cancer, these systems are limited to therapies in which an implantable device can be introduced.

Oral administration has been exploited for most drugs due to several great advantages such as production cost, various packaging as well as user-friendliness. Pills or capsules are general forms of drugs for oral route. Both products in question do not need to be sterilized, hence reducing dramatically production and logistic costs for pharmaceutical industry. Being able to use several excipients is also a good advantage for oral administration type of drug. Extended or sustained drug release can be easily achieved using specific excipients like polymeric matrix based on xanthan gum.[11] Oral drug delivery technologies have been also developed to preserve the drug from the acidic environment of the digestive tract, up to the gastrointestinal barrier where it should be released. However, one disadvantage, specifically in cancer therapy, is that vectors could generate side effects and have limited effectiveness mainly because of the lack of target specificity. Moreover, oral administration might be limiting the bioavailability of the active ingredient. Some of the hydrophobic active ingredients like curcumin show extremely poor bioavailability that might be caused by its insolubility in water, poor absorption, rapid metabolism and systemic elimination.[12] In

addition, absorbed drug must pass the liver that accelerates rapid metabolism. As the result, the drug becomes less active. This phenomenon is often called first-pass effect.[13] Another disadvantage is that drug absorption is highly dependent on the interaction with food in the stomach. For instance, some drugs such as griseofulvin shows poor adsorption in presence of food, however absorption ability of propranolol is enhanced in presence of food. Despite this fact, the relation between drug and food has not been systematically studied, each case should be taken into consideration.[14] Additionaly, the size might also cause a minor problem for patients, particularly in children, who rarely swallow sizable tablets or capsules as a whole.[15] Thus, often most ingredients for drug in tablet form are pharmaceutically inactive excipients, thus reducing or replacing some excipients could reduce drug size and enhance user-friendliness.[16] Actually, many studies have been done to overcome disadvantages concerning oral administration drug. Nonetheless, no 'magical' system has been proposed as a solution to the problems mentioned above, perhaps except for mesoporous silica nanoparticles (MSN). MSN has well ordered mesopores (2 – 50 nm) with high pore volume as well as large surface area. Drug molecules can be encapsulated inside mesopores without difficulty. MSN can also serve as a good protection barrier for drug molecules. Therefore, many problems concerning bioavailability or interaction with food could be resolved or had been already solved.[17]

The field of application for MSN is not limited to oral administration but could be extended to **topical administration**, depending on the target. Indeed, this administration can be divided into two general terms: 1) skin and 2) mucosal membranes system. If the target is the human skin (case 1), one of the traditional formulations of the drug is a cream or ointment for the direct dermal application. Patch form formulation has been also widely used, especially, for stop-smoking therapy.[18] These formulations have numerous advantages e.g. no first-pass effect and user-friendliness. Moreover, controlled drug delivery system could be also achieved using several membrane sheets in the patch formulation. However, the cost of production is not as low as for the tablet or capsule formulations. Particularity, for cream and ointment, highly purified water is needed because of the risk of bacteria proliferation. Furthermore, a large amount of addictives (the toxicity for some of them are still controversial) should be added for the same reason.[19] In addition, for cream and ointment, drug burst release, along with the degradation of the initial formulation, is a limiting factor for certain active ingredients. Targeting mucosal membranes system (case 2) is a more complicated challenge, compared to a direct application on skin. In general, human mucosal membranes like nasal (nose) and buccal (oral) mucosals are 'naked' towards outside and

directly suffer from external environment, due to the lack of physical barriers (skin).[20] Thus, in terms of formulation, only few excipients are allowed and the use of irritating preservatives is strictly prohibited. Moreover, highly clean production conditions and an appropriate logistic system are required, which result in an expensive drug for the final customers. Here, using MSN in formulations can also be an alternative way to overcome these issues, especially in case of the patch formulation for human skin targeting. As explained, a drug that is encapsulated inside MSN is not directly exposed to external environment. A well-protected drug has fewer chances of being degraded, hence additive use is considerably reduced, and a long-term drug release could be also achieved. In addition, Additionally, stimuli-response of MSN to pH of the skin or temperature can provide 'perfect' tools for some formulations that have systematic burst release. (Note that pH of human skin is slightly acidic (4 - 5)[21], and skin temperature is around 31°C[22]). Detailed explanation on stimuli-responsive MSN strategy was also covered later.

MSN would also have a distinguishable position among drugs for intravascular (parenteral) administration. Taking a careful look into the intravascular drug administration, multiply disadvantages have been ignored as a result of the good bioavailability of the drugs. A high concentration of the drug by injection can lead to side effects, so multiple injections with low concentration have been performed causing serious discomforts for patients. For instance, during chemotherapy, antiemetic medication (ondansetron, Zofran as brand name) should be injected several times a day to maintain in the blood the therapeutic concentration. However, MSN, of which the sustained release performance is already confirmed,[2] could be applied to intravascular administration. Through only active ingredient or with small amount of excipients have been used for the injection of the drug formulation, scientists have confirmed that MSN less than 150 nm as diameter have no side effect to rat's cell.[9] Besides, MSN uptake rate into cell (endocytosis) and drug release rate showed that MSN might be an outstanding candidate to replace the traditional injection method.

As highlighted above, MSN revealed distinguished advantages whatever the administration route. Yet the first clinical tests in humans are not planned in the near future. At present time (2015), drug-MSN carriers are only at *in vivo* stage in mouse or rabbit and the first clinical tests are planned for 2017.[23] It seems that to date, the most advanced application of MSN *in vivo* is in bone regeneration. Indeed, MSN embedded inside bioceramic or bioglasses could easily by-pass some problems such as toxicity or bioavailability.[24]

1.2 Nanostructured silica: suitable matrix for loading and release

In the last two decades, investigations on porous materials (i.e. hollow silica) have been engaged in the development of chemical and physicochemical synthesis approaches via sol-gel process[25,26], emulsion/interfacial polymerization methods[27-29] or colloidal templating. Hierarchically ordered porous materials can be prepared via dual templating method, as illustrated in Figure 1.2.

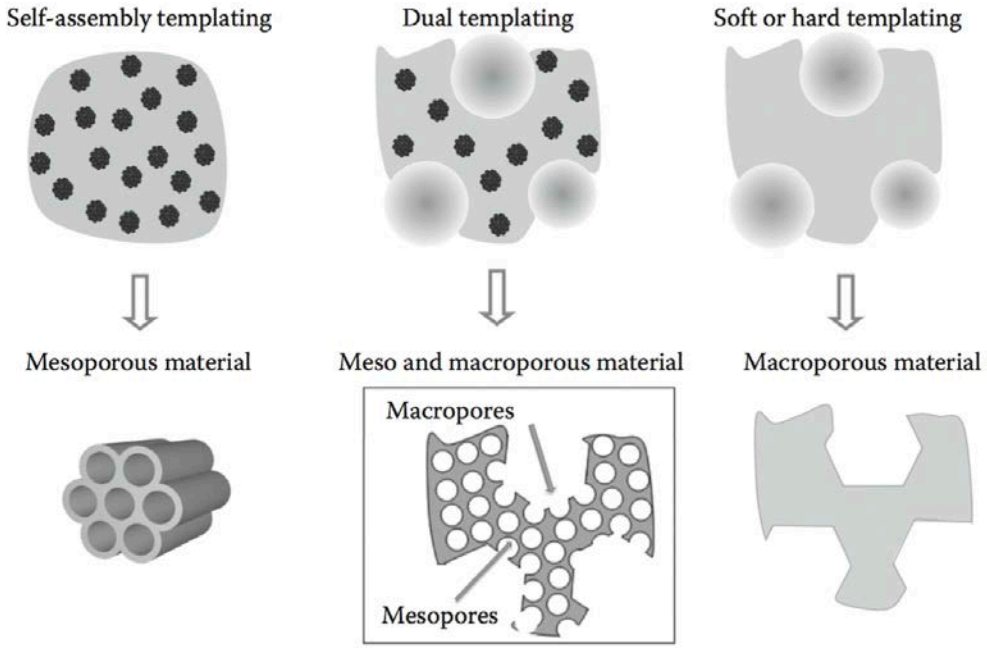

Figure 1.2. Schematic illustration of colloidal templating routes for the synthesis of porous silica mateirals.

Hard templates such as carbon spheres, polymers or metal particle, lead to a good morphology and size control from microns to few nanometers, while with soft templates such as oil and vesicles, the hollow particles present usually poor monodispersity and high deformability due to the soft core. [29,30]

The template-free method seems a new approach for the synthesis of porous materials, especially hollow porous silica. This method combines the advantage of hard- and soft-template approaches avoiding the template-removing procedure. It is based on Ostwald ripening process where small crystals or sol particles dissolve, and redeposit onto larger crystals or sol particles.[31] Then small crystals undergoing dissolution become a nutrient supply for the growth of larger ones. As the system tend to minimize the surface energy,

particles aggregate and the larger ones continue to grow. Void spaces begin to appear progressively during the diffusion of solute outwardly. This solute diffusion phenomenon regulates the thickness of the shell.[32-36] As example, Hal *et al.* prepared hollow silica particles in two steps: hydrolysis of phenyltrimethoxysilane under acidic conditions followed by silane condensation under basic conditions resulting in monodisperse hollow silica particles. The particle sizing has been controlled through hydrolysis time, giving 400 nm in diameter.[37]

Henceforth, spherical hollow silica structures with porous shell are also extensively explored to design controlled delivery biomedical materials. Porous shell exhibits high loading capacity, and could encapsulate small molecules that are generally stimuli sensitive, while in core void space, bulky molecules like genes or biological molecules have been loaded.[38-42] Over time and with the development of new biomedical approaches, magnetic and fluorescent hollow spheres have been preferred for medical imaging applications as markers or trackers for tumor cells.[43-46]

Some others silica matrixes such as nano silica fibers have been investigated to design biomaterials as well, but since there is a limitation in using simple nonporous silica fibers as drug vectors, synthesis research has been rapidly oriented to prepared nanoporous silica. In this context, the work of Stucky *et al.* and Linton *et al.* highlighted the major synthesis parameters capable to influence particle morphology to obtain mesoporous nanorods.

In 2000 Stucky *et al.* were interested in controlling the morphology of mesoporous silica materials using a combination of micelles of block copolymers with cosurfactants, cosolvents or of strong electrolytes. Under acid conditions long mesoporous SBA-15 fibers were successfully prepared by using poly(ethylene oxide)-block-poly(propylene oxide)-block-poly(ethylene oxide) triblock copolymer ($EO_{20}PO_{70}EO_{20}$) as structure directing agent, and tetramethyl orthosilicate (TMOS) as a silica source.[47] More recently Linton *et al.* have investigated the mechanism for the aggregate growth of mesoporous particles in order to control particle size.[48] Furthermore, Ding *et al.* succeeded in obtaining SBA-15 nanorods by adjusting the pH media in the range of 0.5 to 2.5. Through their application, they noticed that SBA-15 rod morphology improved the adsorption of enzymes when compared to conventional spheric particles.[49]

Numerous investigations through the years lead to the synthesis of porous silica nanotubes by variable templating sol-gel methods using inorganic, organic, biological templates, reverse-microemulsions or electrospinning.[50-54] The biosilicification principle inspired from various

marine biological systems, such as diatoms or sponges, is also an interesting route to synthesize hollow porous silica fibers in mild conditions.[55] It was demonstrated that long-chain polyamines are intimately linked to the biosilicification process in the case of diatoms, Following this finding, many efforts have been made in using organic templates such as self-assembled fibrils of polypeptides [56-58] or amine-modified polysaccharides[59] to synthesis of silica nanotubes. In this way, silica with an outer diameter of 15 to 20 nm could be obtained.

As for hexagonal mesoporous silica, silica nanotubes are also designed to be stimuli responsive. The first drug delivery system based on magnetic nanoparticles consisted of mesoporous silica nanorods where pores were end capped by magnetic Fe_3O_4 nanoparticles linked to nanorods through a chemically labile disulfide function. Human cells secrete antioxidant agents such as dihydrolipoic acid (DHLA) and dithiothreitol (DTT) that are capable to cleave disulfide bonds.[60] More importantly, the silica fibers show a strong self-activated luminescence ranging from 300 to 600 nm, and centered at 405 nm, without rare earth or transition metal ions as activators. This sample could be potentially used as an environmental friendly luminescent material. Thereby, interesting optical properties of nanofibers have been enhanced in various researches along the last years. Such as discovered by Hou *et al.* with porous SiO_2 composite fibers. They are focusing on developing synthetic protocols to make high-energy luminescent porous composite fibers of $NaYF_4:Yb^{3+},Er^{3+}@SiO_2$ useful for bioimaging.[61]

Concerning mesoporous silica materials (MSN), since the discovery of MCM-41 mesostructure (Mobil Crystalline Material), many other MSN have been elaborated with different ionic, non-ionic surfactants or copolymers to obtain materials combining variable pore size and morphology together with high surface area and volume.[62-65] The morphology and the size of MSN can be tuned by adjusting pH value, the temperature, the surfactant concentration, the water content and the silica source, afford to.[66] The latest parameters have a strong impact in the silica condensation rate.[67,68]

In biomedical applications, the first example of the use of mesoporous silica nanoparticles (MSN) was reported by Vallet Regí *et al.* in 2001, for the encapsulation of ibuprofen in MCM-41. Since then, mesoporous silica nanoparticles (MSN) were extensively studied to design biomaterials for controlling release delivery of pharmaceutical drugs, genes or proteins and even biocides and nutriments to the target sites. Compared to non-porous silica nanoparticles, mesoporous silica materials with hexagonally ordered pores, present several

advantages such as large specific area, tuneable pores diameter and surface chemistry for hosting molecules with different sizes, shapes and functionalities.

Mesoporous silica material can be functionalized by stimulable molecules or directly by the drug molecule via two main routes. The first modification way is named by one pot where organic molecules are co-condensed at the same time as the silica source. The second one is said by post-synthesis of the silica material. In the latest case, MSN is generally immerged in a solution containing the molecules to be grafted and thus attached covalently or physically (depending on the trigger release) to the silica surface and walls. As an example, Lin *et al.* used different chains length of alkyl methylimidazolium cationic surfactants as template and anti bacterial effect on *Escherichia coli* K12.[70] Today the challenges no longer reside on the synthesis itself, but in the requirements and constant adaptations imposed by the bioscience field.

1.3 Stimuli responsive nanostructured silica materials

Usually mesoporous silica nanoparticles functionalization process can be done following two methods: 1) co-condensation, also called one-pot synthesis and 2) grafting or post-synthesis modification including the surface coating on MSN.[71-76] In general, one of the advantages of co-condensation method is that inorganic-organic hybrid network could be easily obtained.[63,77] Grafting on free silanol groups of MSN could be also efficient approach, especially when external surface modification is needed,[78,79] which could facilitate, for example, the dispersion of MSN in biological environment or to prevent particles aggregation. Another post synthesis functionalization is the imprint coating method, in which MSN are coated with organic molecules containing specific binding such as ligands for ionic complexation.[80-82] Ideally, drug delivery systems (DDS) should be intelligent in sensing the external environment signals. In addition, DDS should release the therapeutic dose of drug *via* appropriate external stimulis.

Indeed, external MSN surface functionalization approach has been used to design drug delivery systems that exhibit multifunctional interactions with specific stimuli, such as external pH level. But also external MSN surface functionalization could be efficient to improve specific cell targeting, prevent burst release or improve biocompatibility and attend colloidal and chemical stability in the environment.[83-85] On the other side, internal

modification of MSN surface with organic entities is generally selected to control drug diffusion, delivery kinetics and stability of the therapeutic molecules.[86,87]

As mentioned previously, stimuli responsive MSN are generally prepared via co-condensation or over a post-synthetic grafting step.[63,88] The challenge is to control the location of the functional groups in mesoporous silica particles. For example, large molecular group like proteins, superparamagnetic iron oxide nanoparticles (SPIONs) or gold nanoparticles (Au-NPs) are used as gatekeepers to block the pore entrances for efficient sealing of the interior of the cargo.[89-92] MSN are sometimes directly functionalized with molecular drug through covalent or coordinative bonds that can be cleaved by specific stimuli such as reducing agents, competitive binding molecules or UV-light.[93-96] Pore sealing can also be achieved by a complete coating of the MSN. For instance, polymers, oligonucleotides or supported lipid bilayers (SLB) have been shown to prevent premature cargo release.[97-106] Often, phase transitions or competitive displacement reactions lead to opening of the pores and efficient cargo delivery.[107,108]

Usually molecules or entities used as stimuli are classified into six categories of stimuli: pH, temperature, redox, magnetic, light and biological stimuli.[109-112] The first works on stimuli responsive materials were focused only on pH and temperature. Now, chemical science has succeeded in combining several stimuli.

1.3.1 pH stimuli-responsive MSN

pH-responsive mesoporous silica nanoparticles (MSN) is one of the earliest investigation in drug delivery since the first application was shown by Vallet-Regí *et al.* in 2001.[69] The use of interaction between the drug and silica matrix, such as hydrogen bonding or electrostatic interaction is common method to load and release the “guest” drug molecule. As already known, these interactions can be more or less strong as a function of the pH. This is the basic concept of pH-responsive drug delivery system based on mesoporous silica nanoparticle. However, without inner surface modification of mesoporous silica, only weak hydrogen bonding involving silanol group could be expected. Thus « guest » drug molecule should contain hydrogen bonding group to improve drug loading efficiency.

To overcome this disadvantage of mesoporous silica as drug delivery system, scientists have conducted several modifications of silica nanoparticles by various functional group such as

amino or carboxylate. Among some outstanding results, Balas *et al.* showed the confinement and the controlled release of alendronate from MCM-41 type mesoporous silica.[113] Alendronate is a bisphosphonate, used as a model drug in osteoporosis treatment. It can be loaded into amino-functionalized mesoporous MCM-41 at pH 4.8 and released by increasing the pH up to 7.4 where electrostatic interaction between guest molecule and host mesoporous silica becomes too weak.

Metal involved coordination bonding based mesoporous silica is also a good approach for pH-responsive drug delivery system. Zheng *et al.* reported a construction of a coordination bonding "host-metal-drug" architecture using amino functionalized mesoporous silica (APS) and doxorubicin (DOX) as model drug.[114] As well known, NH_2-metal or metal-drug coordination bonding can be broken off as pH decreases so that pH can trigger drug release from mesoporous silica material in these systems. Indeed, suitable "host-metal-drug" matching is required for its application and the number of functionalized sites like amino group, should be controlled to reach a maximum drug loading. For instance, "NH_2-Cu-DOX" architecture showed a highly sensitive pH-responsive release profile compared to "NH_2-Zn-DOX" architecture (Figure. 1.3).

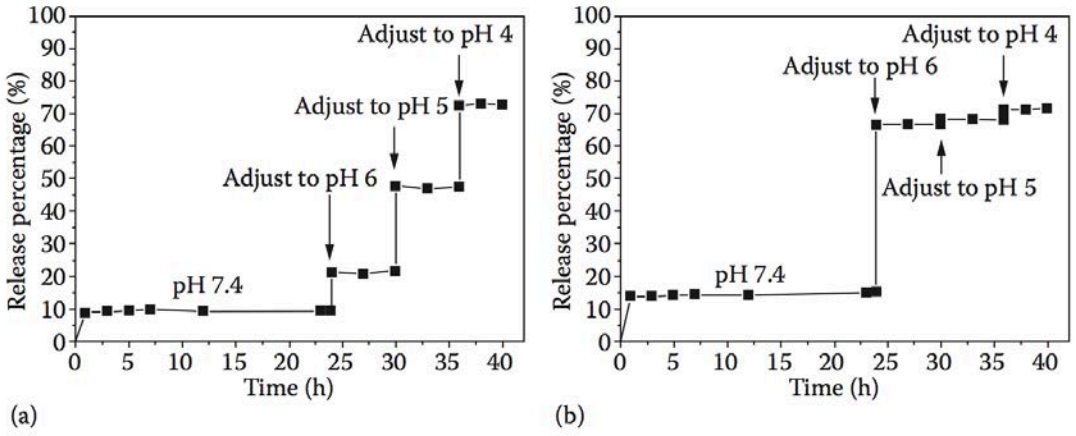

Figure 1.3. pH-responsive DOX release of NH_2–Cu–DOX (a) and NH_2–Zn–DOX (b) by acidification step by step. The AMS (Anionic surfactant templated Mesoporous Silica) nanoparticle used here was synthesized with APS/C_{18}GluA = 2.5. $Cu(CH_3COO)_2$ and $Zn(CH_3COO)_2$ have been used as metal sources.[114]

Although the concept that relies on host-guest interaction showed enormous applications and its potential for pH-responsive drug delivery system, a good matching between guest

molecule and host silica matrix is always necessary, thus a wide use of this strategy is sometime limited.

The limit of host-guest interaction based pH-responsive drug delivery system can be overcome by gatekeeping strategy. In fact, gatekeeping strategy was firstly introduced by Lin and co-workers in 2003 using CdS nanoparticles which capped the mesopore's "gate" that contained the drug.[83] In this system, the stimulus to trigger the drug release is not pH but external magnetic field.

For pH stimuli-responsive drug delivery system, Liu *et al.* developed pH-responsive gold-capped mesoporous silica through acetal linker.[115] Firstly, outer surface of mesoporous silica is functionalized by carboxylic acid group, which can react with one of the amino group of a di-amino di-acetal linker. After drug loading, mesopore's "gates" were capped by carboxylic acid modified gold nanoparticles. The latest were attached to the modified silica surface via the remaining free amino side groups bared by the di-amino di-acetal linker. Thus, the acid cleavable acetal bond linking the modified mesoporous silica to the gold nanoparticles showed an efficient gate-capping ability at neutral pH. Since the stability of acetal bonding is highly depending on pH, drug delivery can be triggered by acidic pH and release rate can be also controlled as a function of pH (Figure 1.4).

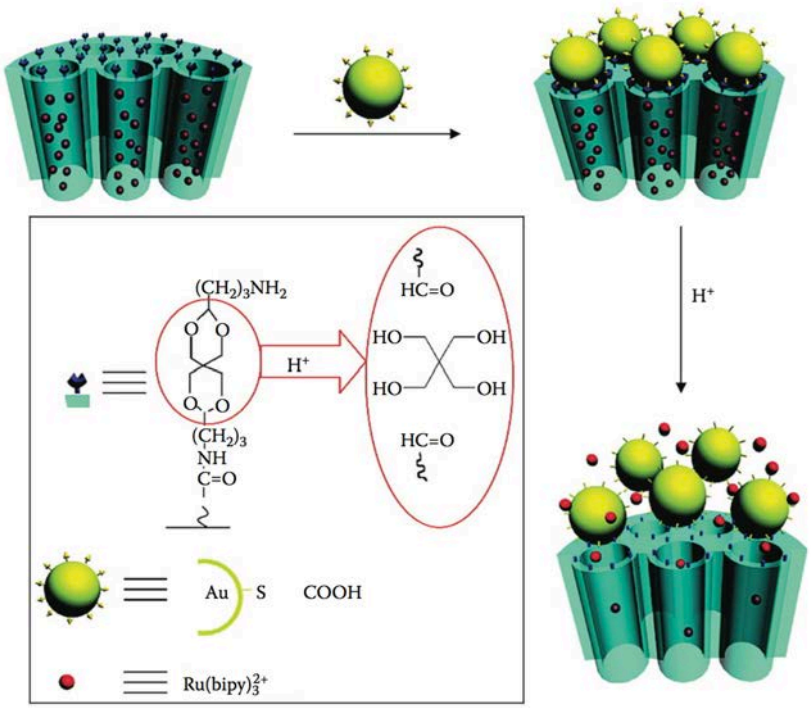

Figure 1.4. Schematic illustration of pH-responsive nanogated ensemble based on gold-capped mesoporous silica through acid-labile acetal linker.[115]

Another strategy for pH-responsive gatekeeping is to use supramolecular system as capping agent.[116-118] For instance, an efficient supramolecular nanovalve based on Cucurbit[6]uril (CB[6]) was developed by Zink and co-workers.[119] Gatekeeping method consists in creating a nanovalve using CB[6]-induced 1, 3-cycloaddition of azidoethylamine on alkyne-functionalized MCM-41. The final material contains two amines groups and CB[6] as gatekeeper on the linker. The nanovalve can be opened by adjusting the pH at 10, in which the deprotonation of amine can disrupt ion-dipole interaction between the linker and CB[6] ring and the RhB (rhodamine B) is released as shown in Figure 1.5.

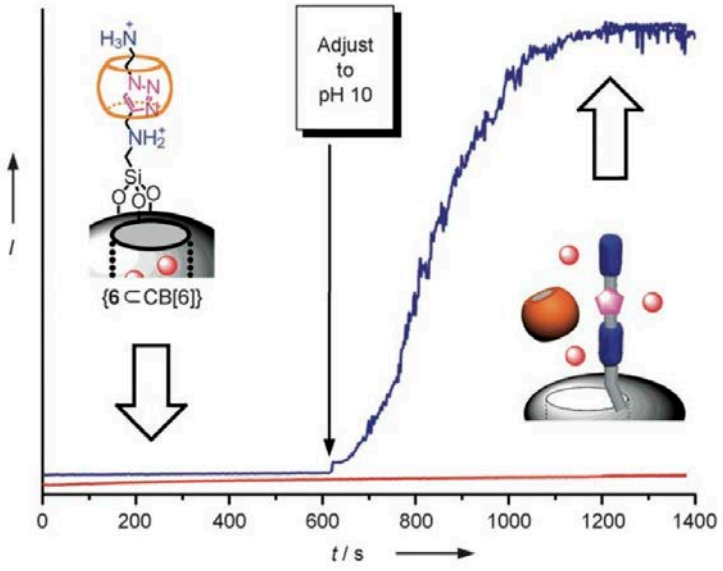

Figure 1.5. Release of the RhB guest molecules monitored by following the luminescence intensity of the solution of nanoparticles with shorter linkers {6 ⊂ CB[6]} (blue trace).[119]

An alternative way to cap mesopore's 'gates' is to use pH-sensitive polymer as coating agent for outer surface of mesoporous silica. A tremendous challenge in oral drug administration is that some drugs based on proteins or peptides undergo degradation at low pH. These drugs absorption should take place in the intestine, an effective drug protection at low pH is required. Choi *et al.* developed polymer-coated spherical mesoporous silica for pH-controlled delivery of insulin.[120] Due to the important molecular size of insulin, the pore diameter of mesoporous silica was tuned up to 32 nm that is 3-10 folds larger than classic mesoporous silica. Moreover, the inner silica surface was modified by amino group to increase insulin loading efficiency. Eudragit® L100, a commun expient in tablet medicines formulation, was used to coat the outer surface of mesoporous silica (Figure 1.6). Eudragit® L100 polymer

coating protects mesoporous silica very efficiently under low pH and it can be dissolved above pH 5.5 - 6.0 provoking drug release.

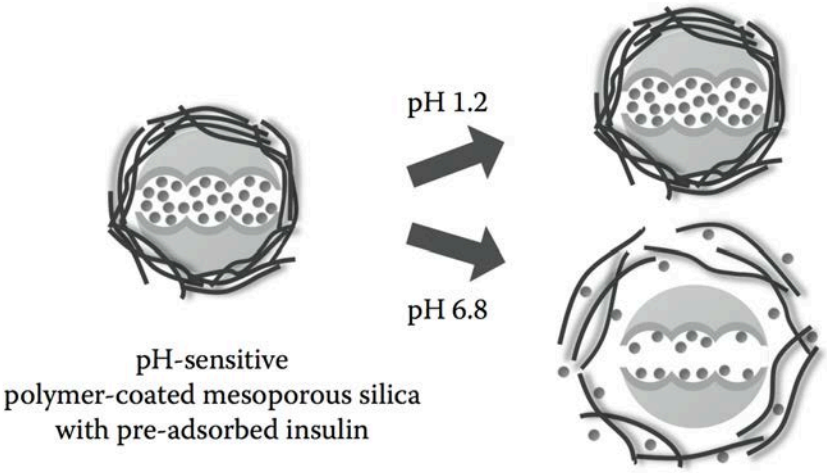

Figure 1.6. Schematic for the pH-controlled insulin delivery system based on pH-sensitive polymer coating of insulin-loaded spherical mesocellular foam (S-MCF) and its pH-responsive release.

Among some biocompatible coating agents, pH-responsive nutraceutical has attracted much attention. Considered as functional food in some countries like Canada, nutraceuticals are biocompatible, biodegradables and their production cost are much lower than classical biopolymers.[121] Guillet-Nicolas *et al.* prepared oral drug delivery system based on MSN functionalized by a pH-responsive nutraceutical, succinylated β-lactoglobulin. They succeeded in preventing drug release in stomach conditions with such a biopolymer coating. In fact, below pH 5, the coated MSN keeps the drug inside of its mesopores due to gelation of the succinylated β-lactoglobubin, which isoelectric point is at pH 5. As pH increases, the biopolymer becomes permeable, allowing the release of the drug.

1.3.2 Temperature-responsive MSN

The first example of temperature-responsive mesoporous silica has been achieved using thermo-sensitive polymer such as Poly(N-isopropylacrylamide) (PNIPAM).[122] PNIPAM and its derivatives present relatively low critical solution temperature (LCST) between 30 and 35°. Under chemical modification of these polymers, the LCST increases up to the local temperature of tumours that is slightly higher than the normal temperature of the human body.[123] At LCST, these polymers undergo a transition of conformation, resulting in the

increase of hydrophobicity due to the lost of hydrogen bonding between the solvent (water in most cases). This transition could be used to trigger the drug release from mesopores.

Zhu *et al*. reported grafting of PNIPAM inside mesoporous silica by atom transfer radical polymerization (ATRP) for the temperature-responsive drug release system.[124] In this system, ibuprofen was used as the model drug and it was attached to the PNIPAM chains inside mesopores *via* hydrogen bonding. The swelled PNIPAM chains prevented the escape of the drug molecules from mesopores, once it was loaded inside. Increasing the temperature above LCST induces the conformation transition of PNIPAM, breaking up of the hydrogen bonding and opening the mesopores by shrink of its own polymer chains, which can trigger the drug release.

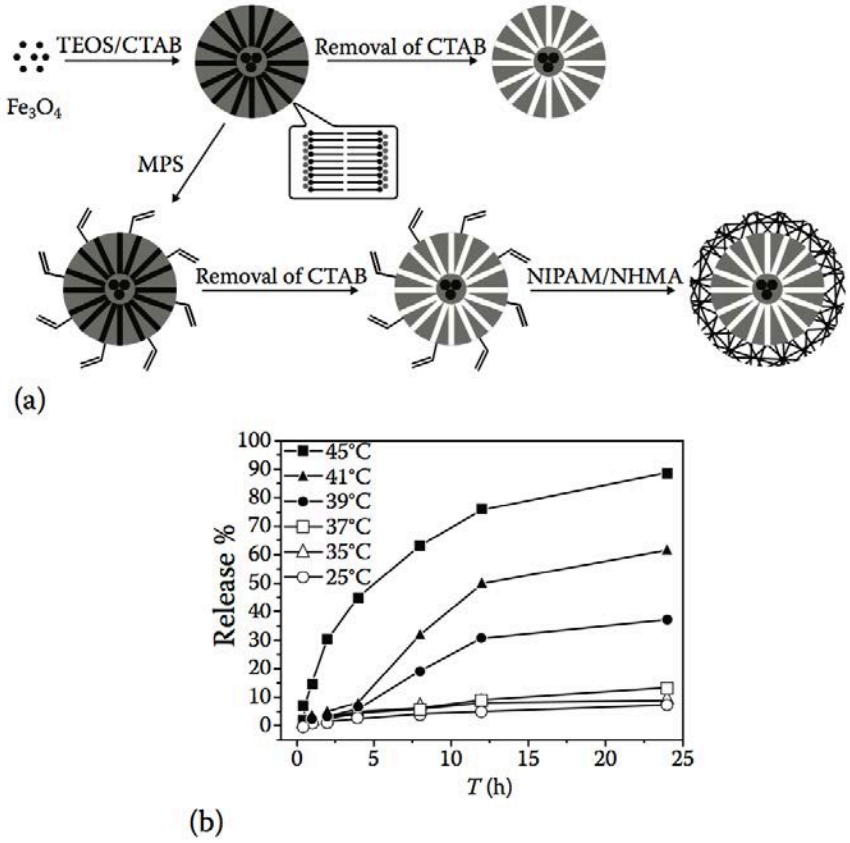

Figure 1.7. (a) Schematic preparation process of magnetic MSN (M-MSN) and M-MSN/ P(NIPAM-co-NHMA). (b) Cumulative drug release of drug-loaded systems in PBS solution (pH 7.4): cumulative drug release from $ZnPcS_4$@M-MSN/P(NIPAM-co-NHMA)-5-10 system in PBS solution at different temperatures. CTAB, cetyltrimethylammonium bromide; MPS, 3-(trimethoxysilyl)propyl methacrylate.[125]

Another strategy which consists in coating the outer surface of mesoporous silica by the derivatives of PINPA was demonstrated by Liu *et al.*[125] N-isopropylacrylamide (NIPA) and

N-hydroxymethyl acryl-amide (NHMA) were co-polymerized at the shell of MCM-41 type silica that already contained Fe_3O_4 as magnetic-responsive agent. The copolymer showed LCST around 38 - 42 °C, more adequate temperature for tumour targeting drug delivery than non-modified PNIPAM. The experimental results showed a highly temperature-responsive drug release profile in which at low temperature, less than 10 % of drug was 'leaked' from mesopores (Figure 1.7).

In the outer surface coating approach, drug release temperature could be also easily customized using paraffins, which have various melting temperatures depending on alkyl chain length. Aznar *et al*. showed paraffin-capped mesoporous silica nanoparticles as temperature-responsive drug cargo.[126] In this case, the outer surface of MCM-41 was functionalized with octadecyltrimethoxysilane. The alkyl chains interaction is mainly driven by London forces, which are able to form a hydrophobic layer around MCM-41. Increasing the temperature above the melting point of paraffins results in mesopore opening and thus the drug could be released.

Schlossbauer *et al.* demonstrated that DNA could be used as an efficient capping agent of mesopores.[127] In their system, the main strategy relies on DNA strand melting property of oligonucleotide at the specific temperature, provoking the mesoporous silica cargo opening in order to release the drug loaded within.

1.3.3 Redox-responsive MSN

Redox-responsiveness is another powerful tool to control drug release from mesoporous silica nanoparticles. Since the cleavage of disulfide bond (-S-S-) takes place in a reducing environment and most intra-cellular compartment can provide such a condition, the use of disulfide bond on mesoporous silica as a couple of redox stimuli is a good strategy to trigger drug release, especially inside cells. Moreover, in many tumour cells the level of glutathione (GSH), a disulfide-reducing agent, is higher than normal cells.[128]

Lin *et al*., who firstly introduced gatekeeping strategy in mesoporous silica, reported CdS nanoparticle-capped mesoporous silica through linkers of disulfide and amino groups on the inner surface of mesopores.[83] Briefly, vancomycin and ATP (a neurotransmitter) were loaded into mesoporous silica, which was further capped by CdS nanoparticles. No leaking of the drugs was observed after capping mesopores. Drug release could be triggered by increasing

the concentration in disulphide reducing-agent (i.e. dithiothreitol (DTT)), which cleaves disulfide bonds and unlocks the mesopores (Figure 1.8).

Again, Lin *et al.* demonstrated that cysteine, which already contains thiol group and might be toxic in extracellular environment, could be loaded in thiol modified mesoporous silica nanoparticle without capping method. Cysteine release can be trigged and regulated by redox-stimuli, in this case, by the intracellular GSH's level.[129]

Other authors also designed redox stimuli-reponsive mesoporous silica based on disulfide bond, using gatekeeping approach with curcurbit[6]uril or a-CD rings[130] or PEG coating method via cysteine based linker.[131]

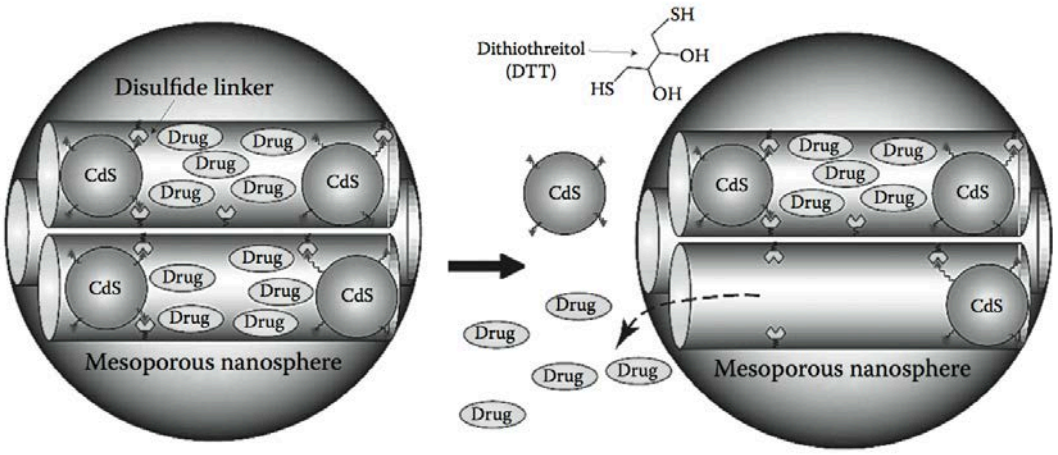

Figure 1.8. Schematic representation of the CdS nanoparticle-capped MSN-based drug/ neurotransmitter delivery system. The controlled-release mechanism of the system is based on chemical reduction of disulfide linkage between the CdS caps and the MSN hosts.[83]

1.3.4 Light-responsive MSN

Photoactive silica materials became also very useful in the control of drug delivery through light stimuli sensitive molecules. In general, they are grafted at the pore outlets and act as gatekeepers. In such kind of systems, the drug delivery is activated by external light and usually drug molecules do not have overlapped light absorption band with the gatekeeper molecules for the release efficiency.

In this context, Fujiwara *et al.* reported the first example of light stimuli-responsive mesoporous silica nanoparticles MCM-41, in which the loading, the storage and the release of model molecules (steroid cholestane, pyrene, phenanthrene and progesterone) were

controlled by light.[132] To do so, they functionalized MCM-41 materials with a photosensitive coumarin derivative, the 7-[(3-triethoxysilyl)propoxy]coumarin, either by post functionalized or co-condensation. Then, drug was loaded into modified MCM-41 by impregnation method. This material was irradiated under UV light (> 310nm for 30 min) in order to form the gatekeepers, namely the cyclobutane rings, which result from the photodimerization reaction between a pair of coumarin groups. Then, the drug was easily released since cyclobutane rings are photocleavable upon UV light irradiation (around 250 nm), as schemed in Figure 1.9.

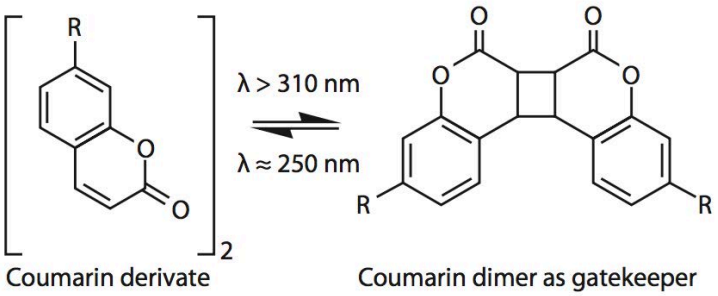

Figure 1.9. Coumarin photodimerization reaction to activate or deactivate gatekeeper dimer.[132]

Mesoporous silica nanoparticle modified with azobenzene moiety has also largely been investigated for their interesting photoreversibility property. As an example, Zink *et al.* reported light stimuli responsive MSN functionalized by azobenzene derivatives used as gatekeepers. They prepared two modified azobenzene molecules presenting *trans*-to-*cis* transition for post-synthesis functionalization of MCM-41 nanoparticles. The azobenzene derivative molecules were grafted inside the MCM-41 pores pointing straight along the channel like a thread when in the *trans* configuration. The latest conformation allowed loading Rhodamine B inside the MCM-41 porosity and either a pyrene-β-cyclodextrin or β-cyclodextrin molecule was chosen as sealing agent. The cargo porosity was opened under UV light irradiation at 351 nm, in which azobenzene derivative molecules adopt *cis* configuration.[133]

In another work, Zink *et al.* coupled the photoisomerization property of the azobenzene derivative moiety with a pH-switchable pseudorotaxanes (curcurbit[6]uril (CB[6])) rings encircling bisammonium derivative stalks) acting as nanovalves of the pores. Adding such a pH-responsive secondary gatekeepers at the outlet of mesopores could reduce drug leaking and also design dual-controllable MSN drug delivery system. The UV-irradiation at 448 nm

provokes continuous photocommutation of azobenzene moiety from *trans* to *cis* configuration inside of the pore. Moreover, under basic pH ion-dipole interaction between CB[6] rings and bisammonium derivative stalks are disrupted. Then the dissociation of the rings releases guest molecules as illustrated in Figure 1.10.[133,134]

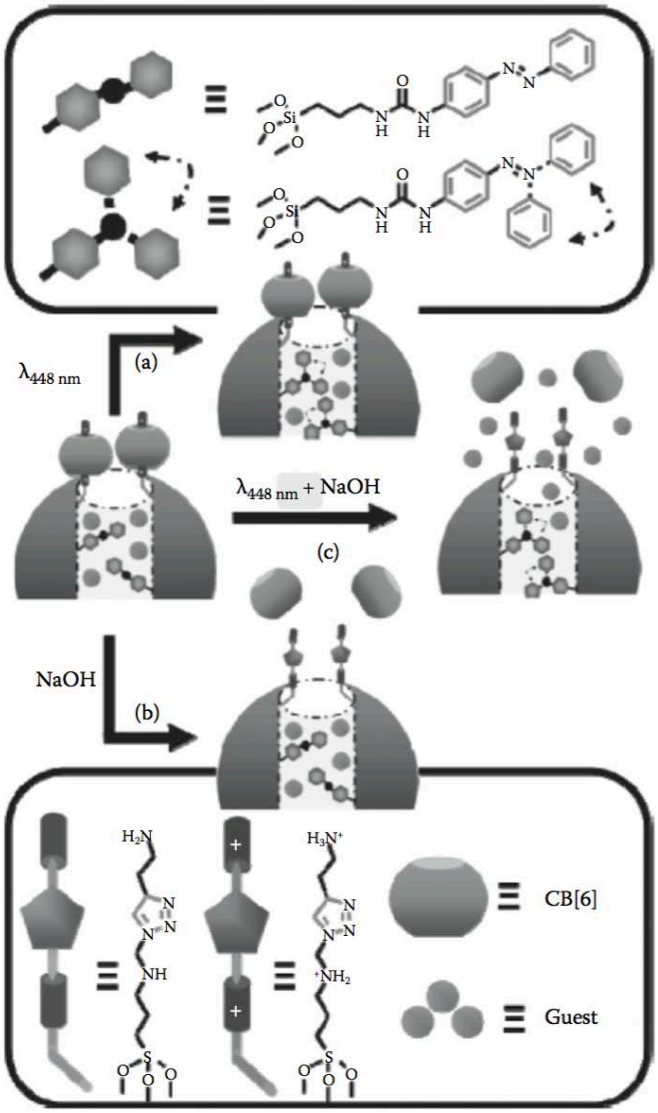

Figure 1.10. Operation of dual-controlled nanoparticles. (a) Excitation with 448 nm light induces the dynamic wagging motion of the nanoimpellers, but the nanovalves remain shut and the contents are contained. (b) Addition of NaOH opens the nanovalves, but the static nanoimpellers are able to keep the contents contained. (c) Simultaneous excitation with 448 nm light and addition of NaOH cause the contents to be released.[133,134]

In some applications needing photostimulation, the encapsulated drug is sensitive to light and it can be degraded, as it is the case for doxourubicin (DOX). Lin *et al*. developed MSN functionalized with aminopropyl groups protected by nitroveratyl function through a

carbamate bond. When the carbamate linker is irradiated at 350 nm, Doxourubicin (DOX) loaded in MSN can be released. In fact, UV-light triggers the deprotection of amine groups, which become positively charged when the process is done in water, thus DOX molecules release is induced by electrostatic repulsion between the respective ammonium moieties. The mechanism was verified by zeta potential measurement that showed the increase of positive charge due to free amino group.[135] Lin *et al.* also designed light-responsive MSN using gold nanoparticles as gatekeep[136] to cap mesopores through a cleavable photolabile linker, named thioundecyl-tetraethyleneglycolester-onitrobenzylethyldimethyl ammonium bromide (TUNA) for intracellular drug delivery. Their system was tested for photoinduced intracellular controlled release of an anticancer drug, paclitaxel, inside of human fibroblast and liver cells. According to the results, endocytosis and drug release were efficient under irradiation (λ = 365nm), preventing zero burst release.

1.3.5 Magnetic-responsive MSN

Building mesoporous silica nanoparticles (MSN) that respond to the magnetic field has attracted a lot of attention for its potential applications. As drug delivery system, magnetic MSN could be guided to the desired site, and then removed after complete release using an external magnetic field. This strategy might be of interest for cancer targeting drugs, showing certain toxicity for organs, in order to reduce side effects. Beside of guiding the drug by magnetic field, magnetic MSN can be used for hyperthermia therapy.[137,138]

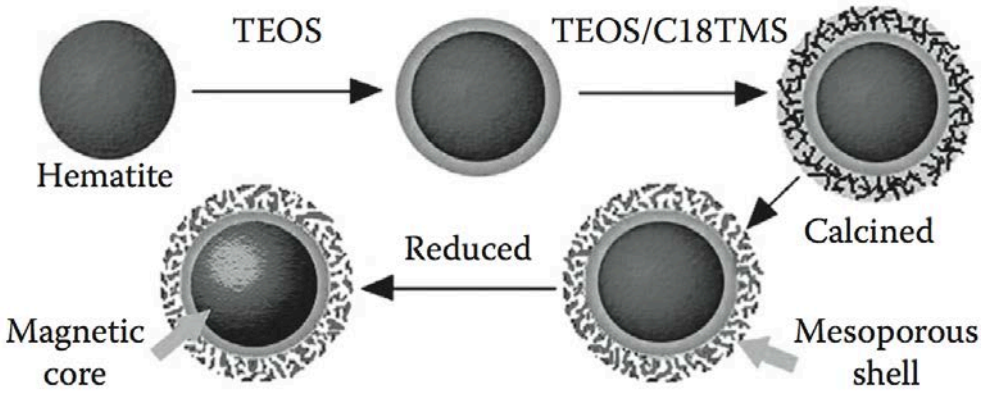

Figure 1.11. Illustration of synthesis of MFeCMS nanospheres. (C18TMS for *n*-octadecyltri-methoxysilane)[142,143]

For instance, superparamagnetic nanoparticles embedded MSN were already widely studied for both drug guide system and hyperthermia properties.[139] However, biocompatibility and toxicity problems is always a limiting factor, thus only magnetite (Fe_3O_4) or maghemite (γ-Fe_2O_3) have been considered for biomedical applications. Though, up to date, more than 1700 publications (based on web of sciences) are dealing with magnetic MSN. However, in this chapter, we focus on some examples that marked a turning point in the biomedical field.

For the synthesis of magnetic MSN, various designs and strategies have been proposed.[140,141] Core-shell structure with magnetic nanoparticle, proposed by Shi *et al*., has been considered as a basic model for magnetic MSN (Figure 1.11).[142,143] Its potential medical applications were confirmed using ibuprofen as well.

Zhao *et al*. have extend core-shell model using several iron sources and also simplified synthesis methods (Figure 1.12).[144,145] Besides of conventional drug molecules, DNA can be carried inside mesopores and delivered using magnetic field (Figure 1.13).[146] Moreover, magnetic MSN have been extensively tested on *in vivo* cells in recent years.[147] The results showed that a core-shell structure, in which metallic nanoparticles do not have direct contact with cellular culture, exhibiting an excellent biocompatibility.

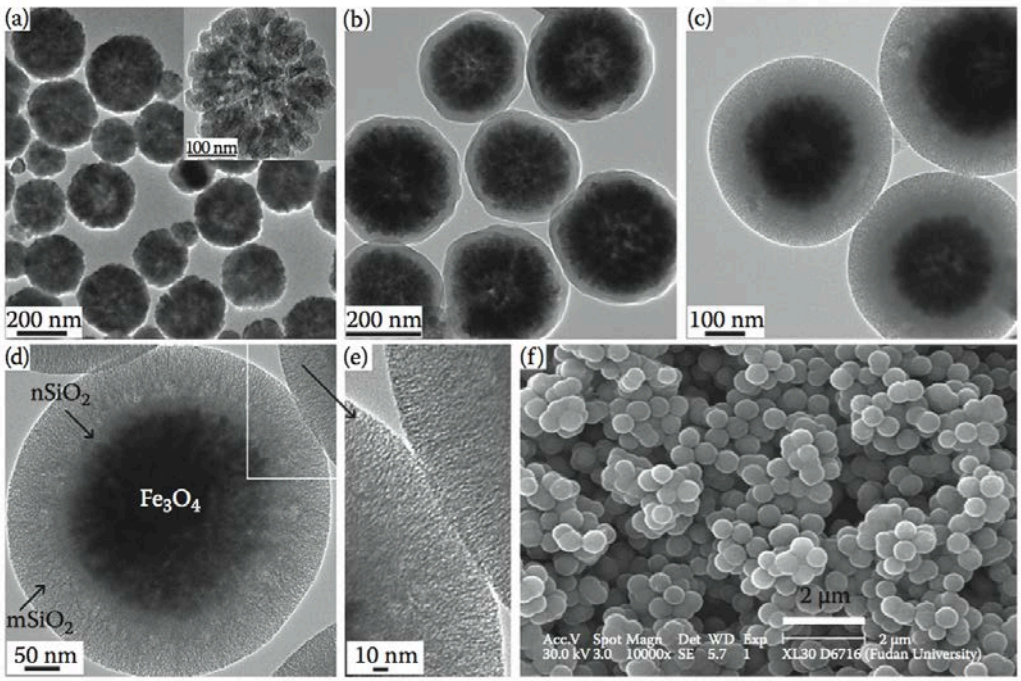

Figure 1.12. TEM images of (a) Fe_3O_4 particles, (b) Fe_3O_4@SiO_2, and (c–e) Fe_3O_4@nSiO_2@ mSiO_2 microspheres, and (f) SEM image of Fe_3O_4@nSiO_2@mSiO_2 microspheres.[144,145]

Embedding magnetic nanoparticles into MSN has been also of interest for scientists. Magnetic nanoparticles can be easily incorporated inside mesopores or on the matrix of silica. Corriu *et al*. reported the synthesis of magnetic silica-based nanocomposites containing magnetite (Fe_3O_4) nanoparticles using internal anchored acetylacetonate groups as a ligand.[148] Huang *et al.* demonstrated controlled and targeting ibuprofen release using magnetic γ-Fe_2O_3@MSN composites with different morphologies.[149]

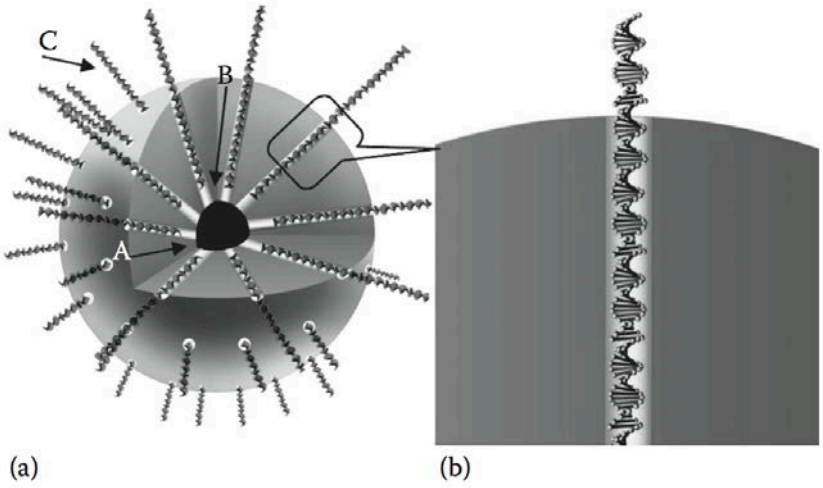

Figure 1.13. (a) Sectional drawing for existent status of DNA in M-MSN mesopores (the empty mesopores were omitted and the DNA chain inside or outside the mesopore was not depicted accurately). Arrow A represented the magnetic core, arrow B represented the meso-pore, and arrow C represented DNA molecule. (b) An enlarged image for DNA molecule in mesopore.[146]

Recently, rattle-type hollow structure has been spotlighted owing to its unique property. Like meso-macroporous materials, hollow cavity can enhance surface area/pore volume ratio meaning also an increase of the drug biding surface/volume. Therefore, more drugs can be encapsulated than into a core-shell model. Shi *et al.* reported rattle-hollow structured magnetic mesoporous silica nanocapsules as a platform for simultaneous cell imaging and anticancer drug delivery (Figure. 1.14).[150,151] As expected, these MSN showed high doxorubicin loading capacity and entrapment efficiency compared to simple core-shell structure.[45,152]

Another type of magnetic mesoporous silica nanoparticles consists of using magnetic nanoparticles as a capping agent for mesopores gate. Lin *et al*. reported MSN capped by Fe_3O_4 nanoparticle via disulfide linker. This double stimuli-responsive system could be used

in more sophisticated applications like targeting by magnetic filed and drug trigger by redox condition. Gate capped MSN with linkers, which response to another stimuli such as light or pH will be or were already discussed in its own part.

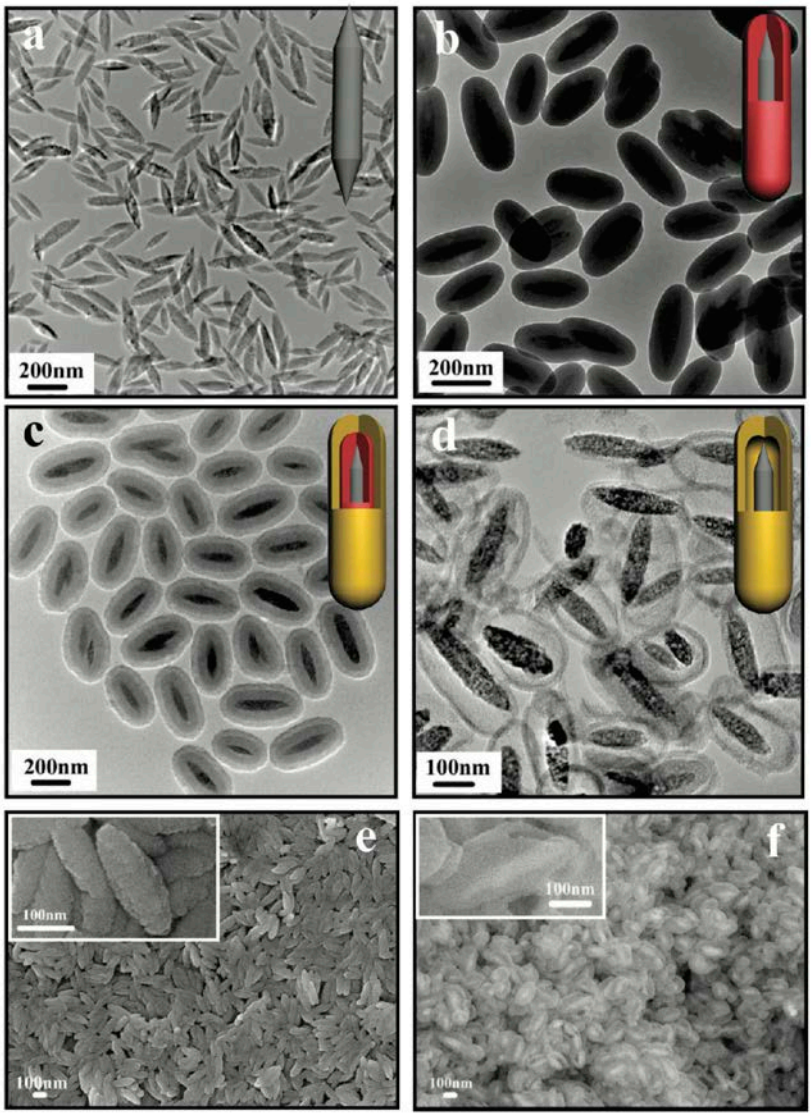

Figure 1.14. TEM images of ellipsoidal (a) Fe_2O_3, (b) Fe_2O_3@SiO_2, (c) Fe_2O_3@SiO_2@ $mSiO_2$, and (d) Fe_3O_4@$mSiO_2$. Secondary electron SEM image of ellipsoidal Fe_2O_3 (e, inset: SEM image at high magnification) and backscattered electron SEM (f) image of ellipsoidal Fe_3O_4@$mSiO_2$ nanocapsules (inset: purposely selected backscattered electron image of broken nanocapsules to reveal the hollow nanostructure).[150,151]

1.3.6 Biological stimuli responsive drug release

Recent improvements on the design of stimuli-responsive drug release systems have been employed to develop biological stimuli carriers. For example, Yu *et al*. showed

programmable drug release from mesoporous silica nanoparticle that responded to biological stimuli.[153] Sulfasalazine (SZ), a pro-drug, was encapsulated in amino functionalized MSN through electrostatic interactions. The material was then coated with succinalyted soy protein isolate (SSPI), which is relatively affordable and considered as a food additive in some countries such as Canada. This system showed no leakage of drug at low pH and in the water because hydrophobic SSPI undergoes hydrolysis only at high pH. In the presence of pancreatin enzyme, which is predominating in the intestine, SSPI is hydrolysed and mesopore gates can be opened. Moreover, azo-reductase produced by colon microflora can cut azo function of sulfasalazine to give active metabolite 5-aminosalycilic acid (Figure 1.15).

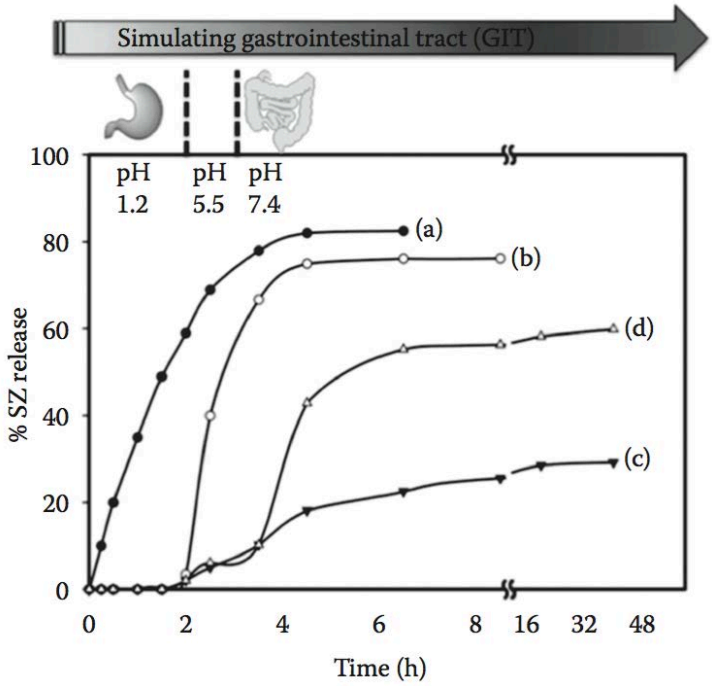

Figure 1.15. Release of profiles of SZ from (a) MCM-41-SZ, (b) MSN-NH_2-SZ, and (c) MSN-NH_2-SZ@SSPI without enzyme, and (d) MSN–NH_2–SZ@SSPI in the presence of enzymes (pepsin at pH 1.2 and pancreatin at pH 7.4) present in simulated GIT fluids.[153]

Qu *et al.* reported DNA-capped MSN for which pores can be opened upon treatment with deoxyribonuclease I (DNase I).[110] DNA was grafted on the surface of MSN via click conjugating method between azide functionalized MSN and aryl modified DNA sequence. The duplex DNA is highly effective capping method so only less than 10 per cent of the drug is leaked without external stimuli. When this system is exposed to DNase I, the duplex DNA could be hydrolysed, opening the mesopores and releasing the drug.

Adenosine triphosphate, ATP, can be used also as biological stimuli for controlled drug release. Indeed, mesopores capping is achieved by the complexation of Cu^{2+} between amino-

functionnalized MSN and L-cysteine modified gold nanoparticles (AuNP) under low pH.[154] ATP, which contains a more effective complexation site than single amino group, was shown to be a biological stimulus to detach gold nanoparticle from mesopores gates through Cu^{2+} complexation. In this investigation, low pH and ATP have been used as biological stimuli for drug release within either, the lysosome in case of low pH, and/or the cytosol that contains high concentration of ATP.

Using FDA-approved peptide drug protamine as coating agent of MSN is an effective way to make biological stimuli-responsive drug delivery system, demonstrated by Raichur *et al.*[155] Indeed, like other coating agents, protamine can effectively protect the encapsulated drug from burst or undesired release. Coating is conducted on amino functionalized MSN using glutaraldehyde as coupling agent. In the presence of the enzyme such as trypsin that recognizes and cut arginine or lysine sites, the protamine coating can dissolve opening the mesopores and releasing the drug.

1.4 Conclusion and perspectives

In this chapter, it is demonstrated that MSN have largely been employed to design efficient drug delivery systems, especially due to their high loading capacity, high stability and the ability to protect the guest molecules from various biochemical attacks. Indeed what encourages many research groups to design MSN drug carriers are the biocompatibility and biodegradability of these materials. In addition, MSN can offer a multitude of functionalization routes that allow decorating either the inner and/or the outer surface, with pH, thermal, light and magnetic stimuli responsive molecules, polymers, metallic nanoparticles and targeting ligands. The latest functionalization strategies have been tailored to control the drug delivery kinetic at the appropriate place with zero premature release together with preventing undesired side effects. For the moment, most *in vitro* studies have evaluated the cytotoxicity, the biocompatibility, biodegradability, the retention of MSN nanocarriers and the understanding of some cellular uptake mechanisms. However, toxicity and intracellular uptake results reported in the literature are specific to each drug delivery system. Moreover, the design of MSN drug carriers with simple and cost-effective way is still needed to demonstrate the potential of MSN as drug delivery systems or biosensors in therapeutic applications.[156,157]

References

1 C. S. Brunner, *Product Genesis*. 2004.

2 I. Slowing, J. Vivero-Escoto, C. Wu, V. Lin, V. *Adv. Drug Deliv. Rev.*, 2008, **60**, 1278–1288.

3 C. Argyo, V. Weiss, C. Bräuchle, T. Bein, *Chem. Mater.*, 2014, **26**, 435–451.

4 A. Popat, J. Liu, G. O. M. Lu, S. Z. Qiao, *J. Mater. Chem.* 2012, **22**, 11173–11178.

5 Y. S. Lin, N. Abadeer, K. R. Hurley, C. L. Haynes, *J. Am. Chem. Soc*., 2011, **133**, 20444–20457.

6 K. Ma, U. Werner-Zwanziger, J. Zwanziger, U. Wiesner, *Chem. Mater*., 2013, **25**, 677–691.

7 J. Kobler, K. Möller, T. Bein, *ACS Nano.*, 2008, **2**, 791–799.

8 M. H. Kim, H. K. Na, Y. K. Kim, S. R. Ryoo, H. S. Cho, K. E. Lee, H. Jeon, R. Ryoo, D. H. Min, *ACS Nano*., 2011, **5**, 3568–3576.

9 K. Zhang, L. L. Xu, J. G. Jiang, N. Calin, K. F. Lam, S. J. Zhang, H. H. Wu, G. D. Wu, B. Albela, L. Bonneviot, *J. Am. Chem. Soc.*, 2013, **135**, 2427–2430.

10 M. Sinn Aw, M. Kurian, D. Losic, *Biomater. Sci.*, 2014, **9**, 9243–9257.

11 M. G. Pankhania, C. D. Melia, J. F. Lampard, Sustained-Release Pharmaceutical Formulation Containing Xanthan Gum; EP 0234670 B1

12 B. B. Aggarwal, A. Kumar, A. C. Bharti, *Anticancer Res.*, 2003, **23**, 363–398.

13 K. C. Kwan, *Drug Metab. Dispos.* 1997, **25**, 1329–1336.

14 U.S. Food and Drug Administration, Avoid Food-Drug Interactions at http://www.fda.gov/downloads/Drugs/ResourcesForYou/Consumers/BuyingUsingMedicineSafely/EnsuringSafeUseofMedicine/GeneralUseofMedicine/UCM229033.pdf

15 E. O. Meltzer, M. J. Welch, N. K. Ostrom, *Clin. Pediatr.*, 2006, **45**, 725–733.

16 U.S. Food and Drug Administration, Inactive Ingredient Database. Available at http://www.accessdata.fda.gov/scripts/cder/iig/index.Cfm

17 S. Jambhrunkar, S. Karmakar, A. Popat, M. Yu, C. Yu, *RSC Adv.* 2014, **4**, 709–712.

18 Schering Corporation A Corp. of NJ, Transdermal Delivery of Nicotine, US 4908213A

19 S. K. Niazi, Handbook of Pharmaceutical Manufacturing Formulations. Informa Healthcare, Switzerland, 2009

20 D. Harris, J. R. Robinson, *J. Pharm. Sci.*, 1992, **81**, 1–10.

21 H. Lambers, S. Piessens, A. Bloem, H. Pronk, P. Finkel, *Int. J. Cosmet. Sci.*, 2006, **28**, 359–370.

22 D. I. Sessler, A. Moayeri, *Anesthesiology,* 1990, **73**, 218–224.

23 Y. Chen, H. Chen, J. Shi, *Adv. Mater.*, 2013, **25**, 3144–3176.

24 D. Arcos, M. Vallet-Regí, *Acta Mater.*, 2013, **61**, 890–911.

25 W. Stober, A. Fink, E. Bohn, *J. Colloid Interface Sci.*, 1968, **26**, 62–69.

26 I. Tissot, J. P. Reymond, F. Lefebvre, E. Bourgeat-Lami, *Chem. Mater.*, 2002, **14**, 1325–1331.

27 C. E. Fowler, D. Khushalani, S. Mann, *Chem. Commun*., 2001, 2028–2029.

28 G. Aharon, M. Yizhak, R. Rohit Kumar, *Adv. Mater.*, 2002, **14**, 1414–1418.

29 A. Stein, S. G. Rudisill, N. D. Petkovich, *Chem. Mater*., 2014, **26**, 259–276.

30 Y. D. Liu, J. Goebl, Y.D. Yin, *Chem. Soc. Rev*. 2005, **21**, 8180–8187.

31 P. W. Voorhees, *J. Stat. Phys*., 1985, **38**, 231–235.

32 J. Liu, F. Liu, K. Gao, J. Wu, D. Xue, *J. Mater. Chem.* 2009, **19**, 6073–12.

33 G. Réthoré, A. Pandit, *Small*, 2010, **6**, 488–498.

34 X. W. D. Lou, L. A. Archer, Z. Yang, *Adv. Mater.*, 2008, **20**, 3987–4019.

35 Y. Zhao, L. Jiang, *Adv. Mater.*, 2009, **21**, 3621–3638.

36 H. C. Zeng, *J. Mater. Chem.* 2011, **21**, 7511–7516.

37 H. J. Hah, J. S. Kim, B. J. Jeon, S. M. Koo, Y. E. Lee, *Chem. Commun.*, 2003, 1712–1712.

38 Y. Zhu, J. Shi, W. Shen, X. Dong, J. Feng, M. Ruan, Y. Li, *Angew. Chem. Int. Ed.*, 2005, **44**, 5083–5087.

39 J. Hu, M. Chen, X. Fang, L. Wu, *Chem. Soc. Rev*., 2011, **40**, 5472–5491.

40 D. A. Wheeler, R. J. Newhouse, H. Wang, S. Zou, J. Z. Zhang, *J. Phys. Chem. C*, 2010, **114**, 18126–18133.

41 A. Pasc, J. L. Blin, M. J. Stébé, J. Ghanbaja, *RSC Adv.*, 2011, **1**, 1204–1206.

42 R. Ravetti-Duran, J. L. Blin, M. J. Stébé, C. Castel, A. Pasc, *J. Mater. Chem.*, 2012, **22**, 21540–21548.

43 J. Z. Zhang, *J. Phys. Chem. Lett*., 2010, **1**, 686–695.

44 X. Jiang, T. L. Ward, Y. S. Cheng, J. Liu, C. J. Brinker, *Chem. Commun*., 2010, **46**, 3019–3021.

45 Y. Zhu, Y. Fang, S. Kaskel, *J. Phys. Chem. C*, 2010, **114**, 16382–16388.

46 F. Lu, A. Popa, S. Zhou, J. J. Zhu, A. C. S. Samia, *Chem. Commun.*, 2013, **49**, 11436–11438.

47 D. Zhao, J. Sun, Q. Li, G. D. Stucky, *Chem. Mater.*, 2000, **12**, 275–279.

48 P. Linton, V. Alfredsson, *Chem. Mater.*, 2008, **20**, 2878–2880.

49 Y. Ding, G. Yin, X. Liao, Z. Huang, X. Chen, Y. Yao, J. Li, *Micropor. Mesopor. Mater*. 2013, **170**, 45–51.

50 W. Shenton, T. Douglas, M. Young, G. Stubbs, S. Mann, *Adv. Mater*., 1999, **11**, 253–256.

51 S. B. Lee, *Science*, 2002, **296**, 2198–2200.

52 K. J. C. Van Bommel, A. Friggeri, S. Shinkai, *Angew. Chem. Int. Ed*., 2003, **42**, 980–999.

53 J. Jang, H. Yoon, *Adv. Mater*., 2004, **16**, 799–802.

54 W. Wang, J. Zhou, S. Zhang, J. Song, H. Duan, H. Zhou, C. Gong, Z. Bao, B. Lu, X. Li, W. Lan, E. Xie, *J. Mater. Chem*., 2010, **20**, 9068–9072.

55 M. Sumper, E. Brunner, *Adv. Funct. Mater*., 2006, **16**, 17–26.

56 S. C. Holmström, P. J. S. King, M. G. Ryadnov, M. F. Butler, S. Mann, D. N. Woolfson, *Langmuir*, 2008, **24**, 11778–11783.

57 A. Altunbas, N. Sharma, M. S. Lamm, C. Yan, R. P. Nagarkar, J. P. Schneider, D. J. Pochan, *ACS Nano*, 2010, **4**, 181–188.

58 S. Wang, X. Ge, J. Xue, M. Fan, L. Mu, Y. Li, H. Xu, J. R. Lu, *Chem. Mater*., 2011, **23**, 2466–2474.

59 C. Zollfrank, H. Scheel, P. Greil, *Adv. Mater*., 2007, **19**, 984–987.

60 S. Giri, B. G. Trewyn, M. P. Stellmaker, V. Lin, *Angew. Chem. Int. Ed.,* 2005, **44**, 5038–5044.

61 Z. Hou, C. Li, P. Ma, Z. Cheng, X. Li, Y. Zhang, Y. Dai, D. Yang, H. Lian, J. Lin, *Adv. Funct. Mater*., 2012, **22**, 2713–2722.

62 C. T. Kersge, M. E. Leonowicz, W. J. Roth, J. C. Vartuli, J. S. Beck, *Nature*, 1992, **359**, 710–712.

63 F. Hoffmann, M. Cornelius, J. Morell, M. Fröba, *Angew. Chem. Int. Ed*., 2006, **45**, 3216–3251.

64 Y. Wan, D. Zhao, *Chem. Rev.*, 2007, *107*, 2821–2860.

65 I. Slowing, J. Vivero-Escoto, B. G. Trewyn, V. Lin, *J. Mater. Chem*., 2010, **20**, 7924–7937.

66 S. H. Wu, C. Y. Mou, H. P. Lin, *Chem. Soc. Rev.,* 2013, **42**, 3862–3875.

67 C. Jeffrey Brinker, Sol-Gel Processing of Silica. *Advances in Chemistry*, 1994, **234**, 361–401.

68 J. Sefcik, A. V. McCormick, *Catal. Today*, 1997, **35**, 205–223.

69 M. Vallet-Regí, A. Rámila, R. P. del Real, J. Pérez-Pariente, *Chem. Mater.*, 2001, **13**, 308–311.

70 C. H. Tsai, J. Vivero-Escoto, I. Slowing, I. J. Fang, B. Trewyn, V. Lin, *Biomaterials* 2004, **4**, 2139–2143.

71 M. Vallet-Regí, F. Balas, D. Arcos, *Angew. Chem. Int. Ed.,* 2007, **46**, 7548–7558.

72 B. Chang, J. Guo, C. Liu, J. Qian, W. Yang, *J. Mater. Chem.,* 2010, **20**, 9941–9947.

73 M. M. Wan, W. J. Qian, W. G. Lin, Y. Zhou, J. H. Zhu, *J. Mater. Chem. B,* 2013, **1**, 3897–3905.

74 D. Brühwiler, *Nanoscale*, 2010, **2**, 887–892.

75 P. Yang, S. Gai, J. Lin, *Chem. Soc. Rev.,* 2012, **41**, 3679–3698.

76 A. Vinu, K. Z. Hossain, K. Ariga, *J. Nanosci. Nanotechnol*., 2005, **5**, 347–371.

77 A. P. Wight, M. E. Davis, *Chem. Rev*., 2002, **102**, 3589–3614.

78 M. H. Lim, A. Stein, *Chem. Mater*., 1999, **11**, 3285–3295.

79 A. Walcarius, M. Etienne, L. Lebeau, *Chem. Mater*., 2003, **15**, 2161–2173.

80 P. Banet, N. Marcotte, D. A. Lerner, D. Brunel, *Langmuir,* 2008, **24**, 9030–9037.

81 E. A. Kadib, N. Katir, M. Bousmina, J. P. Majoral, *New J. Chem.,* 2012, **36**, 241–255.

82 M. Hebrant, M. Rose-Helene, J. P. Joly, A. Walcarius, *Colloids Surf., A,* 2011, **380**, 261–269.

83 C. Y. Lai, B. G. Trewyn, D. M. Jeftinija, K. Jeftinija, X. Xu, S. Jeftinija, V. Lin, *J. Am. Chem. Soc.*, 2003, **125**, 4451–4459.

84 C. Park, K. Oh, S. C. Lee, C. Kim, *Angew. Chem. Int. Ed.*, 2007, **46**, 1455–1457.

85 X. Huang, L. Li, T. Liu, N. Hao, H. Liu, D. Chen, F. Tang, *ACS Nano,* 2011, **5**, 5390–5399.

86 J. M. Rosenholm, M. Lindén, *J. Controlled Release,* 2008, **128**, 157–164.

87 Q. Yang, S. Wang, P. Fan, L. Wang, Y. Di, K. Lin, F. S. Xiao, *Chem. Mater.*, 2005, **17**, 5999–6003.

88 J. Kecht, T. Bein, *Langmuir*, 2008, **24**, 14209–14214.

89 A. Schlossbauer, J. Kecht, T. Bein, *Angew. Chem. Int. Ed*., 2009, **48**, 3092–3095.

90 L. Chen, Y. Wen, B. Su, J. Di, Y. Song, L. Jiang, *J. Mater. Chem*., 2011, **21**, 13811–13816.

91 Y. Cui, H. Dong, X. Cai, D. Wang, Y. Li, *ACS Appl. Mater. Interfaces,* 2012, **4**, 3177–3183.

92 P. Nadrah, U. Maver, A. Jemec, T. Tišler, M. Bele, G. Dražić, M. Benčina, A. Pintar, O. Planinšek, M. Gaberšček, *ACS Appl. Mater. Interfaces,* 2013, **5**, 3908–3915.

93 J. Lu, E. Choi, F. Tamanoi, J. I. Zink, *Small*, 2008, **4**, 421–426.

94 J. Méndez, A. Monteagudo, K. Griebenow, *Bioconjug. Chem*., 2012, **23**, 698–704.

95 W. Fang, J. Yang, J. Gong, N. Zheng, *Adv. Funct. Mater*., 2011, **22**, 842–848.

96 N. Ž. Knežević, B. Trewyn, V. Lin, *Chem. Commun.*, 2011, **47**, 2817–2819.

97 Z. Zhang, L. Wang, J. Wang, X. Jiang, X. Li, Z. Hu, Y. Ji, X. Wu, C. Chen, *Adv. Mater*., 2011, **10**, 476–476.

98 V. Cauda, H. Engelke, A. Sauer, D. Arcizet, J. Rädler, T. Bein, *Nano Lett*., 2010, **10**, 2484–2492.

99 S. A. Mackowiak, A. Schmidt, V. Weiss, C. Argyo, C. von Schirnding, T. Bein, C. Bräuchle, *Nano Lett*., 2013, **13**, 2576–2583.

100 R. Liu, P. Liao, J. Liu, P. Feng, *Langmuir*, 2011, **27**, 3095–3099.

101 X. Yang, X. Liu, X. Liu, F. Pu, J. Ren, X. Qu, *Adv. Mater*., 2012, **24**, 2890–2895.

102 L. S. Wang, L. C. Wu, S. Y. Lu, L. L. Chang, I. T. Teng, C. M. Yang, J. A. Ho, *ACS Nano*, 2010, **4**, 4371–4379.

103 G. Nordlund, J. B. Sing Ng, L. Bergström, P. Brzezinski, *ACS Nano*, 2009, **3**, 2639–2646.

104 J. Liu, X. Jiang, C. Ashley, C. J. Brinker, *J. Am. Chem. Soc*., 2009, **131**, 7567–7569.

105 J. Liu, A. Stace-Naughton, X. Jiang, C. J. Brinker, *J. Am. Chem. Soc.*, 2009, **131**, 1354–1355.

106 C. E. Ashley, E. C. Carnes, K. E. Epler, D. P. Padilla, G. K. Phillips, R. E. Castillo, D. C. Wilkinson, B. S. Wilkinson, C. A. Burgard, R. M. Kalinich, J. L. Townson, B. Chackerian, C. L. Willman, D. S. Peabody, W. Wharton, C. J. Brinker, *ACS Nano*, 2012, **6**, 2174–2188.

107 X. Hu, X. Hao, Y. Wu, J. Zhang, X. Zhang, P. C. Wang, G. Zou, X. J. Liang, *J. Mater. Chem. B*, 2013, **1**, 1109–1118.

108 E. Climent, A. Bernardos, R. Martínez-Máñez, A. Maquieira, M. D. Marcos, N. Pastor-Navarro, R. Puchades, F. Sancenón, J. Soto, P. Amorós, *J. Am. Chem. Soc.*, 2009, **131**, 14075–14080.

109 X. Wu, Z. Wang, D. Zhu, S. Zong, L. Yang, Y. Zhong, Y. Cui, *ACS Appl. Mater. Interfaces*, 2013, **5**, 10895–10903.

110 C. Chen, J. Geng, F. Pu, X. Yang, J. Ren, X. Qu, *Angew. Chem. Int. Ed.*, 2010, **50**, 882–886.

111 P. Zhang, F. Cheng, R. Zhou, J. Cao, J. Li, C. Burda, Q. Min, J. J. Zhu, *Angew. Chem. Int. Ed.*, 2014, **53**, 2371–2375.

112 S. Zhou, X. Du, F. Cui, X. Zhang, *Small*, 2013, **10**, 980–988.

113 F. Balas, M. Manzano, P. Horcajada, M. Vallet-Regí, *J. Am. Chem. Soc.*, 2006, **128**, 8116–8117.

114 H. Zheng, Y. Wang, S. Che, *J. Phys. Chem. C*, 2011, **115**, 16803–16813.

115 R. Liu, Y. Zhang, X. Zhao, A. Agarwal, L. J. Mueller, P. Feng, *J. Am. Chem. Soc.*, 2010, **132**, 1500–1501.

116 C. Yu, M. Luo, F. Zeng, F. Zheng, S. Wu, *Chem. Commun*., 2011, **47**, 9086-9088.

117 H. Kim, S. Kim, C. Park, H. Lee, H. J. Park, C. Kim, *Adv. Mater*., 2010, **22**, 4280–4283.

118 J. Croissant, J. I. Zink, *J. Am. Chem. Soc*., 2012, **134**, 7628–7631.

119 S. Angelos, Y. W. Yang, K. Patel, J. F. Stoddart, J. I. Zink, *Angew. Chem. Int. Ed.*, 2008, **47**, 2222–2226.

120 S. R. Choi, D. J. Jang, S. Kim, S. An, J. Lee, E. Oh, J. Kim, *J. Mater. Chem. B*, 2014, **2**, 616–619.

121 R. Guillet-Nicolas, A. Popat, J. L. Bridot, G. Monteith, S. Z. Qiao, F. Kleitz, *Angew. Chem. Int. Ed.*, 2013, **52**, 2318–2322.

122 K. Murakami, X. Yu, S. Watanabe, T. Kato, Y. Inoue, K. Sugawara, *J. Colloid Interface Sci*. 2011, **354**, 771–776.

123 D. E. Thrall, R. L. Page, M. W. Dewhirst, R. E. Meyer, P. J. Hoopes, J. N. Kornegay, *Cancer Res*., 1986, **46**, 6229–6235.

124 Z. Zhou, S. Zhu, D. Zhang, *J. Mater. Chem.*, 2007, **17**, 2428–2433.

125 C. Liu, J. Guo, W. Yang, J. Hu, C. Wang, S. Fu, *J. Mater. Chem*., 2009, **19**, 4764–4770.

126 E. Aznar, L. Mondragón, J. V. Ros-Lis, F. Sancenón, M. D. Marcos, R. Martínez-Máñez, J. Soto, E. Pérez-Payá, P. Amorós, *Angew. Chem. Int. Ed.*, 2011, **50**, 11172–11175.

127 A. Schlossbauer, S. Warncke, P. M. E. Gramlich, J. Kecht, A. Manetto, T. Carell, T. Bein, *Angew. Chem. Int. Ed.*, 2010, **49**, 4734–4737.

128 G. K. Balendiran, E. Dabur, D. Fraser, *Cell Biochem. Funct*., 2004, **22**, 343–352.

129 R. Mortera, J. Vivero-Escoto, I. Slowing, E. Garrone, B. Onida, V. Lin, *Chem. Commun*., 2009, 3219–3221.

130 T. D. Nguyen, Y. Liu, S. Saha, K. C. F. Leung, J. F. Stoddart, J. I. Zink, J. *Am. Chem. Soc*., 2007, **129**, 626–634.

131 L. Chen, Z. Zheng, J. Wang, X. Wang, *Micropor. Mesopor. Mater*., 2014, **185**, 7–15.

132 N. K. Mal, M. Fujiwara, Y. Tanaka, *Nature,* 2003, **421**, 350–353.

133 D. P. Ferris, Y. L. Zhao, N. M. Khashab, H. A. Khatib, J. F. Stoddart, J. I. Zink, *J. Am. Chem. Soc.*, 2009, **131**, 1686–1688.

134 S. Angelos, Y. W. Yang, N. M. Khashab, J. F. Stoddart, J. I. Zink, *J. Am. Chem. Soc.*, 2009, **131**, 11344–11346.

135 N. Ž. Knežević, B. Trewyn, V. Lin, *Chem. Eur. J.*, 2011, **17**, 3338–3342.

136 J. Vivero-Escoto, I. Slowing, C. Wu, V. Lin, *J. Am. Chem. Soc.*, 2009, **131**, 3462–3463.

137 S. P. Mornet, S. B. Vasseur, F. Grasset, E. Duguet, *J. Mater. Chem.*, 2004, **14**, 2161–2175.

138 M. Mahmoudi, S. Sant, B. Wang, S. Laurent, T. Sen, *Adv. Drug Deliv. Rev.*, 2011, **63**, 24–46.

139 D. Arcos, V. Fal-Miyar, E. Ruiz-Hernández, M. Garcia-Hernández, M. L. Ruiz-González, J. González-Calbet, M. Vallet-Regí, *J. Mater. Chem.*, 2012, **22**, 64–72.

140 N. Ž. Knežević, E. Ruiz-Hernández, W. E. Hennink, M. Vallet-Regí, *RSC Adv.*, 2013, **3**, 9584–9593.

141 T. Sen, A. Sebastianelli, I. J. Bruce, *J. Am. Chem. Soc.*, 2006, **128**, 7130–7131.

142 W. Zhao, J. Gu, L. Zhang, H. Chen, J. Shi, *J. Am. Chem. Soc.*, 2005, **127**, 8916–8917.

143 W. Zhao, J. Shi, H. Chen, L. Zhang, *J. Mater. Res.*, 2011, **21**, 3080–3089.

144 Y. Deng, D. Qi, C. Deng, X. Zhang, D. Zhao, *J. Am. Chem. Soc.*, 2008, **130**, 28–29.

145 L. Zhang, S. Z. Qiao, Y. G. Jin, Z. G. Chen, H. C. Gu, G. Q. Lu, *Adv. Mater.*, 2008, **20**, 805–809.

146 X. Li, J. Zhang, H. Gu, *Langmuir*, 2011, **27**, 6099–6106.

147 C. C. Huang, C. Y. Tsai, H. S. Sheu, K. Y. Chuang, C. H. Su, U. S. Jeng, F. Y. Cheng, C. H. Su, H. Y. Lei, C. S. Yeh, *ACS Nano,* 2011, **5**, 3905–3916.

148 V. Matsura, Y. Guari, J. Larionova, C. Guérin, A. Caneschi, C. Sangregorio, E. Lancelle-Beltran, A. Mehdi, R. J. P. Corriu, *J. Mater. Chem.*, 2004, **14**, 3026–3033.

149 S. Huang, P. Yang, Z. Cheng, C. Li, Y. Fan, D. Kong, J. Lin, *J. Phys. Chem. C,* 2008, **112**, 7130–7137.

150 Y. Chen, H. Chen, D. Zeng, Y. Tian, F. Chen, J. Feng, J. Shi, *ACS Nano*, 2010, **4**, 6001–6013.

151 Y. Chen, H. Chen, L. Guo, Q. He, F. Chen, J. Zhou, J. Feng, J. Shi, *ACS Nano,* 2010, **4**, 529–539.

152 Y. Zhu, E. Kockrick, T. Ikoma, N. Hanagata, S. Kaskel, *Chem. Mater.*, 2009, **21**, 2547–2553.

153 A. Popat, S. Jambhrunkar, J. Zhang, J. Yang, H. Zhang, A. Meka, C. Yu, *Chem. Commun.*, 2014, **50**, 5547–5550.

154 C. Chen, F. Pu, Z. Huang, Z. Liu, J. Ren, X. Qu, *Biomater. Sci*., 2013, **2**, 121–130.

155 K. Radhakrishnan, S. Gupta, D. P. Gnanadhas, P. C. Ramamurthy, D. Chakravortty, A. M. Raichur, *Part. Part. Syst. Charact.*, 2013, **31**, 449–458.

156 Y. S. Lin, K. R. Hurley, C. L. Haynes, *J. Phys. Chem. Lett.*, 2012, 364–374.

157 V. Mamaeva, C. Sahlgren, M. Lindén, *Advanced Drug Delivery Reviews,* 2013, **65**, 689–702.

Résumé en français (Chapitre 1)

Dans ce chapitre, il est montré que les nanoparticles de silice mésoporeuse (MSN) ont été utilisées pour concevoir des systèmes efficaces de délivrance de médicaments, en particulier en raison de leur capacité élevée d'encapsuler des principes actifs, de leur grande stabilité et leur possibilité de protéger les molécules actives dans un environnement biochimique. En effet, les propriétés de biocompatibilité et de biodégradabilité sont à la base du développement de ces matériaux dans ce domaine. En outre, les MSN peuvent offrent une grande variété de voies pour la fonctionnalisation des surfaces de la silice en utilisant des molécules stimuli-sensibles (polymères, nanoparticules métalliques et ligands de ciblage) au pH, à la chaleur, à la lumière et au champ magnétique. Les stratégies récentes de fonctionnalisation ont été adaptées pour contrôler la cinétique de libération de médicament à l'endroit approprié en évitant la libération prématurée afin d'éviter des effets secondaires indésirables. Pour le moment, la plupart des études *in vitro* ont permis d'évaluer la cytotoxicité, la biocompatibilité, la biodégradabilité, la rétention de MSN et la compréhension de certains mécanismes de l'absorption cellulaire. Cependant, la toxicité et les résultats d'absorption intracellulaire décrits dans la littérature sont spécifiques à chaque système d'administration de médicament et ne sont pas encore généralisables. En outre, la conception simple et peu coûteuse de supports de médicaments à base de MSN est nécessaire pour mettre au point des systèmes de délivrance de médicaments ou des biocapteurs pour des applications thérapeutiques.

Chapter 2

Designing stimuli-responsive nano-structured carriers of curcumin

Curcumin, a hydrophobic natural polyphenol with yellow colour that is isolated from the dried root of turmeric, the rhizome of the herb *Curcuma longa*, has been used for centuries in indigenous medicine as anti-inflammatory and anti-oxidant agent.[1] It exhibits pleiotropic pharmacological effects on cardiovascular pulmonary, autoimmune as well as metabolic diseases.[2] Its most interesting potential use is probably against cancer[3,4]: pre-clinical studies have shown that it can inhibit cancer genesis in a variety of cell lines, including breast, cervical, colon, gastric, hepatic, oral epithelial, ovarian, pancreatic, prostate cancer and leukemia.[5] Moreover, it was reported that curcumin caused cell death in eight melanoma cell lines, also in those carrying mutant p53, which are very resistant to conventional chemotherapy.[6] However, practical applications of curcumin have been limited due to its solubility concern.[7] Indeed, curcumin has an extremely low solubility in the range of pH 1.2 to 7.4, which is physiological pH value of human's body, and under alkaline condition, curcumin undergoes a rapid hydrolysis, being decomposed into ferulic acid, its methyl ester and vanillin.[8,9] Curcumin is very susceptible to photochemical and thermal degradation that could be also a problematic for its long term storage.[10,11] Besides, some studies have revealed that its poor absorption and rapid metabolism severely curtail its bioavailability.[12]

These hurdles can be passed through by incorporating curcumin into nanoparticles,[13] liposomes,[14] or micelles,[15] complexing with cyclodextrins (CD) in aqueous solutions,[16,17] or into mesoporous silica.[18] However, the organic matter based drug carriers could be instinctively unstable without post-synthesis treatment like surface coating. Moreover, in some case, a possible drug leaking during storage can occur, limiting a wide application of these drug carriers.[19]

In this chapter, for designing stimuli-responsive drug deliver systems, two approaches were tested: 1) optimization of porous silica materials templated using solid lipid nanoparticles (SLN) and 2) development of a method for surface coating of silica using tannic acid-Fe(III) complex.

Indeed, solid lipid nanoparticles (SLN) that was introduced in 1991 have been considered as an alternative drug carrier system to traditional colloidal drug delivery systems. SLN are generally spherical in shape and consist of solid lipid core stabilized and dispersed in aqueous solution containing surfactant. SLN can be stabilised as dispersion due to electrostatic repulsion and steric hindrance between particles, which are generally provided by surfactants. (Figure 2.1) SLN combine the advantages of several traditional systems:

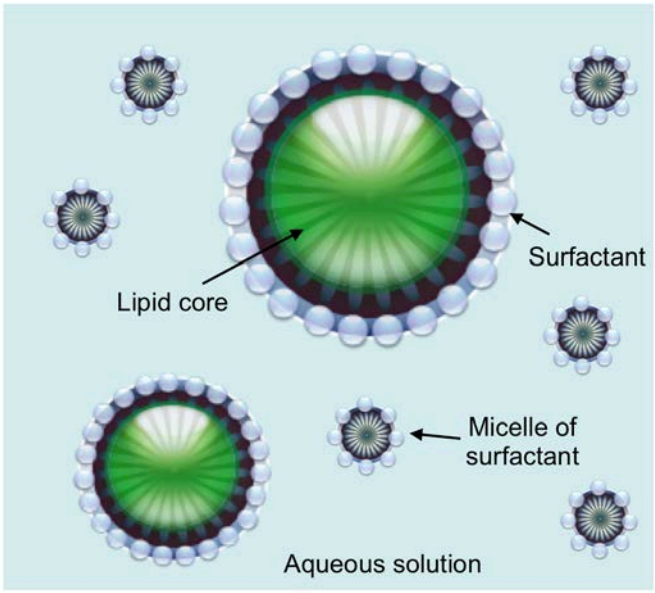

Figure 2.1 Structure of Solid lipid nanoparticle (SLN) stabilized with surfactant molecules in aqueous solution.

First, SLN can be prepared from cost-effective, readily and commercially available materials, without organic synthesis pathway that is generally cost and time consuming process. A variety of lipids such as triglycerides, waxes or fatty acids can be used as solid lipid core. Lecithin, poloxamer, polysorbate or bile acids are mainly used as surfactant, which stabilize solid lipid core. Second, because most of lipids in the market are obtained from natural lipids, the ingredients of SLN can be chosen based on U. S. Food and Drug Administrationin active (FDA) ingredient list,[20] SLN could be thus considered as biocompatible drug delivery system with very low toxicity. In addition, as most of SLN preparations could be done without using any organic solvents, thus SLN can be free of possible toxicity concern. Last, SLN can be prepared using simple and low-cost fashion that is perhaps the most important advantage of SLN over other colloidal drug delivery systems.

However, SLN have also some disadvantages such as poor drug loading capacity,[21,22] drug leaking problem during the storage,[23] or high water content (70 to 99 %). Most of them are related to the structure of some lipids with high crystallinity. For example, a lipid that exhibits high crystallinity might limit drug loading, because there are not enough ‘room’ for ‘guest’ molecules, as the lipid molecules are tightly packed. ‘Guest’ molecules might be expulsed during storage due to high crystallinity of lipids that tend to be re-organized in order to reduce Gibbs-free energy.[23] Indeed, the crystallinity could be reduced using less crystalline lipids or adding co-lipid molecules. However, this approach might lead to the stability issues

like particle size growth or gelation over time.[24] Thus, it is important de develop a method to improve the stability of SLN using inorganic materials such as mesoporous silica, which is described through the first 2 part of this chapter.

In case of surface coating, polymers with stimuli-responsive functions have been mostly used to seal mesopore gates, and the results showed well-controlled stimuli-responsive (pH, temperature, redox) drug release. However, the main drawback of there methods is mutil-step and time consuming synthesis and modification of silica surface. Indeed, very recently, an extremely rapid, one-step method using coordination complex of natural polyphenols, tannic acid and Fe(III) ions has been reported.[25] The resulting film prepared using this complex showed pH-dependent behavior, with a good stability above pH 7 due to multivalent coordination. Afterward, the film becomes less stable as the pH decreases, forming a bis-complex, then a mono-complex between tannic acid and Fe(III) ions. Moreover, tannic acid is already known as non-toxic ingredient as approved by U.S. FDA. Based on this strategy, multi stimuli-responsive mesoporous silica has been also developed and described in the last part of this chapter.

Thereby, it is believed that two approaches mentioned above could be an effective way for designing stimuli-responsive nano-structured carriers of curcumin. More detailed discussions are presented in the following.

Part 2.1

pH-controlled delivery of curcumin from a compartmentalized solid lipid nanoparticle@mesostructured silica matrix

This part was published as: S. Kim, M.-J.-Stébé, J.-L Blin, A. Pasc, pH-controlled delivery of curcumin from a compartmentalized solid lipid nanoparticle@mesostructured silica matrix in *J. Mater. Chem. B,* 2014, **2** 7910-7917.

2.1.1 Introduction

For organic-inorganic materials design, solid lipid nanoparticles that already contain certain amount of surfactants as stabilizing agents, could be used directly to build hierarchical meso-macroporous silica materials with tuneable pore size and morphology as reported in previous work of our group.[26-28] The mechanism proposed to explain the formation of these hierarchically structured macroporous–mesoporous silicas is similar to the one for emulsions (Figure 2.1.1).[29] In such a mechanism, the highly ordered array of mesopores is templated by the micelles (*i.e.* Pluronic P123) and induced via the cooperative templating mechanism (CTM),[26] whereas the macropore network is generated by the lipid nanoparticles dispersed in the continuous medium. Moreover, by changing the surfactant nature, one can tune the size of the mesopores and the morphology of the resulting materials.

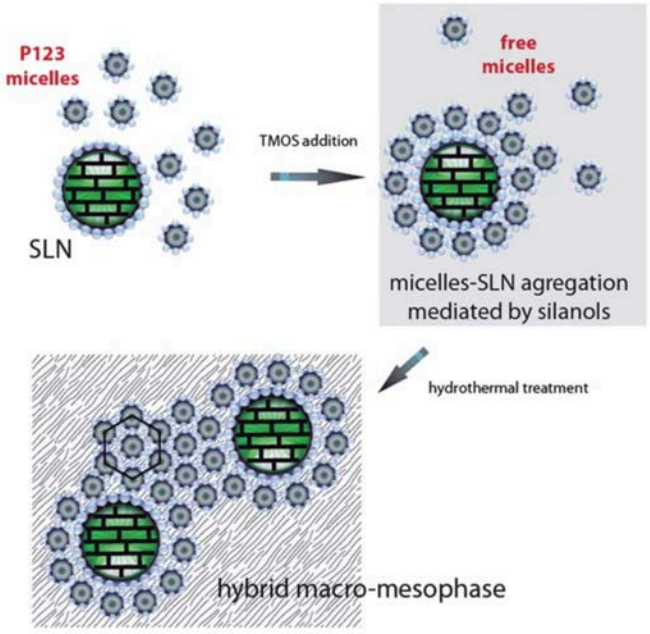

Figure 2.1.1. Proposed mechanistic scheme for the formation of macro– mesostructured silica with a hexagonal mesopore network.

In this part, we extended the use of SLN as both drug loading agents and meso-macropore templates to obtain hybrid organic–inorganic as drug delivery systems with the aim to increase the stability, bioavailability and sustainability of curcumin, through a double encapsulation of the drug into a core–shell nanomatrix. In addition to general characterization of these materials, *in vitro* curcumin release at three different pH values and their cytotoxicity were investigated to demonstrate their potential applications in biomedical fields.

2.1.2 Materials and methods

Chemicals

Tetramethylorthosilicate (TMOS), Pluronic P123, curcumin, hexadecyltrimethylammonium bromide (CTAB), sodium chloride, acetic acid, sodium acetate, potassium chloride, monopotassium phosphate and disodium phosphate were purchased from Sigma-Aldrich. Stearic acid (SA) and N-hexadecylpalmitate (NHP) were purchased from ACROS. Water was deionized using a Milli-Q pack system. All chemicals were used as received without further purification. All buffer solutions were prepared according to the methods described in the European Pharmacopoeia.

Solid Lipid Nanoparticles (SLN) preparation

SLN dispersion was prepared using ultra-sonication of a hot emulsion obtained from a mixture of curcumin and a melted lipid dispersed in aqueous micellar phase. In a typical procedure, the mixture of solid lipid (stearic acid or N-hexadecylpalmitate, 2200 mg) and curcumin (22 mg) were heated and homogenized at 70-80°C. The aqueous phase containing surfactant (6.9 wt.% of Pluronic P123) was heated at the same temperature as the oil phase. The oil phase was added to the aqueous micellar solution and the mixture was sonicated for 3 min with an ultrasonic device. (Branson Sonifier, 40 W output power, 50 % cycle) The hot oil/water emulsion was then cooled to room temperature under vigorous string to afford lipid solidification. Curcumin loaded SLN prepared using N-hexadecylpalmitate (NHP) and stearic acid (SA) were denoted as CU-NHP-SLN and CU-SA-SLN, respectively. Solid lipid nanoparticles without curcumin were also prepared in the same manner for control experiments. These samples were denoted as Blank-NHP-SLN, Blank-SA-SLN, depending on the lipid source. The resulting SLN samples were used for silica mineralization without phase separation.

Synthesis of hybrid SLN–silica materials

Hybrid SLN–silica materials were synthesized as previously reported by our group.[26,27] In a typical procedure, 900 mg of tetramethylorthosilicate (TMOS) was added dropwise into 4 mL of SLN dispersion. The P123/TMOS molar ratio (R) was fixed to 0.008 to obtain hexagonally ordered mesopore structure. The mixture was stirred for 1 h at room temperature and then

transferred into sealed Teflon autoclaves, then was assayed at 70°C for 24 h. Afterwards, as-synthesized hybrid SLN-silica material was dried at 40°C *in vacuo* for 24 h in order to evaporate residual water and methanol. No filtration or separation was performed, as the material was pasty. The materials prepared from CU-NHP-SLN and CU-SA-SLN were denoted as CU-NHP-Mat and CU-SA-Mat. Bare silica materials were also obtained after removal of organic matters (lipid, surfactants) under Soxhelt ethanol extraction for 24 h.

Assay of the content of curcumin in hybrid SLN-silica

5 mL of THF was added to 50 mg of dried hybrid SLN-silica material, and then the sample was sonicated for 30 min in order to dissolve lipid and curcumin into the organic phase. Afterwards, 95 mL of ethanol was added, and the sample was diluted 10-fold using ethanol for UV-Vis spectrometry analysis. The concentration was calculated using a standard curve of curcumin in ethanol containing 0.5 % (v/v) of THF.

Drug partitioning ratio (Curcumin encapsulation efficiency)

To determine the drug partitioning between the lipid core and the micellar phase, 1 mL curcumin loaded CU-NHP-SLN dispersion was added to anhydrous ethanol in order to precipitate NHP, and then the sample was centrifuged at 5000 rpm for 5 min. The precipitate was further washed with 20 mL water 2 times and dried at 40°C *in vacuo* for 24 h. 10 mg of the dried SLN precipitate was dissolved in 25 mL methylene chloride and then analysed by UV-vis spectrometry (UV-Visible CARY3E-Varian) at 423 nm and its concentration was calculated using a standard curve of curcumin in methylene chloride. In the case of stearic acid based SLN dispersion, 1 mL SLN dispersion was filtered using a Millipore membrane (0.20 μm). The filtrate was then washed with water (2 × 20 mL) and further dried at 40°C *in vacuo* for 24 h. 10 mg of the filtrate was analysed by the same method used for NHP based SLN dispersion. The partitioning ratio was calculated by dividing the analysed weight of curcumin in dried lipid to the total weight of curcumin in the SLN formulation.

In vitro drug release experiments

Release experiments were carried out in 3 different buffer solutions, pH 1.2, 4.5 and 7.4. Briefly, 50 mg of curcumin loaded hybrid SLN-silica material was immersed into 50 mL of

buffer solution containing 0.1 wt% of CTAB.[30] The system was maintained at 25°C under magnetic stirring at 100 rpm. At regular intervals, 1.5 mL aliquots were withdrawn and replaced by an equal volume of receiving solution in order to maintain sink condition. The withdrawn samples were centrifuged at 5000 rpm for 5 min and filtered on a 0.45 µm membrane filter (Acrodisc Syringe Filger), and then diluted 4-fold with the same release medium. The curcumin release was analysed using a UV-vis spectrometer at 423 nm and its concentration was calculated using a standard curve of curcumin established for each dissolution medium. The final cumulative release percentage was corrected using a dilution factor. All data reported are the mean value with standard deviation of at least three different experiments.

Cytotoxicity experiment

Cell lines and cell culture: Human pulmonary embryonic fibroblasts were obtained from BioMerieux (Lyon, France). Cells were maintained in modified Eagle's medium (MEM, 41090, Invitrogen, France) for MRC-5 supplemented with 10% decomplemented foetal bovine serum (FBS, 10270, Lot 40Q5150K, Invitrogen, France) without antibiotics at 37°C, 5% CO_2, under a humid atmosphere. MRC-5 cells were plated at 104 cells/well in 96-well plates (831835, Sarstedt, France). Forty-eight hours after plating, the growth medium was removed and replaced with the test solutions (100 µL). After 24 h exposure, viability and cytotoxicity tests were performed.

MTT assay: Viability tests were carried out using a commercially available cell proliferation reagent [3-(4,5-dimethylthiazolyl-2-yl)-2,5-diphenyltetrazolium bromide] (MTT) (135038, Sigma, France).[31] The assay is based on the cleavage of the tetrazolium salt MTT by active mitochondrial dehydrogenases to produce an insoluble purple formazan salt. Since this conversion only occurs with viable cells, it directly correlates with cell count. Experiments were performed in 100 µL of medium in flat-bottom 96-well plates (831835, Sarstedt, France). After 24, 48, 120 and 168 h of incubation, stock MTT solution (5 mg/mL MTT in PBS) was added (10 µL per well) and plates were incubated in a humidified atmosphere with 5% CO_2 at 37 °C for 4 h. Then, insoluble purple formazan was dissolved by adding 100 µL sodium dodecyl sulfate (SDS, L-5750, Sigma, France) (0.1 g/mL SDS in PBS, with 445 µL HCl 0.01 M) to each well, and incubated for 4 h more. The absorbance at A540 nm was measured with a reference wavelength of A690 nm, using an ELISA reader (Multiskan EX,

Thermo Electron Corporation, France). Eight wells per dose and time point were counted in three different experiments.

2.1.3 Results and Discussion

Solid Lipid Nanoparticles (SLN) preparation

Curcumin-loaded solid lipid nanoparticles (CU-SLN), used as both a macro-template for the silica material and a reservoir of curcumin in this study, were prepared by sonicating a hot emulsion containing the melted lipid (cetyl palmitate (NHP) or stearic acid (SA)) and micelles of Pluronic P123. In general, lipids have relatively low melting point (i.e. 52°C for cetyl palmitate), thus hot emulsion technique could be powerful and simple method when it combines with ultra-sonication for SLN preparation. Moreover, compared with other methods like solvent diffusion-evaporation or high-pressure homogenization, hot emulsion technique followed by ultra-sonication needs much less time (~ 5 min). Concerning the composition of SLN, since most of the synthesis parameters were already optimized in the previous work of our group,[26] we focused only on an effective encapsulating of curcumin into solid lipid nanoparticles based on NHP and SA.

First, dynamic light scattering (DLS) measurements were performed on curcumin loaded-SLN and blank SLN in order to determine their size distribution and investigate the influence of guest molecule, curcumin. As shown in Table 2.1.1, a slight increase in mean diameters for curcumin-loaded SLN was observed, compared to those of blank SLN. Zeta potential measurements gave slightly negative values (around -10 mV), which are consistent with molecularly organized systems of non-ionic surfactants (here micelles of P123) that might be adsorbed at the water–SLN interface to stabilize the dispersions.[32,33] The absolute values of the zeta potential are slightly higher for blank-SA-SLN than for blank-NHP-SLN, probably due to the presence of COO^- group of stearic acid that could be located in the P123 layer of solid lipid nanoparticles. This hypothesis will be further discussed using FT-IR and SAXS experiments. However, the zeta potential value does not show a significant change after drug loading, suggesting that the interface of the solid lipid nanoparticles was not affected by loading of small amount of curcumin. (1.0 wt.% with respect to lipid)

SLN formulation	MD (nm)	ZP (mV)	PR (%)
Blank-NHP-SLN	292 ± 35	-11.0 ± 1.4	-
CU-NHP-SLN	313 ± 43	-8.2 ± 2.1	20 ± 3
Blank-SA-SLN	426 ± 38	-16.0 ± 1.4	-
CU-SA-SLN	447 ± 44	-15.1 ± 1.1	65 ± 5

Table 2.1.1. Physicochemical characteristics of SLN; MD stands for mean diameter, ZP for zeta potential, and PR for partitioning ratio.

It was revealed that the drug-partitioning ratio (PR) between the lipid core of SLN and the micelles highly depends on the lipid source. For CU-NHP-SLN, about 80 wt.% of CU is dispersed in the micellar phase, meaning that only 20 % of the curcumin is located in the lipid core. However, the drug-partitioning ratio for CU-SA-SLN drastically increased up to 65 %, probably due to the interaction between stearic acid and curcumin, as confirmed by FT-IR spectra.

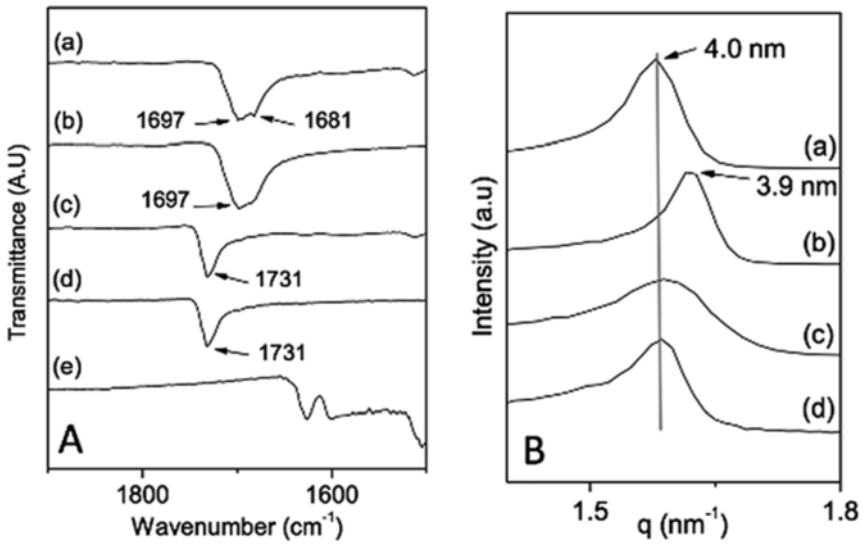

Figure 2.1.2. (A) IR spectra and (B) SAXS pattern of (a) CU-SA-SLN, (b) blank-SA-SLN, (c) blank-NHP-SLN, (d) CU-NHP-SLN, and (e) curcumin

Indeed, according to FT-IR spectra for CU-Lipid-SLN and pure lipids (Figure 2.1.2A), no shift of the *v*CO bond of NHP was observed when adding CU (CU-NHP-SLN, Figure 2.1.2A-d), while, for stearic acid, a more pronounced peak at 1681 cm^{-1} appeared (CU-SA-SLN, Figure 2.1.2A-a). This could be assigned to a *v*CO of the stearic acid forming a

hydrogen bond with the enol form of curcumin, while for CU-NHP-SLN no peak appeared after encapsulation of curcumin due to the lack of carboxyl acid group. (Figure 2.1.3)

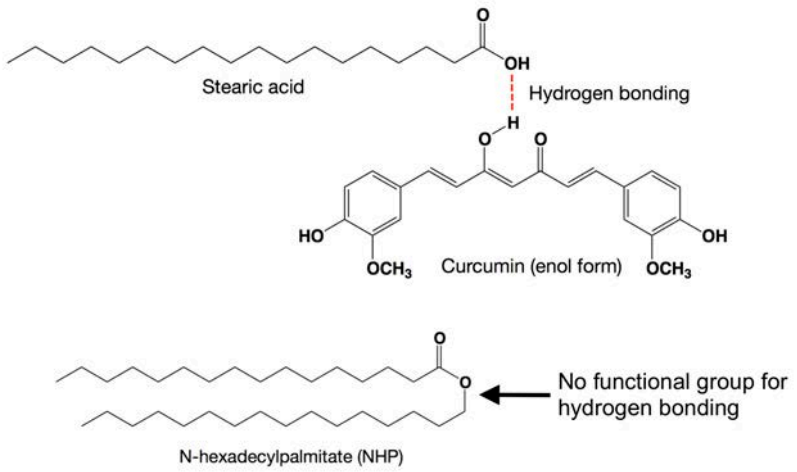

Figure 2.5. Possible hydrogen bonding between lipids and curcumin

SAXS experiments also confirmed the interaction between stearic acid-curcumin. After encapsulation of curcumin in stearic based SLN (CU-SA-SLN), the position of the (001)-reflection is slightly shifted to lower q value compared to blank SA-SLN.[34] (Figure 2.1.2B) This shift could be caused by the interaction between curcumin and stearic acid as shown in FT-IR. For CU-NHP-SLN, the shift is not visible, as the ester functional group of NHP cannot interact with curcumin. Therefore, it is reasonable to assume that the encapsulation rate of curcumin into the lipid core of CU-SA-SLN could be enhanced by hydrogen bonding.[35]

Furthermore, curcumin encapsulation efficiency for each SLN formulation was analysed using nanoparticle-tracking analysis (NTA). (Figure 2.6) Since the curcumin is a fluorescent molecule with a maximum absorbance and emission peaks at 427 nm and 530 nm, and nanoparticle-tracking analysis (NTA) is based on Brownian movement of particles, thus curcumin loaded SLN with 300 nm in diameter could be detected and quantified using nanoparticle-tracking analysis with fluorescence filter. At given concentration, CU-SA-SLN showed more bright points compared to CU-NHP-SLN on nanoparticle-tracking analysis video (captured image), meaning that the encapsulation of curcumin is more efficient for stearic acid based SLN than NHP based SLN. Besides, the curcumin freely dispersed in aqueous micellar solution cannot be detected, since the detection limit of nanoparticle-tracking analysis is 30 nm.

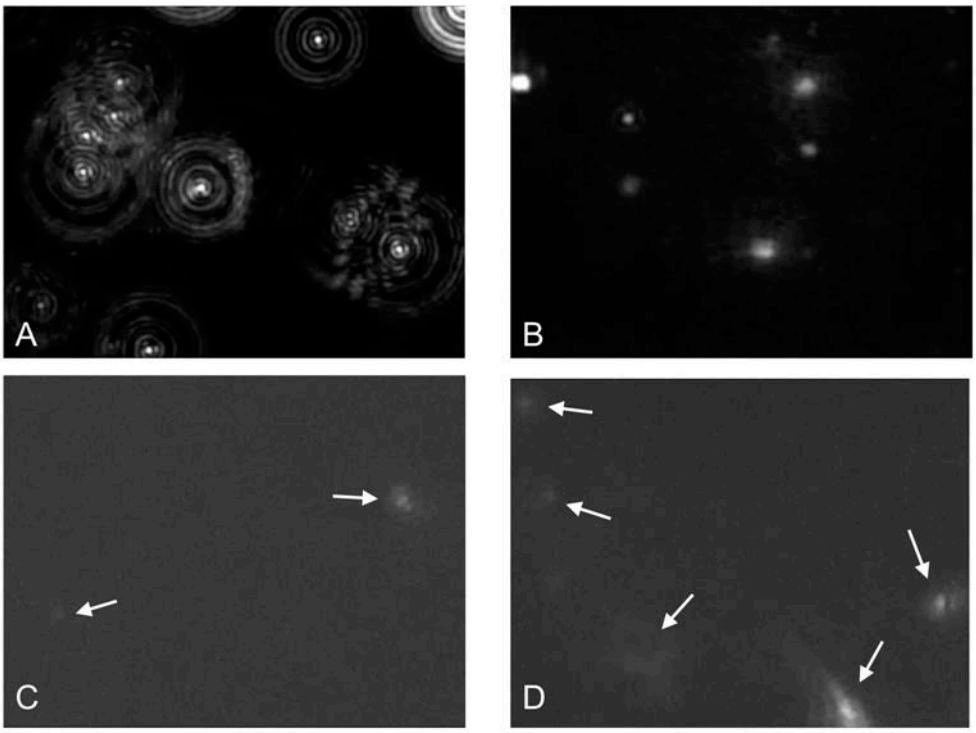

Figure 2.1.4. Captured images of Nanoparticle Tracking Analysis (NTA) for (A) CU-NHP-SLN, (B) CU-SA-SLN without any filter; (C) CU-NHP-SLN, (D) CU-SA-SLN with fluorescence filter. (arrows indicate fluorescence signals of curcumin encapsulated in SLN)

Hybrid SLN-silica materials

Hybrid SLN-silica materials can be obtained by mineralization of CU-SLN dispersion, using tetramethyl orthosilicate (TMOS) as silica precursor, followed by silica hydrolysis-condensation on the surface of SLN. Since SLN dispersion consists of self-assembled surfactant micelles with sub-micron scaled lipid particles, the mineralization occurs through a dual templating mechanism combining cooperative templating (CTM) of micelles and hard templating of lipid nanoparticles that afford mesostructured and macrostructured domain, respectively. Concerning the synthesis of the hybrid materials, since the parameters like temperature, concentration of each ingredient were largely investigated in a previous paper of our group,[26] only the optimal conditions were used to obtain hybrid-silica materials with hexagonally ordered mesopores. (6.9 wt.% of P123 with 10 wt.% of lipid in water) Besides, blank-SLN samples were also mineralized to investigate the effect of curcumin loading in SLN, and it is revealed that a small amount of curcumin (1 wt.% with respect to lipid) did not affect the mesoporosity of silica material. Bare silica materials were also obtained by removing organic matter by soxhlet extraction with ethanol for 24 h for further

characterizations. The silica materials obtained from CU-NHP-SLN and CU-SA-SLN are denoted as CU-NHP-Mat and CU-SA-Mat, respectively.

To investigate the mesostructuring of the silica materials, small-angle X-ray scattering (SAXS) analysis was performed on bare silica materials. The SAXS data for bare CU-NHP-Mat (Figure 2.1.5a), indicates 3 peaks, which can be attributed to the (100), (110) and (200) reflections of the hexagonal structure. In the case of silica material prepared using CU-SA-SLN (CU-SA-MAt, Figure 2.1.5b), the mesopore were hexagonally ordered however the second and the third peak, which correspond to (110) and (200) reflections of the hexagonal structure, were less resolved than in bare silica materials obtained from NHP. This could be due to the carboxyl acid group of stearic acid, which could enhance the silica condensation rate, compared to NHP that has no acidic or basic functional group, as confirmed using the zeta potential measurements. The lattice parameters ($a_0 = 2d_{100}/\sqrt{3}$) for materials were calculated as 12.5 nm and 13.2 nm for CU-NHP-Mat and CU-SA-Mat, respectively.

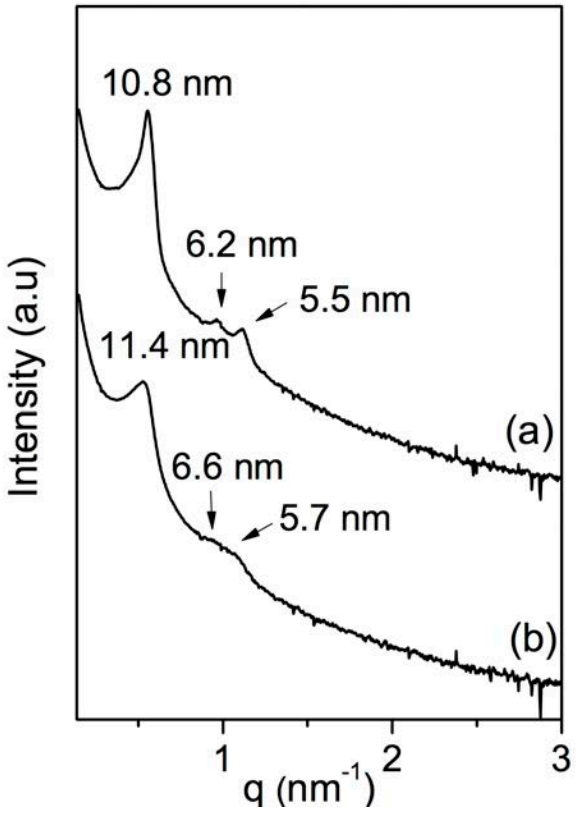

Figure 2.1.5. SAXS pattern of (a) CU-NHP-Mat, (b) CU-SA-Mat after the removal of organic matters.

N_2 adsorption–desorption isotherms for bare silica materials are shown in Figure 2.1.6. According to these graphs, all samples exhibit a type IV isotherm, which is characteristic of mesoporous materials. The specific surface area and pore volume values as well as pore diameter distributions are summarized in Table 2.1.2. The wall thickness of mesopores, deduced by subtracting the pore diameter from the lattice parameter a_0, varied from 5.2 nm to 7.2 nm. These values are higher than those of typical SBA-15 (4 nm), generally prepared using P123 surfactant. This result suggests that the mesostructuring of the silica materials in this work could be more stable than the conventional SBA-15.[36]

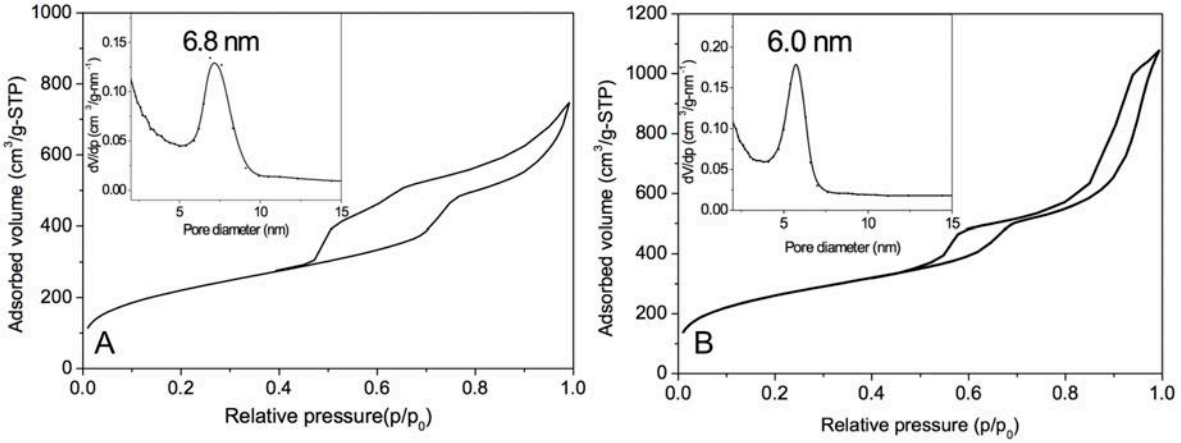

Figure 2.1.6. Nitrogen adsorption–desorption isotherm and pore size distribution (inset) of (A) CU-Mat, (B) CU-SA-Mat.

The imprint of SLN beads on silica materials was confirmed by mercury intrusion porosimetry measurements on bare silica materials. In Figure 2.1.7A, a broad peak centred at 900 nm is observed for CU-NHP-Mat. These macropores are larger than the mean diameter of CU-NHP-SLN, which is around 310 nm. This is probably due to a possible agglomeration of NHP during mineralization by TMOS at 70°C, which is a little higher than melting point of NHP (54°C). For CU-SA-Mat (Figure 2.1.7B), the peak corresponding to macropores is centered on 470 nm that is almost identical to the size of CU-SA-SLN beads (450 nm). This could be explained by the fact that nanoparticles of stearic acid with a melting point of 68°C remain in solid state and do not change their shape during silica condesation at 70°C. Also, the mineralization rate for CU-SA-SLN is faster than CU-NHP-SLN as discussed, an effective silica shell around CU-SA-SLN could be formed at the early time of mineralization step.

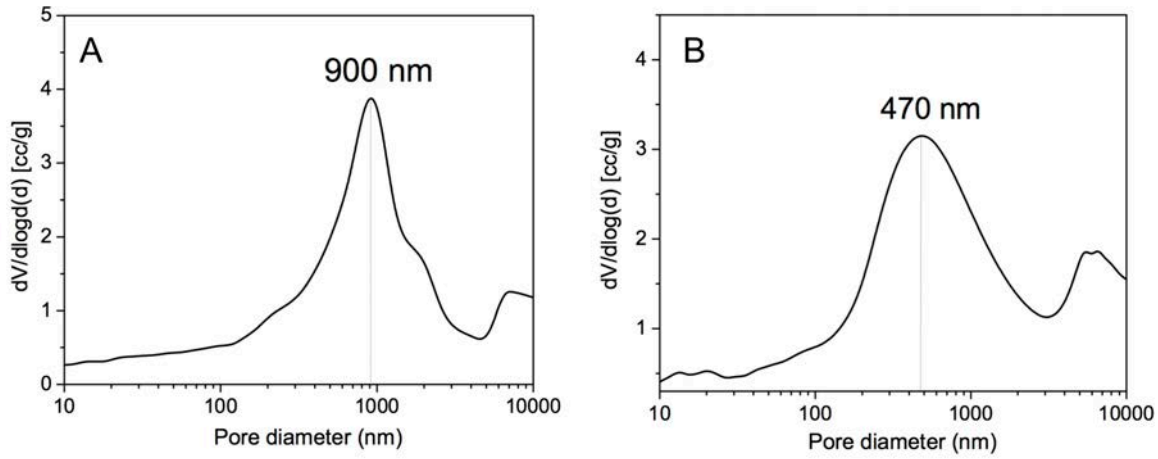

Figure 2.1.7. Macropore size distribution of (A) CU-Mat, (B) CU-SA-Mat determined using Hg porosimetry.

Sample Name	BET surface area (m^2/g)	Mesopore volume (cm^3/g)	Mesopore diameter (nm)	Macropore size (nm)	Lattice Parameter (a_0, nm)	Wall thickness (nm)
CU-NHP-Mat	794	0.83	6.8	900	12.5	5.7
CU-SA-Mat	943	1.22	6.0	470	13.2	7.2

Table 2.1.2. Physicochemical characteristics of bare silica materials.

Clear evidence of macroporosity can be obtained by the morphology studies of these materials using scanning electron microscope. (SEM) (Figure 2.1.8) Sub-micron scaled macropores was observed for both CU-NHP-Mat and CU-SA-Mat.

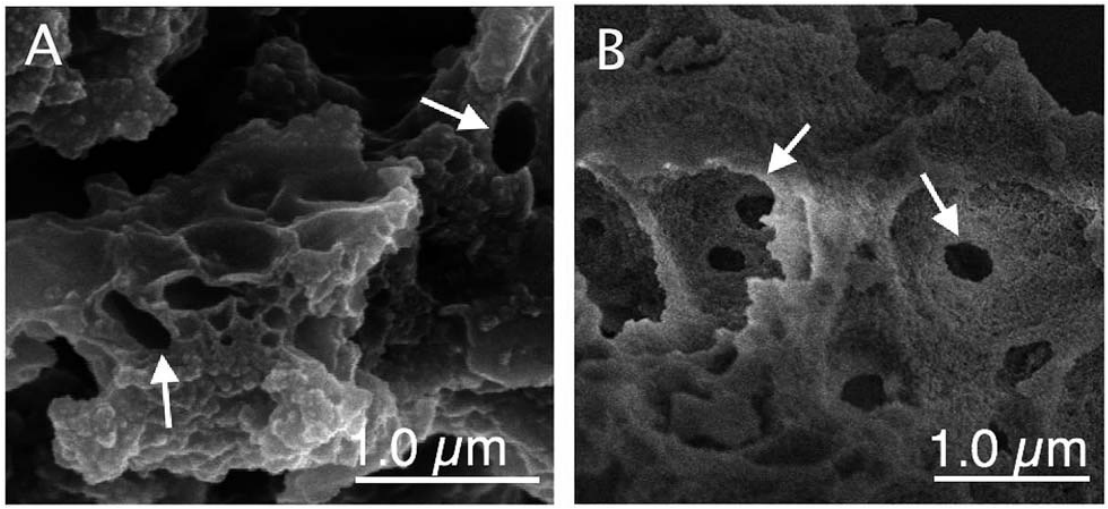

Figure 2.1.8. SEM image of (A) CU-NHP-Mat, (B) CU-SA-Mat after removal of organic matter (arrows indicate macropores)

Transmission electron microscopy (TEM) was performed to visualize macropore and mesopore structures. Macropores are observed for all silica materials and their diameters are in agreement with porosimetry measurements, proving that the imprints of macropores by SLN have been successfully achieved for both materials. (Figure 2.1.9) Also, TEM analysis allows observing the mesoporosity, templated by P123, which diameter is around 6 nm, as calculated by the N_2 adsorption–desorption isotherm study.

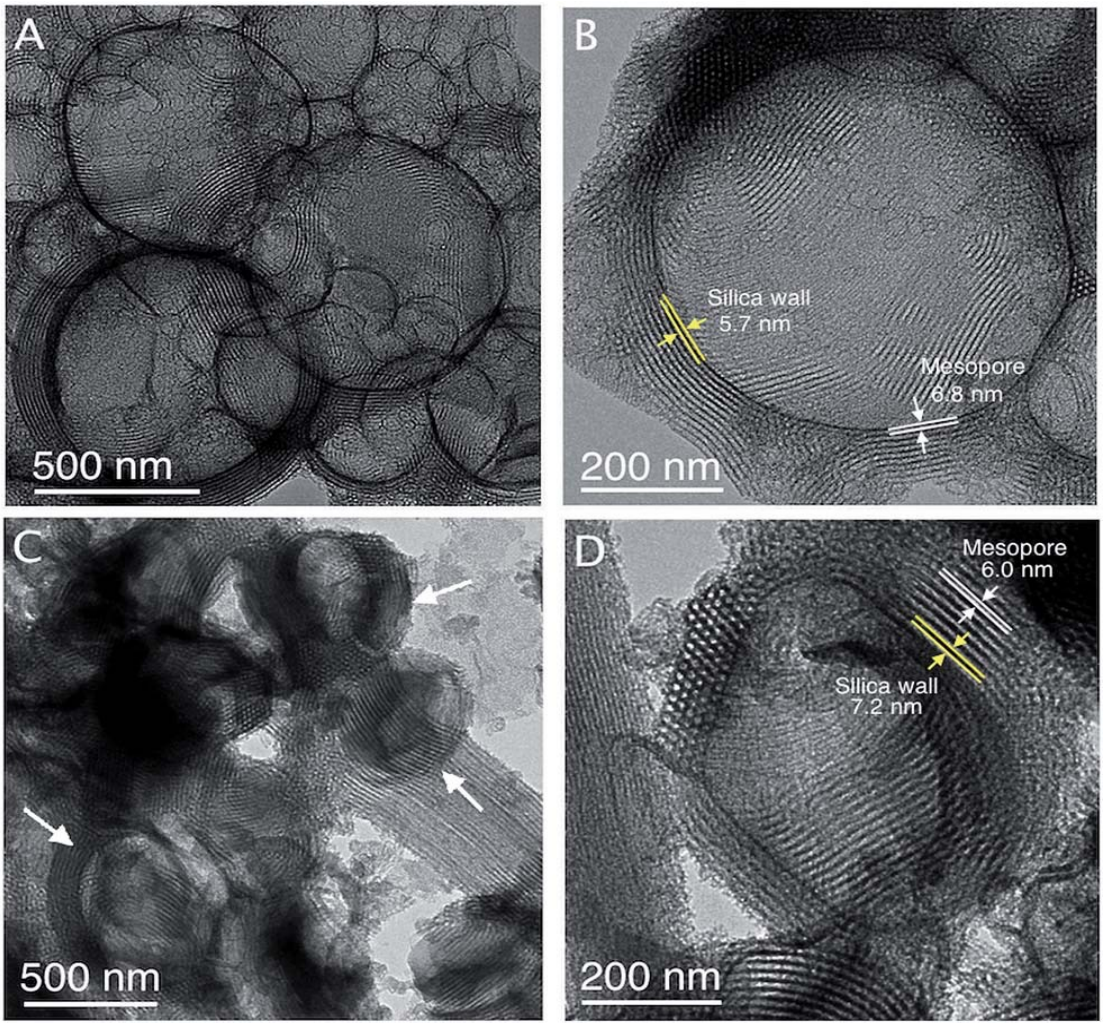

Figure 2.1.9. TEM image of meso-macroporous silica, CU-NHP-Mat (A and B) and CU-SA-Mat (C and D) after removal of organic matter (arrows indicate marcopores)

In vitro curcumin release

The release experiments of CU-loaded hybrid SLN silica materials were carried out at 3 different dissolution media (pH 1.2, 4.5 and 7.4). 0.1% (w/w) of a cationic surfactant, CTAB was added to dissolution media in order to solubilize the curcumin,[37] because curcumin is poorly soluble and degraded in aqueous solution.[38] Before investigating curcumin release, the

stability of curcumin for 5 days and the sink conditions in different dissolution media were verified, showing less than 1% loss of the curcumin.

Figure 2.1.10 and 2.1.11 show the cumulative release of curcumin from hybrid SLN-silica materials at 3 different pH release media. At first, the drug released from CU-NHP-Mat quickly reached the plateau within 6 h at all investigated pH. However, the maximum cumulative release percentage was varied according to the pH, 100%, 88%, and 16% for pH 1.2, 4.5 and 7.4, respectively.

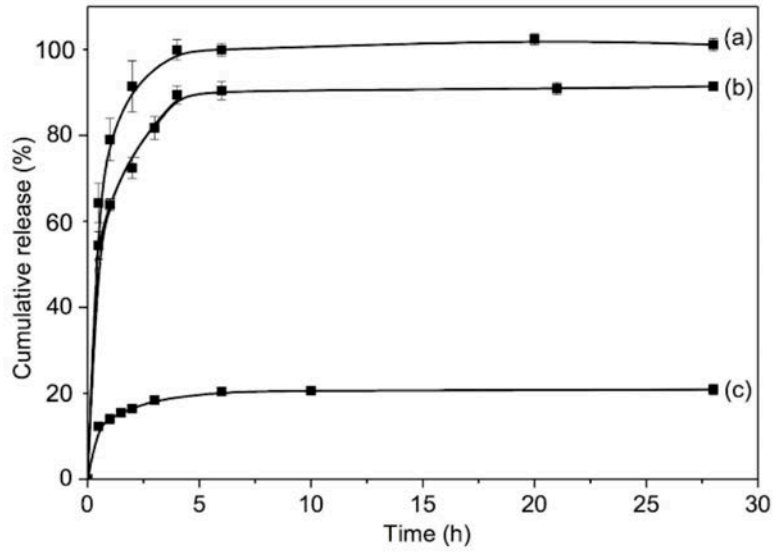

Figure 2.1.10. Cumulative release of curcumin from CU-NHP-Mat at (a) pH 1.2, (b) pH 4.5 and (c) pH 7.4

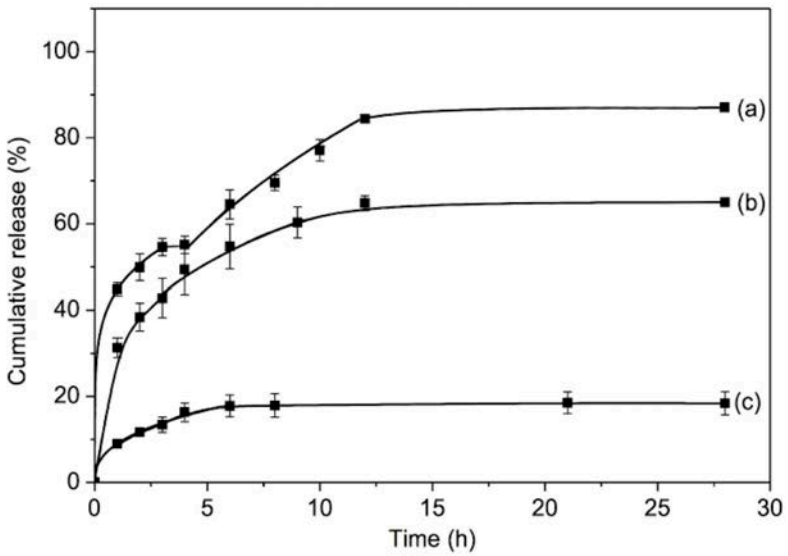

Figure 2.1.11. Cumulative release of curcumin from CU-SA-Mat at (a) pH 1.2, (b) pH 4.5 and (c) pH 7.4

The differences in the curcumin release behaviour could be because of the interaction between curcumin and silanol groups of the surface of silica. One should first note that no deprotonated forms of curcumin are involved in the release mechanism at the investigated pH (1.2, 4.5 and 7.4) since pKa of the most acidic proton is 8.4 (Figure 2.1.12-13). Secondly, through a well-known isoelectric point the value for amorphous silica in water is 2-3,[39] which is based on pKa1= 2.77 ($\equiv SiOH_2^+ \rightarrow \equiv SiOH + H^+$) and pKa2= 6.77 ($\equiv SiOH \rightarrow \equiv SIO^- + H^+$), for the calculation of surface acidity in mesoporous silica, protonation-deprotonation reaction for Q2 silanol ($=Si(OH)_2$) and Q3 silanol ($\equiv$Si–OH) should be also be taken into consideration.[40] Experimental data[41,42] and computational calculations[43] suggested that Q3 silanol on the silica surface has a pKa of 4.5 and Q2 silanol has a pKa of 8.5.

Therefore, in the 1.2-7.4 pH range, only Q3 silanol undergoes deprotonation, while Q2 silanol is not deprotonated. These dominated forms of silica and curcumin as a function of pH are described in Figure 2.1.12. At pH 1.2, only weak dipole–dipole interactions (hydrogen bond, 5.0 kcal mol^{-1}, computational calculation[44-46]) between curcumin and silanol are expected. Those are not strong enough to hold the curcumin inside mesopores and therefore the release kinetics are the highest. At pH 4.5, where pH = pKa of ≡Si–OH, since half of Q3 silanol is protonated, mesoporous silica becomes more effective to hold curcumin than at pH 1.2. Finally, when pH increases to 7.4, all Q3 silanols are deprotonated, being the most effective to hold curcumin via stronger ion–dipole interactions (23 kcal mol^{-1}).

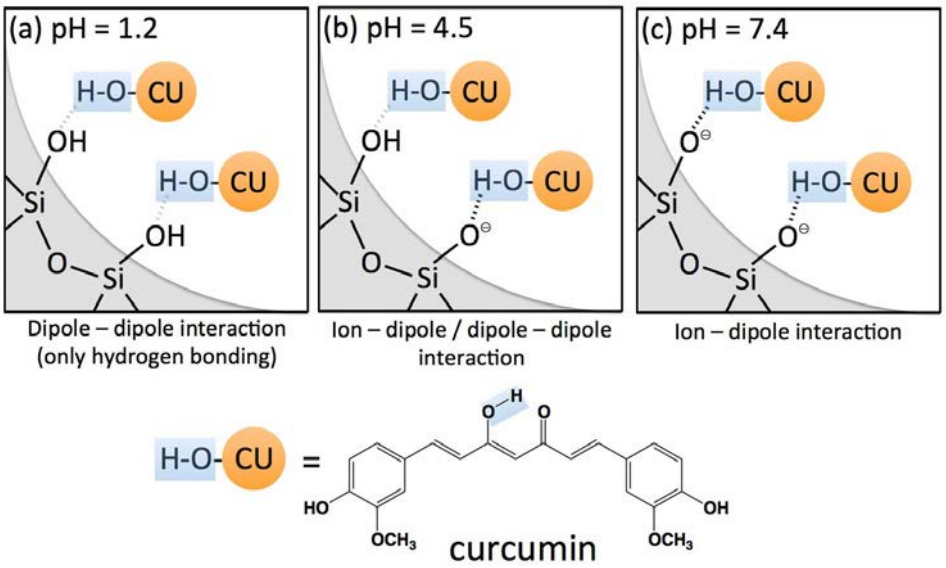

Figure 2.1.12. Possible interactions between curcumin and silanol on a silica surface at (a) pH 1.2, (b) pH 4.5 and (c) pH 7.4

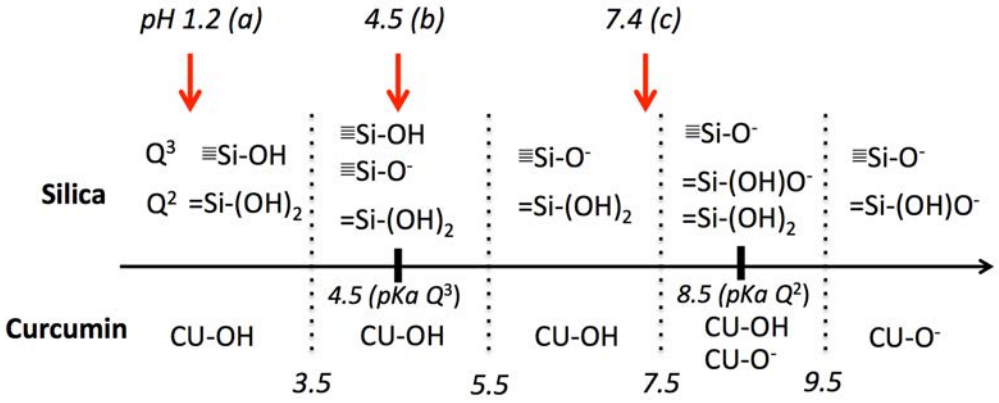

Figure 2.1.13. Dominant forms of silica and curcumin as a function of pH

Curcumin release from CU-SA-Mat (Figure 2.1.11) shows also the pH dependent release pattern (cumulative release: 86, 68 and 18% for pH 1.2, 4.5 and 7.4, respectively). However, the release rate is slower than that of CU-NHP-Mat (12 h vs. 6 h for saturation). It could be related to the higher amount of curcumin in the lipid core, and also to the lipid–curcumin interaction for CU-SA-Mat. Indeed, after the release of curcumin that was encapsulated in mesopores, curcumin is fed only from the solid lipid nanoparticles that act as a drug reservoir. Hence, the release rate becomes mainly dependent on the nature of SLN, which is again, influenced by pH.[47] Interestingly, at pH 1.2, a two-step release pattern was observed with the quasi-stationary state between 3 h and 4 h. This state will be discussed later using a kinetic model. Besides, the presence of this quasi-stationary state was verified more than 10 times.

In addition, the influence of mesoporous structure was also investigated using CU-SA-Mat. A silica material with weak wormlike meso-structure was prepared by adjusting the silica condensation temperature at room temperature for 24 h. Curcumin content assay experiment revealed also that this material contained the same amount of curcumin as the material with hexagonally ordered mesopores, thus the direct comparison of mesostructuring degree was performed through curcumin release study. 50% (v/v) aqueous ethanol was chosen as the release medium in order to investigate not only the structure of mesopore, neglecting other parameters like curcumin-silica interaction, but also the visualization of curcumin release that can be accelerated in aqueous ethanol solution. As shown in Figure 2.1.14, the curcumin release from hexagonally ordered SLN-silica meso-macroporous material shows a significant increase of the drug released up to 20 %, as compared to weak wormlike SLN-silica material that has low mesopore volume. From this result, one can conclude that mesoporous silica shell could be served as the pathway for curcumin release.

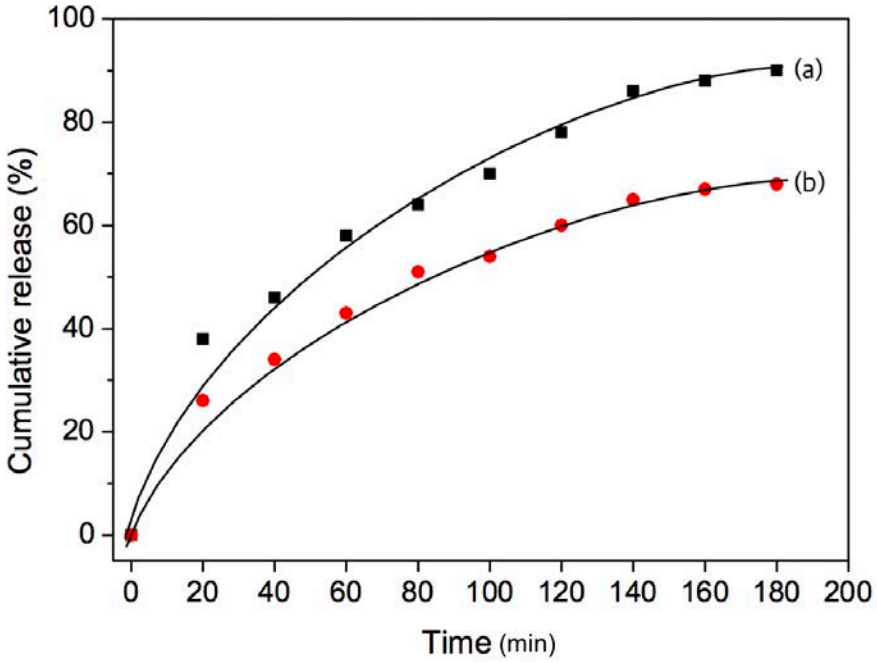

Figure 2.1.14. Cumulative release of curcumin from (a) hexagonally ordered CU-SA-Mat and (b) non ordered CU-SA-Mat at 50 % (v/v) ethanolic solution.

Drug release mechanism modeling

In order to determine the release mechanism, the curcumin release data were analysed and fitted using the Korsmeyer–Peppas model[48] that could be described as the following:

$$\log drug\ release\ (\%) = n \log release\ time(h) + \log K$$

where n for release exponent and K for kinetic constant.

This model has been widely used for investigating of new drug delivery matrix like SLN-silica system of this study. Especially, the fitting parameter, release exponent (n) indicate the dominant release mechanism of drug; n = 0.43 for Fickian diffusion, n < 0.43 for quasi-Fickian diffusion, n > 0.43 for non-Fickian diffusion or other process like erosion combined release. In addition, this model has also another fitting parameter, kinetic constant (K) which could be used in case of drug release rate comparison.

From the result, (Table 2.1.3, Figure 2.1.15) it is revealed that in all cases, the drug release mechanism could be described by the quasi-Fickian drug diffusion process, as all release exponent (n) values are lower than 0.43. However, curcumin release rate, expressed using the kinetic constant, are varied as a function of pH and silica material compositions. The kinetic constants of CU-NHP-Mat are about two times higher than those of CU-SA-Mat, confirming

also our hypothesis concerning the interaction between the lipid and curcumin as discussed previously.

Parameter	CU-NHP-Mat			CU-SA-Mat		
	pH 1.2	pH 4.5	pH 7.4	pH 1.2	pH 4.5	pH 7.4
K (h^{-1})	76.6	63.4	14.2	42.4	31.4	8.9
R^2	0.969	0.991	0.993	0.950	0.994	0.982
n	0.212	0.233	0.211	0.250	0.299	0.411

Table 2.13. Release kinetic parameters obtained using Korsmeyer–Peppas model. K for kinetic constant, R^2 for coefficient of determination and n for release exponent.

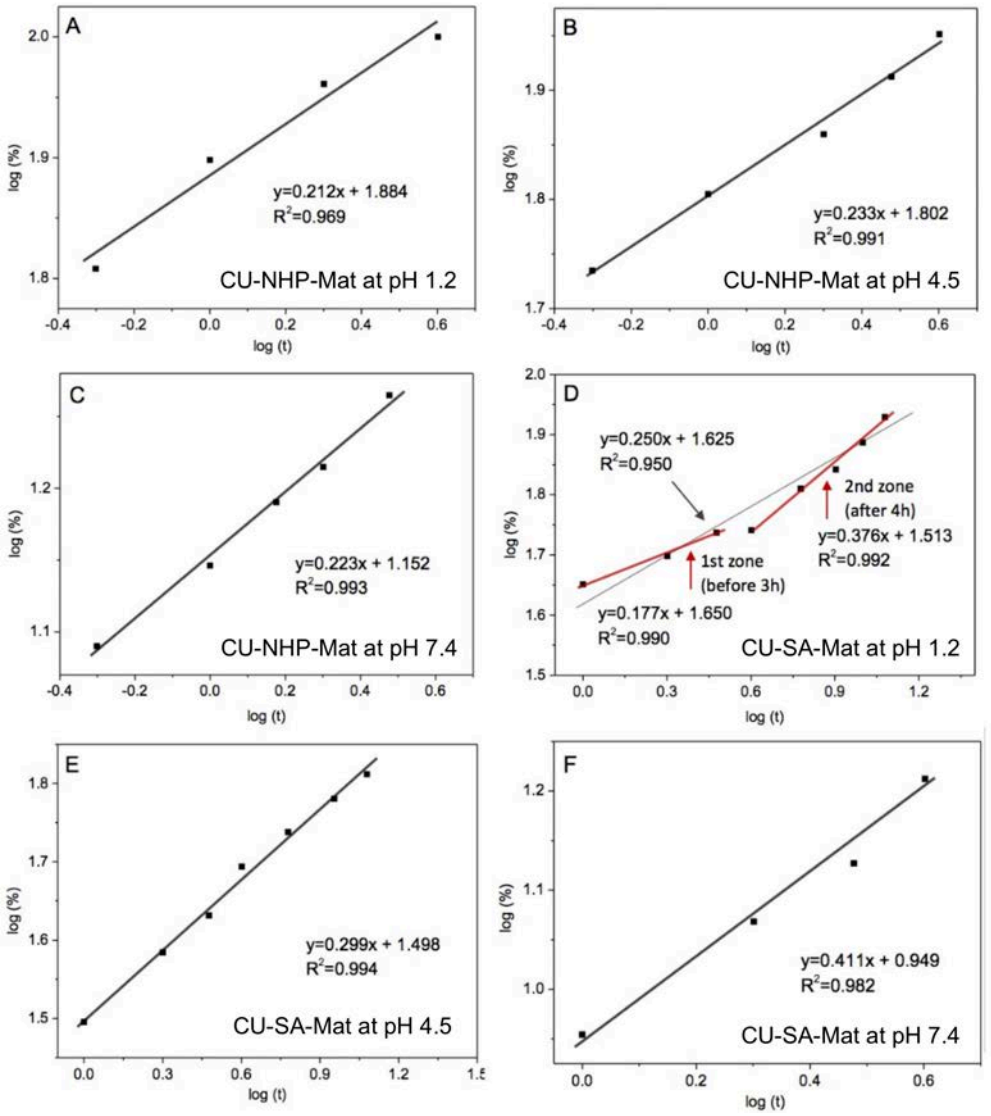

Figure 2.1.15. Fitting graphs using Korsmeyer-Peppas model for silica materials CU-NHP-Mat (A-C) and CU-SA-Mat (D-F).

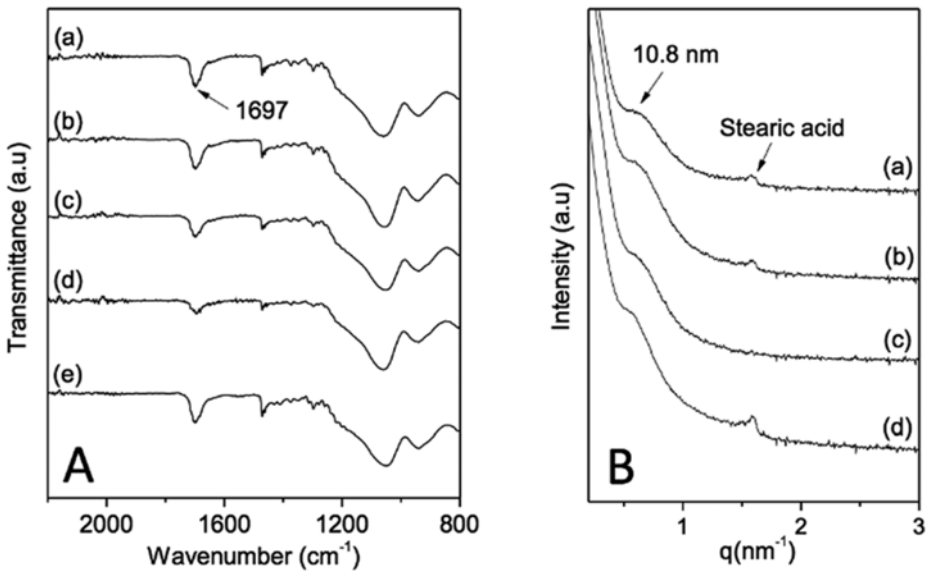

Figure 2.1.16. FT-IR (A) spectra of CU-SA-Mat, (a) as-synthesized material, (b) after 2 h release at pH 1.2, (c) after 4 h release at pH 1.2, (d) after 8 h release at pH 1.2, (e) after 6 h release at pH 7.4; SAXS patterns (B) of CU-SA-Mat, (a) after 2 h release at pH 1.2, (b) after 4 h release at pH 1.2 (c) after 8 h release at pH 1.2 (d) after 6 h release at pH 7.4. All FT-IR peaks are normalized with respect to Si-O-Si stretching peak (around 1100 cm^{-1})

The release pattern for CU-SA-Mat at pH 1.2 is not well fitted using simple Korsmeyer–Peppas model, probably due to the difference of the curcumin release rate from SLN and mesopores. As explained before, for compartmentalized solid lipid nanoparticle@mesostructured silica matrix, the release at pH 1.2 is faster than other pHs, and curcumin release from mesopores is faster than curcumin from SLN. As a result, at pH 1.2, curcumin release from mesopores of CU-SA-Mat finished in 3 h, while curcumin release from SLN dose not start yet.

Fitting on 2 zones with Korsmeyer–Peppas model can confirm this two-step release. At first, it is clearly shown that the correlation coefficient R^2 for both the 1st zone (0.990 before 3 h) and the 2nd zone (0.992 after 4 h) are close to 1. In addition, the kinetic constant for the 1st zone (44.6 h^{-1}) is higher than that for the 2nd zone (33.4 h^{-1}), which explains fast curcumin release from mesopores, compared to the release from SLN. Moreover, the disappearance of stearic acid from CU-SA-Mat over the release time was also verified by SAXS measurements (Figure 2.1.16B). Like in FT-IR experiments (Figure. 2.1.16A), the continuous decrease of the peak corresponding to stearic acid is observed at pH 1.2 (a–c) while this peak remains at pH 7.4 even after 6 h release (d).

From these results, a possible mechanism of drug release from the meso/macro-compartmentalized silica matrix is described in Figure 2.1.17.

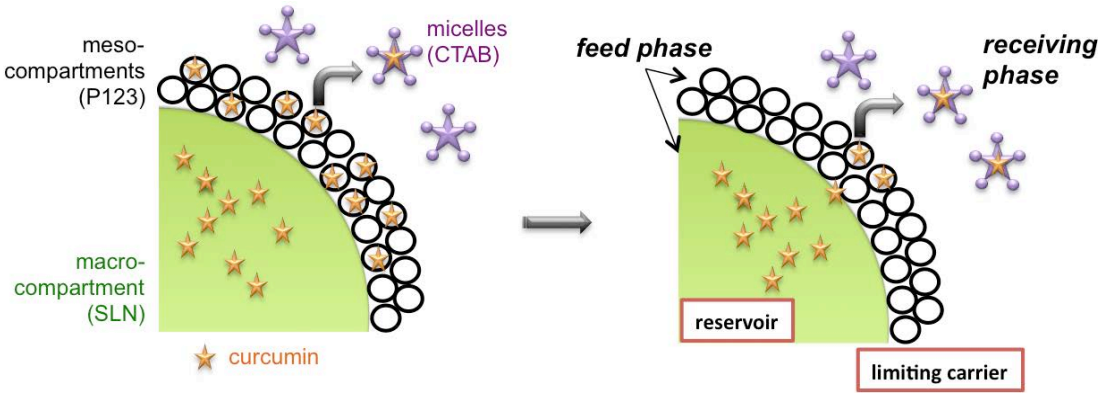

Figure 2.1.17. Graphical representation of the release mechanism of curcumin. The curcumin was firstly released from lipid core, then pass through mesopore before being solubilized in aqueous solution.

Toxicity study of silica materials

Considering the toxicity of designed vectors, it should be noted that all ingredients are excipient approved by the FDA,[20] except N-hexadecylpalmitate (NHP). Thus, for NHP based hybrid SLN-silica material (CU-NHP-Mat), cell viability experiments were performed on MRC-5 cells (Figure 2.1.18) following a standard procedure previously reported.[31,49]

Indeed, the determined IC_{50} (The half maximal inhibitory concentration) values of free curcumin and CU-NHP-Mat were identical after 24 h of treatment, of about 20 mg L^{-1} of curcumin in both cases and of about 4.9 g L^{-1} of NHP–silica in the case of CU-NHP-Mat. At the same concentration in NHP–silica, free of curcumin material Blank-NHP-Mat, 90% of the cells remained viable. These results confirm that NHP, silica, and P123 surfactants were not toxic below this dose. As a matter of fact, the IC_{50} value of CU-NHP-Mat is higher than 18 g L^{-1}. Thus, the newly designed drug-SLN-silica meso/macro-compartmentalized matrix could be of potential interest for biological applications, including drug delivery.

	Concentration in curcumin (mg/L)			Concentration in NHP-Mat (g/L)		
	A	B	C	A	B	C
1	5	5	-	-	1.2	1.2
2	10	10	-	-	2.4	2.4
3	15	15	-	-	3.6	3.6
4	30	30	-	-	7.2	7.2
5	50	50	-	-	12	12
6	75	75	-	-	18	18

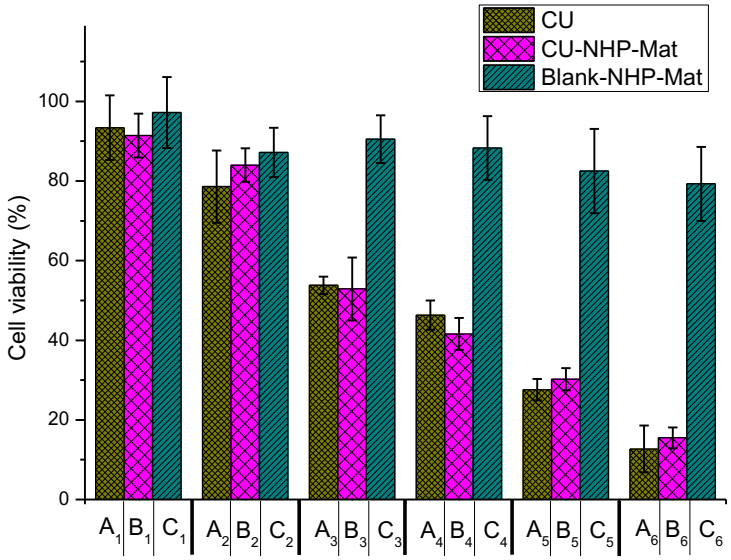

Figure 2.1.18. In vitro cytotoxicity of (A) pure curcumin, (B) CU-NHP-Mat and (C) Blank-NHP-Mat in MRC-5 cell line after 24h

2.1.4 Conclusion

Curcumin-loaded meso-macrostructured silica materials were obtained by mineralizing dispersions of solid lipid nanoparticles in micellar solutions. The partition of curcumin between SLN and micelles of P123 depends on the lipid source (20% for NHP and 65% for SA), due to the difference of the interaction between curcumin and lipid as suggested by FT-IR and SAXS experiments. The hybrid SLN-silica materials, obtained through sol-gel reaction, exhibits dual porosity, macropores that are interconnected *via* mesopores. In addition, the resulting materials could be efficient for long-term storage of active ingredients as the content of curcumin remain above 95% even after 3 months. The release of curcumin in aqueous medium is pH-dependent for both stearic acid and cetyl palmitate-based materials, probably due to the interaction between CU and silanols of the mesopore surface. Moreover, a two-step release pattern was observed for SA-Mat at pH 1.2, as confirmed by FT-IR and SAXS analysis. This result suggests that SLN may act as reservoirs of curcumin, while mesopores act as pathways to control drug release. In conclusion, using SLN/micellar dispersion is a straightforward way to design a novel hybrid-silica drug delivery system with improved stability and sustainability of guest drug release.

Part 2.2

Core-shell microcapsules of solid lipid nanoparticles and mesoporous silica for enhanced oral delivery of curcumin

This part was submitted as: S. Kim, R.Diab, O. Joubert, N. Canilho, A. Pasc, Core-shell microcapsules of solid lipid nanoparticles and mesoporous silica for enhanced oral delivery of curcumin in *Colloids Surf., B.*

2.2.1 Introduction

Mesoporous silica-based vectors used for oral delivery were previously reported.[50] Theses vectors enabled an enhanced intestinal absorption for drugs displaying poor solubility (i.e. fenofibrate[51]), poor permeability (i.e. telmisartan[50]) or for those undergoing cell efflux by *P*-glycoprotein pump such as cyclosporine.[52]

In this part, it is demonstrated that by using solid lipid nanoparticles, it is also possible to design curcumin loaded core-shell type of hybrid mesoporous silica microcapsules, which take advantage of unique properties such as biocompatibility, of both mesoporous silica and solid lipid nanoparticles, in order to improve the bioavailability of curcumin for oral administration, which has been limited, due to the rapid pre-systemic catabolism in the intestinal wall.[53,54] In addition, microcapsule type materials could be more adapted for internalization, compared to block type materials, for which we presented one example with silica in the previous part. To demonstrate the potential application of novel hybrid silica capsule, *in vitro* release of curcumin and cytotoxicity and the cellular uptake using Caco-2 cells were investigated.

2.2.2 Materials and methods

Chemicals

Hexadecyltrimethylammonium bromide (CTAB), Tetramethylorthosilicate (TMOS) were purchased from Sigma-Aldrich. N-hexadecylpalmitate (NHP) was purchased from Acros. Tween 40 (polyoxyethylene (20) sorbitan monopalmitate), ethanol, were purchased from Alfa Aesar. Curcumin and Nile Red were purchased from Aldrich. Water was deionized and purified using a Milli-Q pack system. All reagents were used without further purification. All the release media were prepared according to European Pharmacopoeia 8.0 guidelines - Section 5.17.1.

SLN preparation (CU-SLN)

Curcumin-loaded solid lipid nanoparticles (CU-SLN) were prepared by ultra-sonication of a hot emulsion obtained from a mixture of curcumin and a melted lipid dispersed in a micellar phase as described in previous part.[55] In a typical procedure, the mixture of 430 mg of N-

hexadecylpalmitate (NHP) and 11 mg of curcumin (CU) were heated at 70°C. The aqueous phase containing 1.6 wt.% of Tween 40 was heated at the same temperature as the lipid phase. The oil phase was added to 20 mL of the Tween 40 micellar solution and the mixture was sonicated for 1.5 min with an ultrasonic device (Bandelin sonopuls, HD2200, 52 % of output). The hot o/w emulsion was then rapidly cooled to room temperature under vigorous stirring to afford lipid solidification. The fluorescent, Nile Red labeled CU-SLN were synthesized in a similar manner, by mixing the dye with the melted lipid.

Synthesis of hybrid SLN-silica microcapsules

510 mg of tetramethoxysilane (TMOS) was added dropwise into 20 mL dispersion of CU-SLN. The surfactant/silica molar ratio (R) was 0.07. The mixture was stirred for 1 h and then transferred into sealed Teflon autoclaves, then was assayed at 40°C for 48 h. Afterwards, the material was filtered, washed with water, then dried at 40°C *in vacuo* for 24 h. Besides, the silica microcapsules templated by Nile Red (NR) loaded SLN were also prepared in the same manner.

Assay of the content of curcumin in hybrid SLN-silica microcapsules

5 mL of THF was added to 50 mg of hybrid SLN-silica capsule, then the sample was sonicated for 30 min in order to dissolve lipid (NHP) and curcumin into the organic phase. Afterward, 90 mL of ethanol was added, and the sample was diluted 10-fold using ethanol for UV-Vis spectrometry analysis. The concentration was calculated using a standard curve of curcumin in ethanol.

In vitro curcumin release experiments

Release experiments were carried out in 3 different buffer solutions, pH 1.2, 2.8 and 7.4. Detailed method was described in Part 2.1.

Cell culture

Caco-2 cells (ATCC, HTB-37^{TM}, Manassas, VA, USA) were grown at 37°C under a 5% CO_2 atmosphere in Eagle's minimum essential (EMEM) medium (Sigma Aldrich, Saint-Quentin

Fallavier, France) supplemented with 10% fetal bovine serum (SVF, Eurobio, Les Ulis, France), 1% non-essential amino acids (Sigma Aldrich, Saint-Quentin Fallavier, France), 1% sodium pyruvate (Sigma Aldrich, Saint-Quentin Fallavier, France), 1% antibiotics (100U/mL of penicillin, 0,1 mg/mL streptomycin, Sigma Aldrich, Saint-Quentin Fallavier, France). Cells were trypsinized once a week (Trypsin-EDTA, Sigma Aldrich, Saint-Quentin Fallavier, France), before counting and medium renewal. Passages 35 to 45 were used.

Cytotoxicity assay

Cells were seeded in 96-well plates at a $5x10^4$ cells/cm^2 density. After overnight incubation, medium was removed by aspiration. Fresh medium was added and cells were exposed to blank or loaded MC at equivalent concentrations of encapsulated CU ranging from 5 to 75 mg/L during 24 h. Cell viability was then examined by Neutral Red assay according to Borenfreund *et al*. recommendations.[56] Briefly, after exposure to fluorescently-labeled silica microcapsules, medium was removed and cells were rinsed two times using Hank's balanced salt solution (HBSS) from Sigma Aldrich (Saint-Quentin Fallavier, France). Cells were then incubated with 50 mg/L Neutral Red in medium solution during 4 h. working solution was removed. Cells were rinsed two times with HBSS and lysis solution (50% water, 50% ethanol (v/v) + 1% acetic acid (v/v)) was added. The optical density (OD) was measured using a microplate reader at 540 nm. Cell viability was expressed as the percentage of the OD of the studied condition with respect to the OD of cells incubated with the culture medium only. Results are expressed as the average of three independent biological replicates. Statistical analysis was carried out by the Graphpad Prism 3.0 software package. Difference between groups was analyzed using one-way ANOVA and Bonferroni post-hoc tests. $P < 0.05$ was considered statistically significant.

In vitro cell uptake

Cell uptake was studied using silica microcapsules (MC) labeled with Nile Red (NR). NR is a lipophilic fluorescent probe, thus, it was introduced in the lipid phase forming SLN. Then, fluorescent SLN were mineralized, as described above. Cells were grown on a sterile chambered coverglass (Lab-Tek®, Thermo Scientific, Illkirch-Graffenstaden, France) at a density of 7×10^4 cells/cm^2. After overnight incubation, cells were exposed to Nile Red-labeled microcapsules suspended in EMEM medium for 4 h. Three controls were used, non-

treated cells, cells exposed to Nile Red solution in a mixture of DMSO/water (1/99 v/v) and cells exposed to non-labelled MC-CU. At the end of the incubation period, incubation medium was removed and cells were washed twice with HBSS. Cells were then fixed with 4% (v/v) paraformaldehyde during 15 minutes in the dark at room temperature. After rinsing cells twice with HBSS, Hoechst 33342 (1 mg/L in PBS) was used at room temperature during 15 min in the dark, for nuclei staining. Finally, cells were washed thrice with distillated water, dried at room temperature and conserved in the dark at 4°C. Observations were made using a confocal laser scanning microscope (Leica TCS SP5X, Bensheim, Germany) with a 40.0×/1.25 numerical aperture oil-immersion objective lens.

2.2.3 Results and discussion

Solid lipid nanoparticles (SLN)

Curcumin loaded solid lipid nanoparticles (CU-SLN) were prepared by sonication of hot-melted lipid (NHP) containing curcumin (CU), dispersed in an aqueous micellar solution of Tween 40. Indeed, solid lipid nanoparticles (SLN) are used as both reservoir of curcumin and macro-template during silica condensation. Nanoparticle tracking analysis (NTA) and dynamic light scattering (DLS) measurements of SLN dispersions showed that no significant change in size distribution and zeta potential before and after curcumin encapsulation into SLN, suggesting that curcumin was incorporated inside SLN's core, not located on the interface between SLN and aqueous solution. (Figure 2.2.1a, b, Table 2.2.1)

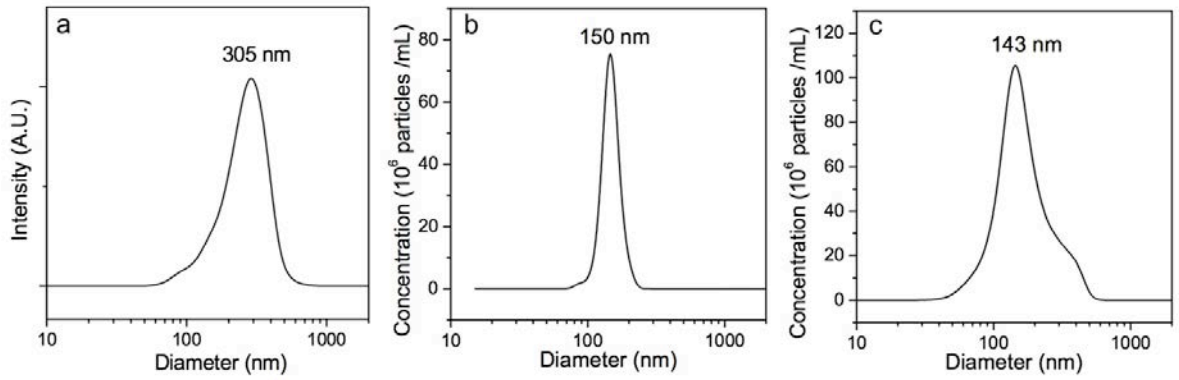

Figure 2.2.1. Size distribution of (a) SLN-CU obtained using DLS (intensity), (b) SLN-CU obtained using NTA (particle number) and (c) SLN-Nile Red obtained using fluorescence mode in NTA.

Sample	SLN	SLN-CU	SLN-Nile Red
Size (nm)[a]	298 ± 49	305 ± 42	301 ± 52
Zeta potential (mV)	-13.0 ± 2.1	-11.8 ± 2.5	-12.5 ± 1.5

Table 3.1. Physicochemical characteristics of SLN (a. Size distributions were measured using DLS)

This phenomenon was also observed for other SLN prepared using Pluronic P123.[55] However, SLN size distribution obtained using NTA is quite different from that of DLS measurement, showing 150 nm of size difference. This size gap might be due to the difference between intensity-based measurements in DLS and particle number counting in NTA. The presence of curcumin encapsulated into the solid core of SLN was proved using the fluorescence mode in the NTA. (Figure 2.2.2) Since NTA can visualize only the particles which size is more than 30 nm, fluorescence signal could be due to the encapsulated curcumin molecules into SLN, rather than free curcumin in the aqueous micellar solution. Moreover, their size and concentration do not significantly change with respect to those obtained without the filter. In order to obtain clear image and size distribution of SLN under fluorescence filter, a hydrophobic fluorescent molecule, Nile Red was encapsulated into lipid core of SLN in the same manner as the preparation of CU-SLN, and characterized using NTA with fluorescence mode. The result showed a clear and evident proof that NHP based SLN can effectively encapsulate hydrophobic molecules such as curcumin or Nile Red without any change in SLN size distribution. (Figure 2.2.2c)

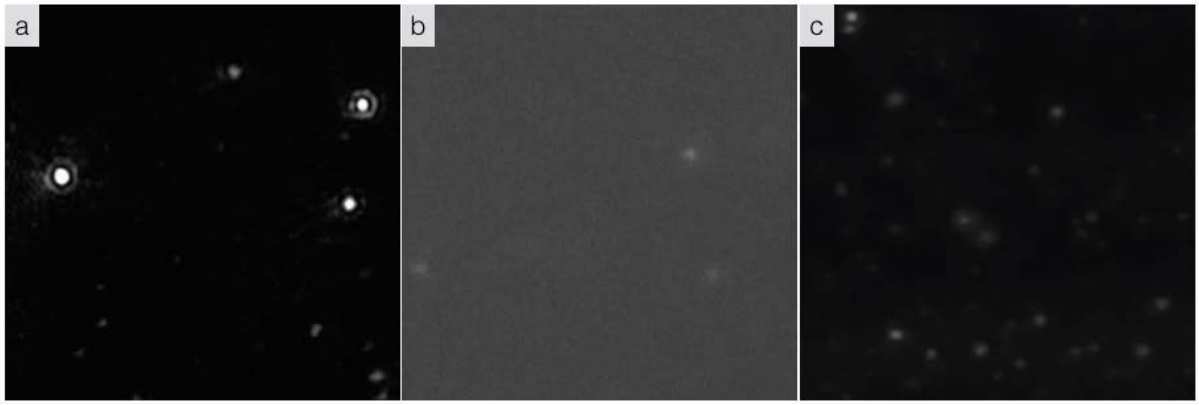

Figure 2.2.2. Captured images of Nanoparticle Tracking Analysis (NTA) for (a) CU-SLN without any filter (b) CU-SLN with fluorescence filter (c) Nile Red-SLN with fluorescence filter.

Silica microcapsules templated by SLN

Curcumin loaded SLN-silica microcapsules (MC-CU) can be obtained by mineralization of CU-SLN dispersion using TMOS as silica precursor, and then followed by silica hydrolysis-condensation on SLN surface. The surfactant/silica molar ratio (R) was fixed to 0.07. Moreover, NHP concentration in SLN dispersion was fixed to 2 wt.% in order to cover all surfaces of SLN by silica precursor, which is a crucial factor for the synthesis of silica capsules, as reported by our group.[26] In addition, since Tween 40 cannot form the cylindrical micelles, it is believed that only silica capsules could be formed. Besides, hollow silica capsule was obtained by removing organic matter by Soxhlet extraction with ethanol. This hollow silica capsule was then characterized using small-angle X-ray scattering (SAXS) in order to investigate the organization of mesopores. As shown in Figure 2.2.3a, the SAXS data shows a weak peak, indicating that the mesopore of silica capsule is ordered in wormlike structure. N_2 absorption-desorption experiment of bare silica capsule showed a type IV isotherm (Figure 2.2.3b), which is characteristic of mesoporous materials. The BET specific surface area and the mesopore volume are 1055 m^2 g^{-1} and 1.3 cm^3 g^{-1}, respectively.

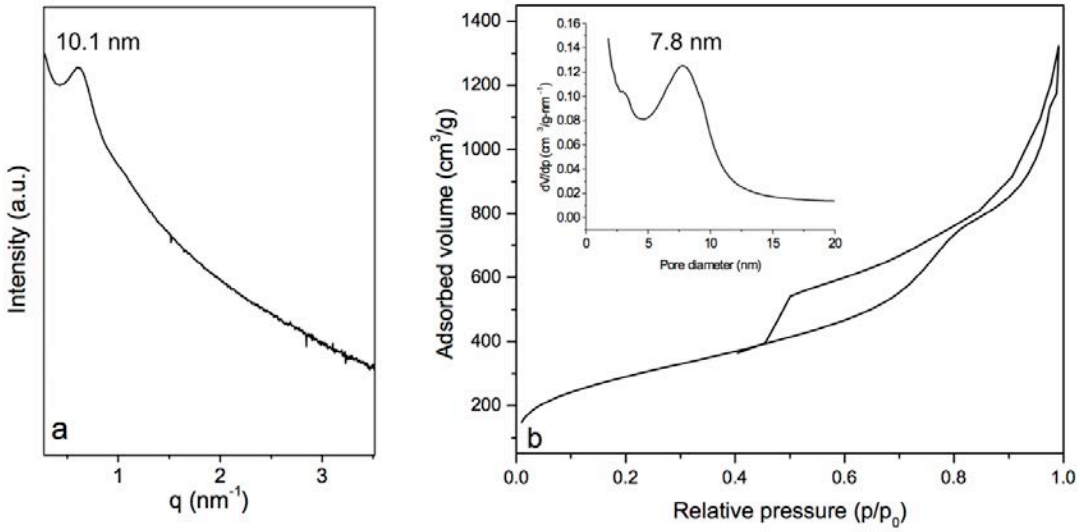

Figure 2.2.3. (a) SAXS and (b) N_2 adsorption-desorption isotherm with pore size distribution (inset) of hollow silica mcirocapsules imprinted with SLN.

The formation of silica capsule imprinted by SLN beads was confirmed by transmission electron microscopy (TEM). As shown in Figure 2.2.4, TEM analysis indicated the hollow cavity inside silica microcapsules with ~ 500 nm in diameter, meaning that the imprints of macropores by SLN have been successfully achieved. However, the size of hollow cavity

larger than that of SLN, could be due to the coalescence of solid lipid nanoparticles during silica condensation.[27,57]

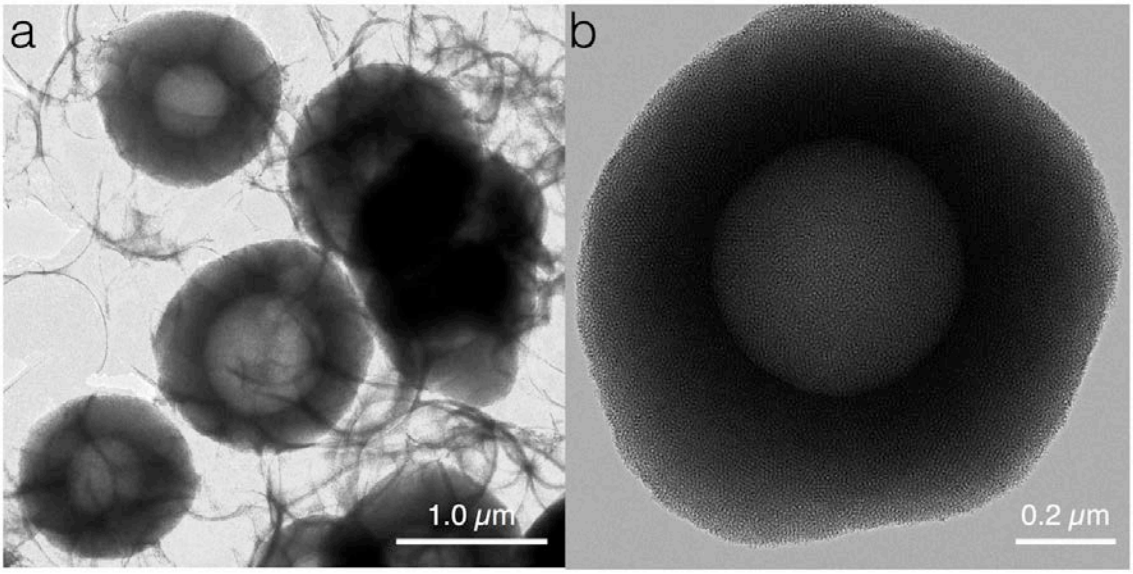

Figure 2.2.4. TEM images of (a) silica microcapsules and (b) zoomed image of a selected microcapsule.

In vitro curcumin release

With the aim to study the influence of pH changes in the gastrointestinal tract on the release profile, the experiments were carried out in different buffer solutions with a progressive rise of pH from 1.2 to 7.4. A cationic surfactant, CTAB (0.1 wt.%) was added to improve the solubility and the stability of curcumin in aqueous solution during the release experiments.[37,38] Figure 2.2.5 shows the cumulative release of curcumin from hybrid SLN-silica microcapsule in release media with different pH. It is clearly shown that the kinetic release profile of curcumin depends on the pH of the release media.

This dependence could be explained by the stability of SLN as a function of pH.[47] Thus, SLN would be rapidly destabilized at pH 1.2, expelling encapsulated curcumin at early release time, whereas at neutral pH like 7.4 SLN could be more stable for long time, keeping curcumin inside SLNs matrix. Interestingly, curcumin release was effectively retained at pH 2.8 without burst release at the early release stage. This result could be due to the isoelectric point of silica that is between 2 and 3. This property of silica could be an advantage for oral administration route, keeping in mind that the average basal pH value in the stomach is 2.16 ± 0.09 for men and 2.79 ± 0.18 for women as measured by Feldman and Barnett in 365

healthy subjects,[58] we can expect that curcumin release from hybrid silica microcapsules in the gastric medium would be effectively retained.

In order to determine the release mechanism, the data were analysed and fitted using the Korsmeyer–Peppas model.[48] (Figure 2.2.6, Table 2.2.2) The release mechanism of curcumin for pH 1.2 and 7.4 could be described by the quasi-Fickian drug diffusion process, since their release exponent (n) values are lower than 0.43. However, curcumin release at pH 2.8 is effectively retained with release exponent (n) of 0.9, which proposes that other processes like a possible aggregation between silica microcapsules could affect curcumin release.

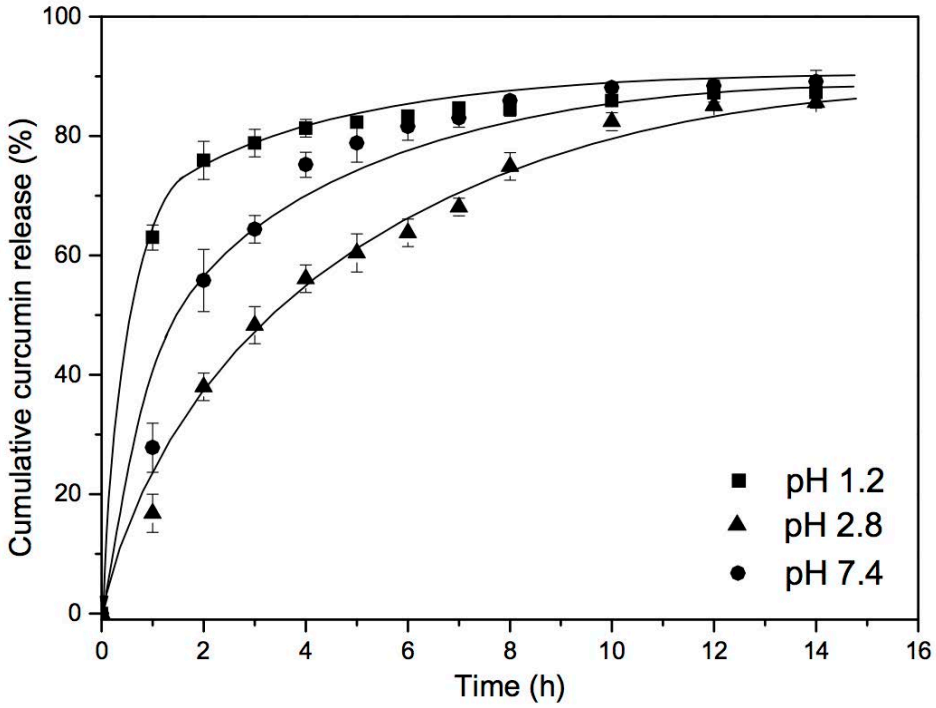

Figure 2.2.5. Cumulative release of curcumin from hybrid SLN-silica microcapsules at different pH

pH	1.2	2.8	7.4
K (h^{-1})	63.1	17.3	30.9
R^2	0.990	0.985	0.960
n	0.191	0.901	0.102

Table 2.2.2. Curcumin release kinetic parameters calculated using Korsmeyer–Peppas model (K: release rate constant, R^2: correlation coefficient, n: release exponent)

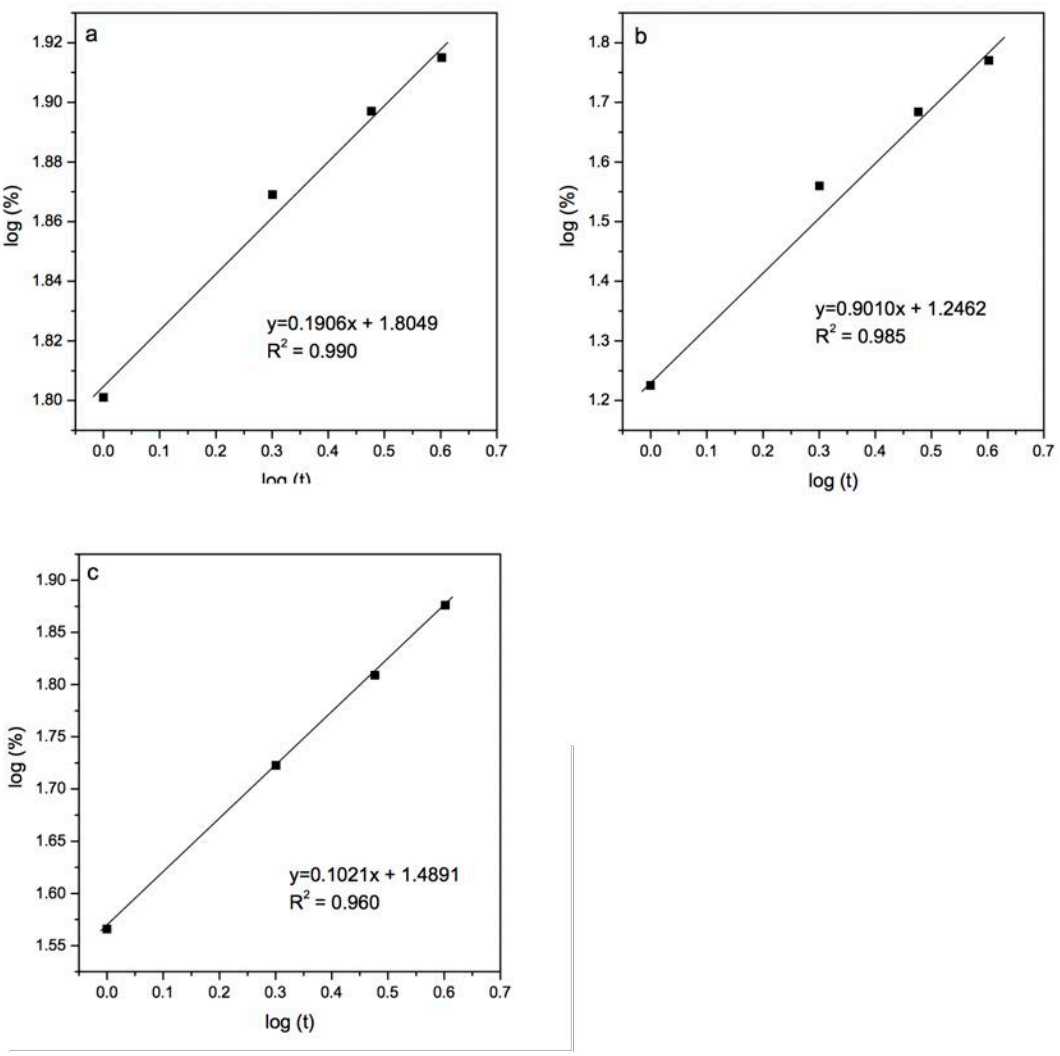

Figure 2.2.6. Fitting graphs of curcumin release data using the Korsmeyer–Peppas model (a) pH 1.2, (b) pH 2.8, and (c) pH 7.4

Biocompatibility studies

The biocompatibility of silica microcapsules was assessed by a cytotoxicity colorimetric assay and by confocal laser scanning microscopy (CLSM). The colorimetric assay determines the uptake and accumulation of a vital dye, *i.e.* neutral red, in the viable and uninjured cells, whereas CLSM visualizes the interactions of fluorescently-labelled microcapsules with cells. Toward this aim, Caco-2 cell line was used.

Caco-2 cell line, obtained from a human colon adenocarcinoma, represents the model of choice to study drug interactions with the intestinal barrier, as they express numerous morphological and functional features of the intestinal epithelium's cells.[59] It is important to

note that Caco-2 monolayer is the unique *in vitro* cell model approved by the FDA for *in vivo* bioavailability and bioequivalence studies for oral solid dosage forms.[60]

Cytotoxicity assay

Toxicity of MC-CU was evaluated after 24 h of incubation and compared to their equivalent amount of blank MC and free CU at the most concentrated microsphere suspension. (Figure 2.2.7) Incubation with MC-CU resulted in a decrease in cell viability with respect to control. Cell viability decreased gradually with increasing MC-CU concentrations till 30 mg/L. Nevertheless, nearly 75% of cells remain viable following the exposure to the highest tested concentration (*i.e.* 75 mg/L expressed as entrapped CU). No significant differences in viability were found between cells exposed to 30, 50 or to 75 mg/L or between cells exposed to loaded or blank microcapsules used at the same equivalent amount of inert materials. These results suggest a good biocompatibility of MC-CU with the intestinal barrier cell model and are consistent with previously published findings about the cytotoxicity of mesoporous silica nano- and microparticles.[61]

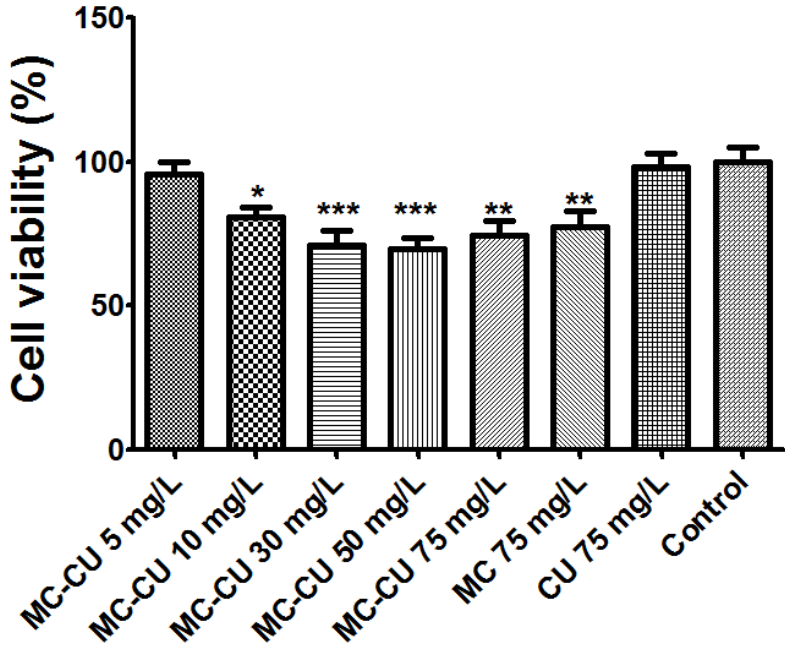

Figure 2.2.7. Viability of caco-2 cells after 24 h-incubation at 37°C with silica microcapsules loaded with curcumin (MC-CU) at equivalent concentrations of entrapped curcumin ranging from 5 to 75 mg/L. Controls are: cells incubated with culture medium (control), solution of curcumin in culture medium at 75 mg/L (CU 75 mg/L) and blank microcapsules at the same equivalent concentration of inert materials as MC-CU 75 mg/L (MC 75 mg/L). The results are expressed as the average of three independent biological replicates. Error bars indicate standard deviations. *$p<0.05$, **$p<0.01$ and ***$p<0.001$ *vs*. control.

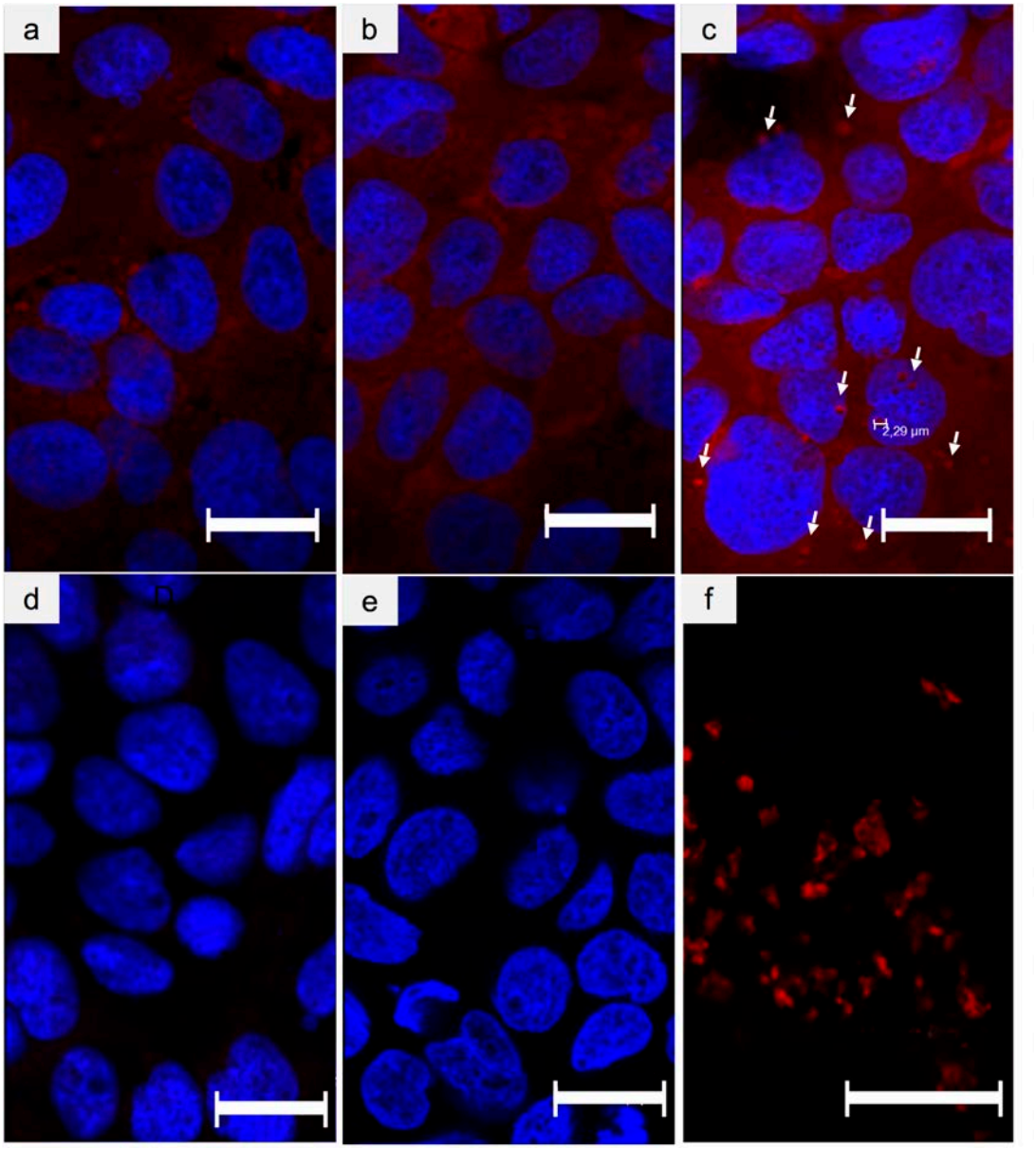

Figure 2.2.8 Confocal microscope images after cell incubation with MC labelled with Nile Red for 4 h. (a), (b) and (c) represent cells incubated with labelled microcapsules at equivalent concentrations of entrapped curcumin of 5, 10 and 30 mg/L, respectively. (d) represents cells incubated in cell culture. (e) represents cells incubated with Nile Red solution in DMSO/water 1/99 (v/v). (f) represents a confocal microscope image of labelled microspheres in a drop of water. Scale bare represents 20.0 µm.

In vitro cell uptake

Cell uptake of microcapsules was investigated by confocal microscopy after 4 h of incubation at different concentrations of entrapped curcumin in the culture medium: 5, 10 and 30 mg/L. For this purpose, microcapsules were labeled with Nile Red (appearing in red). Nuclei were labeled by Hoechst 33342 (appearing in blue), allowing microcapsules to be localized in the

intracellular compartments. The results show a diffusion of NR inside the cells for all the studied concentrations of MC in the culture medium (Figure 2.2.8a, b and c). According to images, the diffusion of NR increased when cells were exposed to increased MC concentration in the culture medium. On the other hand, no diffusion of NR was observed in cells exposed to NR solution in DMSO/water (1/99 v/v) (Figure 2.2.8e). Keeping in mind that, Nile Red is a lipophilic dye and thus can stain cell membranes; we can deduce that the entrapped dye diffuse much more efficiently than the free one. In other words, NR-labeled MC could be readily taken up by Caco-2 cells. Interestingly, the micrograph of cells exposed to 30 mg/L (Figure 2.2.8c) shows RN-labelled MC inside the cells, which was confirmed by checking the different optical sections in the z-stack. Moreover, no significant difference in cell shape was observed for cells exposed to MC when compared to control (non-exposed cells). No feature of cell stress was observed in all the studied conditions, which is in agreement with the cytotoxicity results.

2.2.4 Conclusion

In summary, hybrid solid lipid nanoparticles/mesoporous silica microcapsules have been successfully obtained through the mineralization of dispersions of solid lipid nanoparticles (SLN) in micellar solutions. The resulting hybrid silica microcapsules showed pH-dependent curcumin release, because of the different stability of lipid core as a function of pH value. Interestingly, curcumin release was effectively retained at pH 2.8, showing aggregated silica microcapsules, probably due to the isoelectric point of silica that is included in the gastric pH range (*i.e.* between 2 and 3). This result suggests that the designed silica microcapsules could be used as gastro-resistant delivery systems. Moreover, the results of the cytotoxicity assay suggest the biocompatibility of the developed silica mcirocapsules with Caco-2 cell monolayer model. In addition, CLSM showed a possible cell internalization of silica microcapsules, suggesting their versatility as absorption enhancers or for cell targeting. Therefore, using solid lipid nanoparticles (SLN) is a straightforward way to design pH-responsive hybrid silica microcapsules, showing improved stability, bioavailability and bioinertness. This strategy could provide a promising formulation platform for designing of drug delivery systems with enhanced bioavailability for poorly soluble drugs.[18,62]

Part 2.3

pH- and glutathione-responsive release of curcumin from mesoporous silica nanoparticles coated using tannic acid-Fe(III) complex

This part was published as: S. Kim, S. Philippot, S. Fontanay, R. E. Duval, E. Lamouroux, N. Canilho, A. Pasc, pH- and glutathione-responsive release of curcumin from mesoporous silica nanoparticles coated using tannic acid-Fe(III) complex in *RSC Adv*. 2015, 5, 90550-90558.

2.3.1 Introduction

The development of pH- or glutathione-responsive drug delivery system has been one of the main topics for scientists, because the cancer tissues show generally more acidic environment, and their glutathione (GSH) level are also 4-fold higher than those of normal tissues.[63] Thus, the drug carrier should be stable at physiological condition (pH 7.4) without drug release to reduce the side effect on normal tissue. However, the carrier has to release the encapsulated drug when it reaches to a slight low pH zone such as a cancer tissue enriched environment (pH 5 - 6). In addition, for more efficient targeting drug delivery, it is also preferred that drug release is controlled by glutathione concentration level. For this goal, a gatekeeper approach already showed its excellent efficiency,[64,65] however, metallic nanoparticles as keepers could induce toxicity[66], which might limits their wide and practical applications.

As mentioned in the introduction of this chapter, tannic acid-Fe(III) complex coating method has been proved effective for designing pH-responsive systems like drug carrier without serious toxicity concern. Therefore, being in line with this concept, in this part, it is demonstrated a newly designed drug delivery system using tannic acid-Fe(III) complex deposition on the outer surface of mesoporous silica nanoparticles with the aim to provide pH- and glutathione-reponsive drug release and to reduce the fast release at the early stage as well as to increase the bioavailability. As an application of novel mesoporous silica nanoparticles prepared by tannic acid-Fe(III) complex coating, *in vitro* curcumin release experiments and the cytotoxicity test were carried out. More detailed discussion was covered in the following.

2.3.2 Experimental section

Chemicals

Tetramethylorthosilicate (TMOS), tetraethylorthosilicate (TEOS), Pluronic P123 and hexadecyltrimethylammonium bromide (CTAB), tannic acid (TA), sodium hydroxide (NaOH), glutathione (reduced form (GSH)), and curcumin were purchased from Sigma-Aldrich. Ethanol, methanol and iron (III) chloride ($FeCl_3$) was purchased from Alfa Aesar. Water was deionized and purified using a Milli-Q pack system. All reagents were used as received without any further purification.

Synthesis of mesoporous silica nanoparticles, MCM-41

MCM-41 was synthesized as previously reported in the literature.[67] Briefly, 300 mg of CTAB was dissolved in 120 g of deionized water at 35°C and kept under stirring to obtain a clear solution. Then, 0.35 mL of 2M NaOH solution was added, and the mixture was heated to 80°C. Afterward, 0.67 ml of TEOS was added as silica precursor, kept under continuous stirring for additional 2 h. The as-synthesized product was filtered and washed with deionized water then calcined at 550°C for 5 h, giving mesoporous silica nanoparticles MCM-41.

Curcumin loading into mesoporous silica nanoparticles

Curcumin loading was performed using a rotavapor loading method as reported in the literature.[35] In brief, 10 mg of curcumin was dissolved in 5 mL of methanol, and then 100 mg of MCM-41 was added to this solution. The mixture was sonicated for 5 min, and the solvent was slowly removed using rotary evaporator at 50 °C for 2 h. This product was kept at 30 °C for more than 24 h to remove the residual solvent. Dried curcumin loaded mesoporous silica nanoparticles are denoted as MCM-41-CU.

Coating of curcumin loaded MCM-41 using tannic acid-Fe(III) complex

Deposition of the tannic acid-Fe(III) complex on MCM-41 was conducted by the method reported by Ejima et al.[25] with a slight modification. In brief, 0.020 mL of tannic acid solution (24 mM) and 0.020 mL of $FeCl_3$ solution (24 mM) were added to 4 mL of curcumin loaded MCM-41 (1 mg / 1 mL) under vortex stirring and kept for 30 seconds. 0.15 mL of phosphate buffer solution (pH 8.0, 100 mM) was added to the mixture to raise pH value around 7.2. The resulting suspension product was filtered, and then washed with 3 mL of deionized water to remove free tannic acid-Fe(III) and phosphate salt, then dried at 35 °C for 48 h. The final products, tannic acid-Fe(III) complex coated curcumin loaded silica materials are denoted as MCM-41-CU-TA. Multi-layer coating of curcumin loaded silica materials was performed on MCM-41-CU-TA by repeating the procedure described above up to 3 times, and the product is denoted as MCM-41-CU-TA-*number*, where *number* is the number of repeated coating process. Besides, tannic acid-Fe(III) complex coated silica materials without curcumin loading were also prepared to calculate the weight percentage of tannic acid-Fe(III) complex deposited on the surface of silica materials, and the samples are denoted as MCM-41-TA.

Calculation of curcumin content in the mesoporous silica nanoparticles

10 mg of tannic acid-Fe(III) coated curcumin loaded mesoporous silica nanoparticles, MCM-41-TA-CU was added to 5 mL of 0.1M HCl solution for the decomposition of tannic aicd-Fe(III) complex. Then, 95 mL of THF was added to extract and solubilize curcumin. The solution was analysed using UV-vis spectroscopy. The calculated curcumin content was 8.2 wt.%. (93 % with respect to initially loaded amount)

In vitro drug release experiments

Release experiments were carried out for curcumin MCM-41-CU and TA-Fe(III) coated curcumin loaded MSNs (MCM-41-CU-TA). The material equivalent to 1 mg of curcumin was dispersed in 75 mL of 0.3 wt.% of CTAB contained dissolution medium (pH 7.4, 6.0 and 4.5) using phosphate or acetate buffer system. The ionic strength was adjusted to 10 mM for all dissolution mediums, except glutathion (GSH) triggered curcumin release experiments, where the ionic strength was adjusted to 50 mM. More details for release experiments were described in part 2.1

Cell line and culture conditions

MRC-5 (ATCC CCL-171) human lung fibroblasts were used as model for cytotoxic assays. Cells were grown in Minimum Essential Medium (MEM, 31095-029, Life Technologies-Gibco) supplemented with 10% heat-inactivated fetal calf serum (CVFSV00-0U, Eurobio, Courtaboeuf, France) and 2 mM L-glutamine (G7513-100ML, Sigma Aldrich), at 37°C in a 5% CO_2 humidified atmosphere.

Cytotoxicity assay on MRC5 cell line

The impact of MCM-41, MCM-41-CU, MCM-41-CU-TA, and MCM-41-TA (without curcumin) on cell viability was evaluated by the MTT assay[48] based on the reduction of MTT by mitochondrial succinate dehydrogenase into purple formazan in living cells. Cells were plated at 10^4 cells per well in 96-well tissue culture plates (83.1835, Sarstedt) and grown for 24 hours at 37 °C in a 5% CO_2 atmosphere. Then medium was discarded and replaced by fresh medium containing increasing amounts of tested silica nanoparticles (range 1 to 150 µM curcumin equivalent) previously dispersed in the medium. Three different controls were

added: medium alone, cells in medium and 150 µM curcumin equivalent in medium. Each condition was repeated in eight wells. After 48 h of incubation, medium was discarded and cells were washed with PBS. Hundred microlitres of medium containing 0.5 mg/mL MTT previously prepared in PBS, were added to each well and the plates were incubated for 4 hours at 37°C. Then formazan crystals were dissolved by the addition of 100 µl of SDS (100 µg/mL) and incubation for 3 hours in 37°C. Finally absorbance was measured at 540 nm *vs* 690 nm using a 96-well plate reader (Multiskan EX, Thermo Electron Corporation). Percentages of survival and half maximal inhibitory concentration (IC_{50}) were then calculated.

2.3.3 Results and Discussion

Materials Characterization

In this study, a hydrophobic model drug, curcumin was loaded into mesoporous silica nanoparticles, MCM-41 in order to investigate drug release behavior before/after surface coating using tannic acid-Fe(III) complex. Indeed, practical applications of curcumin have been limited because of it low water solubility at acidic and physiological pH and its rapid hydrolysis under alkaline conditions. In addition, its poor absorption and rapid metabolism in the human body decrease the bioavailability of curcumin.[68] Therefore, to overcome these drawbacks, it is necessary to encapsulate curcumin into a drug delivery system, here into mesoporous silica nanoparticles.

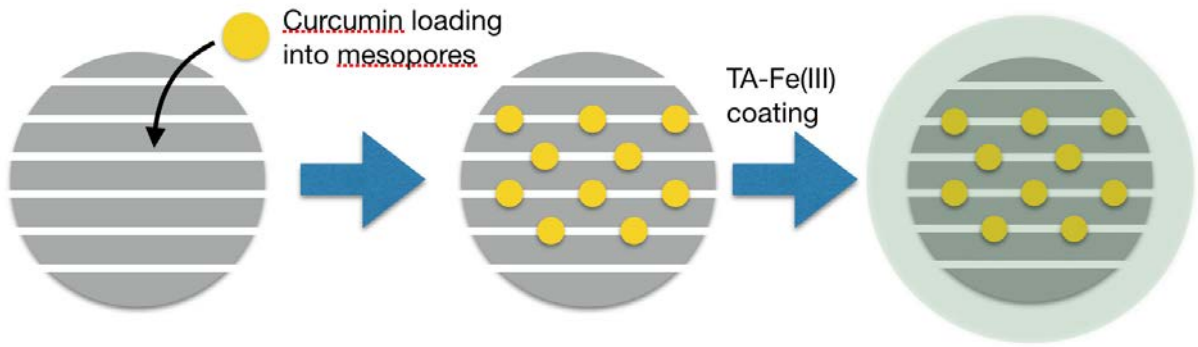

Figure 2.3.1. Syntheic pathway for curcumin loaded mesoporous silica nanoparticles (MSN) using tannic acid-Fe(III) complex.

Small angle X-ray scattering (SAXS) pattern of bare MCM-41(Figure 2.3.2a), exhibit three well resolved peaks at 3.7, 2.1, and 1.8 nm. The ratio of these peaks is 1:$\sqrt{3}$:2, which can be attributed to the (100), (110) and (200) reflections of the hexagonal structure. The corresponding cell parameter a_0 is estimated to be 4.3 nm, which is in accordance with some other results presented elsewhere.[67,69] For curcumin loaded mesoporous silica nanoparticles MCM-41-CU, and for tannic acid-Fe(III) coated silica MCM-41-CU-TA, the spectra are superimposable to those of the bare materials. This indicates that the hexagonal structure is maintained, and that neither the curcumin loading nor the tannic acid-Fe (III) coating seems to affect the structure of the materials.

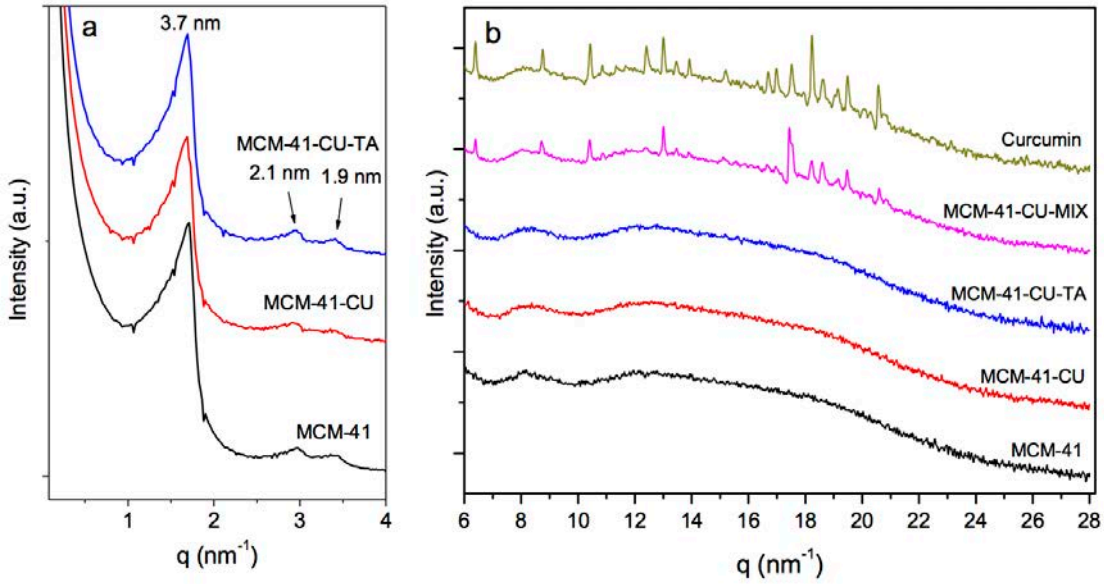

Figure 2.3.2. (a) SAXS patterns of MCM-41 with and without curcumin loading, and before and after surface coating, (b) WAXS patterns of MCM-41 with and without curcumin loading, before and after surface coating, and of physical mixtures of curcumin with MCM-41.

In order to investigate the crystalline phase of curcumin after encapsulation into mesopores, wide angle X-ray scattering (WAXS) experiments were performed. As shown in Figure 2.3.2b, most of pure curcumin's characteristic peaks are observed for physical mixtures of curcumin with silica nanoparticles (MCM-41-CU-MIX), suggesting that curcumin is in its crystallized form in these materials. However, for curcumin loaded mesoporous silica nanoparticles using rotavapor method (MCM-41-CU) and tannic acid-Fe(III) coated curcumin loaded mesoporous silica nanoparticles (MCM-41-CU-TA) no diffraction peak is observed in the high q-region, indicating that curcumin has been well loaded and dispersed over mesopores with an amorphous form or as nano-scale aggregates.[69]

Nitrogen adsorption-desorption isotherm experiments were performed on bare mesoporous silica (MCM-41) and curcumin loaded mesoporous silica MCM-41-CU), showing a type IV isotherm (Figure 2.3.3) with a capillary condensation at a relative pressure p/p_0 in the range of 0.2 - 0.4, which is characteristic of mesoporous materials. The detailed data of surface area, pore volume, and pore diameter as well as lattice parameter are given in Table 1. The surface area and pore volume for silica materials decrease as curcumin is loaded into mesopores, while the decrease of the pore diameter is not distinctive (from 2.3 nm to 2.1 nm). It is thus believed that during the evaporation of methanol at curcumin loading step, given that curcumin presents a hydrophobic nature, curcumin molecules might prefer to get together, forming nano-scale aggregates due to the presence of hydrophilic silanol groups on the surface.

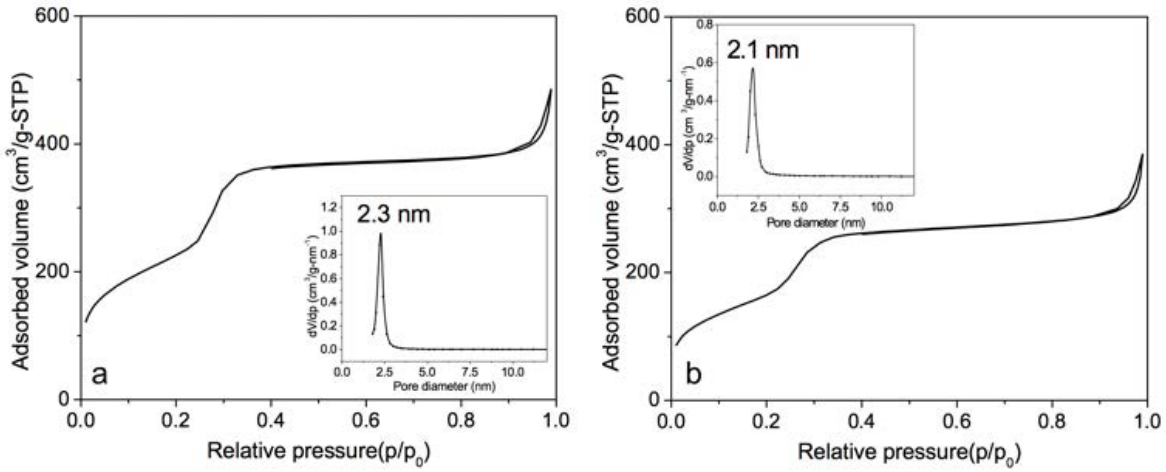

Figure 2.3.3. N_2 adsorption–desorption isotherms and pore size distribution (inset) of (a) MCM-41, (b) MCM-41-CU

Sample	D_P (nm)	S_{BET} (m^2 g^{-1})	V_P (cm^3 g^{-1})
MCM-41	2.3	838	0.52
MCM-41-CU	2.1	640	0.40

Table 2.3.1. Physicochemical properties of silica materials (MCM-41) with and without curcumin loading (D_P = Pore diameter, S_{BET} = BET surface area, V_P = Pore volume)

Indeed, the rotavapor drug loading method has been widely employed for hydrophobic molecules because of its simple procedure and high drug loading efficiency that could reach around 100 %. Moreover, by this method, the drug exhibits very low ratio of crystalline

phase that cannot be obtained by other methods like the fluid bed loading, in which the fast solvent evaporation could induce the crystallization of hydrophobic drug molecules.[35]

The size measurement was performed using dynamic light scattering (DLS) for MCM-41 before/after tannic acid-Fe(III) complex coating. (Figure 2.3.4a) The hydrodynamic mean size of silica nanoparticles is 217 nm for MCM-41, after curcumin loading, and then tannic acid-Fe(III) complex coating, its mean size changed to 225 nm, and 234 nm, respectively. Then, by multiple deposition of tannic acid-Fe(III) complex, the mean size increased to 248 nm, and 265 nm for 2 times (MCM-41-CU-TA-2), and 3 times (MCM-41-CU-TA-3) coated silica nanoparticles, respectively.

The presence of tannic acid-Fe(III) complex in silica materials was confirmed by the evolution of UV-Vis diffuse reflectance spectra. (Figure 2.3.4b) For clarity reasons, only silica materials without curcumin (MCM-41-TA) were analyzed. First, no significant peak was observed for MCM-41. However, for MCM-41-TA, one peak was observed at 307 nm, which corresponds to the tannic acid absorption peak coordinated to the Fe(III) ions, and a broad shoulder around 560 nm could be assigned to charge transfer band from a coordinated tannic acid to Fe(III) ions the tannic acid-Fe(III) complex compound.[70]

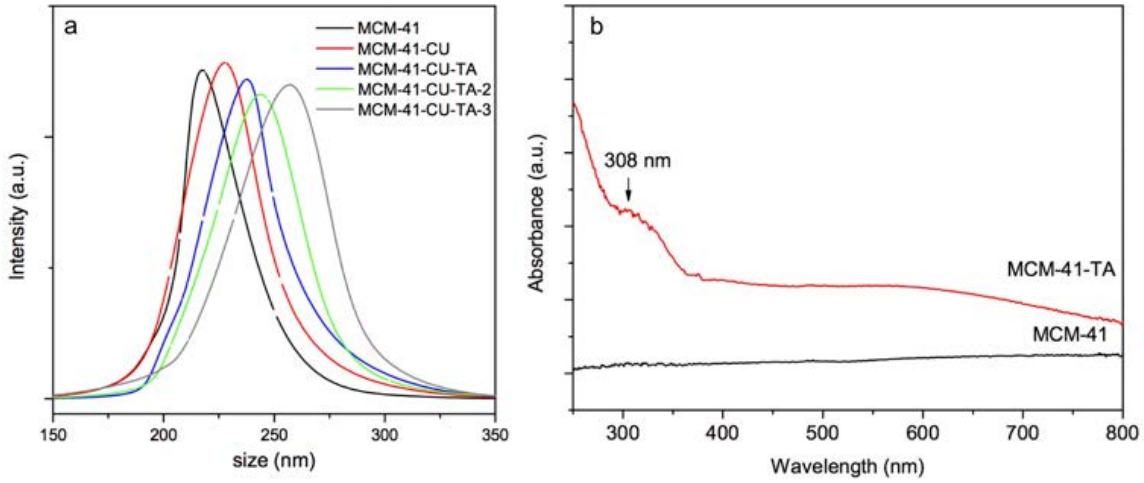

Figure 2.2.4. (a) Size distribution of MCM-41 type silica materials obtained from DLS, (b) UV-vis spectra of MCM-41 and MCM-41-TA. For clarity reasons, UV-vis measurements were performed on the silica materials without curcumin.

The amount of tannic acid-Fe(III) complex deposited on mesoporous silica nanoparticles (MSN) was also calculated. For 4 mg of silica material after coating process, the amount of tannic acid was calculated as following: 24 mol/L * 0.02 mL * 1701 g/mol * 0.125 * 1L/1000mL = 0.102 mg, where 24mol/L is the concentration of tannic acid in stock solution,

0.02 mL for the volume used, 1701 g/mol is molar weight of tannic acid, and 0.125 is the ratio of tannic acid-Fe(III) charge transfer band peak before/after coating process, determined by UV-vis spectroscopy. (Figure 2.3.5) The amount of Fe(III) can be also described in the same manner: 24 mol/L * 0.02 * mL * 55.8 g/mol * 0.33 * 0.125 *1L/1000mL = 0.001 mg of Fe(III) ion, where 55.8 g/mol is molar weight of Fe, 0.33 is the ratio between tannic acid and Fe(III) in the complex. The possibility of Fe (III) ions coordinated to other functional groups was neglected in the calculation. Thus, the weight percent of tannic acid and Fe ions is 2.5 % and less than 0.1 %, respectively.

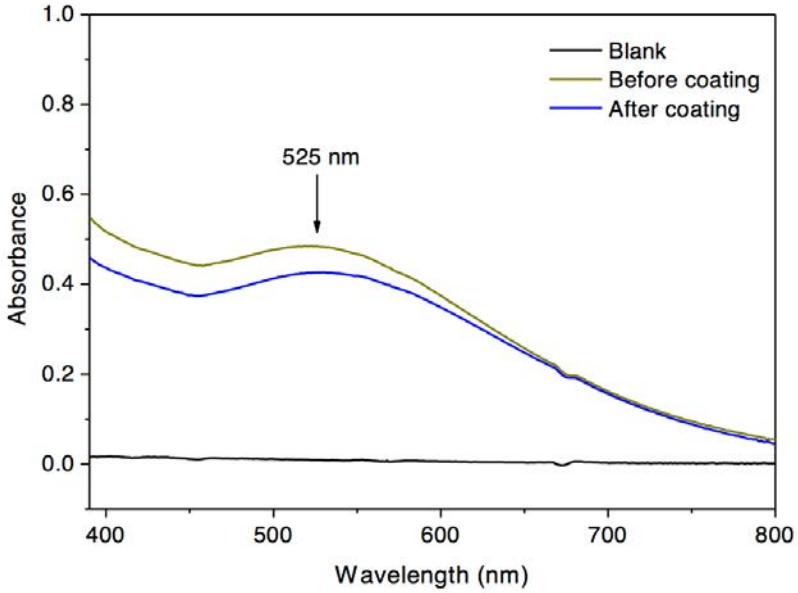

Figure 2.3.5. UV spectra of tannic acid-Fe(III) complex before/after coating process

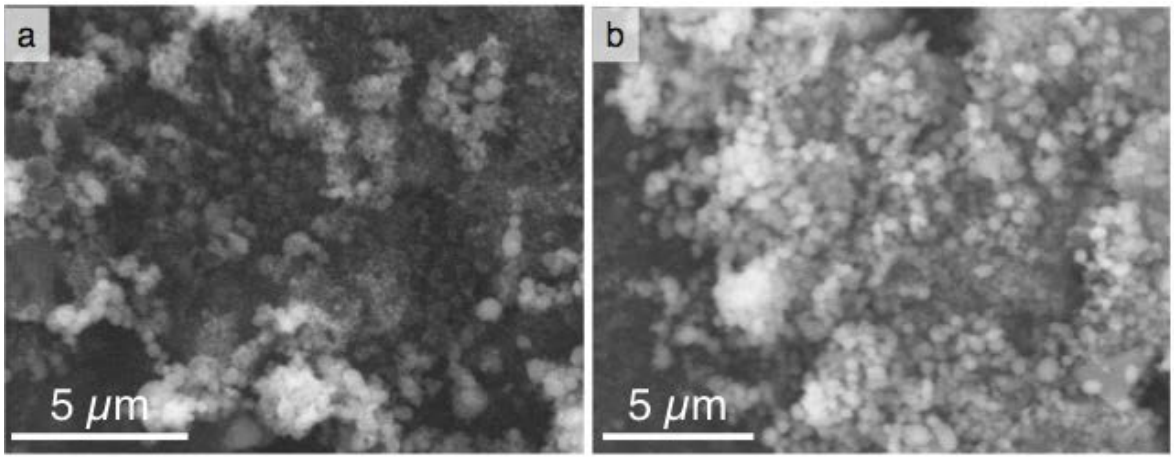

Figure 2.3.6. SEM image of (a) MCM-41, (b) MCM-41-CU-TA

Scanning electron microscopy (SEM) analysis was then conducted to investigate the morphologies and the surface properties of tannic acid-Fe(III) complex coated mesoporous

silica silica nanoparticles. (Figure 2.3.6) Silica materials before/after coating showed a spherical or ellipsoid morphology with a particle size of ~ 150 nm that is in good agreement with the results obtained by DLS measurements. Since the morphology of MCM-41 silica material after tannic acid-Fe(III) coating (MCM-41-CU-TA) remained identical to its starting material (MCM-41), SEM-EDS mapping experiment was performed on MCM-41-CU-TA, showing that Fe atoms were homogenously dispersed over silica material (Figure 2.3.7). By spotting on several areas using SEM-EDS beam, (Figure 2.3.8, Table 2.3.2) it was founded that iron content on the surface of silica materials is ~ 0.2 %, which is higher than the calculated values using UV-Vis (less than 0.1 wt.%), but seems reasonable, since SEM-EDS analysis can measure only the silica surface.

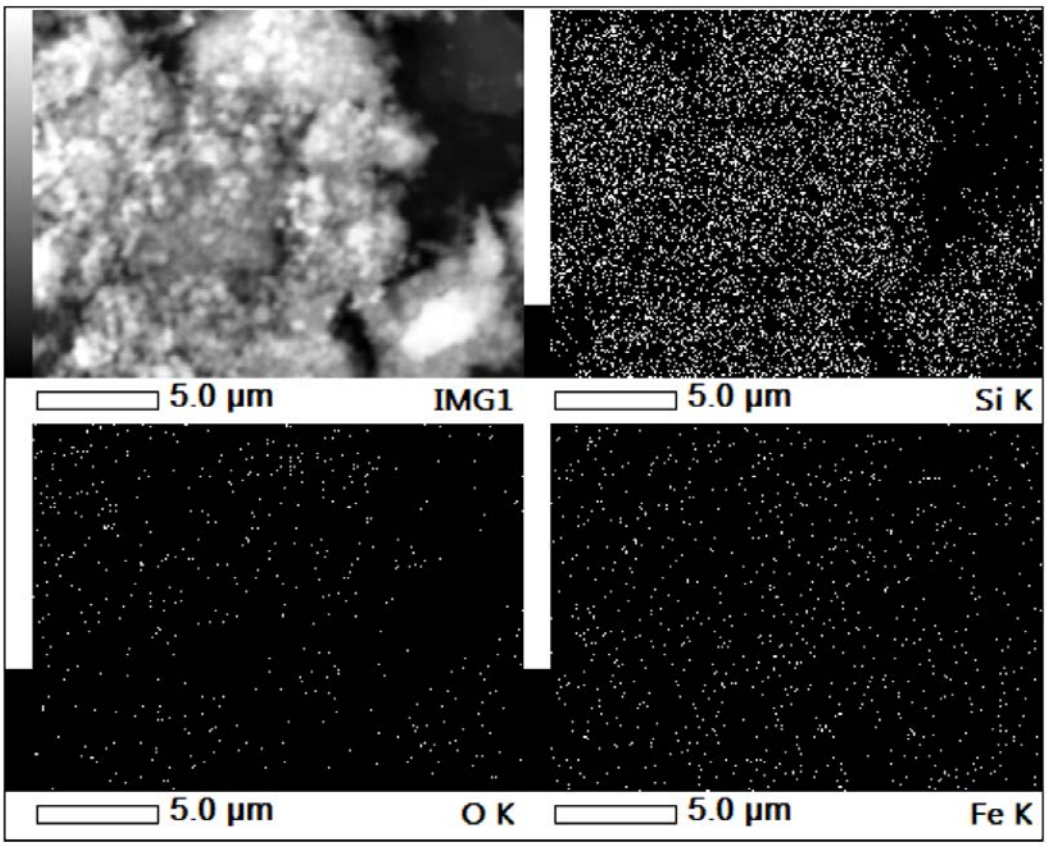

Figure 2.3.7. SEM-EDS mapping image of MCM-41-CU-TA

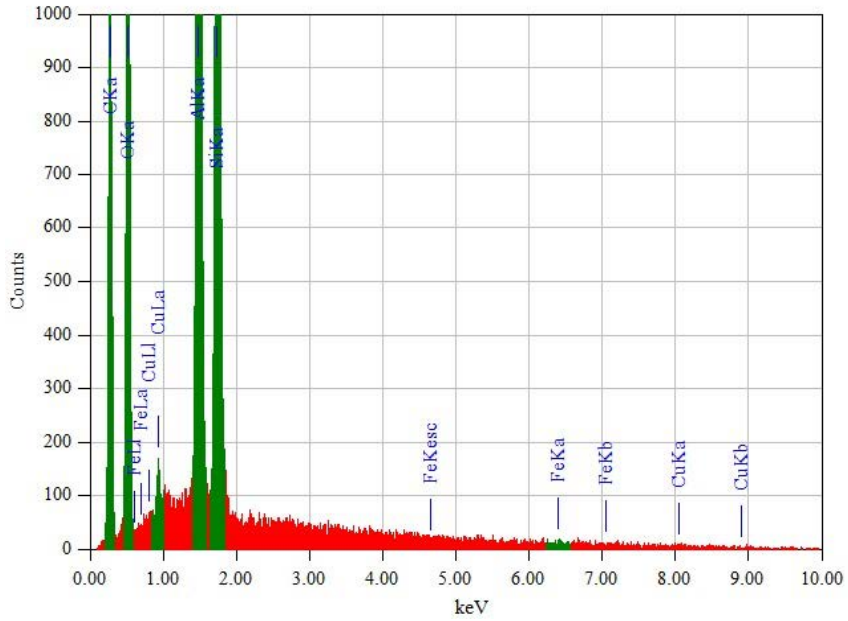

Figure 2.3.8. SEM-EDS elemental analysis of MCM-41-CU-TA

Element	KeV	Mass%	Atom%
O (K)	0.525	67.47	78.50
Si (K)	1.739	32.34	21.43
Fe (K)	6.398	0.19	0.06

Table 2.3.2. SEM-EDS elemental analysis of MCM-41-CU-TA

Further evidence for tannic acid-Fe(III) coating on the surface of silica nanoparticles is provided by the transmission electron microscopy (TEM) images presented in Figure 2.3.8. First, the image for bare MCM-41 (Figure 2.3.9a) showed the typical well-ordered hexagonal pore network in spherical or ellipsoid form with the mean diameter of 155 nm, by counting 20 particles. The presence of tannic acid-Fe(III) complex on the surface of MSN could be visualized after coating (Figure 2.3.9b). Especially, a zoomed image of silica nanoparticles coated 3 times (Figure 2.3.9c) cclearly showed the presence of tannic acid-Fe(III) complex coating on the surface of silica, giving the average thickness of 15 nm with 5 nm as standard deviation, by analyzing 20 particles. From this result, it is assumed that the average thickness of 1 layer of coating could be of 5 nm. The stability of coating as a function of pH was also monitored using TEM analysis. The samples were prepared by incubating mesoporous silica coated 3 times (MCM-41-CU-TA-3) in the buffer solutions of pH 4.5 for 1 h with 15 min of sonication. For the sample incubated at pH 4.5, (Figure 2.3.9d) it was found that most of

tannic acid-Fe(III) complex were removed. This unique pH-dependent property of tannic acid-Fe(III) complex will further be discussed in *in vitro* curcumin release experiments section.

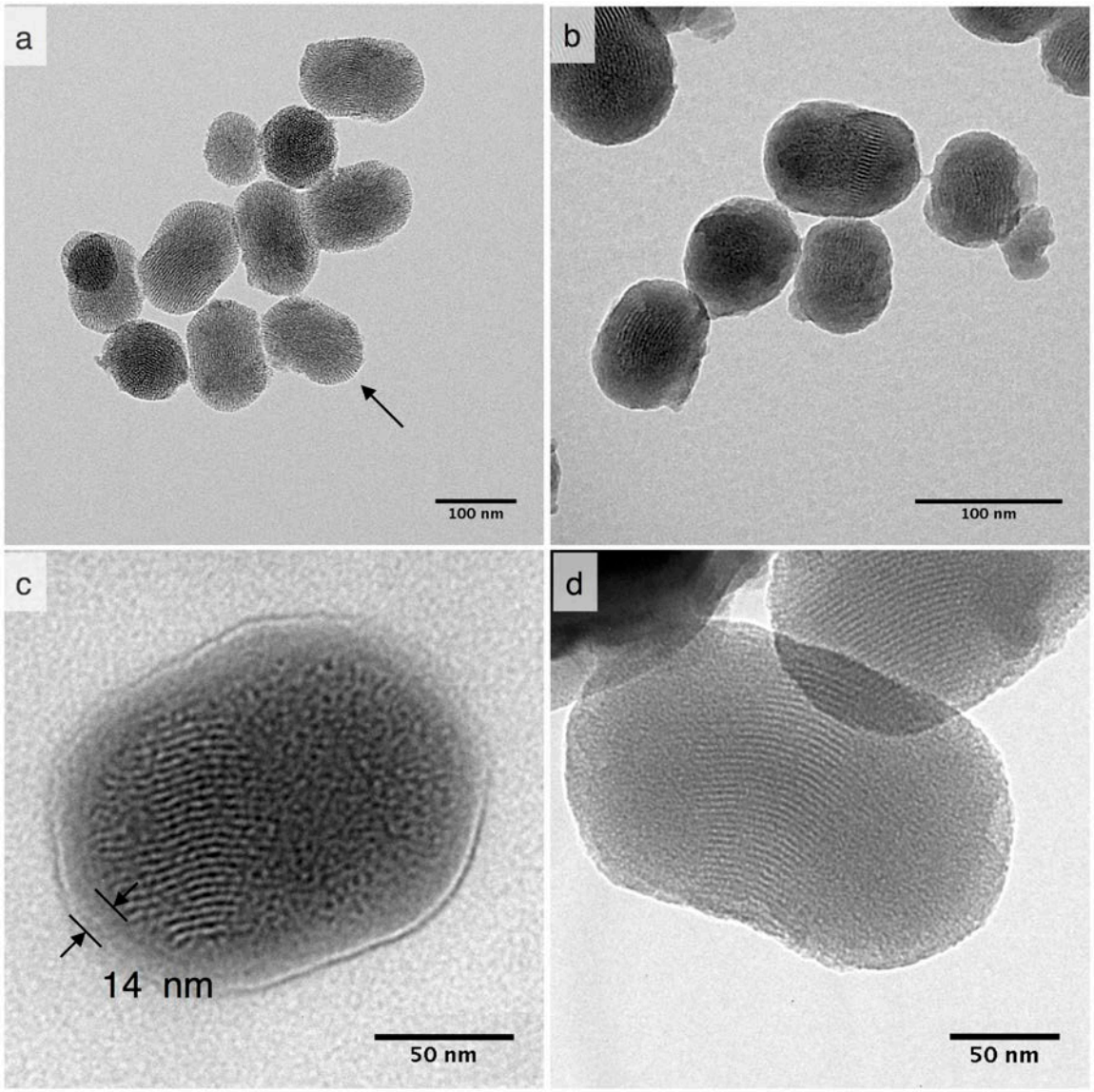

Figure 2.3.9. TEM image of (a) MCM-41 (arrow indicates opened pores), (b) MCM-41-CU-TA, (c) MCM-41-CU-TA-3 (coated 3 times), (d) MCM-41-CU-TA-3 incubated at pH 4.5.

In vitro release experiments

The release experiments of curcumin loaded mesoporous silica nanoparticles (MCM-41-CU) and tannic acid-Fe(III) coated curcumin loaded mesoporous silica nanoparticles (MCM-41-CU-TA) were carried out in 3 different receiving solution (pH 7.4, 6.0 and 4.5) containing 0.3 wt.% of CTAB in order to solubilize the released curcumin[37] that is poorly soluble and

rapidly degraded in water.[38] During the release experiments, the sink conditions were kept by adding the same volume of receiving solution as the withdrawn volume. As shown in Figure 2.3.10a, the curcumin release from tannic acid-Fe(III) coated MCM-41 is significantly decreased compared to non coated silica materials and the release is depending on the pH values. Indeed, at pH values lower than 2 only the mono-complex TA-CU can be formed, while at pH values higher than 7, three moieties of tannic acid are strongly bonded to Fe(III) (Figure 2.3.11).[25] The release of curcumin from MCM-41-CU-TA is effectively retained at pH 7.4, however, it is not completely suppressed, probably due to a good permeability of tannic acid-Fe(III) complex to small molecules like curcumin.[71]

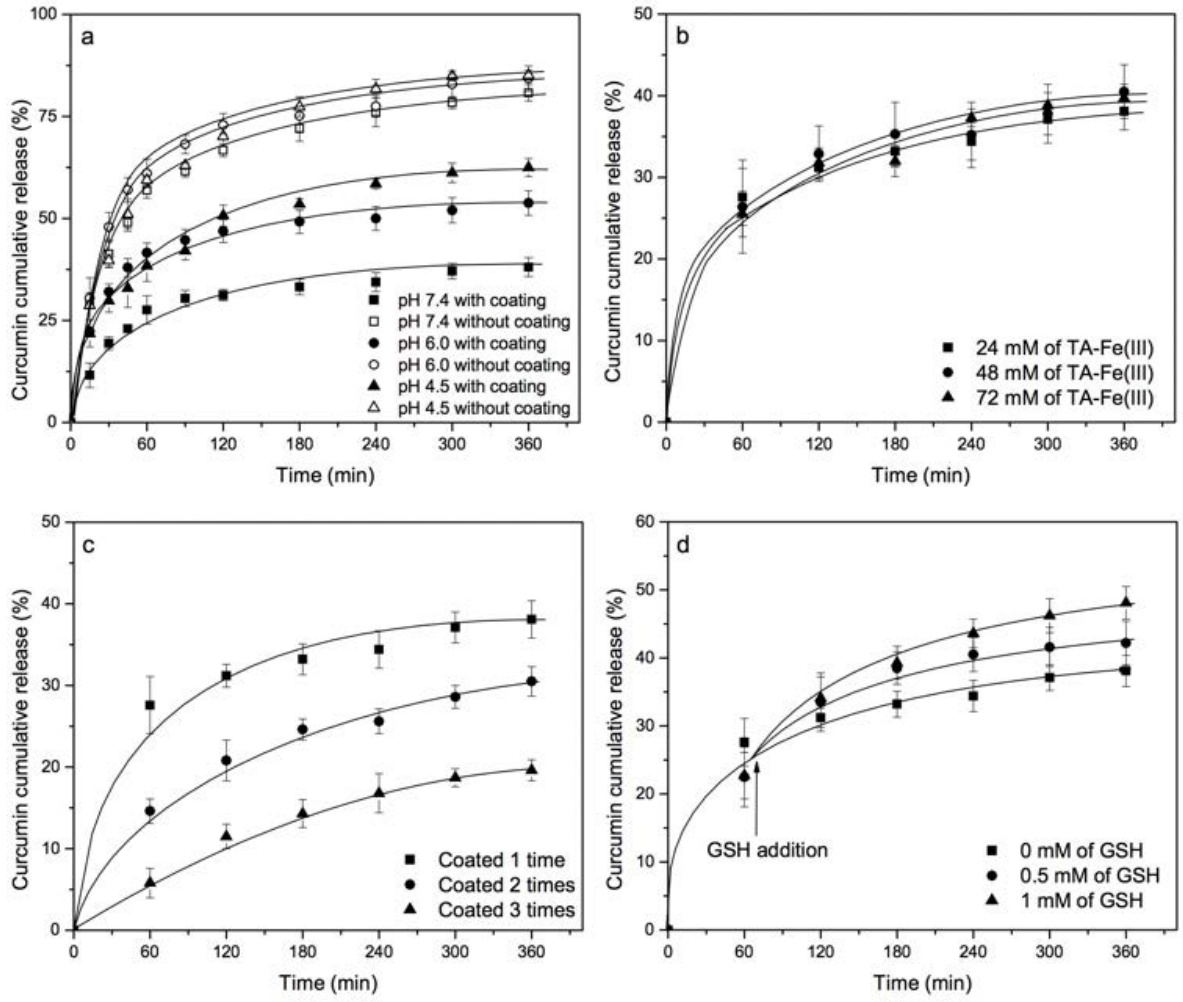

Figure 2.3.10. (a) Cumulative release of curcumin for MCM-41-CU, and MCM-41-CU-TA, (b) Effect of coating agent concentration, (c) Effect of multiple coating, and (d) Effect of glutathione (GSH) concentration level on curcumin release.

Since the curcumin release from tannic acid-Fe(III) coated mesoporous silica nanoparticles showed only tannic acid-Fe(III) coating dependence, the further investigations were conducted by varying some parameters concerning tannic acid-Fe(III) agent complex. First,

the concentration of tannic acid-Fe(III) complex was varied from 24 mM to 72 mM in order to investigate the effect of coating agent concentration on curcumin release. As shown in Figure 2.3.10b, there is no significant improvement of curcumin release at pH 7.4, even with silica material prepared using 72 mM of tannic acid-Fe(III) (MCM-41-CU-TA-72), giving about 40 % of curcumin cumulative release after 360 min, which is similar to the result for the silica material prepared with 24 mM of tannic acid-Fe(III) complex. (MCM-41-CU-TA) However, this result is in agreement with the studies reported by Ejima et al.,[89] showing that the thickness of the complex film is not depending on the tannic acid-Fe(III) concentration. Therefore, it can be concluded that 24 mM as concentration of tannic acid-Fe(III) seems to be enough to cover all the surface of mesoporous silica nanoparticles.

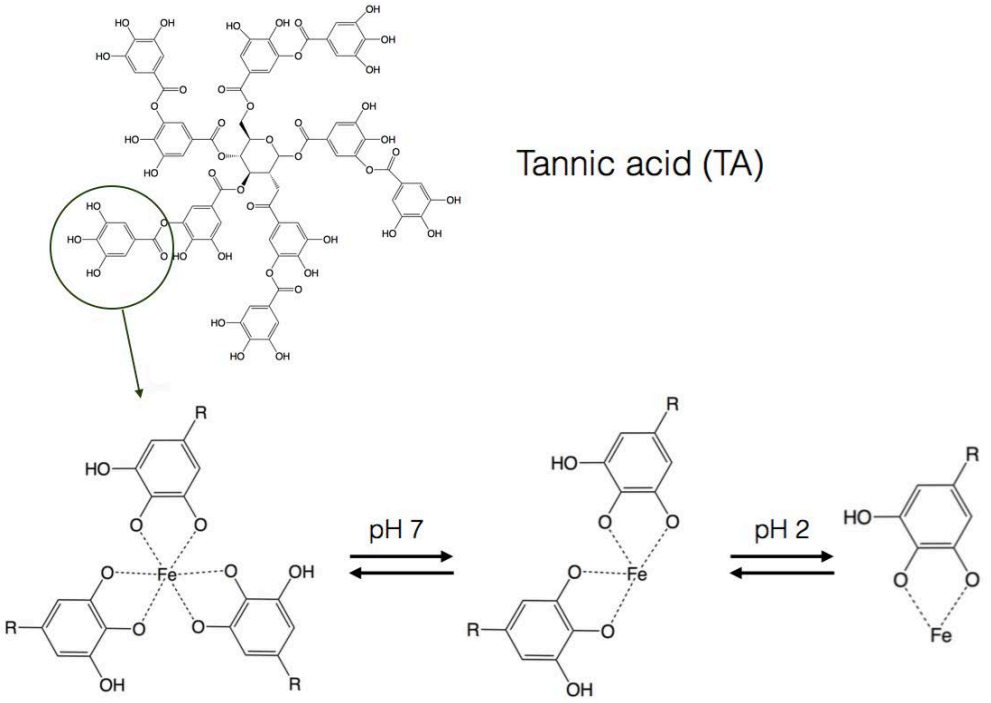

Figure 2.3.11. Dominate complex form of tannic acid-Fe(III) as a function of pH

Afterwards, the effect of multiple coating process on curcumin release was also investigated (Figure 2.3.10c). Indeed, more tannic acid-Fe(III) coating process is repeated, more curcumin release from the silica nanoparticles is effectively retained. For example, curcumin loaed MCM-41 coated 3 times with the complex (MCM-41-CU-TA-3) showed only 17 % of curcumin release after 360 min, while 38 %, and 28 % of curcumin release was obtained for MCM-41-CU-TA (coated 1 time), and MCM-41-CU-TA-2 (coated 2 times), respectively. Thus, contrary to the curcumin release result obtained by the variation of tannic acid-Fe(III) concentration, the multiple coating process seems more efficient to tailor the drug release

profile, which should be due to increased thickness of tannic acid-Fe(III) complex as already discussed in TEM analysis section.

To further investigate a correlation between surface properties of silica materials and curcumin release rate, the evolution of the zeta potential of mesoporous silica nanoparticles was monitored as a function of pH value. (Figure 2.3.12) First, after tannic acid-Fe(III) coating, the zeta potential slight decreased by ~ 5 mV at pH 7.4 (cf. MCM-41-CU *vs* MCM-41-CU-TA or MCM-41 *vs* MCM-41-TA) due to the increase of the negative charge by non-coordinated galloyl groups of tannic acid.[70] Then, in all case the zeta potential values increase as pH value decreases from 7.4 to 4.0, because of the protonation of silnaol groups of the silica surface. However, the increase of zeta potential is not dramatic for tannic acid-Fe(III) coated silica materials (MCM-41-CU-TA) because in the pH range between 6.0 and 4.5, tannic acid-Fe(III) still exists as the bis-complex on the silica surface, which could shield silnaol groups from the solvent. As a result, the surface silanol groups for coated silica materials are less exposed to the dissolution medium, compared to non-coated silica materials, thus the curcumin release could be also retained. Besides, the zeta potential reached around 0 mV at pH 2.5 (data not shown in Figure 2.3.12) for all silica materials with the recovery of its original white color for MCM-41-TA (without curcumin), which indicates the total decomposition of tannic acid-Fe(III) complex as confirmed by TEM analysis.

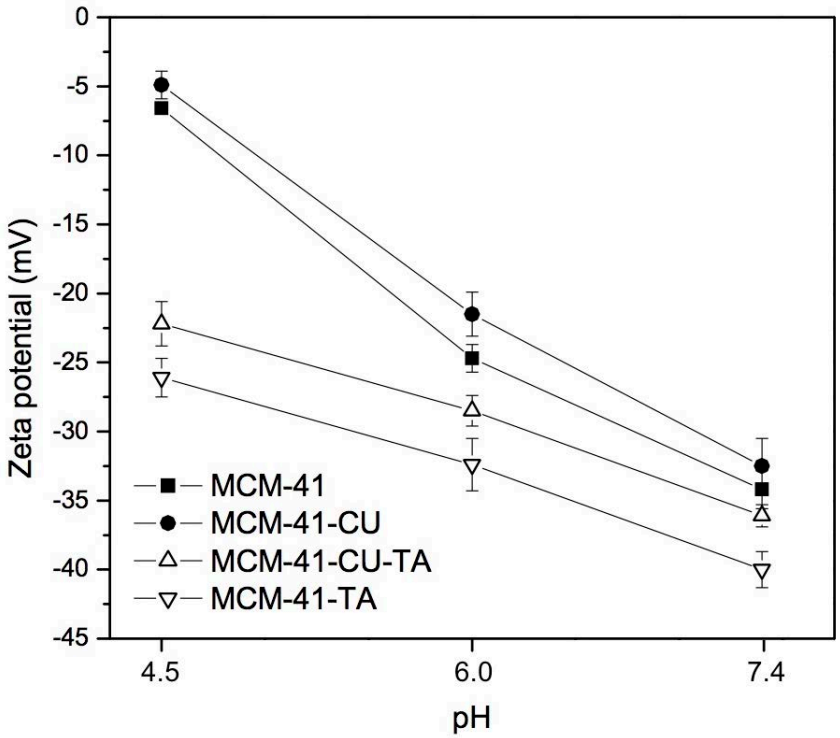

Figure 2.3.12. Dominate complex form of tannic acid-Fe(III) as a function of pH

Finally, since tannic acid-Fe(III) complex could be broken up in the presence of other strong ligands, the responsiveness of tannic acid-Fe(III) coated silica materials to glutathione (GSH) was investigated. Glutathione has been considered as one of the most efficient internal triggers because its concentration is quite different between the exterior (2 μM) and interior (10 mM) of the cells,[72,73] and in some cancer tissues the concentration of GSH could be 4-fold higher than normal tissues. Moreover, because the thiol group of GSH can generally reduces disulfide bond linker, the main approach using GSH trigger is redox-responsive mesopores gatekeeper. However, in this study GSH that contains carboxylate group along with amine group, was used only as a metal chelator in order to break tannic acid-Fe(III) complex. Indeed, it was already reported that contrary to cysteine, GSH cannot reduce Fe(III) ions because of the liganding that occurs between carboxylate group of GSH and iron complex compound, tannic acid-Fe(III).[74] As shown in Figure 2.3.10d, the curcumin release from MCM-41-CU-TA was rapidly increased after adding GSH in dissolution medium of pH 7.4, and the rate of curcumin release could be also controlled by adjusting GSH level from 0 mM to 1.0 mM, which reaches 48 % of curcumin release at 360 min. As a result, it can be concluded that despite of the lack of disulfide bond on tannic acid-Fe(III) complex, the curcumin release can be also triggered upon the glutathione concentration level through the competitive liganding of GSH with Fe(III) ions.

In addition to MCM-41 silica nanoparticles, the feasibility of tannic acid-Fe(III) coating for large pore system was investigated using curcumin loaded SBA-15 silica materials. Curcumin loading was performed in the same manner as for MCM-41. From the SAXS data (Figure 2.3.13a) SBA-15 silica materials exhibit well ordered hexagonal mesopore structure before/after curcumin loading and no bulk aggregation was formed as verified in WAXS data. (Figure 2.3.13b) However, despite of interesting pore size of ~ 7.0 nm, (Figure 2.3.14) the morphology of SBA-15 is not well defined, showing randomly ordered block silica with more than 1 μm in diameter, as observed by TEM and SEM analysis. (Figure 2.3.15-16) Moreover, due to its not-well defined morphology that might cause the bad water-dispersibility, only agglomerated silica materials could be obtained after tannic acid-Fe(III) coating process. (Figure 2.3.15b)

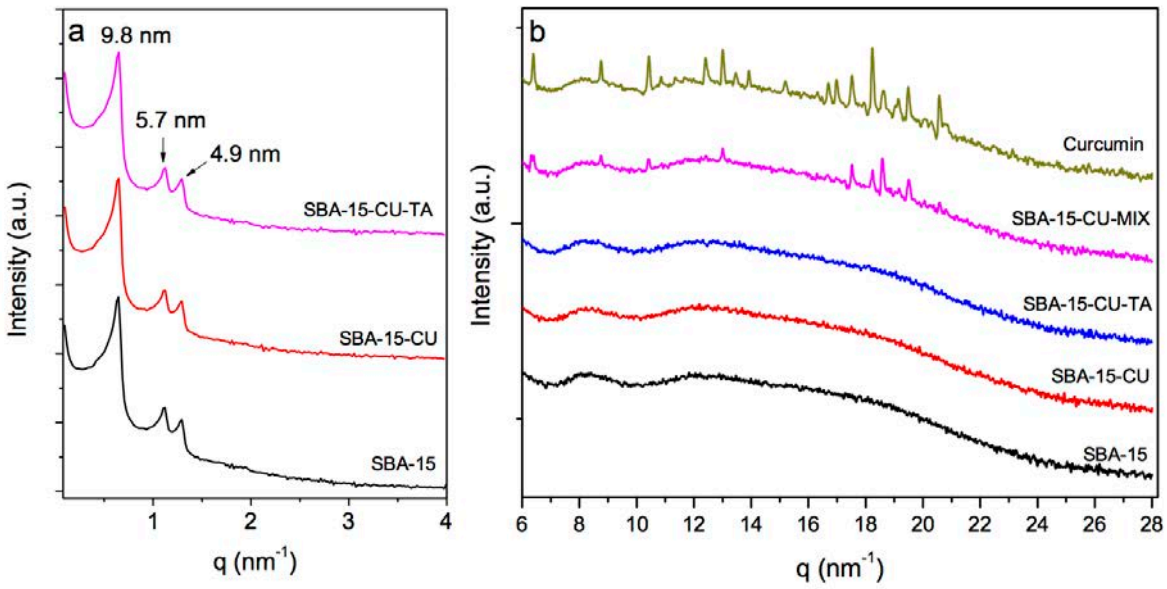

Figure 2.3.13. (a) SAXS patterns of SBA-15 with and without curcumin loading, and before and after surface coating, (b) WAXS patterns of SBA-15 mesoporous materials with and without curcumin loading, before and after surface coating, and of physical mixtures of curcumin with SBA-15.

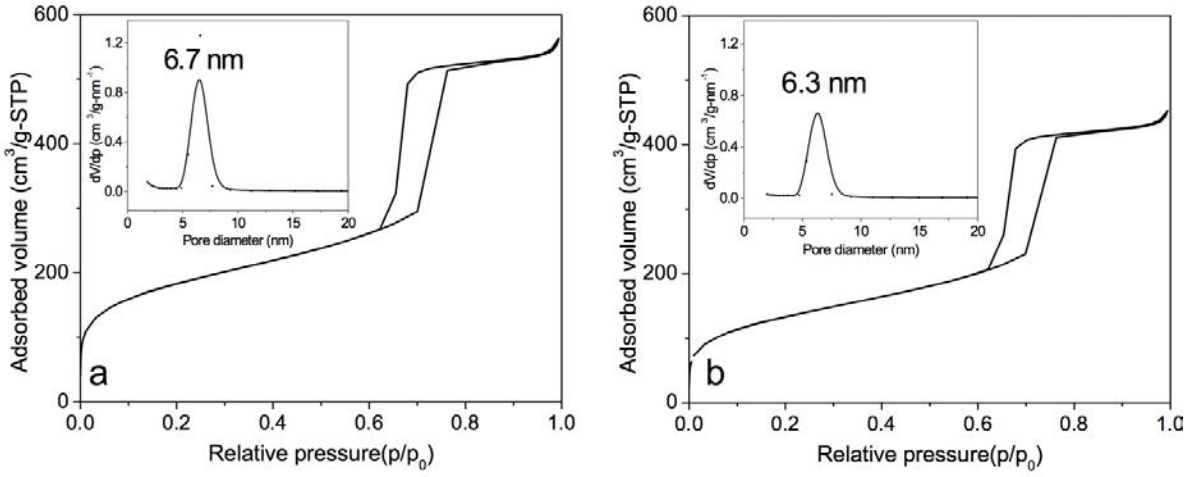

Figure 2.3.14. N_2 adsorption–desorption isotherms and pore size distribution (inset) of (a) SBA-15, (b) SBA-15-CU. The BET specific surface area and the mesopore volume are 638 m^2 g^{-1} and 0.91 cm^3 g^{-1} for (a) SBA-15, 461 m^2 g^{-1} and 0.70 cm^3 g^{-1} for (b) SBA-15-CU, respectively.

However, curcumin release from tannic acid-Fe(III) coated SBA-15 silica material (SBA-15-CU-TA) showed also pH-dependent release pattern, (Figure 2.3.17) while a burst release phenomenon for non-coated SBA-15 (SBA-15-CU) was observed, due to the large pores that provide high diffusion rate. Interestingly, cumulative release values (%) after 360 min are very close to those of coated MCM-41 silica nanoparticles, which suggest that the

decomposition process of tannic acid-Fe(III) complex is the crucial factor for the release of encapsulated molecules. As a result of curcumin release experiments, one can suggest that tannic acid-Fe(III) complex coating is a powerful method for controlling the release of encapsulated molecule, especially for bulky molecules in large pore system. Work is underway for the fine deposition of tannic acid-Fe(III) on spherical silica materials with large pore,[75] with potential applications in pharmaceutics for a controlled release of a enzymatic drug.

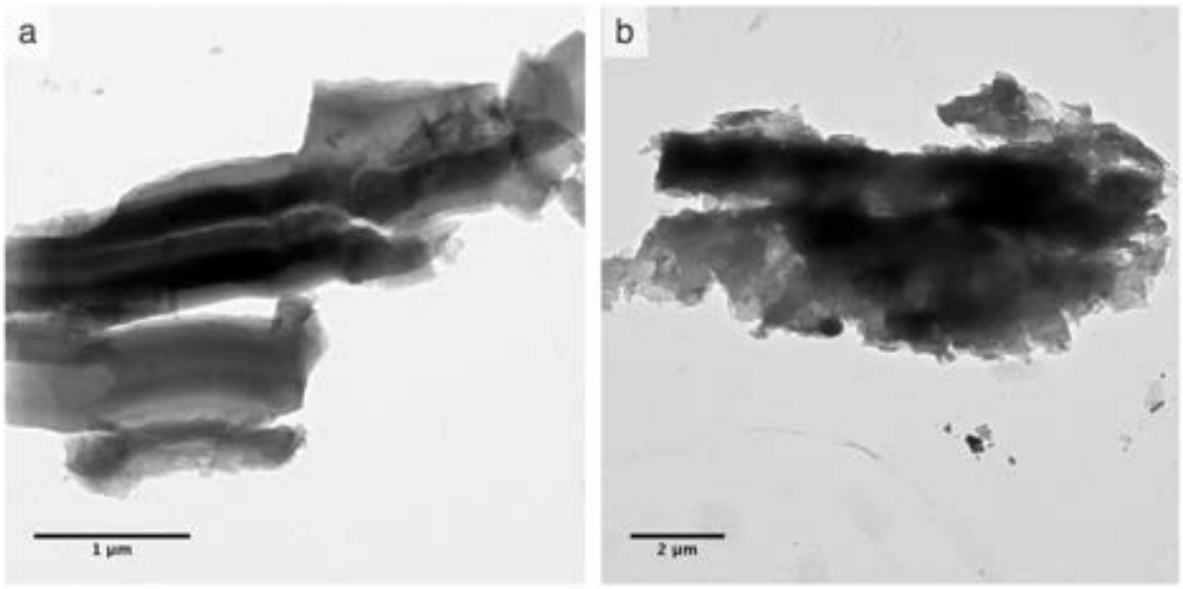

Figure 2.3.15. TEM image of (a) SBA-15, (b) SBA-15-CU-TA

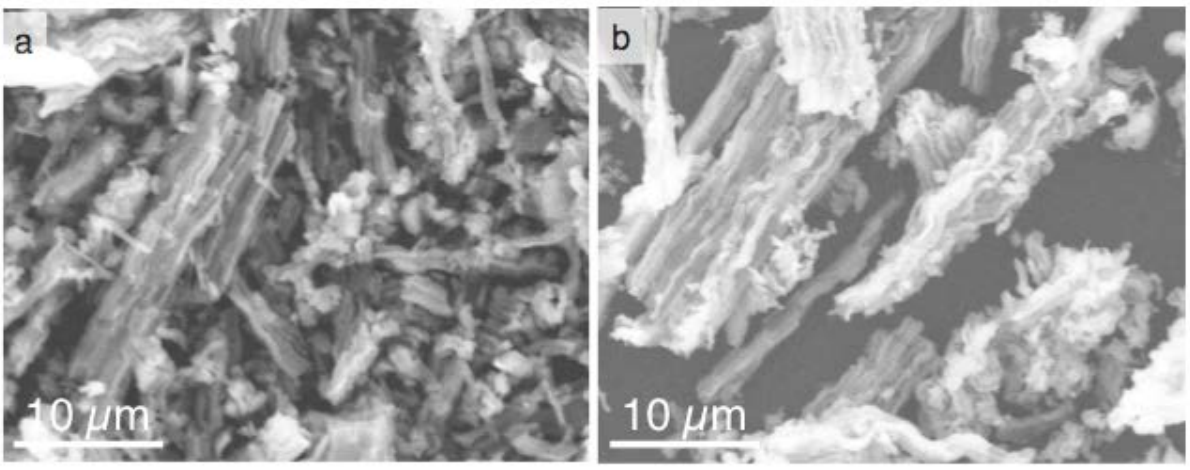

Figure 2.3.16. SEM image of (a) SBA-15, (b) SBA-15-CU-TA

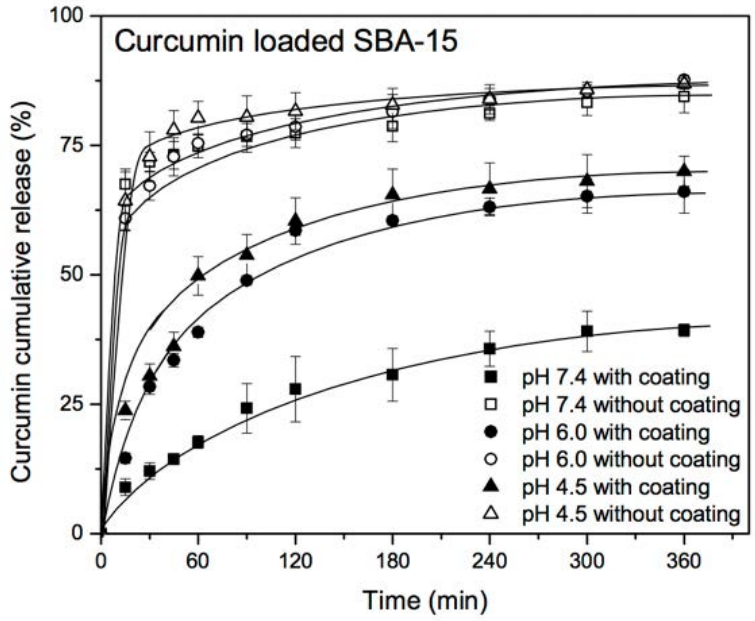

Figure 2.3.17. Cumulative release of curcumin for SBA-15-CU, and SBA-15-CU-TA

Cytotoxicity experiments

The impact of tannic acid coating of mesoporous silica nanoparticles on cell viability was tested with MRC5 cells. (Table 2.3.3) After 48 hours treatment MCM-41 and MCM-41-TA showed no cytotoxicity, meaning that addition of tannic acid-Fe(III) complex on mesoporous silica nanoparticles has negligible impact on cell viability. However, MCM-41-CU and MCM-41-CU-TA induced higher cytotoxicity compared to curcumin alone, which is also in good agreement with previous reported results.[35] As a result, mesoporous silica nanoparticles (MCM-41) coated with tannic acid-Fe(III) would have potential biomedical applications, due to their biocompatibility and bioinertness.

Sample	Curcumin	MCM-41	MCM-41-CU	MCM-41-CU-TA	MCM-41-TA
IC_{50} (μM)	> 150	> 150	22.1	20.2	> 150

Table 2.3.3. Half maximal inhibitory concentration (IC_{50}) of curcumin, MCM-41, MCM-41-CU, MCM-41-CU-TA and MCM-41-TA for the treatment of MRC5 cells (IC_{50} were calculated with respect to the same amount of silica as other materials)

2.3.4 Conclusion

It has been shown that pH-responsive curcumin-loaded mesoporous silica nanoparticles (MSN) were successfully prepared by deposition of tannic acid-Fe(III) complex on the surface of silica. Curcumin, a hydrophobic drug, was encapsulated into mesopores using simple rotary evaporation method, which prevent its crystallization inside pores. The deposition of tannic acid-Fe(III) complex on MSN resulted in multi-responsive drug delivery carrier, which triggers curcumin release upon the variation of pH or glutathione concentration level. Moreover, it was also demonstrated that the sustainability of drug release increased with the number of deposition layers of tannic acid-Fe(III) complex.

Therefore, using tannic acid-Fe(III) complex coating method is a straightforward way to design pH-responsive drug carrier with mesoporous silica materials, showing reduced burst release, improved stability, bioavailability. More important the release is triggered by glutathione, expressed in higher quantity in cancer cells, and by slightly acidic environment as in infected cells. This strategy could provide a general route for designing various systems, combining other stimuli-responsive nanocarriers[76] or sensors.[77] Moreover, due to good biocompatibility of tannic acid,[78] this method would be also useful in various applications such as designing drug delivery systems for *in vivo* biological experiments.[79]

References

1 P. Anand, C. Sundaram, S. Jhurani, A. B. Kunnumakkara and B. B. Aggarwal, *Cancer Letters*, 2008, **267**, 133–164.

2 J. Hintzpeter, J. Hornung, B. Ebert, H.-J. Martin and E. Maser, *Chemico-Biological Interactions*, 2015, **234**, 162–168.

3 T. Kawamori, R. Lubet, V. E. Steele, G. J. Kelloff, R. B. Kaskey, C. V. Rao and B. S. Reddy, *Cancer Res.*, 1999, **59**, 597–601.

4 R. Wilken, M. S. Veena, M. B. Wang and E. S. Srivatsan, *Molecular Cancer*, 2011, **10**, 12–18.

5 B. B. Aggarwal, A. Kumar and A. C. Bharti, *Anticancer Res.*, 2003, **23**, 363–398.

6 J. Bush, *Experimental Cell Research*, 2001, **271**, 305–314.

7 G. Bar-Sela, R. Epelbaum and M. Schaffer, *Curr. Med. Chem.*, 2010, **17**, 190–197.

8 Y. J. Wang, M. H. Pan, A. L. Cheng, L. I. Lin, Y. S. Ho, C. Y. Hsieh and J. K. Lin, *J Pharm Biomed Anal*, 1997, **15**, 1867–1876.

9 M. Bernabé-Pineda, M. T. Ramírez-Silva, M. Romero-Romo, E. González-Vergara and A. Rojas-Hernández, *Spectrochimica Acta Part A: Molecular and Biomolecular Spectroscopy*, 2004, **60**, 1091–1097.

10 M. J. Ansari, S. Ahmad, K. Kohli, J. Ali and R. K. Khar, *J Pharm Biomed Anal*, 2005, **39**, 132–138.

11 E. Pfeiffer, S. Höhle, A. M. Solyom and M. Metzler, *J. Food. Eng.*, 2003, **56**, 257–259.

12 S. Prasad, A. K. Tyagi and B. B. Aggarwal, *Cancer Res Treat*, 2014, **46**, 2–18.

13 S. Bisht, G. Feldmann, S. Soni, R. Ravi, C. Karikar, A. Maitra and A. Maitra, *J Nanobiotechnol*, 2007, **5**, 3–18.

14 Y. Chen, Q. Wu, Z. Zhang, L. Yuan, X. Liu and L. Zhou, *Molecules*, 2012, **17**, 5972–5987.

15 M. Gou, K. Men, H. Shi, M. Xiang, J. Zhang, J. Song, J. Long, Y. Wan, F. Luo, X. Zhao and Z. Qian, *Nanoscale*, 2011, **3**, 1558–1567.

16 P. R. K. Mohan, G. Sreelakshmi, C. V. Muraleedharan and R. Joseph, *Vibrational Spectroscopy*, 2012, 1–8.

17 V. R. Yadav, S. Prasad, R. Kannappan, J. Ravindran, M. M. Chaturvedi, L. Vaahtera, J. Parkkinen and B. B. Aggarwal, *Biochemical Pharmacology*, 2010, **80**, 1021–1032.

18 S. Jambhrunkar, S. Karmakar, A. Popat, M. Yu and C. Yu, *RSC Adv.*, 2014, **4**, 709–712.

19 B. Heurtault, *Biomaterials*, 2003, **24**, 4283–4300.

20 http://www.accessdata.fda.gov/scripts/cder/iig/index.Cfm

21 K. Jores, W. Mehnert, M. Drechsler, H. Bunjes, C. Johann and K. Mäder, *J. Controlled Release*, 2004, **95**, 217–227.

22 P. Khadka, J. Ro, H. Kim, I. Kim, J. T. Kim, H. Kim, J. M. Cho, G. Yun and J. Lee, *Asian J. Pharm. Sci.*, 2014, **9**, 304–316.

23 R. H. Müller, M. Radtke and S. A. Wissing, *Int. J. Pharm.*, 2002, **242**, 121–128.

24 M. Muchow, P. Maincent and R. H. Müller, *Drug. Dev.Ind. Phar.*, 2008, **34**, 1394–1405.

25 H .Ejima, J. J. Richardson, K. Liang, J. P. Best, M. P. van Koeverden, G. K. Such, J. Cui, and F. Caruso, *Science*, 2013, **341**, 154–157

26 R. Ravetti-Duran, J.-L. Blin, M.-J. Stébé, C. Castel and A. Pasc, *J. Mater. Chem.*, 2012, **22**, 21540.

27 A. Pasc, J.-L. Blin, M.-J. Stébé and J. Ghanbaja, *RSC Adv.*, 2011, **1**, 1204-1206.

28 J.-L. Blin, J. Jacoby, S. Kim, M.-J. Stébé, N. Canilho and A. Pasc, *Chem. Commun.*, 2014, **50**, 11871–11874.

29 J. L. Blin, R. Bleta, J. Ghanbaja and M. J. Stebe, *Microporous and Mesoporous Mater.*, 2006, **94**, 74–80.

30 M. H. M. Leung, H. Colangelo and T. W. Kee, *Langmuir*, 2008, **24**, 5672–5675.

31 M. Grare, M. Mourer, S. Fontanay, J.-B. Regnouf-de-Vains, C. Finance and R. E. Duval, *J. Antimicrob. Chemother.*, 2007, **60**, 575–581.

32 A. P. Nayak, W. Tiyaboonchai, S. Patankar, B. Madhusudhan and E. B. Souto, *Colloids Surf., B*, 2010, **81**, 263–273.

33 L. Hu, X. Tang and F. Cui, *J. Pharm. Pharmacol*, 2004, **56**, 1527–1535.

34 S. M. Martins, B. Sarmento, C. Nunes, M. Lúcio, S. Reis and D. C. Ferreira, *Eur J Pharm Biopharm*, 2013, **85**, 488–502.

35 R. Muller, *Eur. J. Pharm. Biopharm.*, 2008, **68**, 535–544.

36 D. Zhao, J. Feng, Q. Huo, N. Melosh, G. Fredrickson, B. Chmelka and G. Stucky, *Science*, 1998, **279**, 548–552.

37 D. Ke, X. Wang, Q. Yang, Y. Niu, S. Chai, Z. Chen, X. An and W. Shen, *Langmuir*, 2011, **27**, 14112–14117.

38 Z. Wang, M. H. M. Leung, T. W. Kee and D. S. English, Langmuir, 2010, **26**, 5520–5526.

39 R. K. Iler, The Chemistry of Silica, Wiley, 1979.

40 S. Ong, X. Zhao and K. B. Eisenthal, *Chem. Phys. Lett.*, 1992, **191**, 327–335.

41 P. B. Petersen and R. J. Saykally, *J. Phys. Chem. B*, 2006, **110**, 15037–15040.

42 J. P. O'Reilly, C. P. Butts, I. A. I'Anso and A. M. Shaw, *J. Am. Chem. Soc.*, 2005, **127**, 1632–1633.

43 K. Leung, I. M. B. Nielsen and L. J. Criscenti, *J. Am. Chem. Soc.*, 2009, **131**, 18358–18365.

44 T. Steiner, *Angew. Chem. Int. Ed. Engl.*, 2002, **41**, 49–76.

45 S. Gronert, *J. Am. Chem. Soc.*, 1993, **115**, 10258–10266.

46 Y. Gu, T. Kar and S. Scheiner, *J. Am. Chem. Soc.*, 1999, **121**, 9411–9422.

47 E. Zimmermann and R. H. Müller, *Eur. J. Pharm. Biopharm.*, 2001, **52**, 203-210.

48 P. Costa and J. M. Sousa Lobo, *Eur J Pharm Sci*, 2001, **13**, 123–133.

49 T. Mosmann, *J. Immunol. Methods*, 1983, **65**, 55–63.

50 Y. Zhang, J. Wang, X. Bai, T. Jiang, Q. Zhang and S. Wang, *Mol. Pharmaceutics*, 2012, **9**, 505–513.

51 Z. Zhao, Y. Gao, C. Wu, Y. Hao, Y. Zhao and J. Xu, *Drug. Dev. Ind. Phar.*, 2015, 1–10.

52 A. Lodha, M. Lodha, A. Patel, J. Chaudhuri, J. Dalal, M. Edwards and D. Douroumis, *J. Pharm. Bioall. Sci.*, 2012, **4**, 92–95.

53 P. Anand, A. B. Kunnumakkara, R. A. Newman and B. B. Aggarwal, *Mol. Pharmaceutics*, 2007, **4**, 807–818.

54 K.-Y. Yang, L.-C. Lin, T.-Y. Tseng, S.-C. Wang and T.-H. Tsai, *J. Chromatogr. B*, 2007, **853**, 183–189.

55 S. Kim, M.-J. Stébé, J.-L. Blin and A. Pasc, *J. Mater. Chem. B*, 2014, **2**, 7910–7917.

56 E. Borenfreund, H. Babich and N. Martin-Alguacil, *Toxicol In Vitro*, 1988, **2**, 1–6.

57 S. Kim, P. Durand, T. Roques-Carmes, J. Eastoe and A. Pasc, 2015, **31**, 1842–1849.

58 M. Feldman and C. Barnett, *Digest Dis Sci*, 1991, **36**, 866–869.

59 Y. Sambuy, I. De Angelis, G. Ranaldi, M. L. Scarino, A. Stammati and F. Zucco, *Cell Biol Toxicol*, 2005, **21**, 1–26.

60 http://www.fda.gov/downloads/drugs/guidance/ucm070246.pdf

61 Q. He, Z. Zhang, Y. Gao, J. Shi and Y. Li, *Small*, 2009, **5**, 2722–2729.

62 R. K. Gangwar, G. B. Tomar, V. A. Dhumale, S. Zinjarde, R. B. Sharma and S. Datar, *J. Agric. Food Chem.*, 2013, 130926133947000–6.

63 K. Engin, D. B. Leeper, J. R. Cater, A. J. Thistlethwaite, L. Tupchong, and J. D. McFarlane, *Int. J. Hyperthermia*, 1995, **11**, 211–216.

64 R. Liu, Y. Zhang, X. Zhao, A. Agarwal, L. J. Mueller, and P. Feng, *J. Am. Chem. Soc.*, 2010, **132**, 1500–1501.

65 J. E. Lee, D. J. Lee, N. Lee, B. H. Kim, S. H. Choi and T. Hyeon, *J. Mater. Chem.*, 2011, **21**, 16869– 16872.

66 A. M. Schrand, M. F. Rahman, S. M. Hussain, J. J. Schlager, D. A. Smith, and A. F. Syed, *Wiley Interdiscip. Rev.: Nanomed. Nanobiotechnol.*, 2010, **2**, 544–568

67 Q. Cai, Z.-S. Luo, W.-Q. Pang, Y.-W. Fan, X.-H. Chen, and F.-Z. Cui, *Chem. Mater.*, 2001, **13**, 258–263.

68 M. Metzler, E. Pfeiffer, S. I. Schulz, J. S. Dempe, *Biofactors*, 2013, **39**, 14-20.

69 S. Jambhrunkar, Z. Qu, A. Popat, J. Yang, O. Noonan, L. Acauan, Y. Ahmad Nor, C. Yu and S. Karmakar, *Mol. Pharmaceutics*, 2014, **11**, 3642–3655.

70 H. Ozawa and M.-A. Haga, *Phys. Chem. Chem. Phys.*, 2015, **17**, 8609–8613

71 M. A. Rahim, H. Ejima, K. L. Cho, K. Kempe, M. Müllner, J. P. Best, and F. Caruso, *Chem. Mater.*, 2014, **26**, 1645–1653.

72 A. N. Koo, H. J. Lee, S. E. Kim, J. H. Chang, C. Park, C. Kim, J. H. Park and S. C. Lee, *Chem. Commun.*, 2008, 6570–3.

73 Y. Cui, H. Dong, X. Cai, D. Wang and Y. Li, *ACS Appl. Mater. Interfaces*, 2012, **4**, 3177–3183.

74 N. Spear and S. D. Aust, *Arch. Biochem. Biophys*. 1994, **312**, 198–202

75 N. Canilho, A. Pasc, M. Emo, M.-J. Stébé and J.-L. Blin, *Soft Matter*, 2013, **9**, 10832.

76 D. Hua, J. Jiang, L. Kuang, J. Jiang, W. Zheng and H. Liang, *Macromolecules*, 2011, **44**, 1298–1302.

77 L. V. Sigolaeva, S. Y. Gladyr, A. P. H. Gelissen, O. Mergel, D. V. Pergushov, I. N. Kurochkin, F. A. Plamper and W. Richtering, *Biomacromolecules*, 2014, **15**, 3735–3745.

78 X. Zhang, M. Liu, X. Zhang, F. Deng, C. Zhou, J. Hui, W. Liu and Y. Wei, *Toxicol. Res.*, 2015, **4**, 160–168.

79 X. Chen, X. Cheng, A. H. Soeriyadi, S. M. Sagnella, X. Lu, J. A. Scott, S. B. Lowe, M. Kavallaris and J. J. Gooding, *Biomater. Sci.*, 2014, **2**, 121–130.

Résumé en français (chapitre 2)

La curcumine, un polyphénol naturel hydrophobe de couleur jaune qui est extrait à partir de la racine de curcuma séchée, le rhizome de la plante *Curcuma longa*, a été utilisée pendant des siècles dans la médecine indigène comme anti-inflammatoire et anti-oxydant.[1] La curcumine a des propriétés liés au pharmacologiques pour des problèmes cardiovasculaires, pulmonaires, auto-immunes ainsi que pour maladies métabolisme.[2] Son utilisation potentielle la plus intéressante est probablement celle qui permettrait de soigner des cancers.[3,4] Des études précliniques ont montré que la curcumine peut inhiber la genèse des cancers dans une variété de lignées cellulaires. (sein, côlon gastrique, hépatique, épithéliale orale, ovaires, pancréas, prostate et leukemia[5]) En outre, il a été montré que la curcumine a provoqué la mort cellulaire dans huit lignées de cellules de mélanome, également dans celles portant les p53 mutants, qui sont très résistantes à la chimiothérapie conventionnel.[6] Cependant, l'utilisation de la curcumine a été limitée en raison de sa faible solubilité en milieu aqueux.[7] En effet, la curcumine a une très faible solubilité dans la gamme de pH 1,2 à 7,4, qui sont des valeurs de pH physiologiques du corps humain, et dans des conditions alcalines la curcumine subit une hydrolyse rapide, en étant décomposée en acide férulique, son ester méthylique et en vanillin.[8,9] La curcumine est également très sensible à la dégradation photochimique et thermique qui est un problème pour son stockage de longue durée.[10,11] En outre, certaines études ont révélé que sa mauvaise absorption et son métabolisme rapide réduisent considérablement sa biodisponibilité.[12]

Ces obstacles peuvent être dépassés en incorporant la curcumine dans des nanoparticules, des liposomes[13,14] des micelles,[15] des complexants à base de cyclodextrines (CD) en solutions aqueuses,[16,17] ou dans des silices mésoporeuse.[18] Cependant, les transporteurs de médicaments à base de matières organiques sont susceptible d'être sans traitement post-synthèse comme par exemple le revêtement de surface. En outre, dans certains cas, une perte de principe actif pendant le stockage pourrait être possible, limitant ainsi l'application de ces vecteurs.[19]

Dans ce chapitre, pour la conception de des systèmes stimuli-sensibles, deux approches ont été testées: 1) mise au point de silices poreuses en utilisant des nanoparticules solides lipidiques (SLN) et 2) développement d'une méthode pour le revêtement de surface de la silice mésoporeuse à l'aide d'un complexe acide tannique-Fe(III).

Tout d'abord, des matériaux hybrides de silice méso- méso-macroporeuses qui contiennent la curcumine ont été préparés à partir de nanoparticules lipidiques solides (SLN). La libération de la curcumine a montré une forte dépendance en fonction du pH. En plus, une libération en deux étapes a été observée à pH 1,2 pour le matériau préparé avec des SLN à base d'acide stéarique, suggérant que les SLN sont des réservoirs pour le principe actif, tandis que les canaux mésoporeux permettent la libération du principe actif. La cytotoxicité a montré que ces matériaux pourraient avoir des applications dans le domaine biomédical avec une bonne biocompatibilité.

Cette méthode a été étendue pour développer des microcapsules hybrids à base de silice '*core-shell'*. Ces matériaux ont montré une dépendance vis à vis du pH pour la libération de la curcumine avec une rétention marquée à pH 2,8, en raison de l'agrégation des particules de silice, du fait que le point isoélectrique de la silice est compromis entre 2 et 3. En plus, le test d'absorption cellulaire a montré que les microcapsules hybrides ont été bien internalisés dans les cellules Caco-2, suggérant de véritables applications potentielles dans le domaine.

En suite, les matériaux silicatés mésoporeux multi stimuli-sensibles ont été développés pour le traitement de tissus cancéreux. Pour cet objectif, une méthode de revêtement en utilisant des complexes l'acide tannique-Fe(III) a été mise en œuvre par addition successive de Fe(III) et d'acide tannique dans la dispersion de silice mésoporeuse chargée en curcumine. Une légère baisse du pH peut déclencher une libération rapide de la curcumine et cette libération peut être contrôlée par la concentration de glutathion (GSH). De ce fait, ces résultats ouvrent une nouvelle voie simple pour développer des systèmes de délivrance de médicaments.

Chapter 3

Magneto-responsive silica materials templated with magneto-responsive surfactants

Although the surfactants containing metal ions have been developed since more than 10 years, their magnetic properties have not been well investigated.[1] One of the most probable reason is that these surfactants have metal ions in their head group, but stabilized by cleating of ligands. Due to their molecular structure, the metal ions in such compounds were isolated, lacking long-range interactions and communication necessary to be magnetically active. [2]

In the ionic liquid field, metal containing ionic liquids (MIL), which combine the general properties of room temperature ionic liquids (RTIL) with those associated with metal ions such as strong responsiveness to an external magnetic field, have also been frequently reported. [3] However, most of reported MILs are limited to derivatives of imidazolium containing short alkyl chain, which exhibit no significant properties related to surfactants.

However, the main breakthrough has come from Eastoe group in UK, which combines advantageous properties of each system, metal containing ionic liquids (MILs) and conventional surfactants containing metal ions.[4] *Eastoe et al*. demonstrated, for the first time, ionic liquid surfactants containing magneto-active metal complex ions such as 1-methyl-3-decylimidazolium tetrachloroferrate. The synthesis of the magnetic ionic liquid surfactants (MILS) could be easily achieved by mixing an iron trihalide with stoichiometric amount of cationic surfactant. MILS showed their critical micelle concentrations (cmc) that are comparable to their original surfactants because tetrahalideferrate anions are not tightly associated to head group of surfactants, showing increased the degree of dissociation. Their shapes in micelles are also very similar to their original surfactants, however no inter-micelles was founded due to bulky tetrahalideferrate anions. Indeed, These MILS are interesting as they are molecular liquids, rather than typical magnetic fluids (ferrofluids), which consist of metallic colloidal particles (10 nm) dispersed in a carrier fluid. Interestingly, MILSs retain a magnetic response even in dilute aqueous solution.

Concerning magnetic properties, the effective magnetic moments (u_{eff}) of iron based magnetic ionic liquid surfactants, represented by $g[S+(S+1)]1/2u_B$, were estimated to be the range of 5.66 – 5.89 u_B at 25°C, which are close to that expected for a paramagnetic S = 5/2 high-spin of Fe(III) ions (spin-only value: 5.92 u_B). The MILS exhibits more effective ability for lowering surface tension compare to parent surfactants, even in the absence of an applied field. Moreover, when magnetic applied like using a magnet in close proximity to aqueous solutions of the MILS, the reduction of surface tension is more pronounced, proposing dual functionalities of these surfactants.

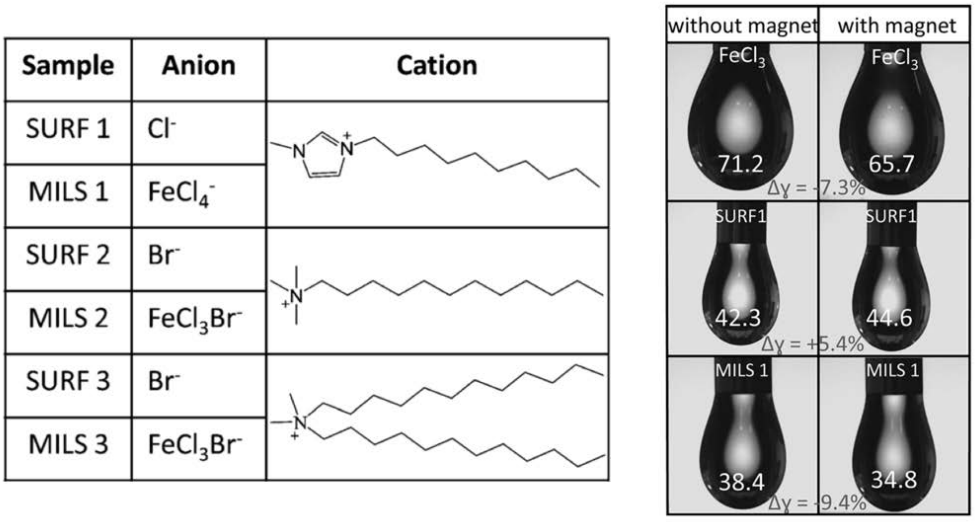

Figure. 3.1 Some example of conventional surfactants (SURF) and their magnetic surfactants (MILS) (left); Response of liquid droplets to the field from a 0.4 T NdFeB magnet. [SURF1]=20 wt%, [MILS1]=20 wt% (right)

As application of MILS, magnetic emulsions could be prepared, which previously had only been realized with nanoparticle-stabilized Pickering type emulsions. Oil-in-water magnetic emulsions prepared from MILS and brine suggest also applications outside of the laboratory, involving environmental clean up and nanomedicine,[5] Magnetic microemulsions using magnetic anionic surfactants were also reported by the same group. Interestingly, these microemulsions exhibit superparamagnetism with effective magnetic moments far above those expected for the solid surfactant. This behaviour arises from the fact that surfactant molecules are partitioned at the water-oil interface, giving only surface anisotropy rather than bulk anisotropy, which is generally observed as solid state of surfactants. By tailoring of size and magnetic properties of these emulsions, it should be possible to bridge the gap between magnetic nanoparticles (minimum size ~400 metal centres) and molecular magnets (maximum size ~20 metal centres).[6]

In this chapter, for designing magneto-responsive silica materials, a new approach using magneto-responsive surfactants will be discussed. First, the synthesis of various magneto-responsive surfactants and their application as magnetic probe for the investigation of self-assembly behaviour such as vesicles formation will be discussed. Then, the synthesis and the magnetization of porous silica material using only magneto-responsive surfactant will be investigated. Then, this magneto-responsive surfactant will be combined with solid lipid nanoparticles (SLN) for the preparation of hierarchical meso-macroporous silica materials

with iron oxide nanoparticles inside. The applications of these resulting materials in various domains including the catalysis will be highlighted.

Part 3.1

Spin crossover as a probe of self-assembly phenomenon of vesicle obtained using magneto-responsive surfactants

This part was submitted as: S. Kim, C. Bellouard, J. Eastoe, S. E. Rogers, N. Canilho, A. Pasc, Spin crossover as a probe of vesicle self-assembly in *J. Am. Chem. Soc.*

3.1.1 Introduction

In recent years, vesicles have been widely studied for potential applications in diverse fields such as biomedicine,[7-10] catalysis[11-13] and cosmetics.[14] Vesicles are spherical self-assembly systems, consisting of lipid bilayer membranes enclosing internal aqueous compartments. Since vesicles are structurally similar to biological membranes, they are considered as cell mimics.[15] Furthermore, vesicles are employed to encapsulate drugs, fragrances or flavors for controlled release. Functional vesicles that respond to external stimuli such as temperature,[16] pH,[17,18] redox,[19,20] and magnetic field grandient[21-23] have widely been studied as drug nanovectors. In terms of triggerable systems, magnetic vesicles have been of significant interest because magnetic properties can be beneficial in applications like magnetic resonance imaging (MRI) or hyperthermia as well as spatial and temporal drug targeting.[24,25]

To generate magnetic vesicles two approaches have been used to date: firstly, loading magnetic nanoparticles in the hollow vesicle cavities[26-28]; and secondly, embedding nanoparticles in the bilayers.[29,30] An alternative strategy is employed here, by introducing magnetic surfactants or lipids in the bilayers.

Recently, magneto-responsive surfactants (MagSurfs)[4] have been introduced opening up a range of interesting magnetic colloidal systems such as micelles,[31] emulsions,[6] solid lipid nanoparticles,[32] organosols[33] or magnetized DNA.[34] These MagSurfs have also been used as structure directing agents for synthesis of magnetic mesoporous silica materials.[35]

In this part, it is demonstrated, new paramagnetic vesicles that can be readily generated from ion pairs of anionic and cationic iron-surfactants. Exploiting the paramagnetic properties Fe^{3+}, it is possible to investigate more accurately the self-assembly of surfactant ion pairs into vesicles and to give a clear picture of the partitioning between vesicles and bulk.

3.1.2 Experimental section

Chemicals

Dodecyltrimethylammonium bromide (DTAB), sodium bis(2-ethylhexyl) sulfosuccinate (NaAOT), iron (III) nitrate anhydride ($Fe(NO_3)_3$), and deuterium oxide (D_2O) were purchased from Sigma-Aldrich. Iron (III) chloride ($FeCl_3$) was purchased from Alfa Aesar. Water was

deionized and purified using a Milli-Q pack system. All reagents were used without further purification.

Synthesis of magnetic surfactant AOT_3F ($(C_{20}H_{37}O_7S)_3Fe$)

250 mL of a saturated aqueous solution of the iron (III) nitrate anhydride was filtered and added to 125 mL of 1.0 mol L^{-1} of NaAOT (sodium bis(2-ethylhexyl) sulfosuccinate) solution prepared in absolute ethanol. 50 mL of diethyl ether was added to the mixture, and then the lower aqueous phase containing excess of iron (III) nitrate was removed. The organic solvent was evaporated using a rotary evaporator and then, the surfactant AOT_3F was dried in vacuo at 60°C for 24 h.

Synthesis of magnetic surfactant DTAF ($CH_3(CH_2)_{11}N(CH_3)_3FeCl_3Br$)

1.63 g of $FeCl_3$ (10.1 mmol) was added to 3.10 g of DTAB (11.0 mmol) that was already dissolved in 50 mL of methanol. Then, the solution was heated to reflux overnight. The methanol was evaporated using a rotary evaporator and then, the surfactant DTAF was dried in vacuo at 60°C for 24 h.

Preparation of magnetic vesicles

Magnetic vesicle solutions were prepared by mixing the magnetic surfactants in D_2O at room temperature under vortex stirring, if necessary. Briefly, 28.1 mg of AOT_3F and 34.2 mg of DTAF were dissolved in 4 mL of D_2O and this solution was denoted as A-series (molar ratio of DTAF/AOT_3F is 3.7). Another vesicle solution was prepared by dissolving 15.0 mg of AOT_3F and 37.0 mg of DTAF in 5 mL of D_2O, which is denoted as B-series (molar ration of DTAF/AOT_3F is 7.8). Vesicle solutions were kept at 25°C for 2 h before further analysis.

Small-Angle Neutron Scattering (SANS)

Scattering was measured on the LOQ and SANS2D diffractometers at the ISIS Facility, Rutherford Appleton Laboratory, United Kingdom. LOQ and SANS2D are both time-of-flight instruments. SANS2D uses neutrons with an incident wavelength of 2.2 Å < λ < 14 Å, and with the 1 m^2 detector offset sideways and vertically by 150 mm, the resulting q range

was 0.006 $Å^{-1}$ < q < 0.7 $Å^{-1}$ For LOQ the incident wavelengths were 2.2 Å < λ < 10 Å, giving 0.006 $Å^{-1}$ < q < 0.24 $Å^{-1}$. Appropriate normalization using site-specific procedures gave the absolute cross section I(q) (cm^{-1}) as a function of the momentum transfer q ($Å^{-1}$). The vesicles samples were placed in Hellma fused silica cuvettes with a path length of 2 mm, which allows an incident beam diameter of 12 mm (on SANS2D and 8 mm LOQ). Raw SANS data were treated by subtracting the scattering of the empty cell and the solvent using appropriate transmission measurements. Any low level of residual incoherent scattering was accounted by a flat background term during the fitting process. Data analyzed were in absolute units, with the scale factors being consistent with expectations based on the sample compositions.

SANS Scattering Laws and Model Fitting

Scattered intensity I(q) is a product of the size and shape of the aggregates (form factor, P(q)) and the interaction between these aggregates (structure factor, S(q)),

$$I(q) \propto P(q,R)S(q)$$

where R is the particle radius.

The vesicle solutions were fitted using the program Sasview using the VesicleModel.

The VesicleModel provides the form factor, P(q), for an unilamellar vesicle. The form factor is normalized by the volume of the shell.

The 1D scattering intensity is calculated in the following way:

$$P(q) = \frac{scale}{V_{shell}}\left[\frac{3V_1(\rho_1-\rho_2)J_1(qR_1)}{qR_1} + \frac{3V_2(\rho_2-\rho_{solv})J_1(qR_2)}{qR_2}\right]^2 + bkg$$

where scale is a scale factor, V_{shell} is the volume of the shell, V_1 is the volume of the core, V_2 is the total volume, R_1 is the radius of the core, R_2 is the outer radius of the shell, ρ_1 is the scattering length density of the core and the solvent, ρ_2 is the scattering length density of the shell, and bkg is the background level, and $J_1 = (sinx - xcosx)/x^2$). The functional form is identical to a "typical" core-shell structure, except that the scattering is normalized by the volume that is contributing to the scattering, namely the volume of the shell alone. Also, the vesicle is best defined in terms of a core radius (= R_1) and a shell thickness, t.

In this model, the adjustable parameters in the model are thickness (t), core radius of the shell (R_1).

Magnetic measurements

Magnetic measurements have been performed with a Physical Properties Measurements System (PPMS) from Quantum Design equipped with ACMS option, and using a sample holder provided for liquids. All measurements have been made with the same heavy water solutions as SANS. The signal contribution of sample holder and heavy water have been measured in the same conditions as the solutions, it is purely diamagnetic and has been systematically subtracted. A remaining diamagnetic contribution arising from the surfactants is taken into account in the fitting procedure. All samples have been introduced directly at 60K in the sample chamber, and temperature measurements have been performed between 60K and 2K under several applied fields with decreasing and increasing temperature at 0.5 K / min. No discrepancies have been observed between both measurements for A- and B-series.

3.1.3 Results and Discussion

Magnetic surfactant and their vesicle formation.

The necessary Fe^{3+} MagSurfs can be prepared from conventional surfactants, cationic dodecyltrimethylammonium bromide (DTAB) and anionic sodium bis(2-ethylhexyl) sulfosuccinate (AOT) to afford DTAF and AOT_3F respectively. The behavior of these MagSurfs (AOT_3F, DTAF) is a little different from the parent surfactants. The single chain surfactnat, DTAF has a critical micelle concentration (CMC) of 13.6 mM at 25°C, which is similar to that of DTAB (15.5 mM).[4] However, its melting point decreases from 246°C to 32°C. Critical micelle concentration of AOT_3F is of 2.2 mM (with respect to AOT moiety), which is also close to CMC of the parent surfactant, AOT (~2.5 mM).[36]

Gentle mixing of two surfactants at a certain ratio r ($r = n_{DTAF} / n_{AOT3F}$ = 3.7 (series Ax) or 7.8 (series Bx)) in a certain concentration range (Table 3.1.1) spontaneously results in magnetic vesicles of about 200 nm in diameter, as determined by dynamic light scattering (DLS) measurements and nanoparticle tracking analysis (NTA).

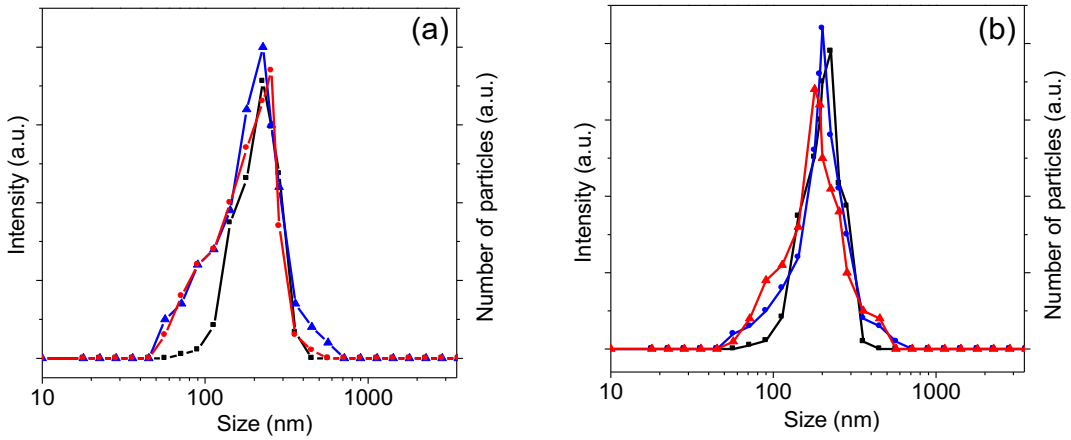

Figure 3.1.1. Size distribution of MagSurf vesicles measured for A1 (a) and B1 (b), using DLS (black, ■), NTA (blue, ▲), and NTA with fluorescence filter (red, ●).

As shown in Figure 3.1.1, the vesicle size distributions do not seem to depend on the composition ratio r. Moreover, the use of a fluorescence filter with NTA allows detection of fluorescent aggregates containing iron ions (Figure 3.1.2). This is the direct proof that the iron counterions are in the vesicle hydration shells.

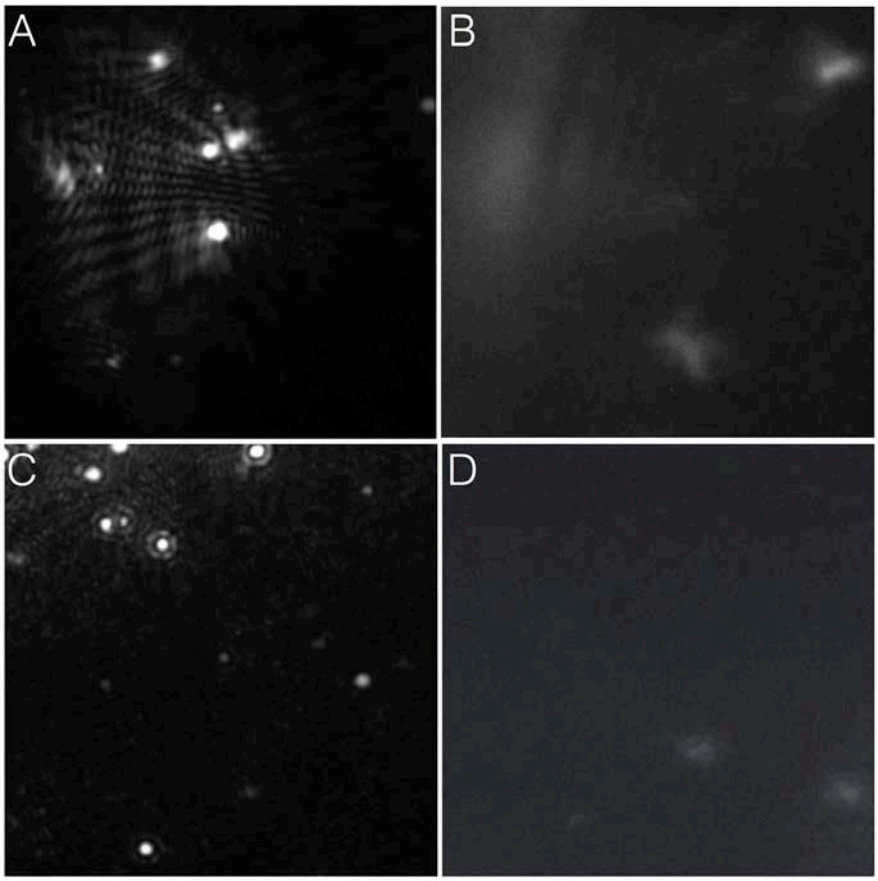

Figure 3.1.2. Captured image of NTA for (A) vesicle A1, (B) vesicle A1 with fluorescence filter, (C) vesicle B1, and (D) vesicle B1 with fluorescence filter.

The structures of these magnetic vesicles were also investigated using small-angle neutron scattering (SANS). Vesicle samples were prepared in D_2O in order to enhance the neutron scattering contrast. Shown in Figure 3.1.3 (a) and (b) are absolute SANS intensities I(q) for the Ax and Bx series as a function of scattering vector q, the curves have also been normalized with respect to the total surfactant concentration C_T (Table 3.1.1). For the A1 to 3 and B1 to 2 samples, the low q regions exhibit clear q^{-2} decays, which is a general feature of SANS from locally planar surface structures, such as bilayers or vesicles.[37] In addition, the normalized SANS data for A1 to 3 (Figure 3.1.3(a)) and B1 to 2 (Figure 3.1.3(b)) show a common q dependence; indicating that the vesicles have similar, concentration-independent structures. The SANS data were fitted using a non-interacting polydisperse vesicle form factor model (programme Sasview,[38] HardsphereStructure for P(Q)*S(Q)). The I(q) profiles from all samples A1 to 3, B1 to 2 are well described by this model, as illustrated in Figure 3.1.3(c) for A1 and B1.

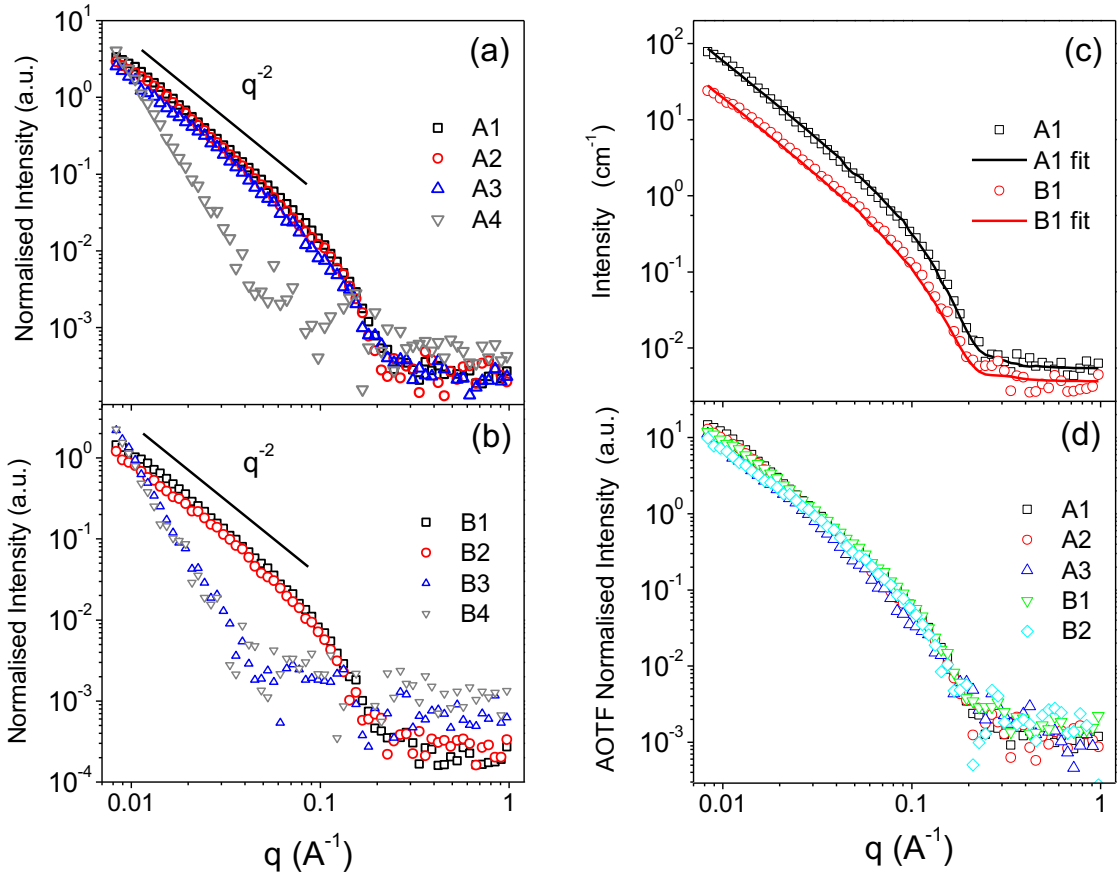

Figure 3.1.3. Small-angle neutron scattering data normalized to total molar MagSurf concentration for (a) Ax, (b) Bx, (c) fitted data for A1 and (d) B1, normalized SANS data with respect to AOT_3F concentration for A1-3 and B1-2

The shell thicknesses τ were approximately 2.5 nm. The fitted values for τ suggest the vesicles are unilamellar, since 2.5 nm corresponds about 2 × C12 alkyl chain lengths. All parameters deduced from DLS and SANS are very similar for the A and B series. (Table 3.1.1) Moreover, the concentration-normalized absolute I(q) superimpose as a function of AOT concentration (Figure 5.3(d)). This shows that the vesicles are not affected by the ratio r, and that vesicle concentration is proportional to AOT concentration for both r ratios. The abrupt change in I(q) observed between A3 and A4 (Figure 5.3(a)) and between B2 and B3 (Figure 5.3(b)) indicates a transition from vesicles towards less well-defined aggregates on dilution. The critical vesicle concentrations (CVCs) can be estimated from these dilution series of I(q): CVC is between 5.4 mM and 2.7 mM (1.16 and 0.58 mM AOT_3F) for the DTAF/ AOT_3F ratio r of 3.7 and between 7.6 mM and 3.8 mM (0.87 and 0.43 mM AOT_3F) for DTAF/ AOT_3F for r = 7.8.

Solution	r[a]	C_T [b]	C_{AOTF}[c]	$f_{5/2}$ [d]	θ (K)
A1	3.7	21.6	4.63	90	-1.1
A2	3.7	10.8	2.31	87	-1.0
A3	3.7	5.4	1.16	89	-1.2
A4	3.7	2.7	0.58	67	-0.9
B1	7.8	15.3	1.74	60	-1.4
B2	7.8	7.6	0.87	60	-1.2
B3	7.8	3.8	0.43	40	-0.2 ± 0.1
B4	7.8	1.9	0.22	23	0

Table 3.1.1. Compositions of the A and B series of MagSurf solutions and parameters deduced from fits of SANS data and magnetization measurements; [a] r is the DTAF/ AOT_3F molar concentration ratio. [b] C_T is the sum of the surfactant molar concentrations expressed in mM. [c] C_{AOTF} is the molar concentration of AOT_3F expressed in mM. [d] **Φ** is the vesicle diameter in nm. deduced from SANS. [d] $f_{5/2}$ is the proportion of S=5/2 (expressed in %) deduced from the fit of M(T, H = 5 kOe).

On the other hand, the critical aggregation concentration (CAC) was estimated using surface tension measurements (Figure 3.1.4). The CAC value, expressed as a function of AOT_3F concentration, is found identical for both DTAF/AOT_3F ratios: about 1.5 10^{-2} mM which corresponds to a total surfactant concentration of 7.10^{-2} mM for r =3.7; and about 0.13 mM for r =7.8.

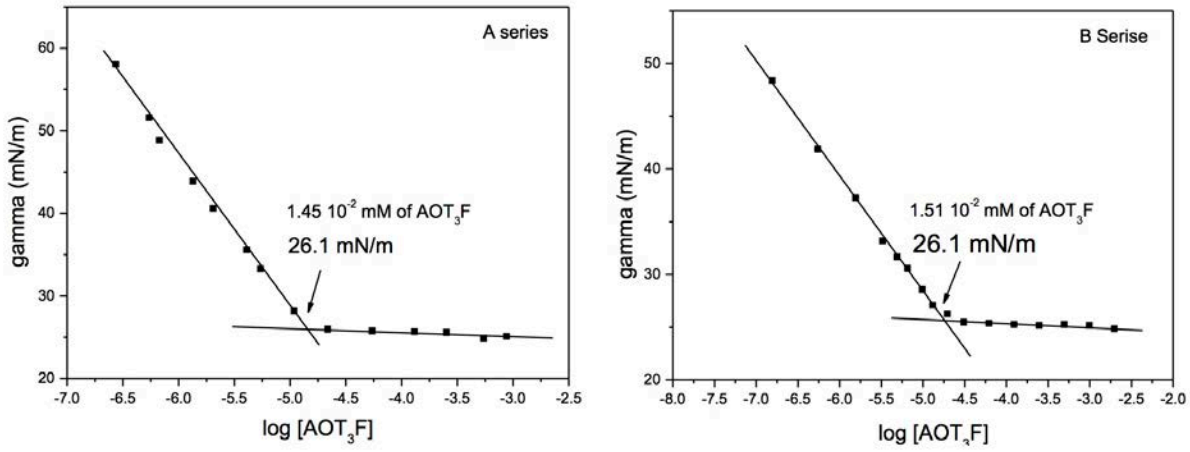

Figure 3.1.4. Critical aggregation concentration (CAC) of vesicle solutions determined using Surface tension measurements.

Magnetic measurements

All these results above suggest that the self-assembly mechanism of AOT_3F and DTAF ion pairs involves a transition from mixed aggregates of floppy bilayer membranes to vesicles. This behavior was already observed for catanionic surfactants that also undergo vesicle formation.[39,40] However, to date no clear evidence of the composition of the vesicle bilayers as well as on the distribution of the surfactants between the bilayers and the bulk has been presented. This is done here, by taking advantage of the paramagnetic properties of these MagSurfs: magnetic measurements were performed at low temperature.

Figure 3.1.5(a) and (b) present the temperature dependence of magnetization measured in an applied field of 70 kOe for the A and B series respectively. Interestingly, these curves exhibit qualitative behaviour which correlates with the SANS data (Figures 5.3(a) and (b)): magnetization of A1-3 and B1-2 reported per Fe weight are almost superimposed as were SANS data, whereas a notable decrease is clearly observed on further dilution, from A3 to A4, and B2 to B3, as the vesicles are disrupted. Moreover, the measured magnetization at low temperature of A1-3 (≈ 420 emu/g) is quite closed to the saturation magnetization of Fe^{3+} ions with S=5/2 ($M_s^{5/2} = 500$ emu/g_{Fe}) whereas it is much lower for B1-2 (≈ 300 emu/g), which has a lower vesicle concentration. The decrease in signal observed after vesicle breakup (from A3 to A4, or B2 to B3) or with decreasing vesicle concentration (from A1-3 to B1-2) is attributed to a Fe^{3+} spin crossover from high spin (5/2) to low spin state (1/2).

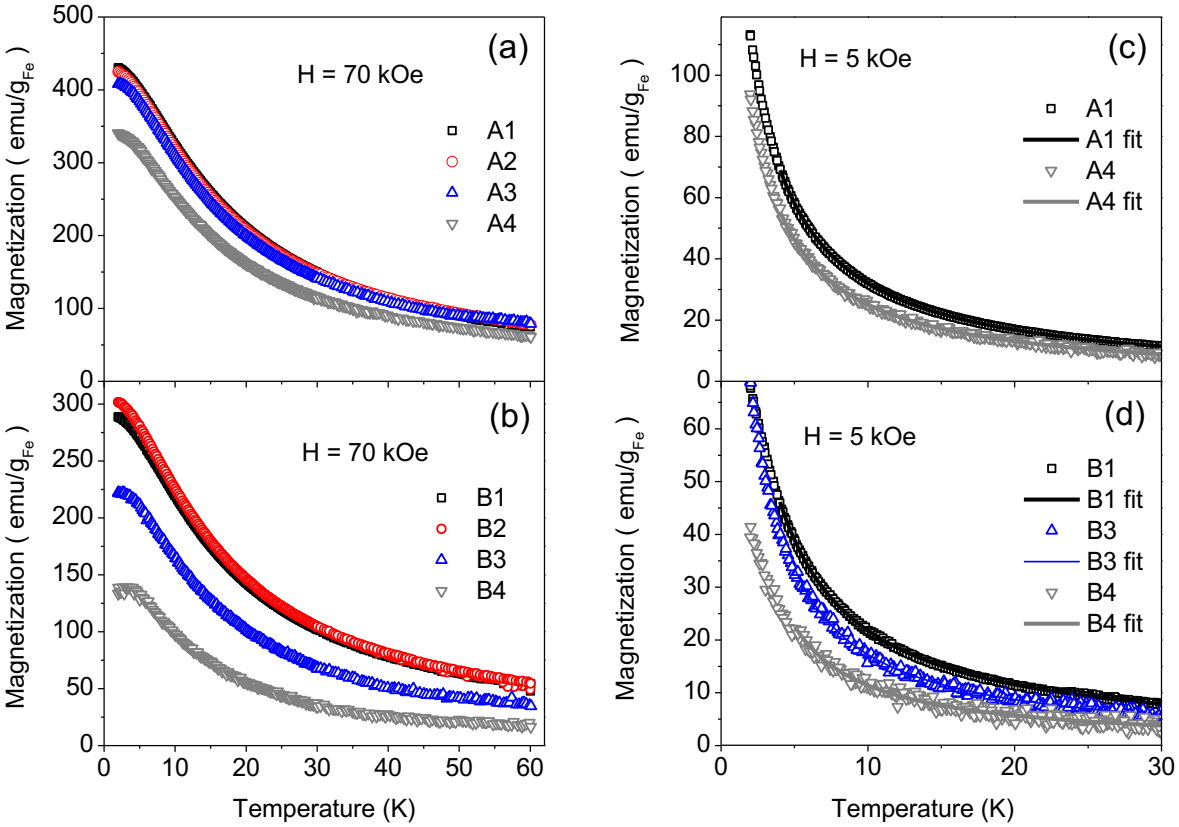

Figure 3.1.5. Magnetization measurements as a function of temperature measured at 70 kOe for (a) A1-4, (b) B1-4 (b) and at 5 kOe for (c) A1&4, (d) B1&3-4. The straight lines in figures (c) and (d) are fits with a sum of two Brillouin functions as described in the text.

To get the fraction of high spins with respect to low spins, the low field (H= 5 kOe) temperature magnetization has been fitted with the contribution of two Brillouin functions as follow.

$$M(H,T) = f_{5/2}\, M_s^{5/2}\, B_{5/2}\,(H, T-\theta) + \left(1 - f_{5/2}\right) M_s^{1/2}\, B_{1/2}\,(H,T) + d(H)$$

$f_{5/2}$ is the fraction of spin 5/2, M_s^x is the saturation magnetization of spin x, $B_x(H,T)$ is the Brillouin function, for S = 5/2, θ is introduced to take into account spin-spin interactions. *d(H)* corresponds the diamagnetic contribution which is temperature independent. The measured magnetization has been corrected for this contribution and plotted in Figure 3.1.5. An additional spin crossover at low temperature (≤ 5 K) is indeed present, as clearly observed in the high field measurements for sample B4 (Figure 3b). As a consequence, to obtain reliable parameters, fitting has been limited to the 4K -60K temperature range for Ax and B1-2, and to 5K - 60K for B3-4. The fitting parameters, $f_{5/2}$ and θ, are reported in Table 3.1.1.

The θ value is close to -1K for the Ax series, which reveals low antiferromagnetic interactions between Fe^{3+} spins which could arise from dipolar interactions. θ is then a function of number and distance between $Fe^{3+}{}_{5/2}$ neighbors. The fact that θ is almost identical for all A series reveals that the local order around Fe^{3+} with S = 5/2 is similar in vesicles (A1-3) and in membranes (A4).

The lines in Figure 3.1.5(c) and (d) correspond to the sum of the Brillouin functions with fitted parameters. The fraction of spins 5/2 : $f_{5/2}$ is reported in Table 3.1.1. Interestingly, the highest $f_{5/2}$ (≈ 87-90%) is found for A1-3, which contains larger vesicle concentration. The presence of high spin state can be associated with long range intermolecular associations, such as vesicles, and low spin state (S=1/2) to Fe sites interacting with water, as expected on the edge of the membrane fragments or non-aggregated monomer in free. As shown by SANS, the vesicle concentration is proportional to AOT_3F concentration, then it can be assumed all AOT_3F is embedded in vesicles for both A-B series. Moreover, assuming that all S = 5/2 spins are incorporated in vesicles for the A series (this assumption is further discussed in supplementary information), the molar ratio ρ of DTAF/ AOT_3F in vesicles can be estimated from the high spin fraction $f_{5/2}(A_{1\text{-}3})$. The number of AOT_3F and DTAF molecules per AOT_3F in vesicles is then given by

$$1 + \rho = f_{5/2}(A_{1-3})\,(1 + r)$$

where r is the molar ratio DTAF/ AOT_3F.

Indeed, this equation can be deduced by assuming that with ρ the molar ratio of DTAF/ AOT_3F in vesicles, all AOT_3F molecules are involved in vesicles, then the concentration of MagSurf molecules involved in vesicles is given by: $(1 + \rho)\, C_{AOTF}$. The concentration of high spins can be estimated from the high spin fraction $f_{5/2}$ and the ratio "r" of DTAF/ AOT_3F in solution. It is given by $f_{5/2}\,(1 + r)\, C_{AOTF}$. If one assumes that all high spins of the solution are involved in vesicles, then both quantities are equal, and one gets: $1 + \rho = f_{5/2}(1 + r)$. With r = 3.68, and $f_{5/2}(A_{1-3}) \approx 89$ %, ρ = 3.15 ≈ 3 is obtained. This ratio of 3 corresponds to the stoichiometric ratio the anionic (AOT) and cationic (DTA) counterparts of the ion pairs. The θ value is close to -1K for the Ax series, which reveals low antiferromagnetic interactions between Fe^{3+} spins which could arise from dipolar interactions. θ is then a function of number and distance between $Fe^{3+}{}_{5/2}$ neighbours. The fact that θ is almost identical for all A series reveals that the local order around Fe^{3+} with S = 5/2 is similar in vesicles (A1-3) and in membranes (A4). Focusing now on the results from the B series.

SANS showed that the vesicles are essentially identical to those of A-series, and that their number density follows AOT_3F concentration, it can be then assumed that ρ ratio is the same, and that all AOT_3F of B1-2 solutions are associated with vesicles. The surfactant concentration constituting the vesicles in B1 is then given by: $(1+\rho)\, C_{AOTF} = 7\ mM$, which corresponds to roughly 46% of the total surfactant concentration. The fraction of $Fe^{3+}{}_{5/2}$ spins should be at least equal to this value, it is in fact higher (60%), as mentioned in Table 3.1.1, implying that some 5/2 spins are involved in others structures than vesicles. In fact, the concentration of the remaining DTAF (outside vesicles) in solutions B1 and B2 is given by $C_T - (1+\rho)\, C_{AOTF}$, that is 8.3 mM and 4.1 mM for B1 and B2 respectively. These concentrations are below the CMC.

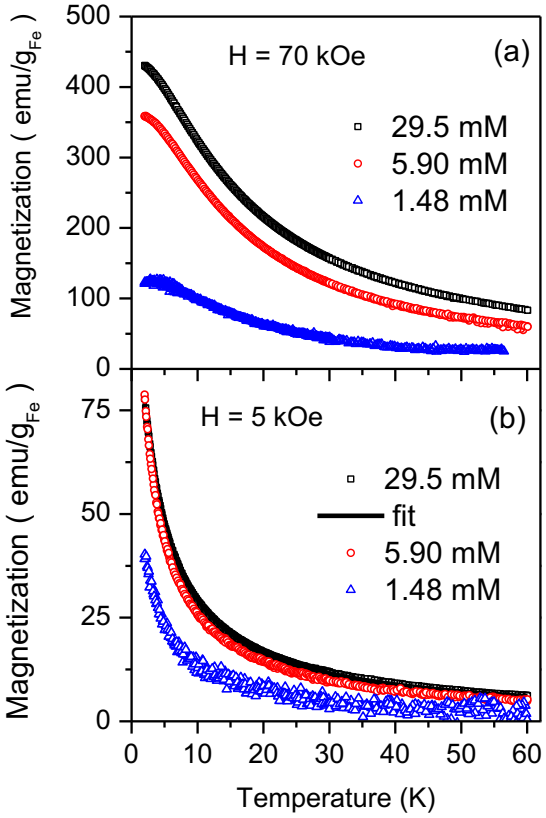

Figure 3.1.6. Magnetization as a function of temperature for 3 DTAF solutions, above the CMC: 29.5 mM and below the CMC: 5.90 and 1.48 mM. (a): H = 70 kOe, (b): H = 5 kOe.

As shown in Figure 3.1.6, a DTAF solution with a concentration of 6.3 mM contains a large amount of spins 5/2 which could be associated with the formation of other (pre-vesicular) aggregates. As a consequence, in B solutions, the high spin Fe^{3+} ions do not occur only in vesicles, but can be also be involved in other DTAF species; nevertheless, it is not possible to determine exactly that concentration. In the case of pure DTAF, the dipolar interaction

between Fe^{3+} spins should be stronger, and another θ value should be introduced, and then there are too many fitting parameters.

Concerning the Ax solutions, for instance A2, the concentration of remaining DTAF is $C_T - (1+\rho)C_{AOTF}$ =1.58 mM. For such low DTAF concentration (Figure 3.1.6), the low spins are dominating the magnetic signal (it represents about 70 % of the signal for T >10K) and the assumption that all high spins are involved in vesicles is quite reasonable. Indeed, the fraction of high spins arising from free DTAF can be evaluated. As the low spin fraction of the A2 solution (≈13%) comes from DTAF, considering that it corresponds to 70 % of the DTAF signal, then the high spin fraction coming from DTAF should be about 4%, The high spins fraction in vesicles would be about 0.83 and ρ is then equal to 2.9 (instead of 3.15 in the first assumption). This calculation validates a-posteriori the final approximation ρ ≈ 3.

As a result of this analysis, more precise concentration conditions for the occurrence of AOT_3F/DTAF vesicles can now be proposed. The AOT_3F concentration must lie between those of A4 and B2 solutions: 0.58 mM < CVC(AOT_3F) < 0.87 mM , and with a proportion of 1 AOT_3F molecule per 3 DTAF molecules, one obtains for the total surfactant critical concentration: 2.3 mM < CVC < 3.5 mM.

As pointed out before, the CAC value expressed as a function of the AOT_3F concentration is identical for both A- and B – series. It seems then that the stoichiometry in aggregates is the same as for vesicles, namely: 1 AOTF and 3 DTAF. Considering a critical AOT_3F concentration of 1.5 10^{-2} mM, the CAC value with a ratio 3/1 would then be 6 10^{-2} mM. This value is almost two orders of magnitude lower than for pure surfactants. This is due to the ion paring and hydrophobic interactions between the anionic and cationic ions.

3.1.4 Conclusion

Novel vesicle systems, comprising paramagnetic ions have been designed with ion pairs of iron-surfactants: DTAF and AOT_3F with two DTAF/AOT_3F molar ratios: 3.7 and 7.8. Using small-angle neutron scattering (SANS), the vesicle sizes are found to be essentially independent of this ratio and vesicle concentration is limited by the AOT_3F concentration. Interestingly, magnetic measurements performed as a function of temperature display similar trends as the SANS data. Through analyses of the paramagnetic signal of Fe^{3+} ions, a correlation between molecular self-assembly state and spin state is established for the first

time. Fe^{3+} ions involved in vesicles are found to be in a high spin state, whereas a transition to less ordered bilayers or monomers occurs with a low spin crossover (Figure 3.1.7).

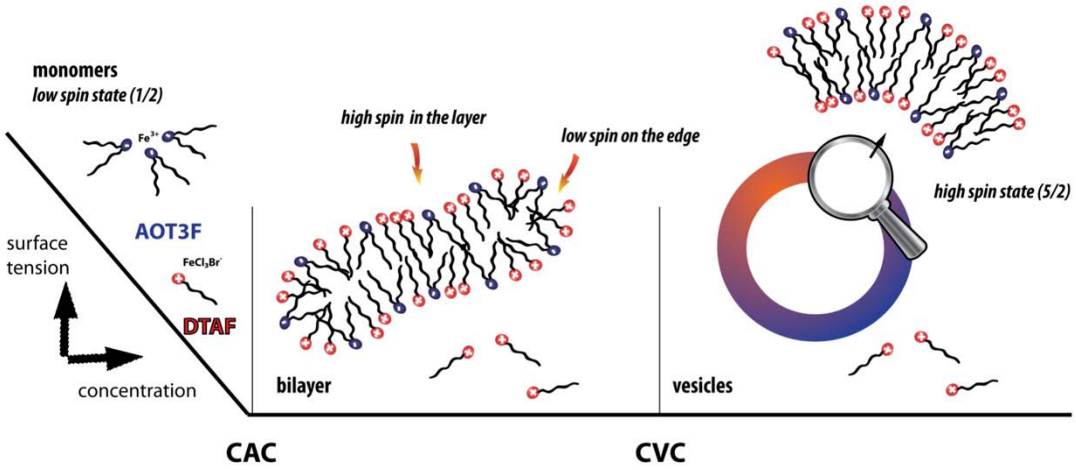

Figure 3.1.7. Schematic representation showing the spin crossover of MagSurfs upon self-assembling: low spin in monomers, low spin and high spin in bilayers and high spin in vesicles

A careful analysis allows deduction of an optimal DTAF/AOT_3F molar ratio (=3) for the generation of vesicles, and the total critical vesicle or aggregate surfactant concentration. This optimal ratio corresponds to the stoichiometric ratio the anionic (AOT) and cationic (DTA) counterparts in ion pairs. Magnetic coupling between Fe spins is observed in vesicles or DTAF micelles, and readily attributed to dipolar interactions. The next is to induce exchange interactions between spins in order to enhance the magnetic response. These newly designed magneto-vesicles, which combine intrinsic magnetic responses and encapsulation properties pave the way for prototype nanocarriers in drug delivery applications triggered by external magnetic fields.

Part 3.2

Nanoparticle-free magnetic mesoporous silica with magneto-responsive surfactants

This part was published as: S. Kim, C. Bellouard, A. Pasc, E. Lamouroux, J.-L. Blin, C. Carteret, Y. Fort, M. Emo, P. Durand, M.-J. Stébé, Nanoparticle-free magnetic mesoporous silica with magneto-responsive surfactants in *J. Mater. Chem. C*, 2013, 1, 6930-6934.

3.2.1 Introduction

While metallosurfactants have been known for many years[41-44] and are already used in the field of catalysis,[45] sensing,[1] or for biomedical applications,[46-48] only recently the magnetic properties of surfactants bearing magneto-responsive centres (Fe, Gd, Ho, and Ce) have been demonstrated.[4,31,49] The magnetic responsiveness of these surfactants is fundamentally different from molecular magnets or ferrofluids, arising from electronic and molecular spin, associated with the ordering in the self-assembled architectures. These newly designed magneto-surfactants (MAGS) have been used to date as novel molecular tools in designing magnetic colloids such as microemulsions[6] or emulsions[5] and were proposed for potential applications in fields that require interfacing magnetic materials, i.e. information storage, electronic, spintronic devices. In addition, most of physical properties of magneto-surfactants are similar to their parents surfactants, thus the magneto-surfactants could be used in the same manner like parents surfactants. For example, it was shown that the magneto-surfactants could magnetize other molecules such as DNA,[34] silica-organosols.[33] Moreover, due to the absence of metallic nanoparticles that are subjected to strict regulation as hazardous products, magneto-surfactants are suitable for biomedical (*i.e.* MRI contrast agents or hyperthermia probes) or for environmental applications (*i.e.* recovery of heavy metals).

In this part, the application of magnetic surfactants for the preparation of nanoparticle-free magnetic mesoporous silica materials was demonstrated. In this case, magneto-surfactants are used as both template and magnetic source for the design of magnetic hard matter.

Indeed, imprinting mesoporous silica materials with magnetic properties is of great fundamental interest since it combines high surface area and pore volume with magnetic responsiveness. Magnetic mesoporous silica may have applications in catalysis,[50-52] sensing,[53,54] separation[55-60] or biomedical fields for simultaneous MR imaging and targeted drug delivery.[61-66] Moreover, since the magnetic centres are homogeneously distributed in the micellar shells, which directly interact with the silica precursors, it is reasonable to assume that they are also well distributed in the pore channels of the resulting magnetic mesoporous silica materials. Taking advantage of this approach, it could be also possible to overcome main drawbacks of conventional magnetic mesoporous silica materials that present, in most case, the inhomogeneities of the final material,[67] due to magnetic nanoparticles embedded into mesoporous silica through multi-step syntheses.

3.2.2 Materials and methods

Chemicals

Tetramethylorthosilicate (TMOS), Hexadecyltrimethylammonium bromide (CTAB), were purchased from Sigma-Aldrich. Methanol, iron (III) chloride ($FeCl_3$) were purchased from Alfa Aesar. Water was deionized using a Milli-Q pack system. All chemicals were used as received without further purification.

Synthesis of magneto-responsive surfactant, CTAF

1.77 g of $FeCl_3$ (11.0 mol) was added to 4.0 g of CTAB (11.0 mmol) that was already dissolved in 50 mL of methanol. Then, the solution was heated to reflux overnight. The methanol was evaporated using a rotary evaporator and then the magnetic-surfactant CTAF was dried *in vacuo* at 60 °C for more than 4 h.

Synthesis of Magnetic Mesoporous silica templated using CTAF

Silica materials were prepared by sol-gel, through the cooperative templating mechanism, from micelles of CTAF and tetramethoxysilane (TMOS) as inorganic precursor. In a typical procedure, 123 mg of CTAF were added in 8 mL of 7.5% of HCl dissolved in H_2O. Then, 296 mg of tetramethyl orthosilicate (TMOS) were added at room temperature and the mixture was stirred for 30 min. The final molar composition of the gel is 1 SiO_2: 0.12 CTAF: 228 H_2O: 8.2 HCl. Then, the mixture was transferred to a Teflon bottle placed in a stainless-steel autoclave at 343 K for 48 h. The resulting product is filtered on a Buchner funnel and dried in air for 24 h. Dry hybrid material (CTAF@SiO_2) was placed in a saturated atmosphere of triethylamine for 5 minutes. The organic template was washed with hexane, the powder was then heated to 70 °C and washed with absolute ethanol to afford Fe@SiO2. Bare silica materials (Bare SiO_2) were also obtained after removal of surfactant, CTAF by extraction with ethanol in a Soxhlet during 24 h.

Magnetic measurements

Magnetic measurements were performed with powder samples (CTAF@SiO2, Fe@SiO2 and bare silica) placed in a capsule and plastic straw with a PPMS Quantum Design instrument in

the 2 K-300 K temperature range and a magnetic field up to 9 T. Raw data have been corrected from the diamagnetic contribution of samples and sample holder.

3.2.3 Results and Discussion

Magnetic surfactant, CTAF

The surfactant used for the synthesis of magnetic mesoporous silica materials (CTAF@SiO_2 and Fe@SiO_2) is CTAF (CetylTrimethylAmmoniumtrichloromonobromoFerrate). It was simply prepared from a common surfactant cetyltrimethylammonium bromide, CTAB and a stoichiometric amount of paramagnetic $FeCl_3$. The successful preparation of the surfactant was verified using elemental analysis (Table 3.2.1) and UV-Visible spectra (Figure 3.2.1) that showed the characteristic bands for the $[FeCl3Br]^-$ ion similar to those for the $[FeBr4]^-$ ion.[68] The surfactant, CTAF exhibits the ionic liquid property with a melting point of 64°C, as determined by differential scanning calorimetry (DSC) (Figure 3.2.2)

Element	% C	% H	% N
Theoretical content	43.30	8.04	2.66
Experimental content	43.70 ± 0.22	7.86 ± 0.35	2.96 ± 0.08

Table 3.2.1. Elemental analysis of CTAF

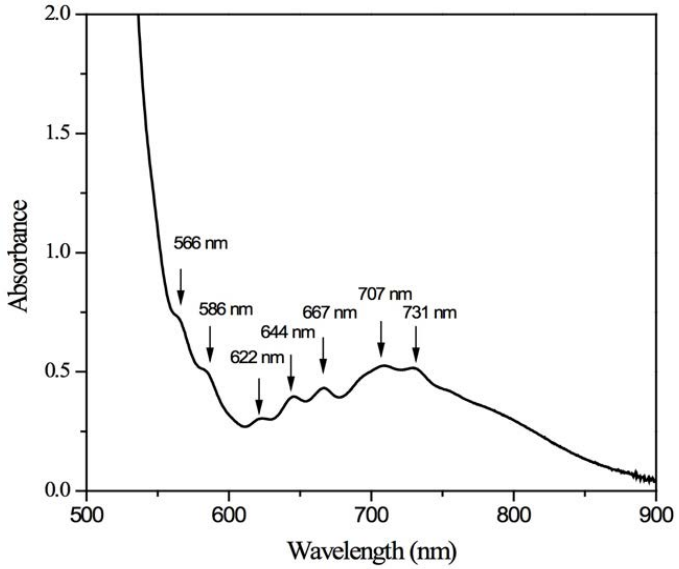

Figure 3.2.1. UV-Visible spectra of CTAF (0.1 M in acetonitrile).

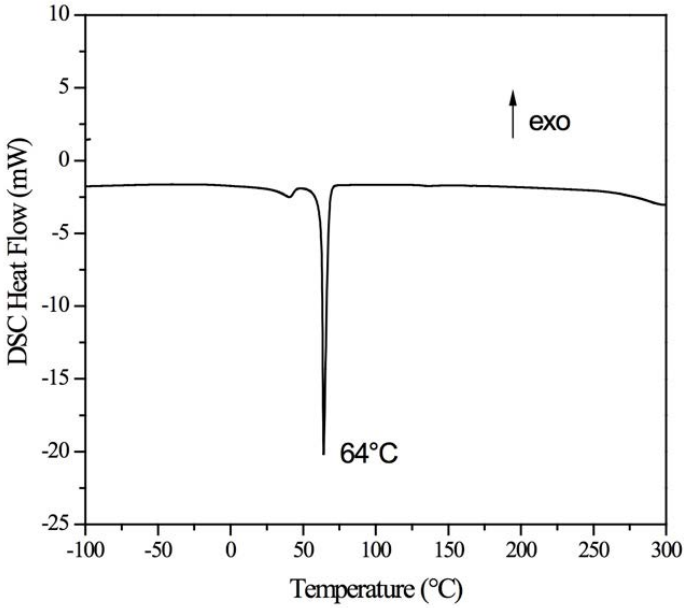

Figure 3.2.2. DSC measurement of magnetic surfactant CTAF

CTAF forms micelles in the rich water phase and a gel phase (L_β) at higher surfactant concentration. (Figure 3.2.3)

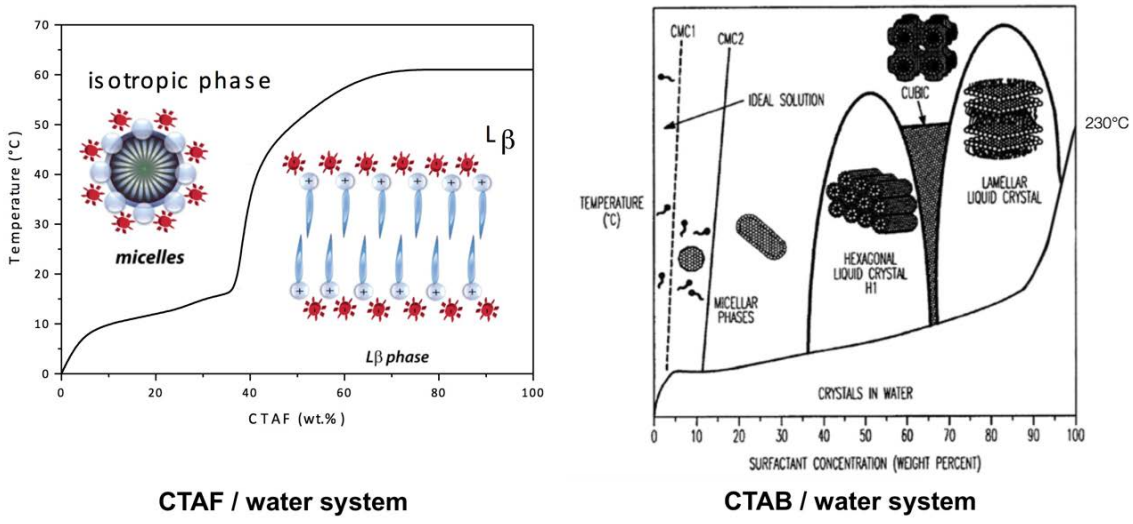

Figure 3.2.3. Concentration-temperature phase diagram of CTAF/water (left) and CTAB/water[69] (right) systems.

Unlike CTAB, no hexagonal or cubic liquid crystal domain was observed on the phase diagram of the magnetic surfactant, CTAF, probably due to the decreased hydrophilicity induced by iron ions. The gel phase melts below 60°C to give an isotropic, micellar phase.

Dynamic light scattering measurements (DLS) show that the micelles have a hydrodynamic diameter of 6 nm. (Figure 3.2.4)

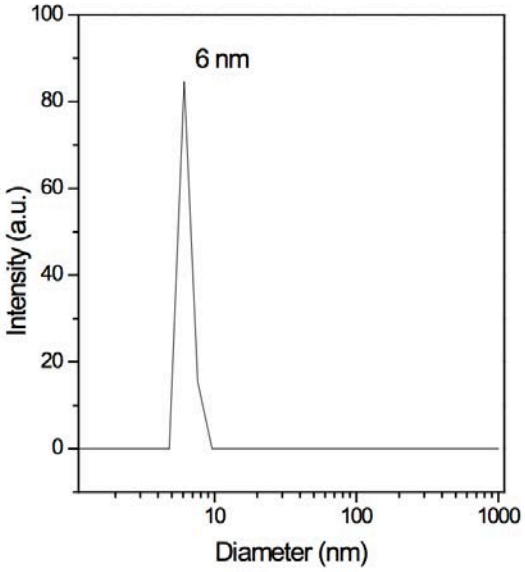

Figure 3.2.4. Size distribution of CTAF micelles in water (1M HCl) measured using DLS.

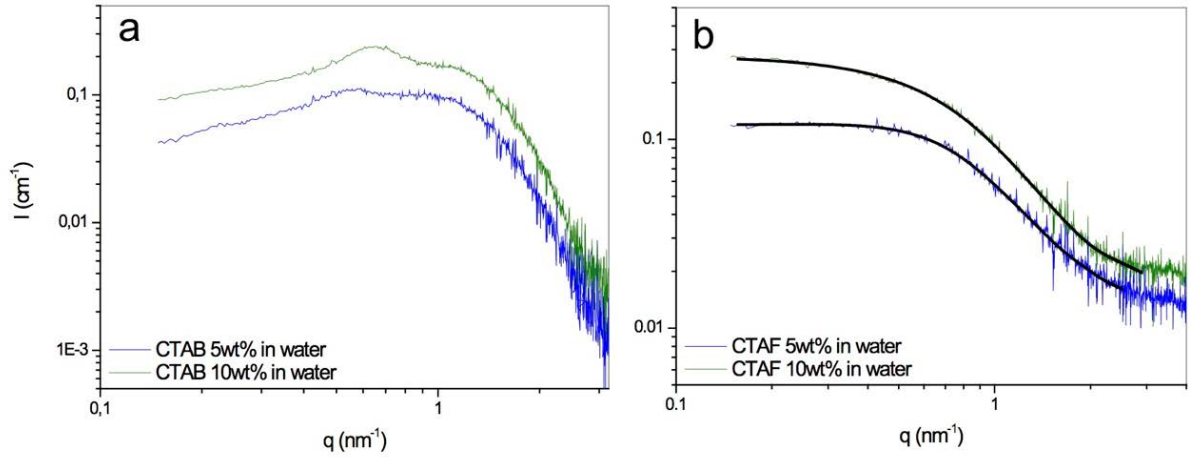

Figure 3.2.5. SAXS patterns (a) of 5 and 10 wt% CTAB in water at 25°C, and (b) of 5 and 10 wt% CTAF in water at 25°C in log-log representation.

Small angle X-ray scattering (SAXS) measurements were performed on 5 and 10 wt.% aqueous solutions of parent surfactant, CTAB, and of magnetic surfactant, CTAF. At the same concentration the scattering curves are different on the entire range of *q* values. Regarding the curves obtained with CTAB solutions (Figure 3.2.5), the intensity is proportional to the dispersed volume fraction for all q values. The presence of an interaction peak at 0.55 nm^{-1} and the strong decrease of the scattered intensity at low q suggest that the

structure factor contributes to the scattering for 5 wt.% of CTAB solutions. At 10 wt.%, the interaction peak is more pronounced and shifted to higher q values, as expected. For CTAF samples, the SAXS profiles are entirely different. The obtained curves do not present any interaction peak, suggesting that the iron inhibits interactions between mecelles. Indeed, as previously reported for an analogous surfactant with a shorter tail (C12), metal halide anions of MAGS might associate by compressing the electrical double layer as compared to regular non-magnetic micelles, thus preventing inter-particle interactions.[4]

Synthesis of Magnetic mesoporous silica templated using CTAF

The preparation of silica materials was performed by a sol-gel procedure through a cooperative mechanism.[69,70] The synthesis consists in mixing micelles of CTAF with a silica precursor (TMOS), followed by the hydrolysis–condensation reactions of the silica source around the organic framework. (Figure 3.2.6) The reaction condition was optimized by varying reaction parameters like concentration of surfactant, temperature, or the molar ratio between the silica source and the surfactant (R), in order to obtain a structured material and a homogeneous distribution of the metallic centres at the surface of the mesopores.

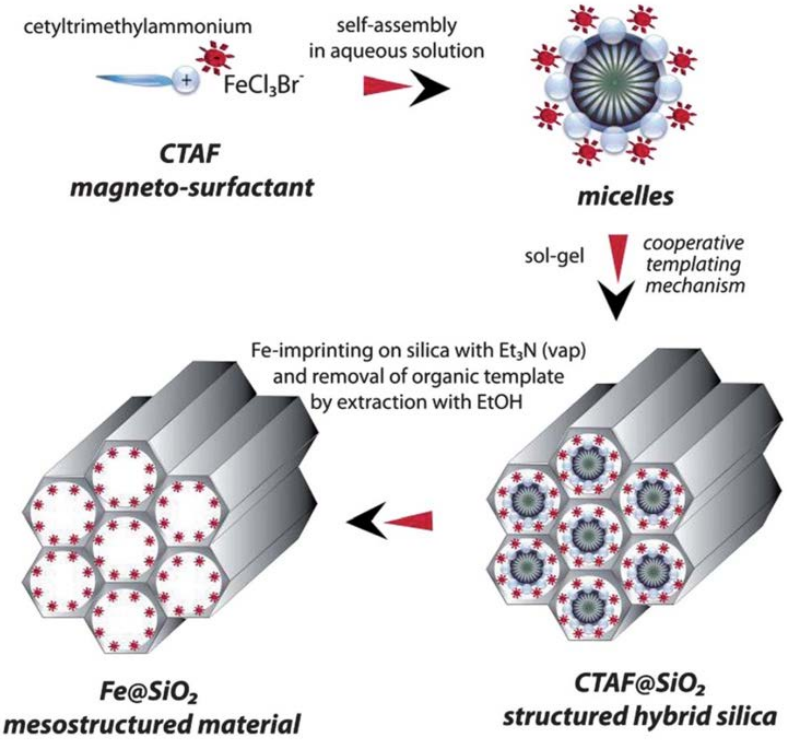

Figure 3.2.6. Schematic illustration of the synthetic pathway for magnetic mesoporous silica through a self-assembly mechanism with CTAF.

Initially, the surfactant/TMOS molar ratio (R) and the concentration of HCl were fixed at 0.12 and 1M, respectively, values which are similar to those used for the synthesis of MCM-41 with CTAB in acidic conditions.[71] In these conditions, the concentration of surfactant (1.5-10wt%) and the temperature of the silica condensation (70, 100°C) were varied, while the duration was kept constant of 24 h. Looking at the SAXS patterns of the obtained materials only a single broad peak is observed for most of the materials. This indicates the formation of a wormhole-like structure, with an interpore distance of about 3.9 nm. In these conditions, the better organisation of the silica was obtained at 100°C and 2.5 wt% of CTAF, since two reflections at 3.9 and 2.3 nm (ratio 1:$\sqrt{3}$) are observed. (Figure 3.2.7)

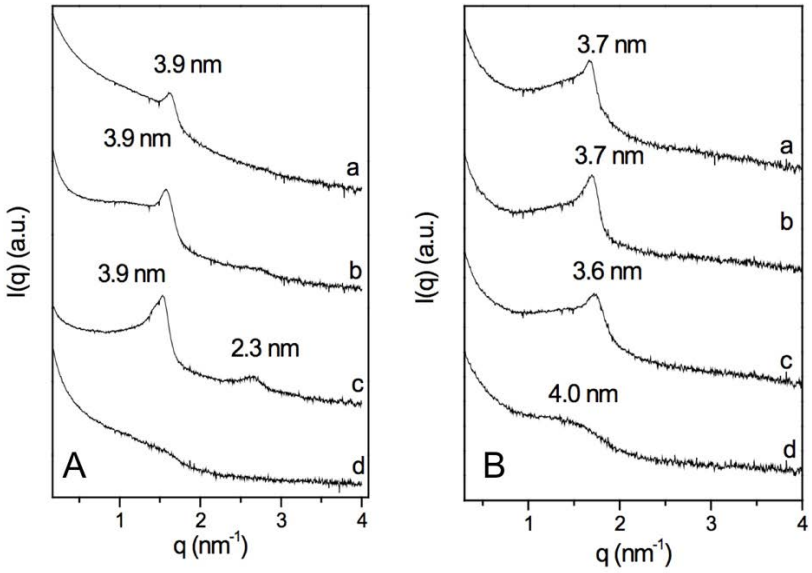

Figure 3.2.7. SAXS data of mesoporous materials prepared at 100°C (A), 70°C (B) at a molar ratio surfactant/TMOS of 0.12 and 15 wt% (a), 10 wt% (b), 2.5 wt% (c), 1.5 wt% (d) of CTAF in a solution of 1M HCl.

Further, the mesostructuring of porous silica with a higher concentration of HCl (2M) as reaction media was investigated. The silica condensation was performed at 70°C for 24 h, and R was fixed to 0.12 and. However, the surfactant concentration was fixed to 1.5 wt.% as this condition gave the narrowest peaks in SAXS pattern as shown in Figure 3.2.8e.

For all materials, nitrogen adsorption-desorption isotherms are of type IV and the calculated pore size are centred on 2.4-2.7 nm. At both surfactant concentrations, for R = 0.08, the silica has necked pores, and a surface area and a pore volume significantly lower than for the materials obtained at R = 0.12 and 0.16. The values of the porosity parameters are given in Table 3.2.2 and Figure 3.2.9.

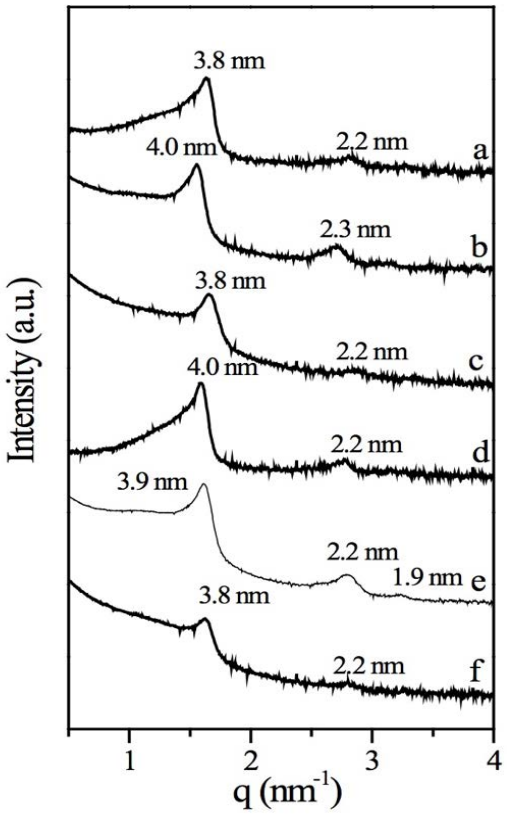

Figure 3.2.8. SAXS data of mesoporous materials prepared with either 2.5 wt% CTAF and R of 0.16 (a), 0.12 (b), 0.08 (c) or with 1.5 wt% CTAF and R of 0.16 (d), 0.12 (e) and 0.08 (f). The reactions were carried out in aqueous solutions of 2 M HCl and silica condensation at 70 °C for 24 h.

Reaction conditions	BET surface area (m^2 g^{-1})	Pore volume (cm^3 g^{-1})
2.5 wt.% of CTAF, R = 0.08	937	0.77
2.5 wt.% of CTAF, R = 0.12	1213	1.05
2.5 wt.% of CTAF, R = 0.16	1078	0.76
1.5 wt.% of CTAF, R = 0.08	860	0.99
1.5 wt.% of CTAF, R = 0.16	1096	0.81

Table 3.2.2. Summary of the BET specific area, and pore volume for the mesoporous silica materials prepared with 2M HCl under a silica condensation at 70 °C for 24 h

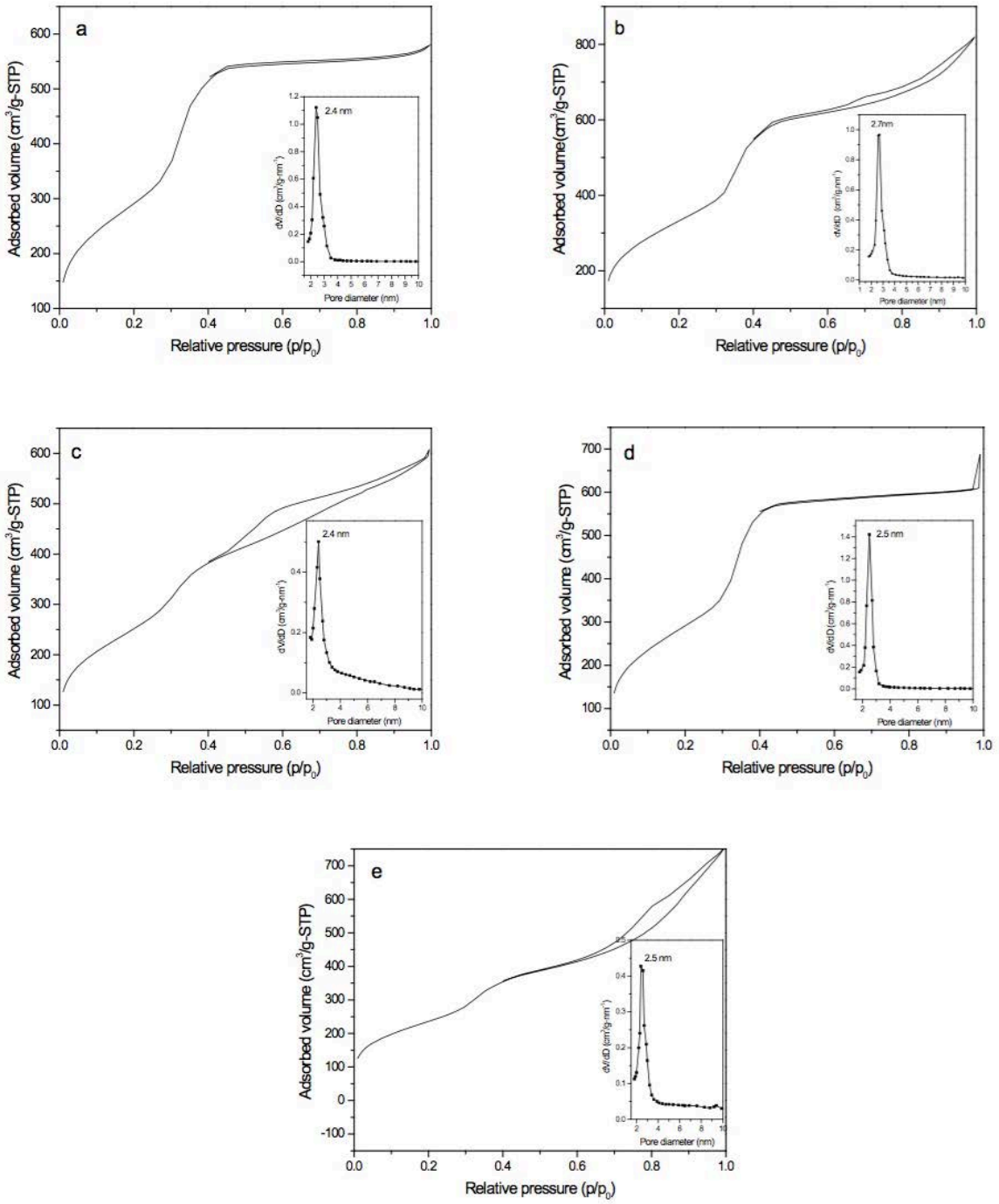

Figure 3.2.9. Nitrogen adsorption/desorption isotherms and the pore diameter (insert) of mesoporous silica materials prepared with either 2.5 wt% CTAF and R of 0.16 (a), 0.12 (b), 0.08 (c) or with 1.5 wt% CTAF and R of 0.16 (d), 0.08 (e). The reactions were carried out in aqueous solutions of 2 M HCl and a silica condensation at 70 °C for 24 h.

Therefore, the further investigation was focused only on the silica material obtained using the optimal condition: 1.5 wt. % of surfactant in 2M HCl with 0.12 of TMOS as molar ratio and 24 h of the silica condensation at 70°C.

As shown in Figure 3.2.10b, SAXS data for the bare SiO_2 mesoporous material, obtained by removing the CTAF surfactant, indicate three peaks at 3.9, 2.2 and 1.9 nm, indexing for $1:\sqrt{3}:2$ that is consistent with a hexagonal phase. The structure of the mesopores was further confirmed by transmission electron microscopy (TEM) micrographs, showing hexagonal stacking of the channels (Figure. 3.2.10e). Without removing the surfactant, the hybrid material CTAF@SiO2 showed two peaks in the SAXS (Figure 6.5c), due to the low electronic density contrast between the silica and the carbon chain of CTAF. Bare mesoporous silica, free of CTAF was characterized using N_2 adsorption–desorption isotherm analyses (Figure 3.2.11a), giving an IV type isotherm that is characteristic of mesoporous materials. The pore size distribution is centred at 2.7 nm, and its specific surface area, pore volume are 966 $m^2\ g^{-1}$, 1.06 $cm^3\ g^{-1}$, respectively. These values are similar to those obtained for a MCM-41 silica material template with CTAB.[71,72] This could be explained by the fact that the CTAF micelles may retain similar size and hydrophobic radius as compared with the parent surfactant, CTAB, as demonstrated by SAXS experiments.

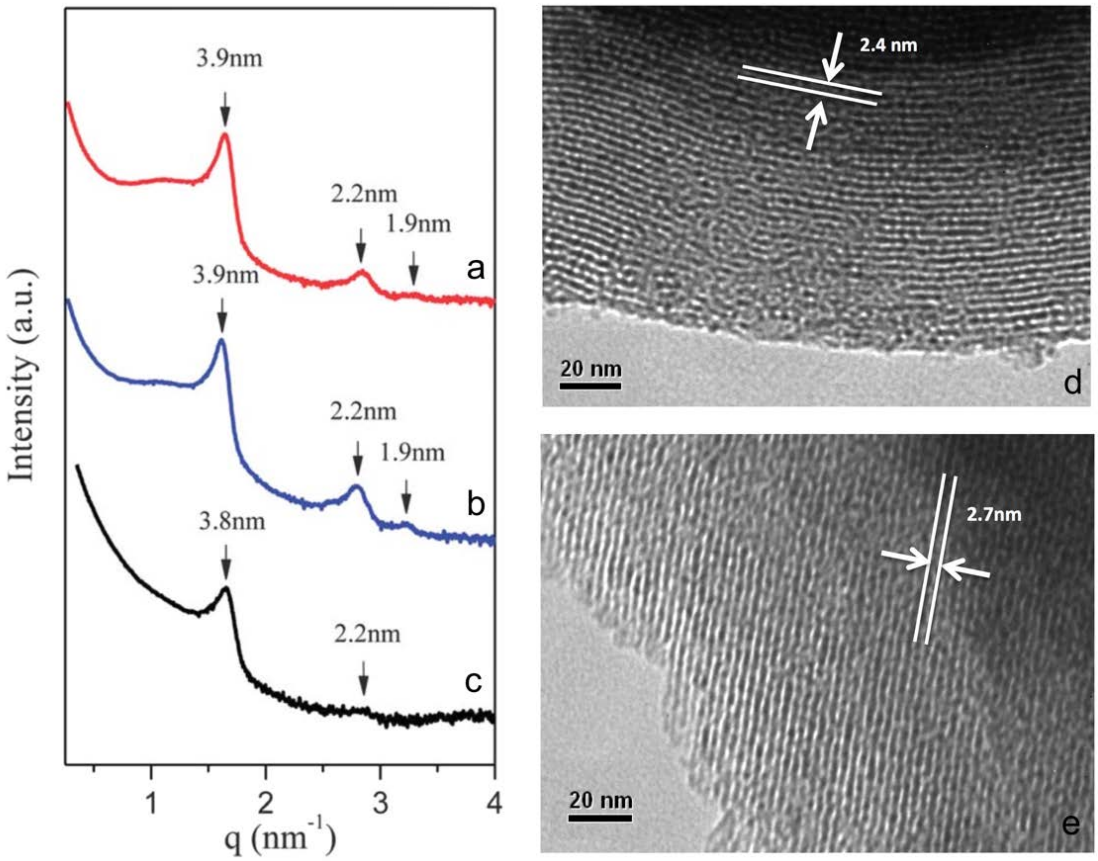

Figure 3.2.10. SAXS patterns for silica materials: (a) Fe@SiO_2, (b) Bare SiO_2, and (c) CTAF@SiO_2; TEM micrograph of (d) Fe@SiO_2, and (f) Bare SiO_2.

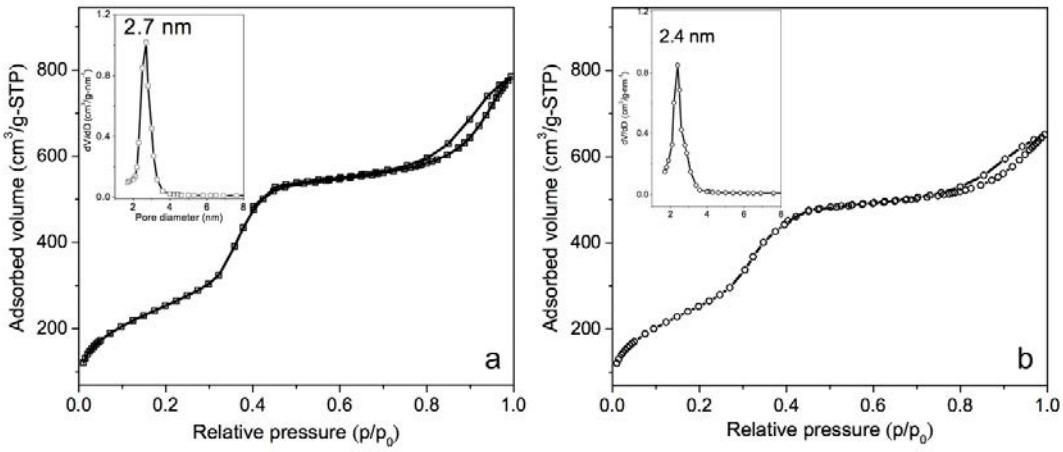

Figure 3.2.11. N_2 adsorption–desorption isotherm of (a) bare mesoporous silica, (b) Fe@SiO_2, and their pore size distribution (inset).

In order to combine magnetic responsiveness and high porosity, iron centres were fixed to the surface of the mesopores, by exposing the hybrid CTAF@SiO_2 to a saturated atmosphere of triethylamine for 5 min, followed by moderate heating at 70°C. This is an essential step in imprinting iron ions onto the silica wall. Indeed, as the silica material is synthesized in acidic conditions, the silanol groups have to be deprotonated for coordinating the iron ions. Finally, the organic part of the surfactant was removed with anhydrous ethanol. The SAXS data showed that the structure of the resulting material Fe@SiO_2 didn't alter (Figure 3.2.10a). However, the diameter of the mesopores was slightly smaller (2.4 nm) than that of the bare silica material (Figure 3.2.11b), with pore volume and surface area that is 0.85 $cm^3\ g^{-1}$ and 967 $m^2\ g^{-1}$, respectively. The estimated wall thickness of the Fe@SiO_2 material was 2.1 nm, whereas 1.8 nm for bare SiO_2.

The coordination of iron in the materials was analysed by the evolution of UV-Vis diffuse-reflectance spectra.[73-75] Characteristic absorption bands of CTAF (Figure 3.2.12a) were in CTAF@SiO_2 (Figure 3.2.12b), but they completely disappeared in the bare SiO_2 (Figure 6.7d). Moreover, Fe@SiO_2 (Figure 3.2.12c) shows an adsorption band at 235 nm, which can be assigned to the charge transfer of pπ–dπ transition between oxygen and iron in the Fe-O-Si bond. This is consistent with tetrahedral iron atoms, isolated from each other. In addition, the absence of any absorbance band above 350 nm in the spectrum reveals also that there is no octahedral iron ion, and consequently no iron oxide nanoparticle in the Fe@SiO_2 material.[75]

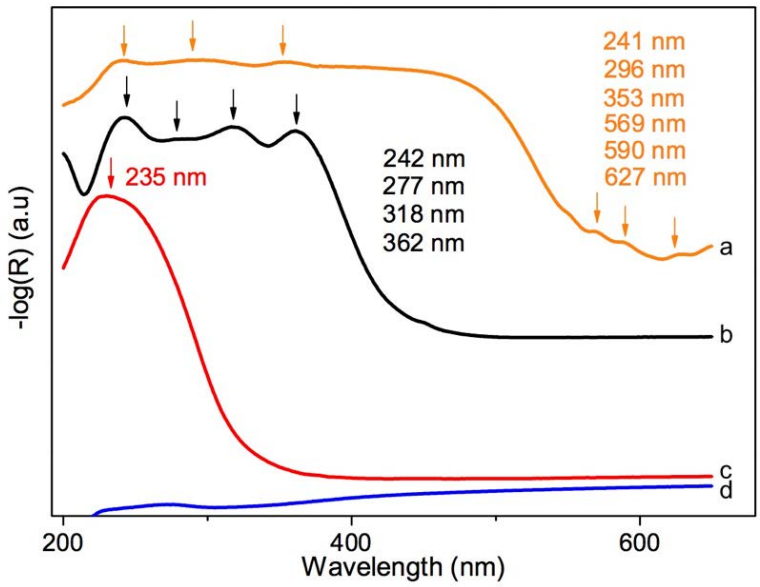

Figure 3.2.12. UV-Visible diffuse reflectance spectra of materials: (a) CTAF, (b) CTAF@SiO_2 (hybrid), (c)Fe@SiO_2, and (d) Bare SiO_2

Magnetic measurements

Starting with magnetic surfactant used in this study, CTAF, magnetic measurement shows a paramagnetic signal in the range of 2 to 300K with high spins state of iron (S=5/2), and the surfactant exhibits antiferromagnetic interactions (Figure 3.2.13a). Concerning silica materials, it is shown that both hybrid CTAF@SiO_2 and organic-free silica, Fe@SiO_2, materials exhibit paramagnetic properties on the entire range of temperature (2 to 300 K), while bare silica is diamagnetic. This clearly indicates that the imprinted iron does not penetrate the silica framework but remains at the surface of the material wall, and the iron could be removed along with its alkyl chain of surfactant by simple ethanol extraction. Figure 3.2.13b presents the raw magnetization at 10 K and 300 K for bare SiO_2, CTAF@SiO_2, and Fe@SiO_2. The samples CTAF@SiO_2 and Fe@SiO_2 exhibit a paramagnetic signal at low temperature, which is amplified by a 1/T factor as the temperature decreases.

As shown in the Figure 3.2.14, after correction of the diamagnetic contribution of the sample and the sample holder, the paramagnetic signals arising from Fe^{3+} ions above 10K can be analysed using Brillouin law fitting. This is consistent with the paramagnetic behaviour of Fe^{3+} magnetic signal and allows quantifying independently the spin and the saturation magnetization. For T > 10 K, Fe^{3+} ions exhibit a S = 5/2 spin state as free Fe^{3+} ions in the high spin state. The saturation magnetization of the samples can be expressed with respect to

the initial weight amount of iron: $M_s(CTAF@SiO_2)$ = 147 emu g^{-1} Fe and $M_s(Fe@SiO_2)$ = 25 emu g^{-1} Fe. From these results and the theoretical value of Fe^{3+} of 5/2 spin (500 emu g^{-1}), the amount of iron in the materials could be estimated to be 1.5 wt.% for $CTAF@SiO_2$ and 0.5 wt.% for the $Fe@SiO_2$.

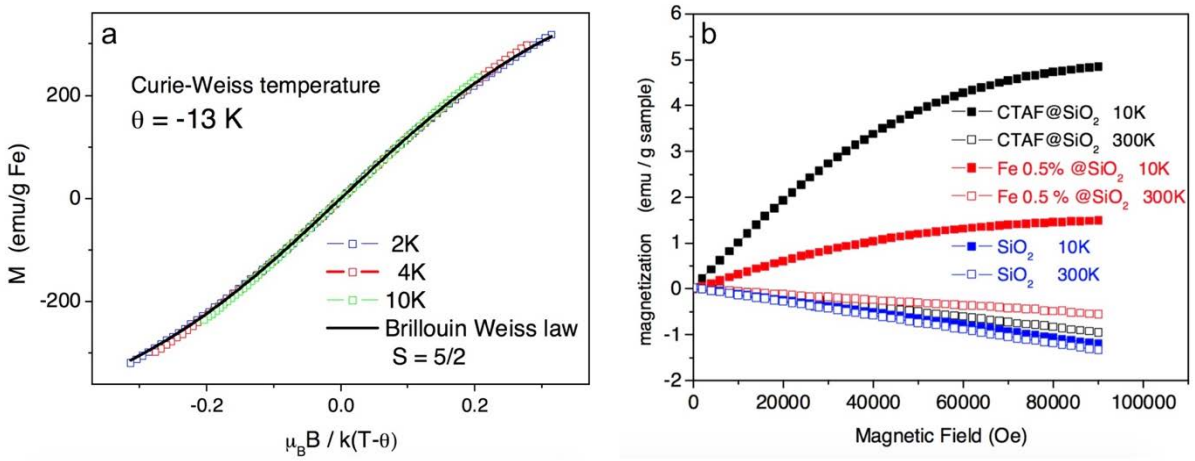

Figure 3.2.13. (a) Magnetization of magnetic surfactant, CTAF as a function of dimensions parameter $\mu_B B/k(T-\theta)$ and its fit with the Brillouin function with S = 5/2; (b) Magnetization of hybrid $CTAF@SiO_2$, $Fe@SiO_2$, and bare SiO_2 as a function of applied magnetic field (Oe) at 10 and 300K.

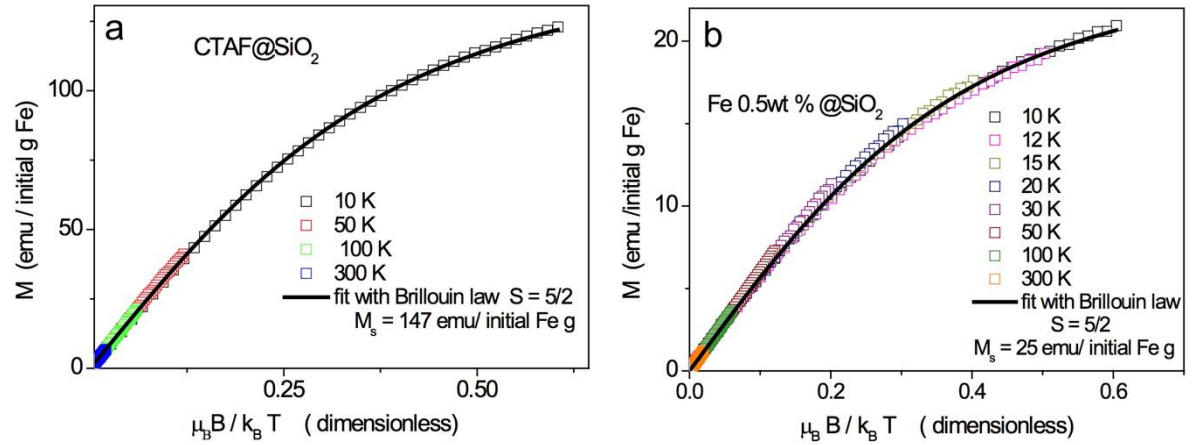

Figure 3.2.14. Magnetization of (a) the hybrid CTAF@SiO2 and (b) Fe@SiO2 samples measured at different temperatures and plotted as a function of the ratio of the magnetic field (B) to temperature (T).

Figure 3.2.15 focuses on the low temperature dependence of the susceptibility measured under an applied magnetic field (B) of 1T. As already discussed (Figure 3.2.13), in this range, the field dependence of the magnetization is linear. The susceptibility can then be compared to the behaviour predicted by the Curie law: $\chi = C_{Fe3+}/T$. Above roughly 8 K for

CTAF@SiO_2 and 12 K for 0.5 wt.% Fe@SiO_2, the susceptibility follows the Curie law behaviour.

However, below these temperatures, a decrease in susceptibility with respect to the Curie behaviour is observed. This feature depends on the cooling rate and presents clear temperature hysteresis behaviour for 0.5 wt.% Fe@SiO_2. Moreover, no field hysteresis has been observed, the system remains paramagnetic over the whole magnetic field and the temperature range explored. As a matter of fact, this deviation from the Curie law with decreasing temperature is attributed in both cases to a high spin–low spin transition of Fe^{3+} ions. Because of the limited temperature range, this spin crossover from 5/2 to 1/2 is not complete. Such a spin crossover can be observed in numerous complex compounds for octahedral sites of Fe^{2+} or Fe^{3+} ions.[76] It can be induced by temperature, pressure, magnetic field or light irradiation.[77] This spin change is readily associated with an anisotropic metal–ligand bond length change. For Fe^{3+}, the low spin state arises from a reduction of the unit cell volume. Moreover, temperature hysteresis and quenching effects are often observed with spin crossover. We point out that the transition temperature is shifted to higher for 0.5 wt.% of Fe@SiO_2, for which the number of occupied Fe sites is reduced.

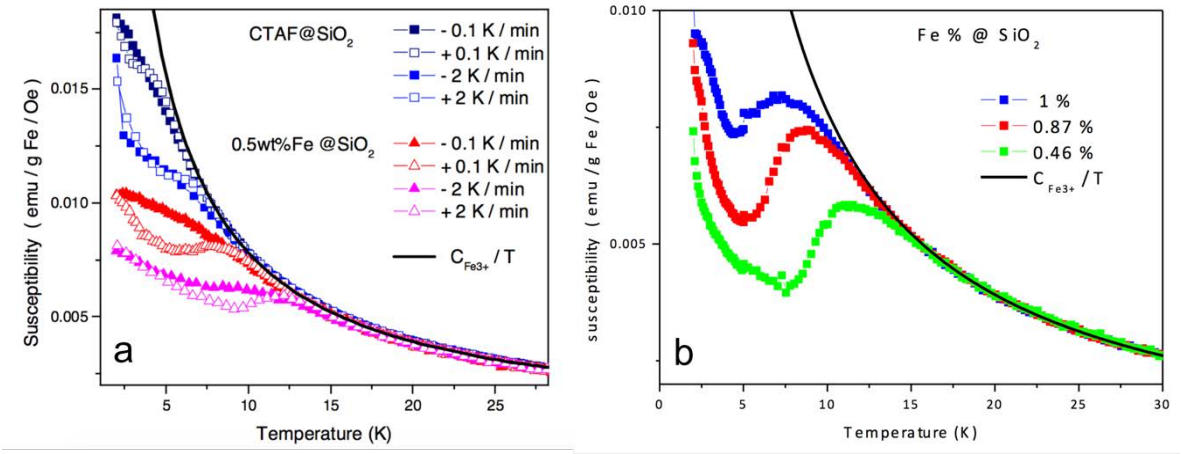

Figure 3.2.15. (a) Low temperature behaviour of χ measured under 1T for CTAF@SiO_2 and 0.5 wt.% Fe@SiO_2. The Curie law behaviour of χ expected for S = 5/2 Fe^{3+} (straight line). Two rates of 0.1 and 2 K min^{-1} with decreasing (-) or increasing (+) temperature. (b) χ of serveral Fe@SiO_2 materials measured with increasing temperature under B = 1T.

Figure 3.2.15b shows the temperature dependence of the susceptibility for several Fe@SiO_2 materials with different contents of Fe^{3+} ions. Indeed, by increasing the duration of the silica condensation from 24 to 72 h, the iron content imprinted in the silica matrix can be varied from 0.5 to 1 wt.%, probably due to high degree of mesoporosity of the silica material

obtained after 72 h of silica condensation. A shift of the transition towards decreasing temperature is observed as the amount of Fe is increased. First order spin transition is relatively rare and usually observed under pressure for metallic nanoparticles (ZnS and TiO_2), in which size and confinement effects in nanomaterials lead to new properties such as increased compressibility (i.e. ZnS) or to new phases (i.e. baddeleyite from anatase TiO_2).[78]

3.2.4 Conclusions

Mesoporous ferrisilicate materials are also of interest in catalysis.[75,79] Templating and magnetizing mesoporous materials with magneto-surfactants may open up the possibility of tailoring the interdistance between the metallic centres. Indeed, it was previously reported that the accessibility of catalytic centres affects the catalytic performance of the system. [80,81] This could be achieved in further work by varying the number of magnetic centres per alkyl chain with di-, tri- or multivalent magneto surfactants. Also, in some catalytic applications it is advantageous to have dispersed single metal centres across the support.[82,83] Improved catalytic,[84-85] sensing[86] or complexing[87] properties could be achieved with bimetallic systems by simply using mixtures of metallo magnetic and non-magnetic surfactants (Fe–Ni, Fe–Co, and Ag–Au) as porogens of the inorganic material. Moreover, 1D nano-objects such as nanowires or nanotubes might be prepared under controlled growth inside the pores of the hexagonal mesoporous silica. Finally, magnetic surfactants could be of interest in structuring and magnetizing other solid materials including polymers.

Part 3.3

Metallo-solid lipid nanoparticles as colloidal tools for meso-macroporous supported catalysts

This part was published as: S. Kim, P. Durand, T. Roques-Carmes, J. Eastoe, A. Pasc, Metallo-solid lipid nanoparticles as colloidal tools for meso-macroporous supported catalysts in *Langmuir*, 2015, **31**, 1842-1849.

3.3.1 Introduction

In this part, it was demonstrated that solid lipid nanoparticles with magnetic surfactants could be used as an excellent colloidal tool for metallic nanoparticles embedded silica materials. As the environmental concerns have been becoming more serious that ever, the homogeneous or heterogeneous catalysis chemistry have received the spotlight from scientists. Especially, heterogeneous catalysts consisting of metal oxides supported on clay,[88-89] silica[90-91] or carbon[92-94] materials have received enormous attention in various fields as organic pollutants degradation. Among them, silica-supported iron oxide has been intensively studied, due to not only its high catalytic ability toward various reactions, but also its relatively low production cost. One of the main applications of silica-supported iron oxide is wastewater treatment such as degradation of organic dyes through Fenton-like reactions.[95,96] Mesoporous silica has also been widely studied as a support material due to its high pore volume, surface area as well as ordered pore network which provide a good active site accessibility.[97,98] Several studies have reported that iron oxide dispersed in mesoporous silica supports shows not only a considerable improvement of catalytic ability, but also better stability of iron oxide, compared to free iron oxide particles.[99-103] This gain of the performance and the stability is mainly contributed by high degree of dispersity of iron oxide, giving high active surface area. In addition, silica support materials combining meso and macroporosity, which would bring higher diffusion and throughput rates though mesopores, could also improve catalytic properties such as reaction rate.[104] Some recent reports have shown the catalytic activity of yolk-shell like structured iron oxide catalysts supported on mesoporous silica with macroporous void spaces.[105-107] Nevertheless, this synthesis requires multiple steps. Moreover, the iron oxide nanoparticles (NPs) have relatively high sizes (~100 nm) and a relative surface/quantity ratio that can still be significantly improved by tailoring NP size.

To overcome aforementioned problems, it was described, herein, the preparation of Fe_2O_3@meso-macroporous silica templated with solid lipid nanoparticles (SLNs) and iron contaning magnetic surfactants as iron source. Like other materials prepared in previous chapters, the one-pot synthesis strategy was adopted. A simple calcination of as-synthesized hybrid material could generate iron oxide nanoparticles and void meso-macropores. The final material was used as application for the degradation of methylene blue (MB) in aqueous solution by a dark Fenton-like reaction initiated by H_2O_2.[108] The key point of this work is that the size of iron oxide nanoparticles embedded in the meso-macroporous matrix has been

decreased to 15-20 nm in diameter, to give high surface area of the active catalytic sites in comparison with the previous sub-micron scald iron oxide.[105-107,109] As a matter of fact, the newly designed Fe_2O_3@meso-macroporous silica matrix can successfully degrade the pollutant with twelve-times less iron oxide than previously reported. [105,110] In addition, by total organic compound (TOC) measurement, it was also shown that the catalyst of this study could effectively degrade organic dyes compounds up to carbon dioxide and water, without any toxic organic compound at the end of catalytic reaction.

3.3.2 Materials and methods

Chemicals

Tetramethylorthosilicate (TMOS), Pluronic P123, and hexadecyltrimethylammonium bromide (CTAB) were purchased from Sigma-Aldrich. N-hexadecylpalmitate (NHP) was purchased from Acros. Ethanol, methanol, and iron(III) chloride ($FeCl_3$) were purchased from Alfa Aesar. Hydrogen Peroxide (H_2O_2, 30 wt.%) was purchased from VWR International. Water was deionized and purified using a Milli-Q pack system. All reagents were used without further purification.

Synthesis of Magnetic Surfactant, CTAF

Magnetic surfactant used in this study was synthesised in part 3.2

Synthesis of SLNs@CTAF

N-hexadecylpalmitate (NHP)-based solid lipid nanoparticles (SLN) were prepared by the ultrasonication of hot emulsion method as described in chapter 2. Briefly, 20 mL of NHP based SLNs dispersed in aqueous micellar solution (6.9 wt % of Pluronic P123) was added to 350 mg of magnetic-surfactant, CTAF and then the mixture was kept under stirring for 1 h in order to solubilize CTAF and to reach the adsorption equilibrium of CTAF on the surface of SLN.

Synthesis of Fe_2O_3@meso-marcoporous silica material (Silicalization of SLNs@CTAF)

A 0.5 mL sample of hydrochloric acid (37 wt.%) was added to 20 mL of SLN dispersion decorated by CTAF (SLN@CTAF), as prepared above. Then, 2.3 g of tetramethylorthosilicate (TMOS) was added dropwise to the solution. The surfactant (P123)/silica precursor (TMOS) molar ratio (R) was 0.016. The mixture was stirred vigorously for 1 h at room temperature then and was held at 40 °C for 24 h, for aging and then kept at 100 °C for 24 h. As-synthesized silica material was dried *in vacuo* at 30 °C for 24 h. "Dried" as-synthesized silica material was calcinated at 550 °C under air (1°C/min) for 6 h to remove organic matters (SLN, P123, CTAF) and form iron oxide nanoparticles.

Catalytic performance of Fe_2O_3@meso-macroporous silica

Fenton-like degradation of methylene blue (MB) in aqueous solution was performed with the Fe_2O_3@meso−macroporous silica (denoted as catalyst). Fifteen milligrams of catalyst (0.86 mg as Fe_2O_3) was added to a 50 mL beaker containing 20 mL of 50 ppm MB solution. Then the suspension was sonicated for 5 min and kept under stirring at least for 2 h to achieve adsorption equilibrium. A 1.2 mL sample of H_2O_2 (30 wt.%) was added to initiate the degradation reaction. No acid or base was added for pH adjustment. All reactions were carried out in the dark to avoid the influence of light. At a given interval, 300 μL of solution was withdrawn and quickly centrifuged at 5000 rpm for 10 min to separate silica material. Then 150 μL of solution was diluted to 3 mL for UV−vis measurement (Agilent CARY-3E). The concentration of methylene blue was calculated using standard calibration curve at 664 nm. Total organic carbon (TOC) analysis was performed for these samples using an Online TOC-VCSH Total Organic Carbon Analyzer. (Shimadzu, Japan) All data reported are the mean (±) standard deviation of at least three different experiments.

Analyses of methylene blue adsorbed on the catalyst

Methylene blue adsorbed on the catalyst was quantified after 1, 3, 5, 7, 10, 12, 16, and 20 h. The catalyst was first filtered, than dried in vacuo at 40 °C for 6 h. Then, adsorbed methylene blue was extracted with ethanol (3 × 20 mL). The concentration of methylene blue was determined spectrophotometrically using standard calibration curve at 655 nm.

The Repeat use of the catalyst

Repeat use of the catalyst was tested in the same conditions as "Catalytic performance of Fe_2O_3@meso−macroporous silica", except that the degradation rate was measured only at 7 h of reaction time. Then, used catalyst was washed with ethanol to remove residual methylene blue, then dried in vacuo at 30 °C for 24 h. The disappearance of C-H stretching peak of methylene blue in IR spectra was also verified before next use.

3.3.3 Results and Discussion

Synthesis of the catalyst, Fe_2O_3@meso−macroporous silica

Fe_2O_3@meso-macroporous silica was prepared (Figure 3.3.1) by adding a silica precursor (tetramethoxylsilane, TMOS) to dispersions of solid lipid nanoparticles (SLN) stabilized by a magnetic-surfactant that was added as co-surfactant as well as iron source. The magnetic-surfactant, CTAF, is simply obtained from cetyltrimethylammonium bromide and iron(III) chloride as described in previous part 3.2. SLN was prepared from cetylpalmitate, pluronic P123, and CTAF by the ultrasonication of hot emulsions followed by solidification.

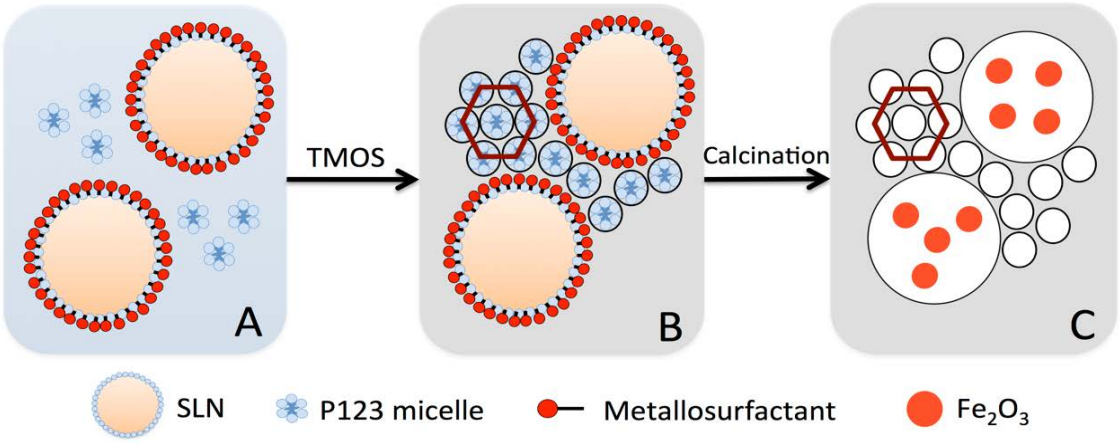

Figure 3.3.1. Synthetic strategy (not to scale): (A) CTAF-stabilized solid lipid nanoparticles (SLN) dispersed in micellar P123; (B) Silica condensation around SLN, giving hexagonally ordered mesopores; (C) Fe_2O_3@meso-macroporous silica obtained by calcination.

SLN size distribution was determined using nanoparticle tracking analysis (NTA) and dynamic light scattering (DLS) showing the size distribution centered on 160 nm and 230 nm, respectively (Figure 3.3.2A and 3.3.2B). This size gap is due to the difference between intensity-based method in DLS and particle number counting method, coupled with Brownian movement measurement in NTA. Moreover, by using the fluorescence mode in the

NTA, the iron-decorated solid lipid nanoparticles were detected and their size and concentration do not significantly change with respect to those obtained without the filter. The fact that the particles are fluorescent is a direct proof that the iron ions are decorating the SLN. Also, as control experiment, only $FeCl_3$ was added to SLN dispersion and measured using a fluorescence filter in the NTA analysis, which gave very weak signal, compared to SLN@CTAF. Indeed, for $FeCl_3$@SLN system, only weak Fe^{3+}-PEO of pluronic P123 interactions could be expected,[111] which are not strong enough to be adsorbed on the SLN surface. The adsorption of CTAF was further confirmed by zeta potential measurements. (Figure 3.3.2C) The values of ζ increased with the concentration of CTAF with respect to NHP, until a plateau was reached at 47 mV and 1.8 wt.% in magnetic-surfactant (16wt% of CTAF in NHP/CTAF mixture and 1.6% as Fe).

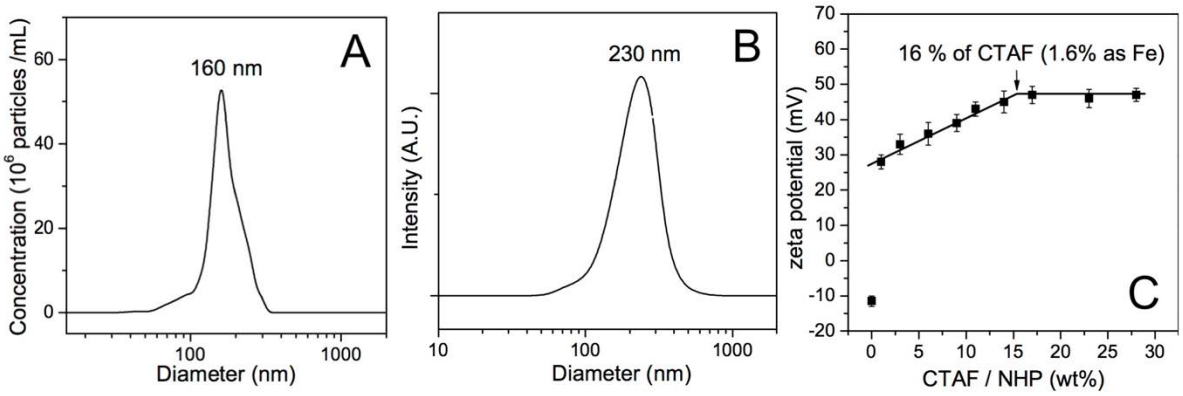

Figure 3.3.2. (A) Size distribution of SLN@CTAF obtained from NTA (particle number counting); (B) Size distribution of SLN@CTAF obtained from DLS (intensity); and (C) SLN zeta potential as a function of CTAF level.

Hierarchical meso–macroporous silica material containing iron oxide nanoparticles was prepared by a dual templating mechanism from a silica precursor (TMOS) and solid lipid nanoparticle dispersions stabilized in aqueous micellar solutions. Indeed, by adding TMOS, the SLN@CTAF dispersions were mineralized through the cooperative templating mechanism (CTM) of micelles and the transcription of SLN bead, used as mesopores and macropores templates, respectively. After TMOS addition, the reaction medium was kept at 40°C for 24 h for again, then at 100°C for 24 h to ensure high degree of hydrolysis/polycondensation of silica precursor. The obtained 'pasty' as-synthesized material was transferred into a petri dish and dried *in vacuo* at 30°C for 24 h. Then, the material was calcined at 550°C in air to remove the organic matter and to form iron oxide particles, giving the final product, Fe_2O_3@meso-macroporous silica. The amount of CTAF used to stabilize

the SLNs was of 1.8 wt%, which corresponds to the minimum for saturation of the SLN surface by magnetic surfactant, as determined using zeta potential measurement.

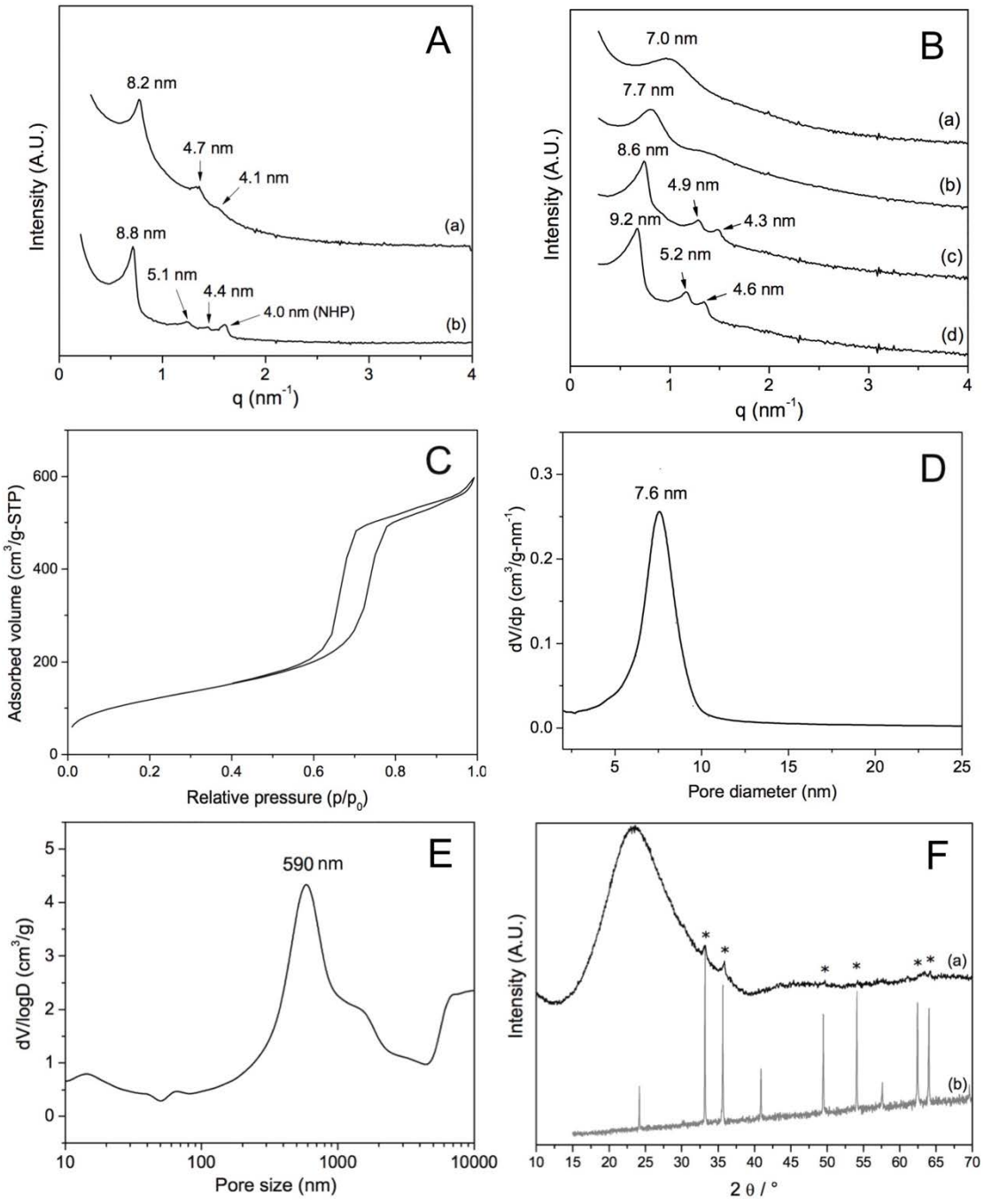

Figure 3.3.3. (A) SAXS patterns of (a) Fe_2O_3@meso-macroporous silica (the catalyst), (b) as-synthesized material; (B) SAXS patterns of meso-macroporous silica prepared with CTAF, (a) 3.0 wt.%, (b) 2.4 wt.%, (c) 1.2 wt.%, and (d) 0.6 wt.%; (C) N_2 adsorptio-desorption isotherms and (D) pore size distribution of the catalyst; (E) Macropore size distribution of the catalyst; (F) (a) XRD pattern of the catalyst, (b) commercial hematite from Sigma-Aldrich.

As shown in Figure 3.3.3A, small-angle X-ray scattering (SAXS) spectra indicated that silica materials synthesized with 1.8 wt.% of CTAF, before and after calcination, gave hexagonally

ordered mesopores, with three peaks at a characteristic ratio of 1:√3:2. For as-synthesized material before removal of organic matters (Figure 3.3.3Ab), it can also noticed that the characteristic repeat distance of the solid lipid L_β phase, indicated by (001) reflection position, remains at the same *q* value (1.57 nm^{-1}). Therefore, it seems that CTAF is not intercalating the hexylpalmitate in the core of the SLN, even during the mineralisation of SLN@CTAF dispersions.

Interestingly, silica materials prepared using more than 1.8 wt.% of CTAF gave only wormlike structure in mesopores with only one peak on the diffractogram (Figure 3.3.3B-a,b). At conc. > 1.8 wt.% in CTAF and 6.9 wt.% in P123, one can observe by DLS a bimodal distribution of micelles, centered on 13 nm (mixed P123/CTAF micelles) and 6 nm (CTAF micelles). In this case, the resulting wormlike network exhibits a smaller repetition distance by SAXS (7.7 nm) and smaller pore size as determined by N_2 adsorption/desorption isotherms (5.6 nm). At conc. < 1.8 wt.% in CTAF and 6.9 wt/% in P123 the hexagonal structuring of the silica material is obtained; the repeat distance (Figure 3.3.3B-c,d) and the pore size (Appendix) decrease with the increasing amount of the magnetic-surfactant, CTAF. This could be explained by the fact that the size of P123 micelles (at 6.9 wt.% P123) decreases by adding CTAF from 21 to 17 nm (0.6 wt.% CTAF), 15 nm (1.2 wt.% CTAF), and 14 nm (1.8 wt.% CTAF). This result could be due to increased interaction between CTAF surfactant and outer EO chain of P123, which results in disturbing of the self-assembly behaviour of P123 micelles.[112,113] This also suggests that the magnetic-surfactant is indeed distributed between the micelles of P123 forming the mesopores and the surface of SLN templating the macropores.

Indeed, the silica materials prepared with more than 1.8 wt.% in CTAF showed iron oxide particles with diameter of 50 – 100 nm and even rod-like iron oxide, due to the absence of well-ordered mesopores.[114] Moreover, some iron oxide particles are located outside the silica matrix as shown in Figure 3.3.4. Therefore, for further discussion on silica material, we focus only on the silica material synthesized under the optimal condition, and this material will be denoted as 'Fe_2O_3@meso-macroporous silica' or simply 'catalyst'.

N_2 absorption-desorption analysis of Fe_2O_3@meso-macroporous silica (catalyst) showed a type IV isotherm (Figure 3.3.3C), which is characteristic of mesoporous materials. The isotherm exhibits a hysteresis loop in accordance with pore necking, due to the interconnected mesopores. At high relative pressure ($P/P_0 > 0.9$), the N_2 adsorbed volume does not reach a plateau, indicating also the presence of secondary porosity such as

macropores. The pore size distribution obtained by the BJH method applied to the adsorption branch isotherm is centred on 7.6 nm (Figure 3.3.3D). The BET specific surface area and the mesopore volume are 432 m^2 g^{-1} and 0.82 cm^3 g^{-1}, respectively.

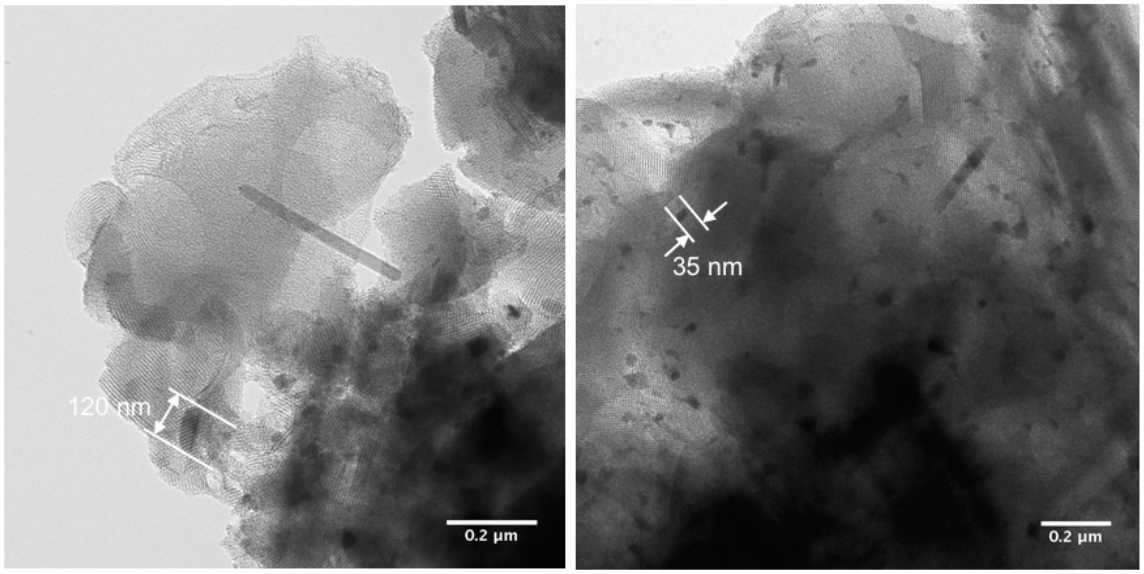

Figure 3.3.4. Two TEM images of silica material prepared using 3.0 wt.% of CTAF. It is clearly shown that the size of metallic particles (probably Fe_2O_3) is bigger than that of the silica material prepared in the optimal condition (Figure 3.3.5A)

The evidence of the macroporosity was confirmed by mercury intrusion porosimetry experiments (Figure 3.3.3E), which exhibits that the macropore size distribution of the silica material is centred at 590 nm, 2 times larger than the SLNs, with diameters about 230 nm. This could be due to the coalescence of lipid nanoparticles, melted at 100°C during the silica condensation, as described in our group's previous work.[115,116]

The mesopore and macropore structures were further confirmed by transmission electron microscopy (TEM) micrographs of Fe_2O_3@meso-macroporous silica, showing macropores with 200-400 nm, interconnected through hexagonally ordered mesopores of about 7.6 nm (Figure 3.3.5A). In addition, TEM images indicated the presence of 15-20 nm iron oxide particles encapsulated within the silica matrix. No particles were found on the outer silica surfaces, implying that iron oxide growth occurred exclusively inside the silica matrix.

XRD patterns (Figure 3.3.3F) of Fe_2O_3@meso-macroporous silica are characteristic of amorphous silica as evidenced by the broad band around 25°. Small, quite broad peaks are also faintly visible (indicated with an asterisk) and are in the same position as crystalline hematite (α-Fe_2O_3). The breadth of the Fe_2O_3 peaks embedded in silica is consistent with

nano-sized particles. Using the Scherrer equation[117] and peaks located at 32.8° and at 35.5° the average size of iron oxide nanoparticles was calculated as 15-20 nm which is in agreement with the values obtained by TEM. (Figure 3.3.6, Table 3.3.1)

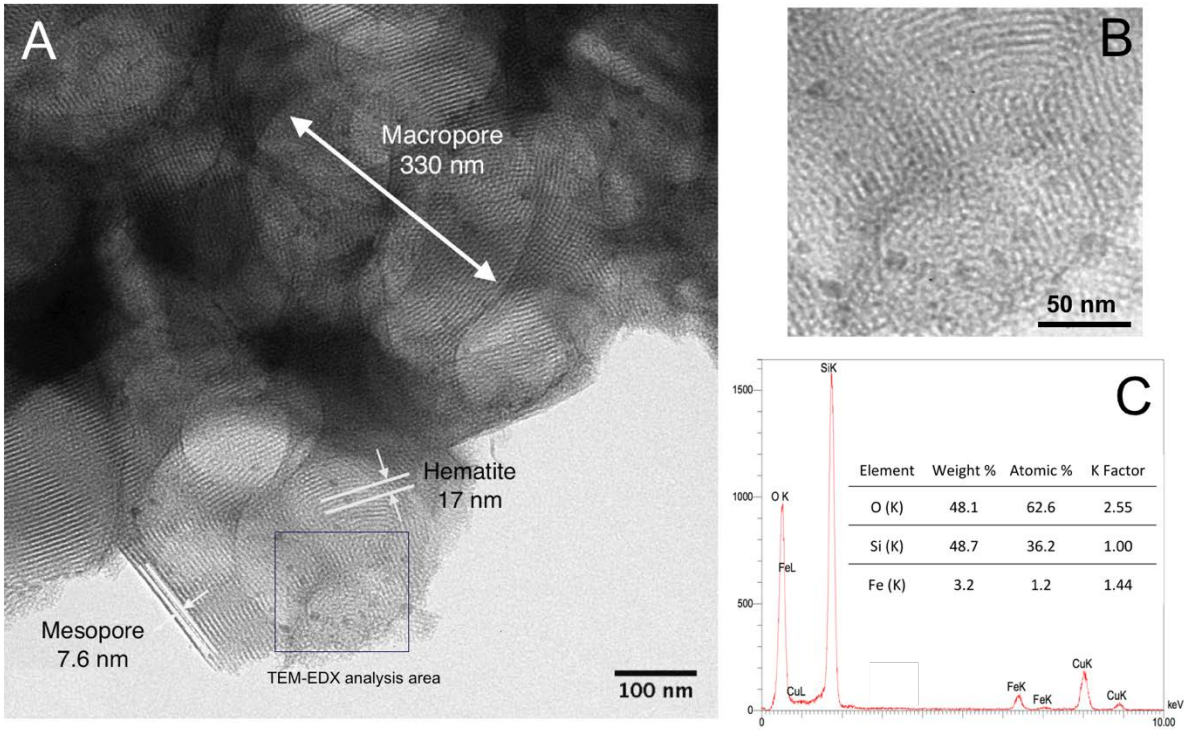

Figure 3.3.5. (A) TEM image of Fe_2O_3@meso-macroporous silica; (B) Zoomed image of TEM-EDX analysis area; (C) TEM-EDX analysis result.

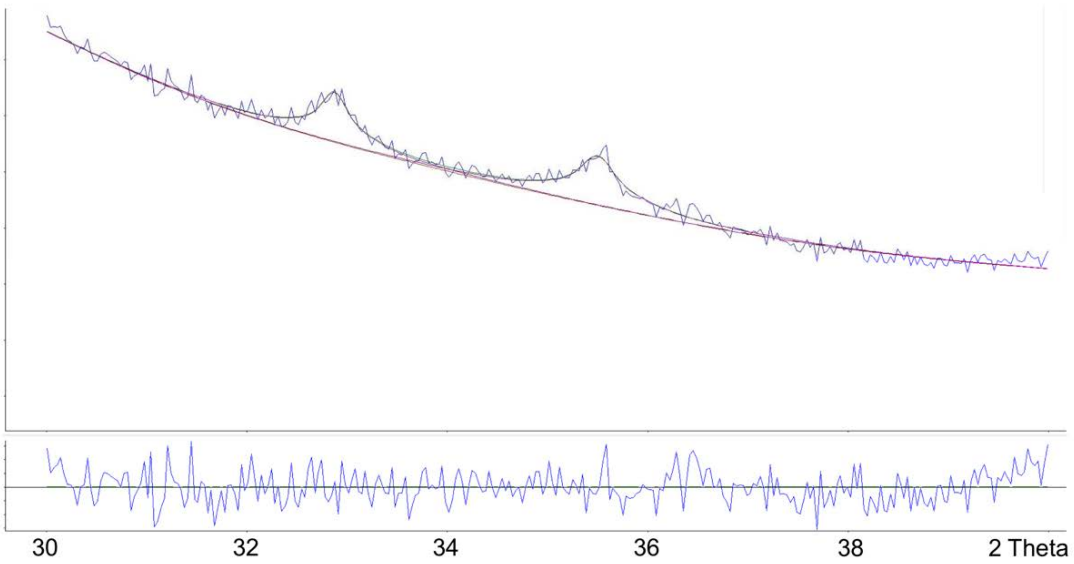

Figure 3.3.6. Zoomed image of XRD of Fe_2O_3@meso-macroporous silica.

Peak #	Position (2θ)	Cos (θ)	FWHM (2θ)	FWHM (rad)	Diameter (nm)
1	32.8	0.959	0.41	$7.16\ 10^{-3}$	20
2	35.5	0.952	0.55	$9.6\ 10^{-3}$	15

Table 3.3.1. Fe_2O_3 nanoparticles size calculated using Scherrer formula

The iron content (4 wt.% Fe, 5.7 wt.% Fe_2O_3) in Fe_2O_3@meso-macro-porous silica was determined using ICP-OES elemental analysis (Table 3.3.2), being in agreement with the TEM-EDX analysis (Figure 3.3.5B and 3.3.5C).

SiO_2	Al_2O_3	Fe_2O_3	MnO	MgO	CaO	Na_2O	K_2O	TiO_2	P_2O_5	Others	Total
87.23	0.04	5.73	0.02	< DL*	< DL	0.02	0.11	< DL	0.24	6.86	100.25

Table 3.3.2. ICP-OES elemental analysis (wt.%) of Fe_2O_3@meso-macroporous silica (DL = detection limit)

Catalytic performance of Fe_2O_3@meso-macroporous silica

Catalytic performance of Fe_2O_3@meso-macroporous silica was tested through dark Fenton-like degradation of methylene blue (MB) in aqueous solution, with H_2O_2 as initiator. Indeed, Fenton-like reactions are considered as effective advanced oxidation processes (AOPs), which are replacing traditional methods like chlorination, for complete dye degradation in water.[118,119] Fenton-like reactions are based on the catalytic production of hydroxyl radicals, HO•, which can degrade organic compounds under mild conditions. The general mechanism of Fenton-like reaction can be described as follows.[119]

$$Fe(III) + H_2O_2 \rightarrow Fe(II) + HO_2\bullet + H^+$$

$$Fe(II) + H_2O_2 \rightarrow Fe(III) + HO\bullet + HO^-$$

$$Fe(III) + HO_2\bullet \rightarrow Fe(II) + O_2 + H^+$$

$$HO_2\bullet \rightarrow H^+ + O_2\bullet^-$$

$$HO\bullet + H_2O_2 \rightarrow HO_2\bullet + H_2O$$

$$\underline{Fe(II) + HO\bullet \rightarrow Fe(III) + HO^-}$$

$$HO\bullet + HO_2\bullet \rightarrow O_2 + HO_2$$

$$2HO_2\bullet \rightarrow H_2O_2 + O_2$$

Organic compound + HO· → degradation

Underlined reaction above indicates a possible scavenger step of real active oxidant, HO· by iron oxide surface, which was partially reduced in Fe(II).

Although Fenton-like reactions are powerful for most of iron-based materials like iron oxide, rapid scavenging of HO· on the iron oxide surface, and a possible aggregation of iron species in aqueous medium could limit wide applications. Thus, the accessibility of contaminants to the reaction site should be improved using support material such as meso-macroporous silica. Moreover, satisfying dispersion of iron species over matrix is also needed for practical application of Fenton-like reactions.[99]

The catalytic assays were performed onto iron oxide@meso-macroporous silica with hexagonally ordered mesopores that has the highest iron content (4.0 wt.% Fe), meaning the one obtained with 1.8 wt.% of CTAF. The catalysis was performed under similar conditions to those reported by Cui *et al.*[105] for direct comparison of catalytic performance of the silica material in this study. (20 mL of 50 ppm methylene blue, 1.2 mL of 30 wt.% of H_2O_2 in dark condition, Figure 3.3.7)

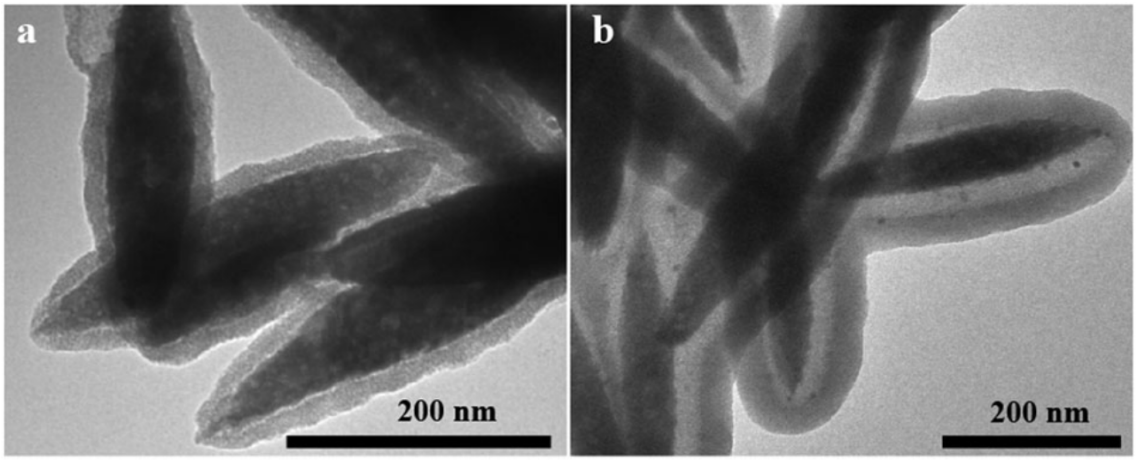

Figure 3.3.7 TEM image of Cui et al's catalyst, the yolk-shell structured Fe_2O_3@mesoporous SiO2 composite with tuned void space size ((a) 5 nm; (b) 40 nm). Methylene blue degradation data cited in this study is the result for the material with void space of 40 nm (b).

As shown in Figure 3.3.8A-a, b, c, in the absence of, either catalyst or H_2O_2, no dye degradation occurred, showing the decrease of concentration, only due to the adsorption of methylene blue on the catalyst. The extent of adsorption of methylene blue in the bare silica is slightly higher than into Fe_2O_3@silica that has a smaller surface area (582 m^2 g^{-1} for bare silica *vs* 432 m^2 g^{-1} for Fe_2O_3@silica). However, in both cases, the porous catalyst adsorbs

0.053 mg MB m^{-2} SiO_2, which is in good agreement with the result reported for other mesoporous silica, 0.050 mg/m^2.[120] This phenomenon is well documented in the literature[120] and it is driven by both electrostatic and hydrophilic interactions between the silica surface and the methylene bleu. Seeing that the amount of methylene bleu adsorbed on the catalyst is similar as reported in the literature, it is supposed that the silica surface coverage by methylene blue is close to a monolayer, and methylene blue is coordinated to silanol (Si-OH) groups of silica surface.[121].

When the maximum adsorption is reached (t=0) the oxidant is added to the solution. Then, a rapid decrease of methylene blue was observed, as 83% of methylene blue degraded after 7 h (Figure 3.3.8A-d). With the catalyst of this work, which contains twelve times less catalytic active site, Fe_2O_3, (15 mg of silica containing 0.86 mg *vs* 10 mg of Fe_2O_3) the conversion rate is similar with Cui's catalyst (Figure 3.3.8A-e). This gain of performance could be due to the smaller nanoparticle size of Fe_2O_3 (15-20 nm *vs* ~100 nm) having higher active surface/iron content, but also to the presence of interconnected macropores through a mesopore network that provides higher diffusion, throughput, or in other words, a decrease of internal flow resistance.

After 12 h a colourless solution with no UV-Vis signal (Figure 3.3.8B-b) was obtained, indicating that all methylene blue in solution had been degraded. Moreover, the extent of methylene blue degradation was examined by total organic carbon (TOC) analysis (Figure 3.3.8B-a). The TOC value of the solution was reduced to 23% after 7 h and to less than 5% after 14 h, showing 2.3 mg carbon/L that is close to the mean value of TOC (2.7 mg carbon/L) measured on more than 400 groundwater samples from 8 European Union countries.[122] This result demonstrates that almost no organic by-products were produced during the degradation. For example in water treatment, total degradation of pollutants is very important, because by-products could be more toxic than the pollutants. This is the case of phenol when considering the degradation of methylene blue.[123]

Figure 3.3.8D shows the variation of methylene blue adsorbed in the meso-macroporous material during Fenton-like reaction. The dye was extracted in ethanol and the quantification was by UV analysis. It appears that total degradation of the methylene blue adsorbed in the material is reached after 20 h. Indeed, the catalyst changes color from dark blue (t = 0), dark green (t = 7) to yellow green (t=14 h) and finally recovers its original colour, yellowish (t = 20h). This rate is a little slower than that of methylene blue in aqueous solution, due to limited movement of methylene blue adsorbed on the silica surface of the catalyst.

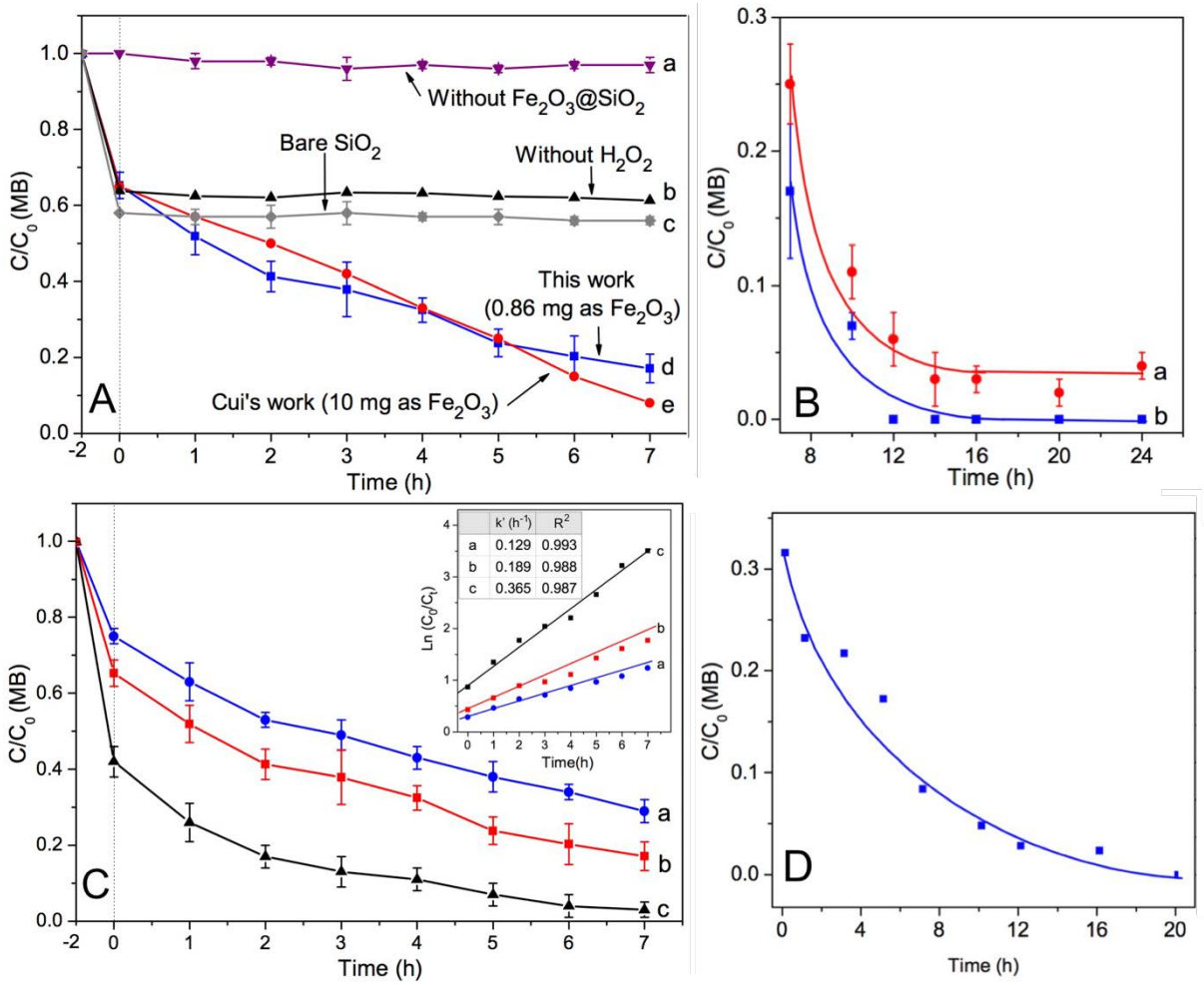

Figure 3.3.8. (A) Dark Fenton-like degradation of methylene blue in solution, (a) for the blind experiment with only H_2O_2 (without any catalyst), (b) for the catalyst made in this work, without H_2O_2, (c) for bare SiO_2, (d) for the catalyst made in this work, (e) for york-shell structured Fe_2O_3@mesoporous silica (reported by Cui et al.[105]); (B) Extended study of methylene blue degradation, using 15mg of catalyst, analysed by (a) UV-Vis and (b) Total Organic Carbon (TOC) measurement; (C) Effect of catalyst amount on methylene blue degradation for (a) 10 mg, (b) 15 mg and (c) 30 mg of catalyst, degradation rate fitted using pseudo-first-order model (inset, k' is the rate constant, R^2 is squared correlation coefficient); (D) Degradation of methylene blue adsorbed on the catalyst, 15 mg of catalyst used, 32.3% of MB adsorbed before H_2O_2 addition.

Finally, it was investigated the influence of the amount of catalyst on the reaction rate. Up to 7 h, methylene blue degradation rate is enhanced as the amount of catalyst increases. The reaction rate could be expressed by a pseudo-first-order model, (Figure 3.3.8C) showing that an increase of the rate constant (k') is in linear relationship with an increase of the amount of catalyst. This result also supports that in this range of concentration, the reaction rate depends only on the amount of the catalyst, and thus the direct comparison of the performance of the catalyst in this study with Cui's catalyst is adequate.

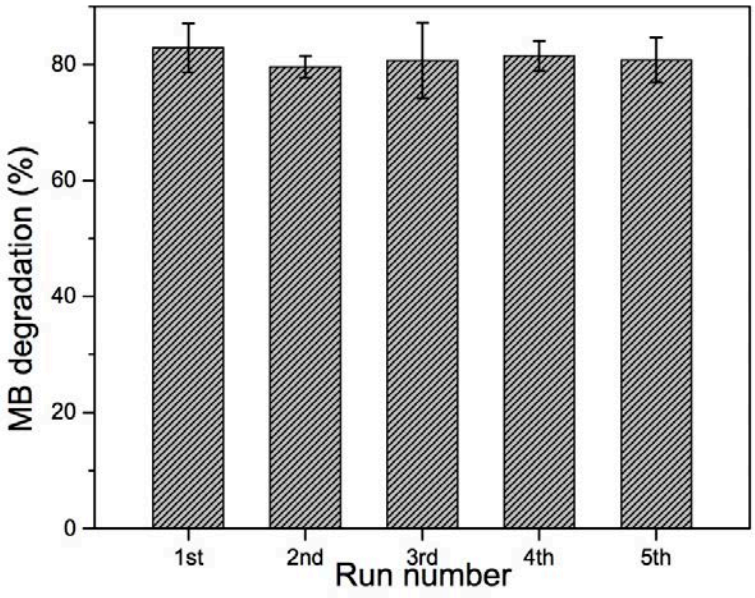

Figure 3.3.9. Repeated usability test of catalyst, 15 mg of catalyst used, and all experiments for catalyst reuse were performed for 7 h.

Reusability studies show (Figure 3.3.9) that after 5 runs, catalytic performance of the catalyst remained quasi-constant (the conversion of methylene blue is of about 83% for 7 h). This result clearly suggests that Fe leaching is limited, due to the silica support and the mild reaction conditions with pH ~ 4.3, in which Fe_2O_3 solubilisation does not occur.[124]

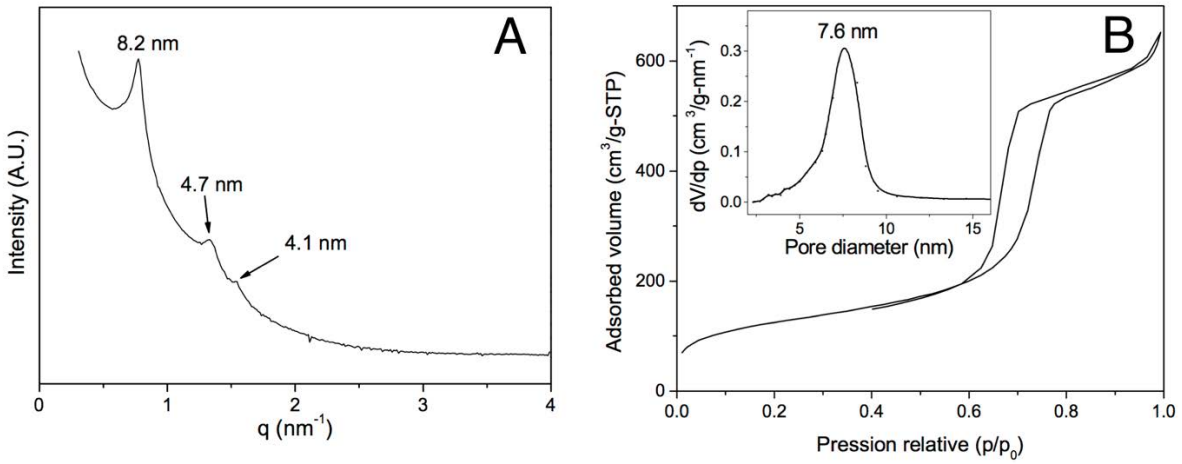

Figure 3.3.10. (A) SAXS patterns of Fe_2O_3@meso-macroporous silica after 5 runs; (B) N_2 adsorption–desorption isotherms and pore size distribution (insert) of Fe_2O_3@meso-macroporous silica after 5 runs.

Moreover, SAXS and N_2 adsorption-desorption studies (Figure 3.3.10) of the catalyst after 5 runs showed that the mesoporous network remained unaltered, giving 441 m^2 g^{-1} as BET specific surface area and 0.87 cm^3 g^{-1} as mesopore volume, which are similar as fresh

catalyst's values. Therefore, it is believed that combining with the application of simple magnetic field like a magnet, the catalyst could be of potential interest for environmental applications including water treatment.

3.3.4 Conclusion

The synthesis of Fe_2O_3 nanoparticles supported in meso-mesoporous silica through a novel and low-cost template, based on solid lipid nanoparticles (SLN) and iron-containing magnetic surfactant has been optimized. The silica material has hexagonally ordered mesopores and interconnected macropores as well as iron oxide nanoparticles of 15-20 nm in diameter. This Fe_2O_3@meso-macroporous silica showed excellent catalytic activity for dark Fenton-like reactions in methylene blue degradation: complete degradation could be achieved even with a small amount of Fe_2O_3,[110,125] due to high surface area/weight ratio of iron oxide and enhanced diffusion owing to macroporosity. This strategy could be used for other metallic or metal oxide nanoparticles embedded in silica matrices,[126,127] for new applications in catalytic processes.

References

1 F. Mancin, P. Scrimin, P. Tecilla and U. Tonellato, *Coordination Chemistry Reviews*, 2009, **253**, 2150–2165.

2 R. E. Del Sesto, T. M. McCleskey, A. K. Burrell, G. A. Baker, J. D. Thompson, B. L. Scott, J. S. Wilkes and P. Williams, *Chem. Commun.*, 2008, 447–449.

3 E. Santos, J. Albo and A. Irabien, *RSC Adv.*, 2014, **4**, 40008–40018.

4 P. Brown, A. Bushmelev, C. P. Butts, J. Cheng, J. Eastoe, I. Grillo, R. K. Heenan and A. M. Schmidt, *Angew. Chem. Int. Ed.*, 2012, **51**, 2414–2416.

5 P. Brown, C. P. Butts, J. Cheng, J. Eastoe, C. A. Russell and G. N. Smith, *Soft Matter*, 2012, **8**, 7545–7546.

6 P. Brown, C. P. Butts, J. Eastoe, S. Glatzel, I. Grillo, S. H. Hall, S. Rogers and K. Trickett, *Soft Matter*, 2012, **8**, 11609–11612.

7 G. P. Kumar and P. Rajeshwarrao, *Acta Pharmaceutica Sinica B*, 2011, **1**, 208–219.

8 C. Sinico and A. M. Fadda, *Expert Opin. Drug Deliv.*, 2009, **6**, 813–825.

9 S. H. Yuk, K. S. Oh, H. Koo, H. Jeon, K. Kim and I. C. Kwon, *Biomaterials*, 2020, **32**, 7924–7931.

10 R. P. Brinkhuis, F. P. J. T. Rutjes and J. C. M. van Hest, *Polym. Chem.*, 2011, **2**, 1449–14.

11 D. P. Debecker, C. Faure, M.-E. Meyre, A. Derré and E. M. Gaigneaux, *Small*, 2008, **4**, 1806–1812.

12 K. Watanabe, S.-Y. Takizawa and S. Murata, *Chem. Lett.*, 2011, **40**, 345–347.

13 Adamala, K.; Szostak, J. W. *Nat Chem*. 2013, **5**, 495–501.

14 A. Al Bawab, N. Heldt and Y. Li, *Journal of Dispersion Science and Technology*, 2005, **26**, 251–256.

15 P. Walde, *Bioessays*, 2010, **32**, 296–303.

16 C. Zhou, X. Cheng, Y. Yan, J. Wang and J. Huang, *Langmuir*, 2014, **30**, 3381–3386.

17 J. Du, Y. Tang, A. L. Lewis and S. P. Armes, *J. Am. Chem. Soc.*, 2005, **127**, 17982–17983.

18 H. Wang, F. Xu, Y. Wang, X. Liu, Q. Jin and J. Ji, *Polym. Chem.*, 2013, **4**, 3012–8.

19 T.-B. Ren, Y. Feng, Z.-H. Zhang, L. Li and Y.-Y. Li, *Soft Matter*, 2011, **7**, 2329–3.

20 Q. Li, X. Chen, B. Jing, Y. Zhao and F. Ma, *Colloids Surf., A*, 2010, **355**, 146–150.

21 S. Lecommandoux, O. Sandre, F. Ch cot, J. Rodriguez-Hernandez and R. Perzynski, *Adv. Mater.*, 2005, **17**, 712–718.

22 G. Beaune, B. Dubertret, O. Clément, C. Vayssettes, V. Cabuil and C. Ménager, *Angew. Chem. Int. Ed.*, 2007, **46**, 5421–5424.

23 F. Ye, Å. Barrefelt, H. Asem, M. Abedi-Valugerdi, I. El-Serafi, M. Saghafian, K. Abu-Salah, S. Alrokayan, M. Muhammed and M. Hassan, *Biomaterials*, 2014, **35**, 3885–3894.

24 C. Sanson, O. Diou, J. Thevenot, E. Ibarboure, A. Soum, A. Brûlet, S. Miraux, E. Thiaudière, S. Tan, A. Brisson, V. Dupuis, O. Sandre and S. Lecommandoux, *ACS Nano*, 2011, **5**, 1122–1140.

25 D. Niu, X. Wang, Y. Li, Y. Zheng, F. Li, H. Chen, J. Gu, W. Zhao and J. Shi, *Adv. Mater.*, 2013, **25**, 2686–2692.

26 X. Yang, S. Pilla, J. J. Grailer, D. A. Steeber, S. Gong, Y. Chen and G. Chen, *J. Mater. Chem.*, 2009, **19**, 5812–5817.

27 X. Yang, J. J. Grailer, I. J. Rowland, A. Javadi, S. A. Hurley, V. Z. Matson, D. A. Steeber and S. Gong, *ACS Nano*, 2010, **4**, 6805–6817.

28 P. Arosio, J. Thevenot, T. Orlando, F. Orsini, M. Corti, M. Mariani, L. Bordonali, C. Innocenti, C. Sangregorio, H. Oliveira, S. Lecommandoux, A. Lascialfari and O. Sandre, *J. Mater. Chem. B*, 2013, **1**, 5317–12.

29 M.-E. Meyre, R. Clérac, S. Mornet, E. Duguet, F. Dole, F. Nallet, O. Lambert, S. Trépout and C. Faure, *Phys. Chem. Chem. Phys.*, 2010, **12**, 12794–12801.

30 J. Zhou, M. Chen and G. Diao, *ACS Appl. Mater. Interfaces*, 2014, **6**, 18538–18542.

31 P. Brown, A. Bushmelev, C. P. Butts, J.-C. Eloi, I. Grillo, P. J. Baker, A. M. Schmidt and J. Eastoe, *Langmuir*, 2013, **29**, 3246–3251.

32 S. Kim, P. Durand, T. Roques-Carmes, J. Eastoe and A. Pasc, *Langmuir*, 2015, **31**, 1842–1849.

33 G. N. Smith and J. Eastoe, *J. Colloid Interface Sci.*, 2014, **426**, 252–255.

34 P. Brown, A. M. Khan, J. P. K. Armstrong, A. W. Perriman, C. P. Butts and J. Eastoe, *Adv. Mater.*, 2012, **24**, 6244–6247.

35 S. Kim, C. Bellouard, A. Pasc, E. Lamouroux, J.-L. Blin, C. Carteret, Y. Fort, M. Emo, P. Durand and M.-J. Stébé, *J. Mater. Chem. C*, 2013, **1**, 6930–6934.

36 C. Lin, J. Zhao and R. Jiang, *Chem. Phys. Lett.*, 2008, **464**, 77–81.

37 F. P. Hubbard, G. Santonicola, E. W. Kaler and N. L. Abbott, 2005, **21**, 6131–6136.

38 http://www.sasview.org/index.html

39 A. Shioi and T. A. Hatton, *Langmuir*, 2002, **18**, 7341–7348.

40 A. J. O'Connor, T. A. Hatton, A. Bose, *Langmuir*, 1997, **13**, 6931–6940.

41 M. de Barros e Silva Botelho, J. M. Fernandez-Hernandez, T. B. de Queiroz, H. Eckert, L. De Cola and A. S. S. de Camargo, *J. Mater. Chem.*, 2011, **21**, 8829–8835.

42 N. Hondow, J. Harowfield, G. Koutsantonis, G. Nealon and M. Saunders, *Microporous and Mesoporous Mater.*, 2012, **151**, 264–270.

43 K. Trickett, D. Xing, J. Eastoe, R. Enick, A. Mohamed, M. J. Hollamby, S. Cummings, S. E. Rogers and R. K. Heenan, *Langmuir*, 2010, **26**, 4732–4737.

44 P. C. Griffiths, I. A. Fallis, C. James, I. R. Morgan, G. Brett, R. K. Heenan, R. Schweins, I. Grillo and A. Paul, *Soft Matter*, 2010, **6**, 1981–1989.

45 M. J. Danks, H. B. Jervis, M. Nowotny, W. Zhou, T. A. Maschmeyer and D. W. Bruce, *Catalysis Letters*, 2002, **82**, 95–98.

46 T. Owen and A. Butler, *Coord. Chem. Rev.*, 2011, **255**, 678–687.

47 P. Gong, Z. Chen, Y. Chen, W. Wang, X. Wang and A. Hu, *Chem. Commun.*, 2011, **47**, 4240–4242.

48 R. S. Kumar and S. Arunachalam, *Biophysical Chemistry*, 2008, **136**, 136–144.

49 P. Brown, C. P. Butts, J. Eastoe, E. Padrón Hernández, F. L. de A. Machado and R. J. de Oliveira, *Chem. Commun.*, 2013, **49**, 2765.

50 S. S. Lee, S. N. Riduan, N. Erathodiyil, J. Lim, J. L. Cheong, J. Cha, Y. Han and J. Y. Ying, *Chem. Eur. J.*, 2012, **18**, 7394–7403.

51 S. Gandhi, S. Sethuraman and U. M. Krishnan, *Macromol. Res.*, 2013, **21**, 833–842.

52 J. Liu, S. Z. Qiao, Q. H. Hu and G. Q. Max Lu, *Small*, 2011, **7**, 425–443.

53 J. M. Rosenholm, C. Sahlgren and M. Lindén, *Nanoscale*, 2010, **2**, 1870–14.

54 M. Hasanzadeh, N. Shadjou and E. Omidinia, *Colloids Surf., B*, 2013, **108**, 52–59.

55 Y. Wang, B. Li, L. Zhang, P. Li, L. Wang and J. Zhang, *Langmuir*, 2012, **28**, 1657–1662.

56 H.-J. Xu, X. Wan, Y. Geng and X.-L. Xu, *Curr. Org. Chem.*, 2015, 17, 1034–1050.

57 J. Wu, P. Su, J. Huang, S. Wang and Y. Yang, *J. Colloid Interface Sci.*, 2013, **399**, 107–114.

58 Y. Wang, S. Liang, B. Chen, F. Guo, S. Yu and Y. Tang, *PLoS ONE*, 2013, **8**, e65634.

59 C. M. Babu, B. Palanisamy, B. Sundaravel, M. Palanichamy and V. Murugesan, *J. Nanosci. Nanotechnol.*, 2013, **13**, 2517–2527.

60 Z. He, D. Liu, R. Li, Z. Zhou and P. Wang, *Analytica Chimica Acta*, 2012, **747**, 29–35.

61 N. Ž. Knežević, E. Ruiz-Hernández, W. E. Hennink and M. Vallet-Regí, *RSC Adv.*, 2013, **3**, 9584–9583.

62 D. Tarn, C. E. Ashley, M. Xue, E. C. Carnes, J. I. Zink and C. J. Brinker, *Acc. Chem. Res.*, 2013, **46**, 792–801.

63 Y. Liu and N. Zhang, *Biomaterials*, 2012, **33**, 5363–5375.

64 S. Zhang, Z. Chu, C. Yin, C. Zhang, G. Lin and Q. Li, *J. Am. Chem. Soc.*, 2013, **135**, 5709–5716.

65 H. Wen, J. Guo, B. Chang and W. Yang, *Eur J Pharm Biopharm*, 2013, **84**, 91–98.

66 S. Zhu, Z. Zhou and D. Zhang, *ChemPhysChem*, 2007, **8**, 2478–2483.

67 D. Carta, S. Bullita, M. F. Casula, A. Casu, A. Falqui and A. Corrias, *ChemPlusChem*, 2013, **78**, 364–374.

68 M. Döbbelin, V. Jovanovski, I. Llarena, L. J. Claros Marfil, G. Cabañero, J. Rodriguez and D. Mecerreyes, *Polym. Chem.*, 2011, **2**, 1275–1279.

69 N. K. Raman, M. T. Anderson and C. J. Brinker, *Chem. Mater*., 1996, **8**, 1682–1701.

70 Q. Huo, D. I. Margolese, U. Ciesla, P. Feng, T. E. Gier, P. Sieger, R. Leon, P. M. Petroff, F. Schüth and G. D. Stucky, *Nature*, 1994, **368**, 317–321

71 Q. Huo, D. I. Margolese and G. D. Stucky, *Chem. Mater.*, 1996, **8**, 1147–1160.

72 J. S. Beck, J. C. Vartuli and W. J. Roth, *J. Am. Chem. Soc.*, 1992, **114**, 10834–10843.

73 Y. Li, Z. Feng, Y. Lian, K. Sun, L. Zhang, G. Jia, Q. Yang and C. Li, *Microporous and Mesoporous Mater.*, 2005, **84**, 41–49.

74 H. Xin, J. Liu, F. Fan, Z. Feng, G. Jia, Q. Yang and C. Li, *Microporous and Mesoporous Mater.*, 2008, **113**, 231–239.

75 B. Li, J. Xu, J. Liu, S. Zuo, Z. Pan and Z. Wu, *J. Colloid Interface Sci.*, 2012, **366**, 114–119.

76 M. A. Halcrow, *Spin-Crossover Materials*, John Wiley & Sons, 2013.

77 P. Á. Szilágyi, S. Dorbes, G. Molnár, J. A. Real, Z. Homonnay, C. Faulmann and A. Bousseksou, *J. Phys. Chem. Solids*, 2008, **69**, 2681–2686.

78 G. Félix, W. Nicolazzi, L. Salmon, G. Molnár, M. Perrier, G. Maurin, J. Larionova, J. Long, Y. Guari and A. Bousseksou, *Phys. Rev. Lett.*, 2013, **110**, 235701–234705.

79 B. Li, J. Xu, J. Liu, Z. Pan, Z. Wu, Z. Zhou and X. Pang, *Materials Letters*, 2012, **78**, 147–149.

80 A. Pasc-Banu, C. Sugisaki, T. Gharsa, J.-D. Marty, I. Gascon, M. Krämer, G. Pozzi, B. Desbat, S. Quici, I. Rico-Lattes and C. Mingotaud, *Chem. Eur. J.*, 2005, **11**, 6032–6039.

81 A. Pasc-Banu, C. Sugisaki, T. Gharsa, J.-D. Marty, I. Gascon, G. Pozzi, S. Quici, I. Rico-Lattes and C. Mingotaud, *Angew. Chem. Int. Ed.*, 2004, **43**, 6174–6177.

82 S. F. J. Hackett, R. M. Brydson, M. H. Gass, I. Harvey, A. D. Newman, K. Wilson and A. F. Lee, *Angew. Chem. Int. Ed.*, 2007, **46**, 8593–8596.

83 S. Wang, A. Y. Borisevich, S. N. Rashkeev, M. V. Glazoff, K. Sohlberg, S. J. Pennycook and S. T. Pantelides, *Nat Mater*, 2004, **3**, 143–146.

84 V. R. Calderone, N. R. Shiju, D. C. Ferré and G. Rothenberg, *Green Chem.*, 2011, **13**, 1950–11.

85 Y. Sugano, Y. Shiraishi, D. Tsukamoto, S. Ichikawa, S. Tanaka and T. Hirai, *Angew. Chem. Int. Ed.*, 2013, **52**, 5295–5299.

86 H. He, X. Xu, H. Wu and Y. Jin, *Adv. Mater.*, 2012, **24**, 1736–1740.

87 R. C. F. Cheung, J. H. Wong and T. B. Ng, *Appl. Microbiol. Biotechnol.*, 2012, **96**, 1411–1420.

88 M. A. De León, J. Castiglioni, J. Bussi and M. Sergio, *Catalysis Today*, 2008, **133-135**, 600–605.

89 E. G. Garrido-Ramírez, B. K. G. Theng and M. L. Mora, *Applied Clay Science*, 2010, **47**, 182–192.

90 Z. Huang, F. Cui, H. Kang, J. Chen, X. Zhang and C. Xia, *Chem. Mater.*, 2008, **20**, 5090–5099.

91 K. Kobayashi, R. Kitaura, Y. Kumai, Y. Goto, S. Inagaki and H. Shinohara, *Carbon*, 2009, **47**, 722–730.

92 W. Chen, X. Pan, M.-G. Willinger, D. S. Su and X. Bao, *J. Am. Chem. Soc.*, 2006, **128**, 3136–3137.

93 Z. Sun, B. Sun, M. Qiao, J. Wei, Q. Yue, C. Wang, Y. Deng, S. Kaliaguine and D. Zhao, *J. Am. Chem. Soc.*, 2012, **134**, 17653–17660.

94 D. S. Su, S. Perathoner and G. Centi, *Chem. Rev.*, 2013, **113**, 5782–5816.

95 N. Ferroudj, J. Nzimoto, A. Davidson, D. Talbot, E. Briot, V. Dupuis, A. Bée, M. S. Medjram and S. Abramson, *Appl. Catal., B*, 2013, **136-137**, 9–18.

96 J. A. Botas, J. A. Melero, F. Martínez and M. I. Pariente, *Catalysis Today*, 2010, **149**, 334–340.

97 H. Zhang, T. J. Bandosz and D. L. Akins, *Chem. Commun.*, 2011, **47**, 7791–3.

98 N. R. Srinivasan and R. Bandyopadhyaya, *Microporous and Mesoporous Mater.*, 2012, **149**, 166–171.

99 A. L.-T. Pham, C. Lee, F. M. Doyle and D. L. Sedlak, *Environ. Sci. Technol.*, 2009, **43**, 8930–8935.

100 Y. Li, Y. Chen, L. Li, J. Gu, W. Zhao, L. Li and J. Shi, *Appl. Catal., A*, 2009, **366**, 57–64.

101 Y. Sun, S. Walspurger, J.-P. Tessonnier, B. Louis and J. Sommer, *Appl. Catal., A*, 2006, **300**, 1–7.

102 I. Ursachi, A. Stancu and A. Vasile, *J. Colloid Interface Sci.*, 2012, **377**, 184–190.

103 A. N. Soon and B. H. Hameed, *Appl. Catal., A*, 2013, **450**, 96–105.

104 C. M. A. Parlett, K. Wilson and A. F. Lee, *Chem. Soc. Rev.*, 2013, **42**, 3876–18.

105 Z.-M. Cui, Z. Chen, C.-Y. Cao, L. Jiang and W.-G. Song, *Chem. Commun.*, 2013, **49**, 2332–3.

106 S. I. R. Castillo, C. E. Pompe, J. van Mourik, D. M. A. Verbart, D. M. E. Thies-Weesie, P. E. de Jongh and A. P. Philipse, *J. Mater. Chem. A*, 2014, **2**, 10193–9.

107 T. Zeng, X. Zhang, S. Wang, Y. Ma, H. Niu and Y. Cai, *Chem. Eur. J.*, 2014, **20**, 6474–6481.

108 E. Neyens and J. Baeyens, *J. Hazard. Mater.*, 2003, **98**, 33–50.

109 F. Martínez, G. Calleja, J. A. Melero and R. Molina, *Appl. Catal., B*, 2005, **60**, 181–190.

110 T. T. Vu and G. Marbán, *Appl. Catal., B*, 2014, **152-153**, 51–58.

111 R. Zhang, H. Dai, Y. Du, L. Zhang, J. Deng, Y. Xia, Z. Zhao, X. Meng and Y. Liu, *Inorg. Chem.*, 2011, **50**, 2534–2544.

112 R. Cardoso da Silva, G. Olofsson, K. Schillén and W. Loh, *J. Phys. Chem. B*, 2002, **106**, 1239–1246.

113 W.-H. Zhang, L. Zhang, J. Xiu, Z. Shen, Y. Li, P. Ying and C. Li, *Microporous and Mesoporous Mater.*, 2006, **89**, 179–185.

114 M. A. Ballem, F. Söderlind, P. Nordblad, P.-O. Käll and M. Odén, *Microporous and Mesoporous Mater.*, 2013, **168**, 221–224.

115 R. Ravetti-Duran, J.-L. Blin, M.-J. Stébé, C. Castel and A. Pasc, *J. Mater. Chem.*, 2012, **22**, 21540–21548.

116 A. Pasc, J.-L. Blin, M.-J. Stébé and J. Ghanbaja, *RSC Adv.*, 2011, **1**, 1204–1206.

117 U. Holzwarth and N. Gibson, *Nature Nanotech.*, 2011, **6**, 534–534.

118 M. A. Oturan and J.-J. Aaron, *Crit. Rev. Environ. Sci. Technol.*, 2014, **44**, 2577–2641.

119 B. Ensing, F. Buda and E. J. Baerends, *J. Phys. Chem. A*, 2003, **107**, 5722–5731.

120 K. Y. Ho, G. McKay and K. L. Yeung, *Langmuir*, 2003, **19**, 3019–3024.

121 C. Kaewprasit, E. Hequet, N. Abidi, J. P. Gourlot, *The Journal of Cotton Science*, 1998, **2**, 164–173

122 D.C. Gooddy, K. Hinsby, Organic Quality of Groundwaters, in Natural Groundwater Quality; Edmunds, W. M., Shand, P., Eds.;Wiley- Blackwell Publishing, Ltd: Oxford, UK, 2008.

123 A. Houas, H. Lachheb, M. Ksibi and E. Elaloui, *Appl. Catal., B* 2001, **31**, 145–157.

124 J.-H. Jang, B. A. Dempsey and W. D. Burgos, *Environ. Sci. Technol.*, 2007, **41**, 7303–7308.

125 Z.-M. Cui, Z. Chen, C.-Y. Cao, L. Jiang and W.-G. Song, *Chem. Commun.*, 2013, **49**, 2332–2334.

126 J. Strunk, W. C. Vining and A. T. Bell, *J. Phys. Chem. C*, 2011, **115**, 4114–4126.

127 Y. Xu, D. Chen, X. Jiao and K. Xue, *J. Phys. Chem. C*, 2007, **111**, 16284–16289.

Résumé en français (Chapitre 3)

Bien que les tensioactifs contenant des ions métalliques ont été développés depuis plus d'une dizaine d'années, leurs propriétés magnétiques n'ont pas été encore bien étudiées.[1] Une des raisons probables est que ces tensioactifs ont des ions métalliques au niveau de la tête polaire, qui sont stabilisés par des ligands. En raison de leur structure moléculaire, les ions métalliques dans ces composés ont pu être isolés et leurs faibles interactions à longue portée les empêchent d'être magnétiquement actifs.[2]

Dans le domaine des liquides ioniques, les liquides ioniques métalliques (MIL), qui combinent les propriétés générales des liquides ioniques à température ambiante (RTIL) avec celles qui sont associées avec des ions métalliques qui one sur fortes réactivités sous un champ magnétique externe, font l'objet de plusieurs publications.[3] Cependant, la plupart des liquides ioniques métalliques décrits sont limités à des dérivés d'imidazolium contenant une courte chaîne alkyle, qui ne présente pas de propriétés notables de tensioactifs.

Cependant, une avancée importante a été apportée par le groupe d'*Eastoe* au Royaume-Uni, qui combine les propriétés intéressantes des liquides ioniques (MIL) et tensioactifs classiques contenant des ions métalliques.[4] *Eastoe et al*. ont synthétisé, pour la première fois, des tensioactifs ioniques liquides qui ont des ions métalliques magnéto-actif tel que le 1-méthyl-3-decylimidazolium tétrachloroferrate. La synthèse de ces tensioactifs ioniques liquides magnétiques (MILS) peut être facilement réalisée en mélangeant un trihalogénure de fer avec un tensioactif cationique à quantité stoechiométrique. Les tensioactifs ioniques liquides magnétiques possèdent une concentration de micelle critique (CMC) qui est comparable aux tensioactifs parents parce que les anions tetrahalideferrate ne sont pas étroitement associés à la tête. La structure des micelles est également similaire à celles des micelles parents, mais aucune interaction entre micelles n'a été observée en raison de l'encombrement des anions tetrahalideferrate. En effet, ces tensioactifs magnétiques sont intéressants car ce sont des liquides moléculaires, plutôt que des fluides magnétiques (ferrofluides), qui sont constitués de particules colloïdales métalliques (10 nm) dispersées dans un fluide porteur. Il faut noter que, MILS peuvent garder une réponse magnétique, même en solution aqueuse diluée.

Dans ce chapitre, une nouvelle approche en utilisant des tensioactifs ioniques liquides magnétiques est proposée pour la conception de matériaux de silice magnétique. Tout d'abord, la description de la synthèse de divers tensioactifs ioniques liquides magnétiques a été mise au point comme sonde magnétique pour étudier le mécanisme d'auto-assemblage de vésicules.

Ensuite, la synthèse et l’étude de propriétés magnétiques de silices poreuses en utilisant uniquement des tensioactifs ioniques liquides magnétiques sont abordées. Puis, ces composés sont combinés avec des nanoparticules lipidiques solides (SLN) pour la préparation de silices méso-macroporeuses associées à des nanoparticules d'oxyde de fer qui ont été utilisées en catalyse.

D’abord, les propriétés de synthèse et d'auto-assemblage de tensioactifs magnétiques ont été étudiées. Des vésicules, formés avec deux tensioactifs magnétiques, ont été caractérisés par s*mall-angle neutron scattering* (SANS), diffusion de lumière dynamique (DLS) et *nanoparticles tracking analysis* (NTA). Les résultats montrent que la taille des vésicules sont indépendantes de la concentration et de la proportion des 2 tensioactifs. De plus, un phénomène de transition de spin avant / après formation de vésicules a été observé, permettant de proposer un mécanisme d'auto-assemblage des vésicules.

Ensuite, les tensioactifs magnétiques ont été utilisés pour le développement de silices mésoporeuse magnétiques. Il a été montré que des ions Fe ont été adsorbés sur la surface des mésopores sur 3 nm d'épaisseur sans formation de nanoparticules métalliques. Il a été également observé qu’un phénomène de transition de spin de Fe (III) est présent lorsque la température est inférieure à 10 K. Cette anomalie serait due à la réduction de volume pour des Fe (III), induit par la présence des canaux mésoporeux, dont le diamètre est de 2,4 nm.

Enfin, les tensioactifs magnétiques ont été utilisés pour la conception d’un catalyseur. Cette fois, le tensioactif magnétique avec les ions Fe jouent le rôle de co-tensioactif pour les nanoparticules lipidiques solides (SLN). Le catalyseur à silice méso-macroporese a été obtenu par addition d'un précurseur de silice, suivie par une calcination qui permet de former des nanoparticules d'oxyde de fer. La réaction de *Dark-Fenton* pour la dégradation de bleu de méthylène a été testée, et montre que la performance catalytique est bonne due à la structure méso-macroporeuse de la silice.

General Conclusion

Designing smart drug delivery system is one of the main challenges in biomedical fields. Mesoporous silica materials have been considered as promising candidates for this object, providing the uniform pore network and the good biocompatibility. In addition, hydrophobic drugs encapsulated in mesoporous silica materials show improved bioavailability, due to reduced drug particles size. Hence, the development of stimuli-responsive mesoporous silica materials has been of great importance for practical applications of hydrophobic drugs in clinic.

In this work, we focused on the development of stimuli-responsive drug delivery system based on mesoporous and hierarchical meso-macroporous silica materials by proposing original approaches such as solid lipid nanoparticles (SLN) or magneto-responsive surfactant template strategies.

First, curcumin-loaded meso–macrostructured silica materials were developed by mineralizing dispersions of solid lipid nanoparticles (SLN). It was revealed that the partition of curcumin between SLN and micelles depends on the nature of lipid of SLN (20% for cetyl palmitate and 65% for stearic acid), due to the interaction between lipid and curcumin, as confirmed by SAXS and FT-IR. The release of curcumin is pH-dependent for both stearic acid and cetyl palmitate-based silica materials. Moreover, a two-step release pattern was observed for stearic acid SLN based silica materials at pH 1.2, which suggest that SLN acts as reservoirs of curcumin, whereas mesopores are the pathways of curcumin release. The cytotoxicity study suggests that the newly designed hybrid organic-inorganic silica materials could have potential applications in biomedical fields with improved stability and sustainability of guest drug release.

Based on the method applied in the first work, hybrid core-shell silica microcapsules using solid lipid nanoparticles were obtained. Curcumin-loaded microcapsules are 2 μm- sized with wormlike mesoporous silica shell of 0.3 μm in thickness as characterized by SAXS, N_2 adsorption/desorption, and TEM measurements. These materials also showed pH dependent *in vitro* release profile with marked drug retention at pH 2.8, due to the aggregation of silica particles explained by the isoelectric point of silica of about 2 - 3. This property of silica could be an advantage for oral administration route, because the average basal pH value in the stomach is between 2 - 3, which could effectively retain curcumin release from silica microcapsules. Moreover, the cell-uptake test revealed that fluorescent-labelled hybrid SLN-

silica microcapsules were well internalized into Caco-2 cells, confirming the possibility to use these capsules for gut cells targeting drug release.

Multi stimuli-responsive drug delivery system is also particularly interesting to better control the release profile of drug. Especially, cancer tissues exhibit lower pH value and higher concentration level of glutathione (GSH) than normal tissues. Thus, a careful but simple tailoring of stimuli-responsiveness of mesoporous silica materials is needed for the treatment of cancer tissues with anti-cancer drug such as curcumin. For this goal, tannic acid-Fe(III) complex coated mesoporous silica nanoparticles was developed by successive addition of iron (III) ions and tannic acid in the dispersion of curcumin loaded mesoporous silica. TEM experiments confirmed that tannic acid-Fe(III) complex of about 5.3 nm in thickness was deposited on the surface of silica nanoparticles, which provides pH and glutathione (GSH) responsiveness. The release of curcumin was effectively retained under physiological condition (pH 7.4), while a rapid curcumin release was triggered by lowering the pH to 6.0 or 4.5. In addition, curcumin release could be controlled by adjusting the glutathione (GSH) level. Hence, these results would allow developing novel and simple pH- and glutathione-responsive drug delivery systems with potential applications in biomedicine fields.

Second, the magneto-responsive surfactants were chosen for the design of magneto-responsive mesoporous silica materials. For this, the synthesis and self-assembly properties of magneto-responsive surfactants were firstly studied. Novel vesicle systems, which consist of ion pair of magneto-responsive surfactants, were developed. Small-angle neutron scattering (SANS), dynamic light scattering (DLS) and nanoparticles tracking analysis (NTA) experiments showed that the vesicle sizes are independent of the ratio of ion pair and vesicles solution concentration. The magnetic properties measurements revealed spin transition phenomenon before/after vesicle formation, which allow proposing the mechanism of vesicles formation.

These magneto-responsive surfactants were then used as both structure directing agent and iron source for magnetic mesoporous silica materials. The materials were characterized using Small-angle neutron scattering (SAXS), N_2 adsorption/desorption, Diffuse Reflectance UV-Vis and TEM measurements, showing that iron ions were imprinted on the surface of mesopore with 3 nm in thickness without forming metallic nanoparticles. Importantly, by magnetic measurement, it was observed that the spin crossover for Fe(III) arises when decreasing the temperature under 10 K. This abnormality would be due to the reduction of

cell volume for Fe (III), caused by mesopore, which diameter is 2.4 nm. As further applications, magneto-responsive might open up the possibility of tailoring the interdistance between the metallic centres, improving the performance of some catalytic reactions. Moreover, homogenously dispersed catalytic metallic centre across the support could be of interest for the design of the high performance catalysts.

Finally, magneto-responsive surfactants were employed for designing iron oxide embedded meso-macroporous silica supported catalyst. Magneto-responsive surfactant with iron ions was used as co-surfactant to stabilize solid lipid nanoparticles (SLN). The surfactant amount needed was determined by monitoring zeta potential of magneto-responsive surfactant decorated solid lipid nanoparticles. The catalyst was then obtained by addition of silica precursor, followed by the calcination that allows forming iron oxide nanoparticles across silica matrix. The catalyst was characterized using SAXS, powder XRD, N_2 adsorption/desorption, TEM-EDX, ICP-OES, which proved hierarchical structure of meso-macropores and the crystalline phase, the size and the weight percent of iron oxide nanoparticles as hematite, 10- 20 nm and 4 wt.%, respectively. As application, dark Fenton-like reaction towards methylene blue degradation was tested with newly designed catalyst, which showed almost same catalytic performance with only 10 % of active catalytic centre, compared with conventional iron oxide based catalysts.

In summary, stimuli-responsive mesoporous silica materials have been developed based on two original approaches using 1) solid lipid nanoparticles (SLN), 2) magneto-responsive surfactants for various applications, including encapsulation/release of hydrophobic drug and catalysis. It was shown that the design of silica materials could be achieved by simple, but efficient methods, resulting in biocompatible drug delivery system or magneto-responsive silica materials. Although any biomedical application was not demonstrated using magneto-responsive silica materials, it is obvious that these materials could be applied in biomedicine domain as targeting drug delivery system under magnetic fields. Therefore, this work would be of interest for large audience of chemists or in various fields of chemical engineering, biology and nanomedicine.

Conclusion Générale

La conception de systèmes intelligents de délivrance de médicaments est un grand défi dans le domaine biomédical. Dans ce cadre, les matériaux silicatés mésoporeux sont considérés comme des candidats prometteurs puisqu'ils possèdent un réseau de pores homogènes et une bonne biocompatibilité. En outre, les médicaments hydrophobes encapsulées dans de tels matériaux présentent une meilleure biodisponibilité, en raison de la réduction de taille des particules de médicament. Par conséquent, le développement de matériaux silicatés mésoporeux stimuli-sensibles est d'une grande importance pour véhiculer des médicaments hydrophobes.

Dans ce travail, nous nous sommes concentrés sur le développement de systèmes de délivrance de médicaments stimuli-sensibles à base de matériaux silicatés mésoporeux et méso-macroporeux en proposant des approches originales en utilisant des nanoparticules solides lipidiques (SLN) ou des tensioactifs magnétiques.

Tout d'abord, les matériaux silicatés méso-macroporeux chargés en curcumin ont été préparés par minéralisation de dispersions de nanoparticules lipidiques solides (SLN). Il a été révélé que la répartition de la curcumine entre les SLN et les micelles dépend de la nature du lipide du SLN (20% pour palmitate cétylique et 65% pour acide stéarique), en raison des interactions entre le lipide et la curcumine. La libération de la curcumine est dépendante du pH pour les matériaux à base de palmitate cétylique ou d'acide stéarique. La libération de la curcumine à pH 1,2 se fait en 2 étapes pour les matériaux synthétisés avec les SLN composé d'acide stéarique, ce qui suggère que les SLN agissent comme des réservoirs pour la curcumine, tandis que les mésopores permettent de libérer la curcumine. L'étude de cytotoxicité suggère aussi que les matériaux hybrides organiques-inorganiques pourraient avoir une meilleure stabilité et la durabilité que les systèmes existants.

La même méthode a été adaptée pour préparer des microcapsules hybrides de silice '*core-shell*' à base des nanoparticules lipidiques solides. Les microcapsules chargées en curcumine ont une taille de 2 µm et la coquille de silice mésoporeuse est de 0,3 um d'épaisseur. La libération de la curcumine à partir de ces matériaux est également dépendt du pH et une rétention marquée à pH 2,8 a été mise en évidence, en raison de l'agrégation des particules de silice, puisque le point isoélectrique de la silice est entre pH 2 et 3. Cette propriété de la silice pourrait être mise à profit pour l'administration orale, puisque la valeur du pH moyen dans

l'estomac est entre 2 – 3. La curcumine pourrait ainsi être retenue dans les microcapsules de silice. En outre, le test d'absorption cellulaire a révélé que les microcapsules hybrides SLN-silice marquées par une molécule fluorescente, *Nile Red*, ont été bien internalisées dans les cellules Caco-2, confirmant la possibilité d'utiliser ces capsules pour vectoriser des principes actifs les cellules de l'intestin.

Les systèmes de délivrance de médicaments à caractère multi stimuli-sensibles sont particulièrement intéressants pour mieux contrôler le profil de libération du médicament. En particulier, les tissus cancéreux ont un faible pH, et une forte concentration en glutathion (GSH) par rapport aux tissus normaux. Ainsi, les matériaux silicatés mésoporeux dopés en curcumine peuvent être adaptés pour le traitement de tissus cancéreux. Pour atteindre cet objectif, des nanoparticules de silice mésoporeuse enrobées d'un complexe d'acide tannique-Fe(III) ont été préparées par addition successive de fer (III) et d'acide tannique dans une dispersion aqueuse de silice mésoporeuse dopée en curcumine. Les analyses TEM ont confirmé que le complexe d'acide tannique-Fe (III) a bien été déposé sur la surface de nanoparticules de silice sur une épaisseur de 5,3 nm, ce qui conduit à un système sensible au pH et au glutathion (GSH). La curcumine est effectivement retenue dans les conditions physiologiques (pH 7,4), tandis que la libération de la curcumine est déclenchée aux pH inférieurs à 7.4. En outre, la libération de la curcumine peut être contrôlée en ajustant la concentration du glutathion (GSH). Par conséquent, ces résultats prometteurs pourraient conduire au développement des systèmes de délivrance de médicaments simples et sensibles au pH et au glutathion pour applications dans le domaine de la biomédecine.

D'autre part, des tensioactifs magnétiques ont été synthétisés pour concevoir des silices mésoporeuses magnétiques. Les propriétés d'auto-assemblage de tensioactifs magnétique ont été étudiées et un nouveau système de vésicules, composé de deux tensioactifs magnétiques contenant du Fe, a pu être ainsi préparé. La diffusion des neutrons aux petits angles (SANS), la diffusion de lumière dynamique (DLS) et l'analyse du suivi des particules (NTA) ont montré que la taille des vésicules sont indépendantes de la proportion des deux tensioactifs et de la concentration en vésicule. Les mesures des propriétés magnétiques ont mis en évidence un phénomène de transition de spin avant / après la formation de vésicules, lequel participe à la compréhension du qui mécanisme de formation de ces vésicules.

Ces tensioactifs magnétiques ont ensuite été utilisés à la fois comme agent de structuration et comme source du fer pour la préparation de silices mésoporeuse magnétiques. Les matériaux

ont été caractérisés en utilisant la diffusion des rayons X aux petits angles (SAXS), l'adsorption / désorption d'azote, la réflectance diffuse UV-Vis et le TEM. Il ressort que les ions Fe ont été adsorbés sur la surface des mésopores sur l'épaisseur de 3 nm sans formation de nanoparticules métalliques. Par des mesures de magnétisme, on a observé que les *spin crossover* de Fe (III) se produit lorsque la température inférieure est à 10 K. Cette anomalie serait due à la réduction du volume des cellules de Fe (III), due à la présences des mésopores, dont le diamètre est de 2,4 nm. Comme d'autres applications, la magnéto-sensibilité permettre la possibilité d'adapter à la demande l'interdistance entre les centres métalliques pour l'amélioration de la performance de certaines réactions catalytiques. Avec une dispersion homogène des centres métalliques catalytiques, on peut espérer concevoir des catalyseurs de haute performance.

Enfin, les tensioactifs magnétiques ont été utilisés pour la conception d'un catalyseur à base de silice méso-macroporeuse en présence d'oxyde de fer. Un tensioactif magnétique qui contient des ions Fe a été utilisé comme co-tensioactif pour stabiliser les nanoparticules lipidiques solides (SLN). La quantité de tensioactif nécessaire a été déterminée par potentiel. Le catalyseur a été ensuite obtenu par addition d'un précurseur de silice, suivie par une calcination qui permet de former des nanoparticules d'oxyde de fer au sein de la matrice de silice. Le catalyseur a été caractérisé en utilisant le SAXS, le XRD, l'adsorption / désorption d'azote, le TEM-EDX, l'ICP-OES. La structure hiérarchisée méso-macropores et la présence de la phase cristalline, la taille (10 - 20 nm) et le pourcentage (4% en poids) des nanoparticules d'oxyde de fer sont ainsi mis en évidence. La réaction de *Dark-Fenton* pour dégrader le bleu de méthylène a été testée. Les résultats montrent que la performance catalytique avec seulement 10% de centre catalytique actif est la même que les catalyseurs classiques à base d'oxyde de fer.

En résumé, les silices mésoporeues stimuli-sensibles ont été développés sur la base de deux approches originales 1) utilisation de nanoparticules lipidiques solides (SLN), 2) utilisation de tensioactifs magnétiques pour l'encapsulation / libération de médicament hydrophobe et pour la catalyse. Il a été montré que la conception de ces matériaux peuvent être réalisée par des procédés simples, mais efficaces, ce qui permet d'espérer au développement de système biocompatible de délivrance de médicament ou de matériaux silicatés magnésiques. Bien qu'aucune application biomédicale n'ait été à ce jour démontrée en utilisant des matériaux silicatés magnétiques, les résultats obtenus dans ce travail ont un véritable potentiel d'application dans le domaine biomédical en tant que vecteur de médicament sous champ

magnétique. Par conséquent, ce travail est d'intérêt pour un large public qui va de la chimie ou à divers domaines du génie chimique, de la biologie et de la nanomédecine.

Appendix

- Techniques of Characterization

Small angle X-ray scattering (SAXS)

Small angle X-ray scattering (SAXS) is an analytical method to determine the structure of particle systems in terms of averaged particle sizes or shapes, such as organized molecular systems containing surfactant molecules. This technique is based on the differences in electron densities between the scattering objects and continuous medium. The intensity distribution curves = f (q) of micelles, microemulsions can be accessed using theoretical models of geometry and size of aggregates, as well as among aggregation (number of surfactants per micelle), the conformations of the hydrophilic chains and hydrophobic and other parameters describing the system. For samples with a regular organization, for example liquid crystal phases, the diffraction beam of photons X on different planes of the structure leads to the observation of peaks caused by Bragg geometry characteristics of the system. The repeat distance between these planes diffraction is given by Bragg's law:

$$2d_{h,k,l} \sin\theta = n\lambda$$

where $d_{h,k,l}$ is for Bragg distance, θ for half-angle diffraction, n for order of reflection (integer) and λ for wavelength of X-rays.

The relationship between the repeat distances determined from the Bragg reflection reveals the structure of the studied system. According to Bragg's law, in the range of small angle, the greater the distance of repetition is, the smaller the angle between the diffracted beam and direct beam is. Herein the distances repetition of the studied systems are in the size order of several nanometer, the diffraction angles are small, hereupon in order to detect the diffracted beam, the apparatus requires an important distance between sample and detector.

Hexagonal structure consists of infinitely long cylinders packed in a hexagonal array. The X-ray diffraction on a hexagonal structure leads to the appearance of Bragg reflection with decreasing intensity whose positions are defined by q_0, $q_1 = 3\ q_0$, $q_2 = 2q_0$, $q_3 = 7q_0$,etc…

These reflections are due to the diffraction of incident beam on different planes. (Figure A1) From the geometrical considerations, the composition of system and the partial volumes of hydrophobic and hydrophilic parts of surfactant, it is also possible to calculate the structural parameters from the repetition distance, such as hydrophobic radius and the cross-sectional area.

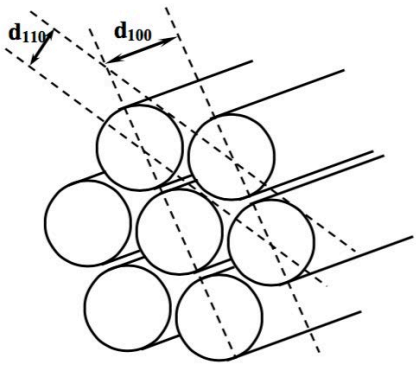

Figure A1. Hexagonal structure of packed cylinders.

In this work, detailed configuration and setting values used for the measurement of porous silica materials are described as following: small angle X-ray Scattering (SAXS) measurements for silica materials were carried out on a SAXSess mc^2 (Anton Paar) apparatus, using a line-collimation system. This instrument is attached to a ID 3003 laboratory X-Ray generator (General Electric) equipped with a sealed X-Ray tube (PANalytical, $\lambda_{Cu,\ K\alpha}$ = 0.1542 nm) operating at 40 kV and 50 mA. A multilayer mirror and a block collimator provide a monochromatic primary beam. A translucent beam stop allows the measurement of an attenuated primary beam at q=0. Samples were sealed between two sheets of Kapton® polyimide film, before being placed inside an evacuated sample chamber, and exposed to X-Ray beam for 15 minutes. Scattering of X-Ray beam was recorded on an Image Plate detector, with a sample-detector distance of 261.2 mm. All the data were then corrected for the background scattering from the Kapton® and for slit-smearing effects by a desmearing procedure using the Lake method.

Nitrogen adsorption-desorption analysis

The knowledge of the pore-network texture based on physical adsorption-desorption analyses is fundamental to the characterization of nanometric powders. In our study, we employ this method to determine the pore sizes and specific surface area of the mesoporous materials.

In 1938, by introducing a number of simplifying assumptions, Stephen Brunauer, Paul Emmett and Edward Teller were able to extend the Langmuir mechanism to multilayer adsorption and obtain an isotherm equation (the BET equation)

Introducing mathematical algorithms to this method, the differences between adsorption and desorption isotherms are discussed and the main parameters values were determined, such as specific surface area, pore volume and pores size distribution. The specific surface area is calculated from the monolayer volume at low pressures and molecular area per an adsorbed molecular:

$$S_{BET} = \frac{V_m}{V_{mol}} N_a \sigma$$

where σ is for molecular area per an adsorbed molecular (16.2 $Å^2$ for N_2 at - 196°C), V_{mol} for molar volume of gas and N_a for Avogadro number.

Experimental adsorption isotherm recorded in the literature has a wide variety of forms. Nevertheless, the majority of these isotherms, which result from physical adsorption may conveniently be grouped into six classes in the IUPAC classification (Figure A2).

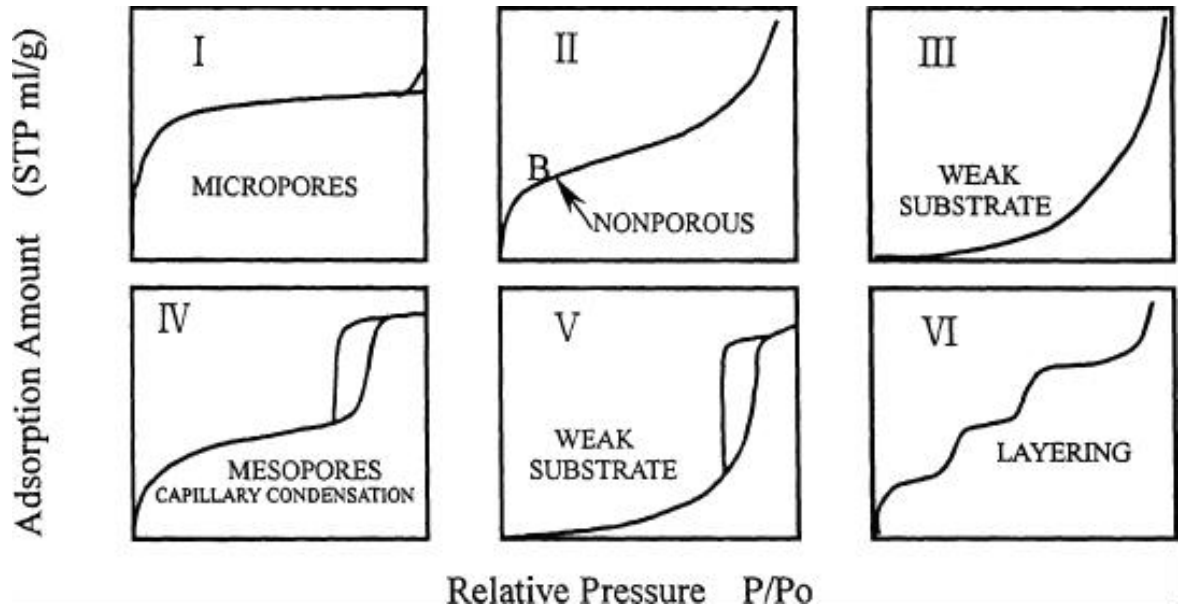

Figure A2. IUPAC classification of adsorption isotherms.

- Type I isotherm indicates the existence of micropores in the given system. It rises sharply at low relative pressures and reaches a plateau: the amount adsorbed by the unit mass of solid approaches a limiting value as p/p0 goes to 1.

- Type II isotherm is obtained with non-porous or macroporous adsorbents, which allow unrestricted monolayer-multilayer adsorption to occur at high p/p0.

- Type III isotherm is not common. This feature is indicative of weak adsorbent-adsorbate interactions.

- Type IV isotherm indicates the existence of mesopores in the given system. Its initial region is closely related to the Type II isotherm, trends to level off at high relative pressures. It exhibits a hysteresis loop, the lower branch of which represents measurements obtained by progressive addition of gas of the adsorbent and the upper branch by progressive withdrawal. The hysteresis loop is usually associated with the filling and emptying of the mesopores by capillary condensation.

- Type V isotherm is relatively rare. As in the case of Type III isotherm, it levels off at high relative pressures, which is indicative of weak adsorbent-adsorbate interactions. In addition, it also exhibits a hysteresis loop, which is associated with the mechanism of pore filling and emptying.

- Type VI isotherm is also relatively rare and is associated with layer-by-layer adsorption on a highly uniform surface.

Thanks to its inert and reversible adsorption properties, nitrogen (at -196°C) is generally considered to be the most suitable adsorptive for standard surface area determination. For this purpose, nitrogen adsorption-desorption isotherms were obtained at -196°C, over a wide relative pressure range from 0.01 to 0.995, with a volumetric adsorption analyser TRISTAR 3000 manufactured by Micromeritics. The samples were degassed under vacuum for several hours before nitrogen adsorption measurements to remove water and CO_2 physisorbed in the pores of material.

The pore diameter and the pore size distribution were determined by the BJH (Barret, Joyner and Halenda) method. Except using a model of the adsorbent as a collection of cylindrical pores, this theory is based on the phenomenon of capillary condensation which appears in the mesopores and the applicability of simple Kelvin equation which involves the assumption of hemispherical meniscus with zero contact angles.

$$ln\frac{P}{P_0} = \frac{\gamma V_m}{(r_p - t)RT}$$

where γ is for surface tension at given temperature T, r_p for pore radius and t for thickness of an adsorbed layer.

This method is applied to the adsorption branch of the isotherm in case of there is interconnected pore network which could induce the desorption branch of the isotherm give incorrect information in the calculation. Based on an iterative calculation, it allows the calculation of the amount of adsorbed gas between a given pressure interval. From the value of pore radius as a function of relative pressure, it is possible to determine the accumulated volume of all these intervals depending on the pore radius. Although it is well-known that this method gives an underestimated pore size around 20% and that some new methods have been developed, we used it here for the sake of simplicity and this mathematical algorithm does not significantly affect the results as it is a systematic comparison.

Dynamic light scattering (DLS)

Dynamic light scattering (DLS) (also known as Photon Correlation Spectroscopy or Quasi-Elastic Light Scattering) is a technique in physics, which is used to determine the size distribution profile of small particles such as micelles, microemulsions and solid lipid nanoparticles.

In the limit of infinite dilution, the apparent hydrodynamic radius R_h can be estimated from the Stokes-Einstein equation. Apparently, the apparent hydrodynamic radius includes solvent effects.

$$D = \frac{K_b T}{6\pi\eta R_h}$$

where K_b stands for Boltzmann constant, T for temperature, η for viscosity and R_h for particle radius.

In our work, DLS is employed to study size distributions of micelles, solid lipid nanoparticles as well as mesoporous silica nanoparticles.. DLS experiments were carried out using a Zeta 3000HS (Malvern Instruments, Ltd. UK) at 25 °C. It is equipped with an argon laser (= 633 nm) with variable intensity, which allows covering the wide size range involved. The hydrodynamic radius measurements were carried out at a scattering angle of 90°. Almost all the samples were diluted with water before the measurement.

Mercury porosimetry

This technique was used in order to determine the size of macropores present in the materials with a hierarchical porosity. Being capable of measuring pore diameters up to a few tens of micrometers, it is complementary to the adsorption-desorption of nitrogen that allows knowing the pore size in the meso and macropore scale. Mercury porosimetry is based on the non-wetting properties of mercury. When mercury is in contact with a solid, it does not adsorb on the walls immediately, because it has a high surface tension. This causes a resistance, which prevents the penetration of mercury into the pores. This resistance can be overcome if an external pressure is applied.

There is a relationship between this pressure and the pore size of which is given by the equation of Washburn, which can be expressed as follow:

$$D = -\left(\frac{1}{P}\right) 4\gamma cos\varphi$$

where D stands for pore diameter, P for the applied pressure, γ for the surface tension, and φ for contact angle. The applied pressure (P) can be obtained form the volume (V) of mercury penetrating the pores. Although pores are rarely cylindrical, the use of this model is generally accepted as the practical manner in mercury porosimetry. In this work, mercury intrusion porosimetry experiments were performed using Micrometiric AutoPore IV.

Scanning electron microscopy (SEM)

The scanning electron microscope (SEM) is a type of electron microscope that images the sample surface by scanning it with a high-energy beam of electrons in a raster scan pattern. The electrons interact with the atoms that make up the sample producing signals that contain information about the sample's surface topography, composition and other properties such as electrical conductivity. Due to the very narrow electron beam, SEM micrographs have a large depth of field yielding a characteristic three-dimensional appearance useful for understanding the surface structure of a sample. A wide range of magnifications is possible, from about 10 times (about equivalent to that of a powerful hand-lens) to more than 500,000 times, about 250 times the magnification limit of the best light microscopes. Thus we are able to observe the particle morphology closely on a very fine scale.

For conventional imaging in the SEM, specimens must be electrically conductive, at least at the surface, and electrically grounded to prevent the accumulation of electrostatic charge at the surface. Nonconductive specimens are therefore usually coated with an ultrathin coating of electrically conducting material, commonly gold or graphite, deposited on the sample either by low vacuum sputter coating or by high vacuum evaporation.

The technique of SEM is to focus on a surface of specimen by lens using a condensed electron beam. The interaction between electrons and the material leads to the backscattered electron emission, X-rays, secondary electrons and so on. These electrons are collected by a detector, converted to a voltage and finally amplified. The apparatus used in this study is microscope HITACHI, S-models 2500 at 15 KeV.

Transmission electron microscopy (TEM)

The transmission electron microscopy allows the observation of a local arrangement of the pores of the material and therefore cannot replace the DRX or SAXS giving an overall view of the composite structure. The image comes from the interactions occurring during the passage of an electron beam accelerated by a high voltage across the sample.

The samples were prepared by dispersing in ethanol under sonication and then a few drops are deposited on the analysis plate, which is generally a holey carbon coated copper grid. The principle is to send a beam of accelerated electrons to 105 volts on an ultra-thin sample (a few hundred nanometers) and analyse the transmitted beam. It gives the information about the crystal structure of the compound through the diffraction properties of the electrons and the contrast is dependent on the atomic number of the element. In this work, all experiments were performed on a Philips / FEI CM200 200 keV.

Abstract:

This work is to prepare stimuli-responsive porous silica materials based on solid lipid nanoparticles (SLN) and magnetic surfactants. To develop this study, several surfactants systems were used to synthesize silica materials with controlled porosity via protocols described in the literature or developed in the laboratory. Different stimuli-responsive characters were introduced in porous silica materials as a function of system used: solid lipid nanoparticles (SLN) for pH-sensitive and magnetic-sensitive surfactants for magnetic silica materials.

First, the materials synthesized with solid lipid nanoparticles (SLN) were used for the delivery of an anti-carcinogenic drug, curcumin. A coating method on silica surface was also used to better control the release of curcumin. Secondly, the responsiveness to the magnetic field was introduced in silica materials using the magnetic surfactants. Their self-assembly properties (i.e. micelles, vesicles) were studied and their applications in the synthesis of magnetic porous silica materials were investigated. Finally, the magnetic solid lipid nanoparticles have been prepared by combining SLN with magnetic surfactants, which have been used for the synthesis of meso-macroporous silica catalyst encapsulating iron oxide nanoparticles.

Keywords: meso-macroporous silica, solid lipid nanoparticles (SLN), vectorization, curcumin, magneto-responsive surfactants, magnetic properties.

Résumé:

Ce travail a consisté à préparer des matériaux silicatés poreux à caractère stimuli-sensible à base de nanoparticules lipidiques solides (SLN) et de tensioactifs magnétiques. Plusieurs systèmes à base de tensioactifs ont été utilisés afin de synthétiser des matériaux silicatés à porosité contrôlée en utilisant des méthodes décrites dans la littérature ou mises au point au laboratoire. De différents caractères stimuli-sensible ont été introduits dans les matériaux silicatés poreux en fonction de système utilisé: les nanoparticules lipidiques solides (SLN) pour les matériaux sensible au pH et les tensioactifs magnétiques pour les matériaux sensible au champ magnétique.

Premièrement, les matériaux à base de nanoparticules lipidiques solides (SLN) ont été utilisés pour la vectorisation d'un principe actif, la curcumine. La libération de la curcumine a été contrôlée en fonction de pH. Un revêtement sur la surface silice a été également employé pour mieux contrôler la libération de la curcumine. D'autre part, la sensibilité au champ magnétique a été introduite dans des silices mésoporeuse en utilisant des tensioactifs magnétiques. Leurs propriétés d'auto-assemblage (*i.e.* micelles, vésicules) ont été mise en évidence. Ainsi, la synthèse de matériaux silicatés poreux à caractère magnétique-sensible a été effectuées en utilisant ces tensioactifs. Enfin, les SLN magnétiques ont été préparés en combinant les SLN avec un tensioactif magnétique, qui ont été servi pour la synthèse de catalyseur à base de la silice méso-macroporeuse dopée en nanoparticules d'oxyde de fer.

Mots clés : silice méso-macroporeuse, nanoparticules lipidiques solides, vectorisation, tensioactifs magnétiques, curcumine, propriétés magnétiques